Algorithms for handling arbitrary lineshape distortions in Magnetic Resonance Spectroscopy and Spectroscopic Imaging

Emil Horia Popa

N° d'ordre : 123-2010 Année 2010

THESE

présentée devant

l'UNIVERSITE CLAUDE BERNARD - LYON I

pour l'obtention

du DIPLOME DE DOCTORAT

(arrêté du 7 août 2006)

par

POPA Emil Horia

Algorithms for Handling Arbitrary Lineshape Distortions in Magnetic Resonance Spectroscopy and Spectroscopic Imaging.

Soutenue le 15 Juillet 2010

Spécialité : **Images et Systèmes**

Directeur de thèse : **Danielle GRAVERON-DEMILLY**

JURY :	**André BRIGUET**	Président
	Sylviane CONFORT GOUNY	Rapporteur
	Danielle GRAVERON-DEMILLY	Directeur
	Marijn KRUISKAMP	Examinateur
	Vladimir MLYNARIK	Examinateur
	Dominique SAPPEY-MARINIER	Examinateur
	Johannes SLOTBOOM	Invité
	Dirk VAN ORMONDT	Rapporteur
	Steve WILLIAMS	Examinateur

UNIVERSITE CLAUDE BERNARD - LYON 1

Président de l'Université	**M. le Professeur L. Collet**
Vice-président du Conseil Scientifique	M. le Professeur J-F. Mornex
Vice-président du Conseil d'Administration	M. le Professeur G. Annat
Vice-président du Conseil des Etudes et de la Vie Universitaire	M. le Professeur D. Simon
Secrétaire Général	M. G. Gay

COMPOSANTES SANTE

Faculté de Médecine Lyon Est – Claude Bernard	Directeur : M. le Professeur J. Etienne
Faculté de Médecine Lyon Sud – Charles Mérieux	Directeur : M. le Professeur F-N. Gilly
UFR d'Odontologie	Directeur : M. le Professeur D. Bourgeois
Institut des Sciences Pharmaceutiques et Biologiques	Directeur : M. le Professeur F. Locher
Institut des Sciences et Techniques de Réadaptation	Directeur : M. le Professeur Y. Matillon
Département de Biologie Humaine	Directeur : M. le Professeur P. Farge

COMPOSANTES ET DEPARTEMENTS DE SCIENCES ET TECHNOLOGIE

Faculté des Sciences et Technologies	Directeur : M. le Professeur F. Gieres
Département Biologie	Directeur : M. le Professeur C. Gautier
Département Chimie Biochimie	Directeur : Mme le Professeur H. Parrot
Département GEP	Directeur : M. N. Siauve
Département Informatique	Directeur : M. le Professeur S. Akkouche
Département Mathématiques	Directeur : M. le Professeur A. Goldman
Département Mécanique	Directeur : M. le Professeur H. Ben Hadid
Département Physique	Directeur : Mme S. Fleck
Département Sciences de la Terre	Directeur : M. le Professeur P. Hantzpergue
UFR Sciences et Techniques des Activités Physiques et Sportives	Directeur : M. C. Collignon
Observatoire de Lyon	Directeur : M. B. Guiderdoni
Ecole Polytechnique Universitaire de Lyon 1	Directeur : M. le Professeur J. Lieto
Institut Universitaire de Technologie de Lyon 1	Directeur : M. le Professeur C. Coulet
Institut de Science Financière et d'Assurance	Directeur : M. le Professeur J-C. Augros
Institut Universitaire de Formation des Maîtres	Directeur : M R. Bernard

Abstract

Magnetic Resonance Spectroscopy (MRS) and Spectroscopic Imaging (MRSI) play an emerging role in clinical assessment, providing *in vivo* estimation of disease markers while being non-invasive and applicable to a large range of tissues. However, static magnetic field inhomogeneity, as well as eddy currents in the acquisition hardware, cause important distortions in the lineshape of acquired NMR spectra, possibly inducing significant bias in the estimation of metabolite concentrations. In the post-acquisition stage, this is classically handled through the use of pre-processing methods to correct the dataset lineshape, or through the introduction of more complex analytical model functions.

This thesis concentrates on handling arbitrary lineshape distortions in the case of quantitation methods that use a metabolite basis-set as prior knowledge. Current approaches are assessed, and a novel approach is proposed, based on adapting the basis-set lineshape to the measured signal. Assuming a common lineshape to all spectral components, a new method is derived and implemented, featuring time domain local regression (LOWESS) filtering. Validation is performed on synthetic signals as well as on *in vitro* phantom data. Finally, a completely new approach to MRS quantitation is proposed, centred on the use of the compact spectral support of the estimated common lineshape. The new metabolite estimators are tested alone, as well as coupled with the more common residual-sum-of-squares MLE estimator, significantly reducing quantitation bias for high signal-to-noise ratio data.

Résumé

La Spectroscopie et l'Imagerie Spectroscopique de Résonance Magnétique (ISRM) jouent un rôle émergent parmi les outils cliniques, en donnant accès, d'une manière complètement non-invasive, aux concentrations des métabolites *in vivo*. Néanmoins, les inhomogénéités du champ magnétique, ainsi que les courants de Foucault, produisent des distorsions significatives de la forme de raie des spectres, induisant des conséquences importantes en terme de biais lors de l'estimation des concentrations. Lors des traitements post-acquisition, cela est habituellement traité à l'aide des méthodes de pré-traitement, ou bien par l'introduction de fonctions analytiques plus complexes.

Cette thèse se concentre sur la prise en compte de distorsions arbitraires de la forme de raie, dans le cas des méthodes qui utilisent une base de métabolites comme connaissance *a priori*. L'état de l'art est évalué, et une nouvelle approche est proposée, fondée sur l'adaptation de l'amortissement de la base des métabolite au signal acquis. La forme de raie présumée commune à tous les métabolites est estimée et filtrée à l'aide de la méthode LOWESS. L'approche est validée sur des signaux simulés, ainsi que sur des données acquises *in vitro*. Finalement, une deuxième approche novatrice est proposée, fondée sur l'utilisation des propriétés spectrales de la forme de raie commune. Le nouvel estimateur est testé seul, mais aussi associé avec l'estimateur classique de maximum de vraisemblance, démontrant une réduction significative du biais dans le cas des signaux à haut rapport signal-sur-bruit.

Acknowledgments

In the words of J-B. Poullet “research is seldom the work of one person”. The list of the persons that have helped me accomplish this work is too long to write here. For this reason, with few exceptions, I would not like to mention names, but rather groups of people, that through their invaluable contributions have made this thesis possible. However, I am personally indebted to all and each of the people who helped me, through scientific, administrative and personal challenges, and have thus rendered this thesis accomplished.

I am heartily thankful to my supervisor, Danielle Graveron-Demilly, whose encouragement, guidance and support from the initial to the final level enabled me to develop an understanding of the subject. I would like to give my special thanks to Dirk van Ormondt, to whom I am personally indebted. None of what is written in this thesis would have been here without the scientific and personal contributions of Mr. van Ormondt.

I owe my deepest gratitude to the members of the defense jury, who have honored me by reading and evaluating this work. Their invaluable remarks, as well as their critical perspectives have improved this work and shed new light on many issues. I would also like to acknowledge here the support of Philips Medical Systems NL, that in association with CNRS has provided the main funding for this work.

Special thanks go to all the members of the FAST network, that through their critical remarks have helped me improve the quality of this work. I would like to especially acknowledge the time I have spent in the teams of KU Leuven and MPI Leipzig, that through critical discussions have shed new lights on the research topics and have fostered new approaches.

I would also like to thank CREATIS-LRMN for welcoming me *au labo*. Special thanks go to the the *ALGECO inmates*, with whom I spent most of the time in the four years working for this thesis. I am also especially grateful to the laboratory staff, that I have bothered on many occasions, but that has always been supportive in my passage though the administrative maze.

I am indebted to all the colleagues that have helped me in the teaching tasks, let it be in the GEP UFR at Universié Lyon 1 or with the Département GE at INSA Lyon. Teaching has been an excellent experience, and I owe it to you. And of course, to the students, that through their hard work and inquisitive spirit have made every day seem a new challenge.

Last, but certainly not least, I would like to express my deepest gratitude to my family. Their unconditional support have made the darkest times easier to bear. This thesis would have certainly not been written without the invariable support and understanding of my wife, Alexandra. I would also like to thank *Bubulique* for being, although certainly without knowing it yet, a constant encouragement and bringer of hope in the critical last months of this work.

Notations

Greek letters

α	Damping factor
γ	Proton gyro-magnetic ratio
δ	Chemical shift (in ppm)
ϵ	noise
λ	Smoothing hyper-parameter
ν	Normalized frequency
σ	Nuclear shielding constant *or* Standard Deviation
φ	Phase
ω	Angular speed

Latin letters

B_0	Static magnetic field
B_1	RF pulse
c	Metabolite concentration
f	Frequency shift (Hz)
G_x, G_y, G_z	Magnetic gradient fields associated with the gradient coils.
$\mathbf{H}$	Hessian matrix
$\mathbf{J}$	Jacobian matrix
t_s	sampling time

Abbreviations

AMARES	Advanced Method for Accurate,Robust and Efficient Spectral fitting
AQSES	Accurate Quantitation of Short Echo time domain Signals[138]
AWG(N)	Additive White Gaussian (Noise)
BSR	Bias to standard deviation ratio
CI	Confidence Interval
CR(LV)B	Cramér-Rao (Lower Variance) Bounds [45, 152]
DF	Degrees of Freedom
DFT	Discrete Fourier Transform
ECC	Eddy Current Correction
ECD	Estimated Common Decay
FFT	Fast Fourier Transform [43]
FD	Frequency domain
HSVD	Hankel Singular Matrix Decomposition

iid	independent and identically distributed
LCModel	Linear Combination of Model [145]
LOWESS	Locally Weighted regression and smoothing scatter-plots [38]
LS	Least Squares
MC	Monte Carlo
MLE	Maximum Likelihood Estimator
MRS	Magnetic Resonance Spectroscopy
MRSI	Magnetic Resonance Spectroscopic Imaging
NLLS	Non-Linear Least Squares
NMR	Nuclear Magnetic Resonance
QUEST	Quantitation based on quantum estimation [156]
RMSE	Root Mean Square of Error
ROI	Region of Interest
SNR	Signal-to-Noise Ratio
TD	Time Domain
UdES	Undamped Estimated Signal
VOI	Volume of Interest
VARPRO	Variable Projection

Metabolite abbreviations

Cho	Choline	Lip	Lipids
Cr	Creatine	mI	Myo-inositol
Glc	D-Glucose	MM	Macromolecules
Gln	Glutamine	NAA	N-acetylaspartate
Glu	Glutamate	NAAG	N-Acetylaspartateglutamate
Gly	Glycine	PCr	Phosphocreatine
Lac	Lactate	tCr	Total Creatine (Cr+PCr)

Other symbols

$\Re\{z\}$	Real part of complex number z
$\|z\|$	Module of complex number z
$\imath$	Square complex root of -1 ($\imath = \sqrt{-1}$)
$\mathcal{N}$	normalizing factor *or* normal distribution
$\sqcup(\nu_{\min}, \nu_{\max})$	Inverted gate function ($\sqcup(\nu) = 0$ if $\nu_{\min} \leq \nu \leq \nu_{\max}$, and 1 otherwise)
$\mathbf{x} \odot \mathbf{y}$	Element-wise product of vectors $\mathbf{x}$ and $\mathbf{y}$ (Hadamard product).
$\mathcal{L}_2$	Total mean energy (the L_2 norm)
$\mathbb{E}[\cdot]$	Expectation operator
$\mathfrak{C}_1$	Cost function corresponding to LS residue
$\mathfrak{C}_2$	Cost function corresponding to spectral compactness (*cf.* chapter IV)
$\hat{\mathbf{p}}$	Estimated parameters
$\check{\mathbf{p}}$	True, unknown parameters

Contents

Préambule

Dès l'année 1959, le docteur E. Odeblad, écrivait sur la Résonance Magnétique Nucléaire (RMN) : "La RMN semble avoir maintes possibilités pour l'étude, de manière non invasive, de multiple problèmes en biologie et médecine... Avec le développement de l'instrumentation en RMN dans les laboratoires médicaux, cette technique va être utilisée en routine pour les diagnostics cliniques." [124] En 2010, les prévisions de Dr. Odeblad peuvent être considérées comme réalisées, car la majorité des grands hôpitaux possèdent des scanners RMN. De plus, grâce aux progrès techniques, à une vaste recherche méthodologique et à l'accroissement des ressources de calcul, une riche palette d'outils issus de la RMN est devenue accessible.

Parmi les nombreuses méthodes fondées sur la RMN, deux approches sont particulièrement intéressantes dans le cadre de cette thèse. La Spectroscopie RMN (SRM) et l'Imagerie Spectroscopique par RMN (ISRM) fournissent l'estimation des concentrations de différents métabolites [1] , *in vivo*, en s'affranchissant des procédures invasives (*e.g.* la biopsie) ou semi-invasives (*e.g.* des injections de marqueurs). L'absence d'effets secondaires connus et la nature non-invasive des méthodes (I)SRM ont rendu possible l'utilisation de ces techniques RMN dans des domaines peu explorés auparavant, comme le métabolisme du cerveau et du foie, ou l'imagerie pédiatrique.

Les pathologies du cerveau sont particulièrement intéressantes pour la communauté scientifique à cause du rôle qu'elles jouent dans les maladies liées au vieillissement des populations, surtout dans les pays développés. Les techniques de SRM et ISRM constituent des outils importants dans l'étude des pathologies du cerveau [44] comme : les accidents vasculaires cérébraux (AVC), les maladies neurodégénératives (Parkinson, Alzheimer), la sclérose en plaques [176], les affections neurologiques (l'épilepsie), les maladies mentales, etc. Parmi les moyens dérivés de (I)SRM on pourrait aussi mentionner des outils de diagnostic et pronostic (*ie.* études préopératoires [2]), de guidage du geste chirurgical ou biopsique ou bien du suivi postopératoire ou therapeutique (*ie.* analyse de l'efficacité du traitement, dépistage des récidives tumorales, prévention des complications, etc.).

Néanmoins, les études (I)SRM ne se limitent pas au cerveau. La SRM du cœur [80] et de la musculature striée [20] utilisent principalement des noyaux ^{31}P pour évaluer le métabolisme énergétique du phosphate, même si des techniques complémentaires existent basées sur des noyaux ^{1}H, ^{23}Na ou ^{13}C (hyperpolarisé). Des applications pour l'étude du foie [59] ou du pancréas [128], de même que la détection des néoplasmes (cancer de la prostate [118] et du sein [76]), sont également basées sur les techniques SRM. La méthode HRMAS (High-Resolution Magic Angle Spinning), même si impraticable *in vivo*, représente un outil précieux pour les analyses *ex vivo* à cause de sa très haute résolution spectrale.

1. Dans le contexte de ce travail, un métabolite est un composant biochimique qui participe, ou est le produit d'un ou plusieurs chemins métaboliques. Généralement ce terme est réservé aux composants de petites tailles.

Cependant, la RMN en général et les techniques I(SRM) en particulier, comportent de nombreux défis, surtout par leur besoin d'un savoir-faire interdisciplinaire. Le processus d'acquisition des signaux RMN n'est pas simple, et son développement nécessite l'interaction de spécialistes de nombreux domaines, comme l'électronique, l'ingénierie, les mathématiques, la physique quantique, etc. Une fois le signal acquis, quelques paramètres seulement (*ie.* les concentrations des métabolites) sont estimés, grâce à des méthodes non-triviales d'estimation paramétriques et/ou de traitement de signal. Pour les médecins, ce système complexe est automatisé et devient une boîte noire, devant mesurer et retourner un résultat avec un minimum de paramètres à configurer.

Avec les améliorations spectaculaires des performances des matériels et grâce à l'accessibilité aux ressources de calcul bon marché, le perfectionnement des techniques de traitement de signal associées à la RMN devient essentiel. A l'heure actuelle, les méthodes de quantification ne permettent pas la récupération intégrale de l'information suite à l'acquisition du signal. De plus, la mauvaise compréhension par les utilisateurs (les médecins), des limites liées aux algorithmes de quantification génère souvent des interprétations erronées des résultats ou peut engendrer le choix de protocoles de quantification sous-optimaux.

Objectifs et plan de la thèse

Cette thèse a pour objectif la mise en évidence de certains problèmes liés au traitement de signal et à l'estimation paramétrique à l'intérieur de cette boîte noire et de proposer des nouvelles méthodes et stratégies pour surmonter ses limitations. Une approche pédagogique est employée pour assurer un meilleur transfert de connaissances entre les spécialistes du traitement de signal et les utilisateurs des méthodes de quantification. La problématique de la quantification en RMN est construite depuis les bases physiques du phénomène et jusqu'à une estimation plus générale du modèle, avec un ajout de diverses informations complémentaires, nécessaires à la compréhension clinique, mathématique et numérique des méthodes de quantification SRM. Certaines questions, actuellement peu développées, comme l'estimation de la qualité de quantification, sont également traitées et le savoir-faire sur le sujet est passé en revue.

Cette thèse est structurée en deux grandes parties. La première partie, composée des chapitres I et II, passe en revue les techniques et approches existantes en RMN. Par ailleurs, la deuxième partie (troisième et quatrième chapitres), présente des approches nouvelles ayant pour but d'améliorer l'estimation des paramètres SRM.

Première partie

Dans le premier chapitre, nous présentons les bases physiques et méthodologiques de la spectroscopie et de l'imagerie spectroscopique par résonance magnétique. Nous décrivons d'abord le phénomène physique de la Résonance Magnétique Nucléaire, en insistant sur l'influence d'un champ magnétique hétérogène sur le signal acquis. Ensuite, la méthodologie d'acquisition est brièvement explorée, aussi bien pour la spectroscopie que pour l'imagerie spectroscopique. Finalement, les composants chimiques (métabolites) les plus utilisés dans l'étude par RM du cerveau sont décrits.

Le deuxième chapitre se concentre sur les problématiques liées au traitement de signal et à l'estimation paramétrique en SRM. Dans une première approche, à partir des relations

introduites dans le chapitre précèdent, un modèle du signal SRM est proposé. La forme de raie est introduite naturellement, à partir de l'influence du champ magnétique statique inhomogène. Cela permet aussi de poser le problème inverse de la SRM : comment à partir du signal acquis, sujet à de multiples facteurs, peut-on isoler et quantifier l'effet de la concentration de chaque métabolite ? Le reste du chapitre est consacré aux moyens mis en œuvre pour la résolution de ce problème inverse.

Le premier moyen analysé est l'emploi des transformations mathématiques pour décomposer le signal en une somme de signaux plus simples. La Transformée de Fourier est brièvement expliquée, ainsi que d'autres alternatives comme la décomposition en valeurs singulières (SVD) ou la Transformée de Padé.

Ensuite, nous traitons des techniques plus complexes, fondées sur l'inclusion de l'information *a priori* via un modèle physique. Les méthodes les plus pertinentes pour cette thèse sont décrites plus en détails, dans un format commun, facilitant la comparaison, tandis que le reste de l'état de l'art est présenté d'une manière plus brève.

L'avant-dernière section du chapitre II est consacrée à la prise en compte de la forme de raie des spectres RMN. Quelques techniques utilisées à ce jour sont répertoriées.

Enfin, la dernière section du chapitre touche une problématique d'un fort intérêt clinique, mais qui, à notre avis, à été insuffisamment traitée dans le monde RMN : l'estimation de la qualité des valeurs quantifiées. La théorie de Bayes liant incertitudes et erreurs est discutée, ainsi qu'une palette d'outils permettant de construire un intervalle de confiance pour les valeurs estimées, mais aussi des approches proposées dans le monde RMN pour rejeter des valeurs estimées aberrantes.

Deuxième partie

Le chapitre III est dédié aux études sur l'influence et l'estimation d'une forme de raie quelconque, commune à tous les métabolites, issue principalement des effets d'inhomogénéité du champ magnétique B_0.

Tout d'abord une étude a été menée pour comparer plusieurs approches de prise en compte d'une forme de raie non Lorentzienne. Des simulations Monte Carlo, ainsi qu'une démarche plus théorique, via les Bornes de Cramér-Rao, ont démontré que la meilleure approche est d'adapter la connaissance *a priori* (base des métabolites) au signal, et non l'inverse.

Ensuite, nous proposons une nouvelle technique pour estimer une forme de raie commune à tous les métabolites, sans utiliser une raie de référence. Cela est fait à partir d'un modèle du signal non-amorti, qui permet d'estimer une version bruitée de la fonction d'amortissement (forme de raie) commune (estimated common damping - ECD function). Ensuite, l'ECD est filtré, et la nouvelle information est utilisée pour adapter l'amortissement des signaux de la base des métabolites. Plusieurs études Monte Carlo sont menées pour valider et analyser la solution proposée. La même démarche est aussi utilisée sur des signaux réels de fantômes, issus d'une étude sur la sclérose en plaques.

Dans le quatrième chapitre, une nouvelle approche de quantification est proposée, fondée sur des principes développés dans le chapitre précèdent. Ainsi, au lieu d'estimer la ECD et ensuite l'utiliser pour améliorer la base des métabolites, on l'utilise comme une fonction coût pour estimer directement les paramètres d'intérêt (les concentrations). Alors que cette approche novatrice n'est pas encore assez développée pour être appliquée *in vivo*, nous en démontrons sa preuve de concept, avec un fort potentiel de développement ultérieur.

Les travaux mentionnés dans la deuxième moitié de cette thèse ont été réalisés en forte collaboration dans le cadre du projet européen FAST [2], et plus spécialement avec l'Université Technique (TU) au Delft, en Pays-Bas. Pour des travaux complémentaires, dans le cadre du même projet, voir les travaux de Osorio Garcia et al.[126, 127] à l'Université Catholique de Louvain (K.U. Leuven), en Belgique.

2. FAST, Advanced Signal-Processing for Ultra-Fast Magnetic Resonance Spectroscopic Imaging, and Training, (MRTN-CT-2006-035801) is a Research and Training Network (RTN) granted by Marie Curie Actions in the 6th Framework Program (2007-2010). URL : `http://www.fast-mariecurie-rtn-project.eu/`

Introduction

As early as 1959, Dr. E. Odeblad, a physician, wrote about nuclear magnetic resonance (NMR): "NMR really seems to possess extensive possibilities to help study, in a non-invasive way, many problems in biology and medicine ... When instruments for NMR become more common and available at medical laboratories, we may expect direct routine clinical diagnosis with this new technique" [124]. In 2010, Odeblad's prediction can undoubtedly be considered accomplished, with NMR machines installed in most major hospital centres. Moreover, advancements in hardware, as well as significant research in methodology and the increased computation resources available, have rendered accessible a large NMR-related tool-set, including whole-body MR Imaging (MRI), Diffusion MRI (DTI), MR angiography, functional MRI (fMRI) , MR Spectroscopy (MRS), MR spectroscopic imaging (MRSI), etc.

Among the large palette of methods engendered by NMR, two methods are of special interest to this thesis. NMR Spectroscopy, and the related NMR Spectroscopic Imaging allow estimation of different metabolite[3] concentrations, *in vivo*, without the use of invasive (*ie.* : biopsy) or semi-invasive (*ie.* injected markers) procedures. The lack of significant known side-effects, together with the non-invasive nature of MRS(I), have allowed the use of these NMR techniques in previously under-explored fields, such as brain and liver metabolomics or pædiatric imagery.

Brain pathologies are of special interest to the research community mainly due to the importance they play in health problems associated with ageing populations, especially in developed countries. MRS and MRSI have brought critical tools in the study of brain pathologies[44], including: cerebrovascular accidents (strokes), neurodegenerative diseases (Parkinson's, Alzheimer's, etc.), multiple sclerosis[176], neurological disorders (*ie.* epilepsy), psychiatric disorders, etc. Clinical tools derived from MRS(I) also include exploratory and assessment studies (*ie.* pre-surgery) [2], interventional guidance (*ie.* for biopsy or surgery) or follow-up studies (*ie.* non-invasive graft monitoring [12]).

MRS(I) studies have not been limited to the brain. MR spectroscopy of the heart[80] and skeletal muscles [20] focuses mainly on ^{31}P nuclei to determine the high-energy phosphate metabolism, although some applications have been also developed for ^{1}H, ^{23}Na or (hyperpolarized) ^{13}C nuclei. Hepatic [59] and pancreatic [128] applications, as well as neoplasia detection (*ie.* prostate [118] and breast cancer [76]) also strongly benefit from MRS. Worth mentioning here is also High-resolution Magic Angle Spinning (HRMAS) spectroscopy, that although, not practicable *in vivo*, proves to be an invaluable tool in *ex vivo* analysis.

However, NMR, in general, and MRS(I) in particular still pose great challenges, mainly due to requiring a wide interdisciplinary know-how. The NMR acquisition process is not simple, and its development requires interaction between specialists in many fields, such as

3. In the context of this work, a metabolite is defined as a biochemical compound that participates, or is the product of one or more metabolic pathways. Generally the term is restricted to molecules of small size.

electronics, electrical engineering, mathematics, quantum Physics, etc. Once a signal is acquired, only some parameters of interest (such as metabolite concentrations) are extracted through non-trivial parameter estimation and/or signal processing. All this system is commonly used by medical practitioners, mainly as a "one-button black-box", that is expected to measure and give a result, with as few parameters to configure as possible.

With hardware performances dramatically improving lately, and with computing resources available at very low cost, improvement of the signal processing associated with NMR measurement becomes very important. High fields and low signal-to-noise ratios have made apparent that current quantitation [4] do not allow full recovery of the information available after signal acquisition. Moreover, misunderstanding of quantitation algorithm limitations often leads to incorrect interpretation of the results by users (*ie.* clinical practitioners) or to the choice of a quantitation protocol that is sub-optimal.

Goal and outline of the thesis

This thesis attempts to review some problems linked to the signal processing inside the "one-button black box", and propose new methods and strategies to overcome its limitations. A pedagogical approach is preferred so as to contribute to better know-how "perfusion" between signal processing specialists and quantitation "users". The NMR quantitation paradigm is built from the physical background to a more general estimation model, and various adjacent information critical to the understanding of MRS quantitation clinically, mathematically or numerically, are provided. Some of the issues that are currently underdeveloped, such as estimation of the quantitation quality, are also discussed, and current know-how on the subject is reviewed.

This manuscript is structured in four chapters, the first two of which review current techniques and procedures, while the latter two propose novel strategies to deal with lineshape accommodation.

Chapter I introduces the main principles of different NMR techniques pertinent to this study. Physical mechanisms are briefly described, allowing establishment of the main equations of importance to this thesis. A minimal metabolomical background familiarizes the reader with the main functions and current knowledge on commonly ^{1}H-MRS-studied brain metabolites.

Chapter II reviews signal processing concepts associated with MRS and MRSI. Spectral analysis concepts are briefly described, including a short review of current methods to accommodate lineshape distortions. Numerical methods that are currently significant for MRS quantitation are described, with a stress on algorithms taking into consideration significant *a priori* information. Finally, a section is dedicated to methods of assessing the quality of the results obtained from MRS and MRSI studies.

Chapter III focuses on the influence of lineshape distortions in MRS quantitation, especially when no reference peak is available. Different lineshape accommodation strategies

4. In this context quantitation refers to the process of estimating physical variables (quantities) from a NMR-generated signal.

are compared via Monte Carlo studies as well as via Cramér-Rao Lower Bounds analytical considerations. A novel approach to deal with lineshape distortion is proposed, based on the assumption that all peaks share the same lineshape. The ensuing algorithm is further studied, both analytically and using Monte Carlo approaches, and a local filtering technique is proposed to improve the estimated common decay (ECD) signal. Finally, quantitation results are shown for both MC studies and an *in vivo* dataset.

Chapter IV proposes a new approach to MRS quantitation, based on the assumption of a common decay function of limited effective spectral support. Unlike traditional approaches, this method does not attempt to estimate a common lineshape, but estimates directly the metabolite parameters by minimizing the spectral support of the assumed common lineshape. Extensive description of the method is given, as well of its numerical implementation using analytically-derived Jacobian matrices. A validation study of the novel method is described, where its performances are compared to those of methods currently used, as well as to those proposed in the previous chapter. In the end of the chapter, several prospective improvements are discussed, including a time domain implementation.

The work described in chapters III and IV has been done in close collaboration with TU Delft, NL, in the general framework of the FAST [5] Marie Curie Research and Training Network (RTN). For complementary work, also see the works of Osorio Garcia et al. [126, 127], at KU Leuven, Belgium, also part of the FAST network.

5. FAST, Advanced Signal-Processing for Ultra-Fast Magnetic Resonance Spectroscopic Imaging, and Training, (MRTN-CT-2006-035801) is a Research and Training Network (RTN) granted by Marie Curie Actions in the 6th Framework Program (2007-2010). URL: `http://www.fast-mariecurie-rtn-project.eu/`

Chapter I

In vivo MRS and MRSI

This chapter provides the necessary basis to understand the forming and acquisition of Nuclear Magnetic Resonance (NMR) signals. The first section summarily introduces the physics involved in NMR phenomena. The second section describes the basis of NMR Spectroscopy (MRS), while the third section briefly describes NMR Spectroscopic Imaging (MRSI) concepts. The main metabolites used in a brain MRS are mentioned in the last section.

I.1 Nuclear Magnetic Resonance Basic Concepts

Nuclear Magnetic Resonance (NMR) is based on the quantum-physical property of elementary particles called 'spin'. This concept (though not the name) has been first introduced by Wolfgang Pauli in 1924, and its relationship with relativistic quantum physics has been further developed by Paul Dirac in 1928. In quantum mechanics, the spin angular momentum of a system is quantized, meaning that it can only take some discrete values, given by:

$$|\vec{S}| = \hbar\sqrt{s(s+1)} \tag{I.1}$$

where $\hbar$ is the reduced Plank constant, and s is the non-negative spin quantum number. The value of s depends only on the type of the particle, and can only take integer or half-integer values (0, 1/2, 1, 3/2, *etc.*). The total spin of particle system (also called net spin) is given by the sum of spins of all its elementary components. *Nuclear* Magnetic Resonance uses the spin properties associated with *nuclei*. The nuclear net spin depends on the number of protons and neutrons:

- If the number of neutrons and the number of protons are both even, the nuclear net spin is null.
- If the number of neutrons plus the number of protons is odd, the nucleus possesses half-integer spin (*ie.* $\frac{1}{2}$, $\frac{3}{2}$).
- If the number of neutrons and the number of protons are both odd, the nucleus possesses integer spin (*ie.* 1, 2, 3)

If the spin is projected on a privileged axis, denoted z from now on, quantum physics allows the magnitude of the projection to take only $2s + 1$ discrete values given by :

$$S_z = m\hbar \ , \text{ with } m = -s \dots s \tag{I.2}$$

Particles with a spin can possess a magnetic dipole moment just as any electrically-charged body in classical electrodynamics. If a particle has a charge q, a mass M and a spin S, then the magnitude of its intrinsic magnetic moment μ is given by:

$$\mu = g\frac{q}{2M}S \tag{I.3}$$

where g is a dimensionless quantity called *g-factor*.

The projection on the z axis of the magnetic dipole moment is given by

$$\begin{aligned}\mu_z &= mg\frac{q\hbar}{2M} \\ &= m\gamma\hbar \ , \text{ with } m = -s \dots s\end{aligned} \tag{I.4}$$

The constant $\gamma = q/2M$ is called the *gyro-magnetic ratio* and is specific to each nucleus type. For the proton $^1H^+$ its value is [123]:

$$\begin{aligned}\gamma_p &= 2.675222099 \times 10^8 \ \ \mathrm{s^{-1}T^{-1}} \\ \gamma_p &\equiv \frac{\gamma_p}{2\pi} = 42.5774821 \ \ \mathrm{MHz\ T^{-1}}\end{aligned} \tag{I.5}$$

In the absence of an exterior magnetic field, no privileged direction exists[1] and so, the individual spins have random orientations, summing up to a null overall magnetization. However, when an exterior magnetic field $\vec{B_0}$ is applied, oriented on the $\vec{z}$ axis, then the individual spins align with $\vec{B_0}$. In the case of atoms having a nuclear net spin equal to $\frac{1}{2}$, such as ^{1}H, ^{13}C or ^{19}F, the magnetic quantum number m can only take the values $-\frac{1}{2}$ and $+\frac{1}{2}$. The energy corresponding to each possible state m is calculated as the scalar product of the magnetization and the magnetic field

$$E_m = -\mu_z B_0 = -\gamma m\hbar B_0 \tag{I.6}$$

The difference in energy between levels (also called transition energy) in the case of $\frac{1}{2}$ nuclear net spin nuclei is then

$$\triangle E = E_{-\frac{1}{2}} - E_{\frac{1}{2}} = \gamma\hbar B_0 \tag{I.7}$$

This generates a difference in the equilibrium populations between the two states, slightly overpopulating the lower energy level corresponding to $m = +\frac{1}{2}$. The populations that occupy the two possible states can be calculated, according to the Boltzmann statistics, as

$$\frac{N^-}{N^+} = \exp(-\frac{\triangle E}{k_B T}) \tag{I.8}$$

where $k_B = 1.3805 \times 10^{-23} \ \ JK^{-1}$ is Boltzmann's constant, T is the temperature and N^+ and N^- are the respective populations corresponding to $m = +\frac{1}{2}$ and $m = -\frac{1}{2}$. At room temperature ($T \approx 300K$), the relative difference in population when a magnetic field $B_0 = 1\ T$ is applied is of the order of

$$\frac{N^- - N^+}{N^- + N^+} = \frac{1 - \exp(-\gamma\hbar B_0/k_B T)}{1 + \exp(-\gamma\hbar B_0/k_B T)} \approx 3.4 \times 10^{-6} \tag{I.9}$$

1. Consistent orientation of the spins may exist even without the existence of an external magnetic field (*cf.* ferromagnetism). However this is not discussed in this context, as it has little relevance to MRS.

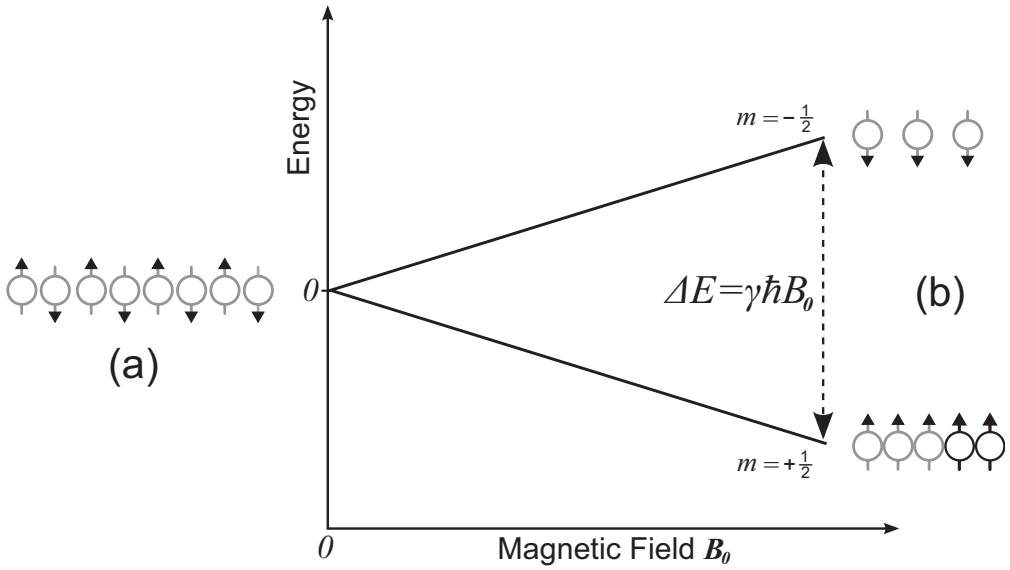

Figure I.1: *Energy level differentiation of* ^1H *nuclear spins under the influence of an external field* B_0*. When the magnetic field is degenerate (a) all spins share the same energy level and the sum of magnetizations is null, since individual pairs cancel themselves out (greyed out). When* $B_0 \neq 0$ *(b) more spins occupy the low energy parallel state* $(m = +\frac{1}{2})$ *than the high energy anti-parallel state* $(m = -\frac{1}{2})$*. In this case the overall resulting sum of magnetic moments is not zero any more, making apparent a macroscopic magnetization given by the sum of the surplus* $+\frac{1}{2}$ *spins (not greyed out).*

If a radio frequency oscillating magnetic field (RF pulse) B_1 is applied to the system, in such a way that the energy of the electromagnetic wave is $h\nu = \triangle E = \frac{h\gamma B_0}{2\pi}$, the system becomes resonant and may absorb the radiation. The corresponding frequency of the radiation, referred to as Larmor's frequency, is thus given by

$$\nu_0 = \frac{\gamma B_0}{2\pi} \equiv \gamma B_0 \tag{I.10}$$

From a quantum physical point of view, a part of the population on the lower energy level $m = +\frac{1}{2}$ is moved on the higher energetic level $m = -\frac{1}{2}$, leading to an unstable population distribution. If the excitation is stopped, the system will return to the corresponding equilibrium Boltzmann distribution, by spin-lattice relaxation mechanisms.

Although the explanation of the NMR phenomena is only possible by means of quantum physics, a more classical approach permits a simpler explanation, better suited for the purpose of this work. While not all relaxation phenomena can be explained through the classical physical approach, it provides nevertheless sufficient background to treat paradigms pertinent to this work.

Thus, the nuclei can be seen as macro-particles, obeying to the laws of Newtonian physics. In the presence of a magnetic field, the particles would spin themselves around the direction $\vec{z}$ of the magnetic field $\vec{B}_0$. The angular speed of rotation is given by Larmor's equation:

$$\omega_0 = 2\pi f_0 = \gamma B_0 \tag{I.11}$$

If a rotating electro-magnetic field B_1 is applied to the system and if the angular frequency of the rotation is equal to the Larmor frequency, then the movement of one spin can be written very simply in the frame of reference rotating with ω_0 around the $\vec{z}$ axis. This frame

of reference will be referred to as $R'(0, \vec{x}', \vec{y}', \vec{z})$, so as to differentiate it from the fixed lab frame of reference $R(0, \vec{x}, \vec{y}, \vec{z})$. If the instant $\vec{B}_1$ field is created so as to be perpendicular to $\vec{B}_0$ (and thus also to $\vec{z}$), then the spin will be subject to a torque $\vec{\mu} \wedge \vec{B}$ that will rotate it around the instant $\vec{B}_1$ direction. The final angle of the spin in the rotating reference R' is given by

$$\theta = 2\pi\gamma\tau B_1 \tag{I.12}$$

where τ is the time lapse during which $\vec{B}_1$ has been applied.

Seen from the laboratory frame of reference R, the particle is engaged in a movement of precession around the static magnetic field $\vec{B}_0$.

I.1.1 Macroscopic evolution of the magnetization

Given the number of spins in any physical sample, it becomes apparent that a description of the magnetization for each spin is of limited interest. What is far more appealing is the evolution of the overall magnetization (given by the sum of all individual spins). This process, as seen in the lab frame of reference R is given by the Bloch [23] equation :

$$\left(\frac{d\ \vec{M}\ (t)}{dt}\right)_R = -\gamma\ \vec{B}\ (t) \wedge \vec{M}\ (t) - \left(\frac{M_z(t) - M_0}{T_1}\right)\vec{z} - \left(\frac{M_x(t)\vec{x} + M_y(t)\vec{y}}{T_2^\star}\right) \tag{I.13}$$

where M_0 is the macroscopic magnetization at equilibrium and $\vec{M} = M_x\vec{x} + M_y\vec{y} + M_z\vec{z}$ the decomposition of the macroscopic magnetization in the lab frame of reference R. T_1 and $T_2^\star$ represent two time constants that are characteristic for the transient process of return to equilibrium. In NMR experiments it is usual to decompose $\vec{B} = \vec{B}_0 + \vec{B}_1$, where $\vec{B}_0$ is a static magnetic field and $B_1(t)$ is time varying (*cf.* §I.1.1.1).

The macroscopic magnetization can be detected through the current it induces in a receiver coil. Since the longitudinal magnetization is too weak to be detected, being superposed to the much higher static field B_0, the main focus of NMR acquisition is the retrieval of the transversal magnetization evolution $\vec{M}_{xy}(t)$. This is usually done using a receiver coil that is in a plane perpendicular to $\vec{B}_0$. The currents induced in this coil are thus proportional to the transversal magnetization projected on the coil support axis.

The detected signal in the receiving coil, proportional to the electromagnetic force induced in the receiving coil, is given [75, §7.2] by Eq.I.14:

$$s_x(t) \propto \frac{d}{dt}\int_{sample} \vec{M}\ (\vec{r}, t) \cdot \vec{B}^{receive} d^3r \tag{I.14}$$

where $\vec{B}^{receive}$ is the magnetic field per unit current that would be generated by coil at $\vec{r}$. Eq.I.14 shows that the acquired signal depends on both the sample magnetizations and on the characteristics of the receiving antenna. Furthermore, if the transversal magnetization is assumed to have an exponentially decaying sinusoidal dependency (*cf.* I.16), the signal is shown to be also proportional to the Larmor frequency [75, §7.3].

In order to help the subsequent data analysis, a complex signal s is constructed from s_x and s_y as follows:

$$s(t) = s_x(t) + \imath s_y(t), \quad \text{where } \imath = \sqrt{-1} \tag{I.15}$$

I.1.1.1 One pulse sequence

The solutions of the Bloch equations depend of course on the time sequence formed by the values of $\vec{B_1}(t)$, also called the B_1 pulse. To get a better understanding of the mechanisms involved, it is common to study the evolution of $\vec{M}$ in a simple case: the one pulse sequence.

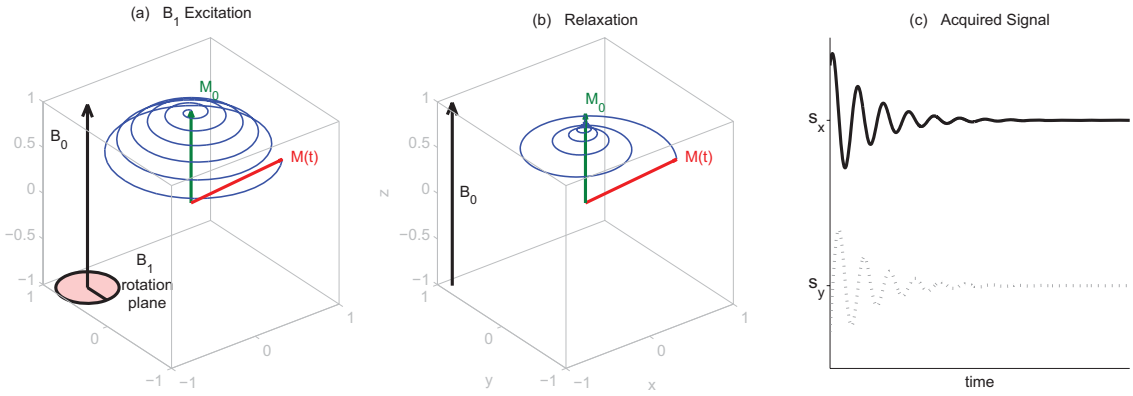

Figure I.2: *Evolution of the macro magnetization during a 'one pulse' MRS sequence. During the excitation phase (a) the electromagnetic pulse B_1 is applied. In the relaxation phase (b) the spins go back to the equilibrium state. The ensuing varying magnetic field produces electric currents in the receiver coil, that can be measured via the voltage they induce (c).*

1. **Equilibrium** - All spins are in a statistical equilibrium, defined by Boltzmann statistics. The overall magnetization has the value M_0 and is parallel to $\vec{B_0}$: $\vec{M}(0) = M_0 \frac{\vec{B_0}}{B_0}$
2. B_1 **pulse** - Precession movement. Longitudinal $\vec{M}_z$ component decreases and transversal $\vec{M}_x y$ component increases. The movement is governed by Eq.I.12.
3. **Relaxation** - The electromagnetic pulse B_1 is not applied any more. The system returns (slowly) to the equilibrium state. The solutions to the Bloch equations (and thus the acquired signal s) are complex decaying exponentials:

$$s(t) = c \ \exp\left(\frac{-t}{T_2}\right) \ \exp(\imath 2\pi f_0 t) \ \exp(\imath\varphi) \tag{I.16}$$

In equation I.16, c is a constant of proportionality that takes into account mainly the gain of the acquisition chain and the local density of spins and φ is a dephasing due to the arbitrary choice of the R reference frame. T_2 is called the transversal relaxation time constant, and depends on the interaction between the spin and its environment. The signal $s(t)$ is usually referred to as Free Induction Decay (FID). By extension, this name is also used to describe the right (decaying) part of an echo, in the case when the RF pulse sequence used is more complicated than the 'one pulse'.

The longitudinal macroscopic magnetization M_z cannot be usually directly measured due to its very small variation compared to the collinear B_0 field. Its evolution is also governed by an exponential increase with a time constant T_1 called longitudinal relaxation time. The law of longitudinal magnetization regrowth is

$$M_z(t) = M_0 \left[1 - \exp\left(\frac{-t}{T_1}\right)\right] \tag{I.17}$$

with M_0 the longitudinal magnetization at equilibrium.

I.1.2 Transversal relaxation in an inhomogeneous B_0 field

Until now it has been assumed that the applied B_0 field is perfectly homogeneous and constant in time. In reality it is not possible technologically to generate such a magnetic field. In the following studies it is assumed here that B_0 variations in time are negligible when compared to the spatial inhomogeneity, and thus only the latter is taken into consideration. The most significant reasons that spatial static (B_0) inhomogeneities occur relate to (a) the design and manufacturing of the coils, (b) the ferro-magnetic materials in the immediate environment of the scanner installations (*ie.* metallic doors, wiring) and (c) magnetic susceptibility variation in *in vivo* and *in vitro* samples. While (a) and (b) are experiment independent, and are usually minimized during manufacturing and installation, (c) has to be optimized at each experiment.

The procedure of optimizing static field homogeneity is referred to as "shimming", and is usually achieved using additional coils, called shim coils. Prior to the acquisition proper, algorithms such as FASTMAP [70, 71] or PACMAP [202] are used to adjust the currents in the shim coils so as to optimize B_0 homogeneity. However, due to the limited number of shim coils, residual static inhomogeneity persists, especially in the high frequency spatial domain.

According to Eq. I.11, a spin at the position (x, y, z) will rotate at the frequency $f_0(x, y, z) = \frac{\gamma}{2\pi} B_0(x, y, z)$. Assuming an ideal RF pulse[2], at the beginning of the relaxation time all spins are in phase. The overall evolution of s is given by an integral over all the spins in the excited Volume Of Interest (VOI) :

$$\begin{aligned}
s(t) &= \iiint_{VOI} s(x, y, z, t)\ dxdydz \\
&= \iiint_{VOI} \left[c\ \exp\left(\frac{-t}{T_2}\right)\ \exp(\imath 2\pi f_0 t)\ \exp(\imath\varphi) \right]\ dxdydz \\
&= c\ \exp\left(\frac{-t}{T_2}\right) \exp(\imath\varphi) \iiint_{VOI} \exp(\imath 2\pi f_0(x, y, z)t)\ dxdydz \\
&= c\ \exp\left(\frac{-t}{T_2}\right)\ \exp(\imath 2\pi f_0 t)\ \exp(\imath\varphi) \quad \iiint_{VOI} \exp[\imath 2\pi\ \triangle f_0(x, y, z)\ t]\ dxdydz \\
&= \underbrace{c\ \exp\left(\frac{-t}{T_2}\right)\ \exp(\imath 2\pi f_0 t)\ \exp(\imath\varphi)}_{a.} \quad \underbrace{\iiint_{VOI} \exp[\imath\gamma\triangle B_0(x, y, z)\ t]\ dxdydz}_{b.}
\end{aligned} \tag{I.18}$$

As it can be seen in Eq. I.18, the effect of B_0 inhomogeneity is apparent in the form of an extra damping function (b.), depending on the distribution of the B_0, that multiplies the ideal FID (a.), see Eq.I.16. The decaying nature of the (b.) term, although computable in the case of a known $\triangle B_0$ distribution, can be more easily described using the instant phase $\varphi = \int_0^t \gamma\triangle B_0 dt$ spatial distribution. For small t the instant phase distribution is a scaled (in width) version of the $\triangle B_0$ distribution. For bigger t, while the unwrapped instant phase remains a scaled B_0 distribution, due to the periodic nature of the phase, it tends towards an uniform distribution. This, in turn causes the average instant phase to tend towards zero, that is the expected value of the phase when it is uniformly distributed between 0 and 2π.

2. The same reasons that cause static inhomogeneity may also cause RF (B_1) inhomogeneity. Furthermore, undesired B_1 spatial variability is increased because of the generally small size of the emitter coil (leading to localized non-uniform radiation pattern), as well as by the increasing wave-like behaviour of the RF pulse at high fields Fischi Gómez [60].

Because of the decaying nature of term (b.), it is commonly replaced by a decaying exponential[3] $\exp(-t \cdot T_{\text{inhomo}}^{-1})$, where T_{inhomo} describes the inhomogeneity of the static field. In this case, the Eq.I.18 can be rewritten as

$$s(t) = c \ \exp\left(\frac{-t}{T_2^*}\right) \ \exp(\imath 2\pi f_0 t) \ \exp(\imath\varphi)$$
$$\text{with } \frac{1}{T_2^*} = \frac{1}{T_2} + \frac{1}{T_{\text{inhomo}}} \tag{I.19}$$

I.1.3 Gradient coils and pulse sequences

The influence of the local variations of the B_0 magnetic field can be also be used in order to obtain more information about the sample that is being analysed by NMR. In this case a second field, collinear with the original is applied via additional coils, called gradient coils. The additional magnetic field produced by the gradient coils shall be referred as $\vec{G}$. Its norm G is generally of the form $G(t, x, y, z)$, having both a spatial and a temporal variation.

Generally, the spatial variation of the gradient field is given by the superposition of three linearly varying gradient fields:

$$\vec{G}(x, y, z) = [G_x(x) + G_y(y) + G_z(z)]\,\vec{z} \tag{I.20}$$
$$G_x(x) = xG_{x0} + g_x$$
$$G_x(x) = yG_{y0} + g_y$$
$$G_x(x) = zG_{z0} + g_z \tag{I.21}$$

The temporal variation of the gradient field is controlled by the acquisition chain. Together with the variation of the electromagnetic pulse B_1 it forms the backbone of the program called 'pulse sequence' that drives the acquisition (*cf.* §I.2.3 for examples). The effective means of controlling the gradient coils depend on the hardware, but are generally implemented as the reading of a "pulse program", that itself can be created directly by the user, or compiled from another higher-level programming language. To this day, pulse programs (pulse sequence implementations) remain very machine-related, making pulse programs effectively non-portable from one manufacturer to another, and sometimes even between machines coming from the same manufacturer.

I.2 Magnetic Resonance Spectroscopy

Magnetic Resonance Spectroscopy (MRS)100. + is a technique allowing the non-invasive characterization of a sample by means of spectral NMR signatures of its chemical components. It is widely used in chemistry and bio-chemistry for the characterization of unknown compounds or for information on their three-dimensional structure. Due to its non-invasive nature, it has also recently been used in medical and pharmaceutical applications. Following is a brief explanation of the basic concepts of MRS, some considerations on the pulse sequences specific to MRS, as well as a non-exhaustive list of metabolites that are currently investigated in brain MRS studies.

3. For a study on the validity of assuming that the inhomogeneity contribution adds exponential decay, see [73].

I.2.1 Principles

Individual nuclei lie, in solid and liquid matter, in close proximity to each other. Due to the complex structure of molecules, different nuclei in a molecule can be subjected to a level of magnetic shielding due to other magnetic momenta in close proximity. As the influence of neighbours diminishes drastically with distance (proportionally to the square of the distance), only the closest neighbours present a coherent quantifiable influence. This allows the detection of chemical groups and is a major method of compound structure analysis in chemistry.

In liquids, the two main effects that influence the magnetic resonance frequency of nuclear spins are (a) the nuclear shielding due to the electron orbitals and (b) the spin-spin interactions between nuclei in close proximity. In the following subsections the two mechanisms are briefly discussed.

I.2.1.1 Chemical shift

Due to the presence of electron orbitals around the nuclei, the magnetic field seen by the nuclear spins is not equal to the external field B_0, but needs to be corrected by the magnetic field produced by the orbiting electrons (see Fig.I.3a):

$$B = B_0 \ (1 - \sigma) \tag{I.22}$$

where σ is called the shielding (or screening) constant and it is specific to each atom in a molecule. In order to understand how this works, consider the simplest case of ^{1}H atom, consisting of the proton $^1H^+$ and the enveloping s orbital. Under an external magnetic field, the electron adopts, according to Lentz's law, a trajectory so that it creates an opposing field to B_0, so that the field "seen" by the nucleus is diminished. It is said in this case that the s electron orbital shields the nucleus, creating a diamagnetic shift. For more complicated orbitals, the concept is the same, but due to the non-symmetrical orbital clouds, the induced shielding is more complex, and can be paramagnetic as well as diamagnetic. Furthermore, due to electron exchanges and orbital deforming as the result of other atoms, the induced electron magnetic field may depend on many local chemical conditions, such as temperature, pH, etc.

In order to describe nuclear shielding, the term "chemical shift" is used, because the nuclei are seen as if their Larmor resonance frequency is shifted relative to the reference frequency corresponding to the static field B_0:

$$f = \underbrace{\gamma B_0}_{f_0} - \underbrace{\sigma\gamma B_0}_{\triangle f} \tag{I.23}$$

Expressing the chemical shift in Hz would require the magnetic field to be known. In order to bypass this, a derived quantity called frequency deviation [4] (δ) is computed as a ratio between $\triangle f$ and f_0. The frequency deviation depends solely on the atom's specific shielding constant and, since $\triangle f$ is of the order of Hz while f_0 is in the Mhz range, it is usually expressed in parts-per-million (ppm), using a reference resonance frequency f_{ref}. In ^{1}H and

4. Please note that it is common to use, by extension, "frequency shift" or "chemical shift" instead of "frequency deviation". For clarity, the measuring unit should be checked: ppm indicate frequency deviations, while Hz indicate frequency shifts.

^{13}C MRS, tetramethylsilane (TMS) and 4,4-dimethyl-4-silapentane-1-sulfonic acid (DSS) are the most commonly used references.

The relationship between shielding constants (σ), resonance frequencies (f, in MHz), chemical shifts ($\triangle f$, in Hz) and frequency deviation (δ, in ppm) can be summarized by:

$$\delta = \frac{f - f_{\text{ref}}}{f_{\text{ref}}} = \frac{\triangle f}{f_{\text{ref}}} = \frac{\sigma - \sigma_{\text{ref}}}{\sigma_{\text{ref}}} \tag{I.24}$$

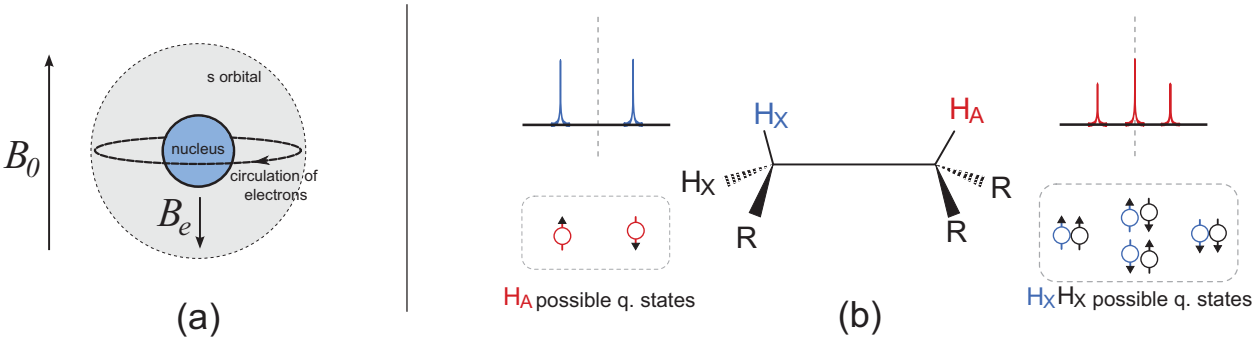

Figure I.3: *Main mechanisms responsible for frequency shifts in MRS. (a) Nuclear shielding modifies the field experienced by the nucleus due to the extra field B_e generated by mobile electrons. The simpler case of an s orbital is presented here, where due to orbital symmetry the extra field is subtracted from B_0. (b) Illustration of first order J-coupling generated splitting of spectral peaks from nearby nuclei. The presence of two H_x nuclei, with 4 possible overall states (two of which are equivalent), causes the H_A peak to split into a triplet with relative intensities (1:2:1). Partially adapted from [90].*

I.2.1.2 Spin-spin coupling

The second major mechanism that causes spectral lines to shift is the effect of neighbouring nuclear groups. This influence is present in two forms: the dipolar coupling, representing interaction through space, and the scalar coupling, representing interaction through the electrons in chemical bonds. Even though dipolar interactions are the main mechanisms for relaxation in liquids, there is no net interaction between nuclei since rapid molecular tumbling averages the dipolar interactions to zero[50, §1.10]. However, interactions through electrons in chemical bonds do not average to zero and give rise to the phenomenon of scalar coupling, also termed "Spin-spin splitting" or "J coupling".

A comprehensive explanation of J-coupling is only possible through quantum physics, and goes beyond the scope of this work. In order to compute the signal given by spin-spin splitting, the different quantum states must be described, and the results weighted by the probability of each state. Assume a nucleus k, with N_k vicinal nuclear spins, assume the probability of a state n among the $N_k + 1$ possible ones is given by $\mathcal{P}_k(n)$, with the

corresponding J coupling constant $J_{n,k}$. The expected signal is given by (see Eq.I.16):

$$\begin{aligned} s_k(t) &= \sum_{n=0}^{N_k} \left[\exp\left(-\frac{t}{T_2}\right) \ \exp[\imath 2\pi (f_0 + J_{k,n})t] \ \exp(\imath\varphi) \ \mathcal{P}_k(n) \right] \\ &= \exp\left(-\frac{t}{T_2}\right) \ \exp(\imath 2\pi f_0 t) \ \exp(\imath\varphi) \underbrace{\sum_{n=0}^{N_k} [\exp(\imath 2\pi J_{k,n} t)\mathcal{P}_k(n)]}_{\text{J coupling effect}} \\ &= \exp\left(-\frac{t}{T_2}\right) \ \exp(\imath 2\pi f_0 t) \ \exp(\imath\varphi) \ \Upsilon_k(t) \end{aligned} \tag{I.25}$$

where Υ_k is the function composed on frequency-shifted complex sinusoids, describing the peak-splitting due to J-coupling.

Generally, nuclear groups consisting N nuclei cause splitting of neighbouring group peaks into $N+1$ components (*cf.* Fig.I.3b), distributed in area according to the Pascal triangle (*ie.* a group of 3 protons would case splitting into a quartet with relative intensities $1:3:3:1$). This splitting pattern assumes that J coupling constants are small in comparison to chemical shift (spectra that obey this rule are termed "first-order"). In cases when group frequency shift and J-coupling effects are comparable, second-order coupling must also be taken into consideration, yielding more complex patterns. Furthermore, other factors, such as molecule geometry, can also increase splitting pattern complexity.

An important thing to notice here is the measuring unit used for J-coupling description. Since the energy level alterations produced by the neighbouring nuclear spins do not depend on the external B_0 static field, J-coupling constants are usually expressed in Hz (they normally range up to 20Hz).

I.2.1.3 From nuclear environment to molecular MRS signatures

As seen in the previous two subsections, nuclear spin response to RF stimulation is affected by nuclear shielding (chemical shift) as well as by nearby groups of nuclei. The combined effects, in conjunction with theoretical data coming from molecular-level chemistry (*ie.* predicted molecule geometry, electro-negativity, etc.) allows in-depth analysis of chemical and biochemical compounds through NMR. Furthermore as in other spectrometry domains, it allows identification of present chemical compounds, while also providing quantitative information. This latter application is mostly used in clinical MRS [5].

In order to understand how the MRS signature of a molecule is used as *a priori* information, consider a nuclear spin k, described by the shielding constant σ_k and by the vicinity of N_k nuclear groups. According to §I.2.1.1-I.2.1.2, the ideal *expected* MRS signal generated by the nucleus k is

$$\begin{aligned} s_k(t) &= \exp\left(-\frac{t}{T_{2,k}}\right) \ \exp[\imath 2\pi f_0 (1-\sigma_k)t] \ \exp(\imath\varphi) \ \Upsilon_k(t) \\ &= \exp\left(-\frac{t}{T_{2,k}}\right) \ \exp(\imath 2\pi f_0 t) \ \exp(\imath\varphi) \ \exp(-2\pi f_0 \sigma_k t)\Upsilon_k(t) \end{aligned} \tag{I.26}$$

5. The term "MRS" is usually used to describe *in vivo* spectroscopy, while "NMR Spectroscopy" is generally used to describe applications in analytical chemistry, such as protein structure reconstruction. In this thesis, MRS is the centre of focus.

The total MRS signal b_m given by a molecule m in ideal conditions is the sum of all the nuclear contributions $k = 1 \dots K_m$.

$$\begin{aligned} b_m(t) &= \sum_{k=1}^{K_m} s_{m,k}(t) \\ &= \exp(\imath 2\pi f_0 t) \sum_{1}^{K_m} \left[\exp\left(-\frac{t}{T_{2,k}}\right) \exp(\imath\varphi) \exp(-2\pi f_0 \sigma_k t) \Upsilon_k(t) \right] \end{aligned} \tag{I.27}$$

This signal, described by Eq.I.27, is specific to each molecule. The collection of these molecule-specific signals is called a 'metabolite basis set' and it contains the basic information needed to interpret Magnetic Resonance Spectroscopy (MRS) signals. Furthermore, the signal basis-set can be measured or simulated.

Given a volume V_{VOI}, the total numbers of molecules for each metabolite $m = 1 \dots M$ can be computed as $V_{VOI} \times c_m$, where c_m is the concentration of metabolite m. Then, the overall acquired signal can be modelled as:

$$s(t) \propto V_{VOI} \sum_{m=1}^{M} [c_m b_m(t)] \tag{I.28}$$

Assuming the basis-set signals $\{b_m(t)\}_{m=1\dots M}$ are perfectly known, information about the concentration of different metabolites can be extracted from a signal containing multiple compounds, by solving the inverse problem associated with Eq.I.28. However field inhomogeneities have not been included in this model. For a more in-depth model, as well as a description of techniques used to solve the inverse problem see chapter II.

I.2.2 HRMAS

High Resolution Magic Angle Spinning (HRMAS) [4] is a technique available for *ex vivo* studies, where the sample is placed on a rotor and turned at high angular velocities, at the magic angle. This reduces the transversal decay effect, providing spectra with very narrow peaks (width at half height of less then 0.5 Hz). For an example of HRMAS spectra, see Fig.I.12 on page 30.

I.2.3 Some NMR Spectroscopy pulse sequences

NMR Spectroscopy is performed on modern scanners using pre-programmed control sequences of the acquisition hardware, that are usually referred to as Pulse Sequences. Contrary to what the name might suggest, pulse sequences describe not only the RF pulse being transmitted, but also the exact evolution of main static gradients as well as all hardware timings and signal sampling during the process. Implementing a pulse sequence is usually a manufacturer-specific procedure (if not machine specific), and is done generally outside the clinical framework. However, clinically-available pulse sequences have usually a certain number of parameters that are software-encoded and can be changed in clinical use to accommodate specific targeting. Following is a non-exhaustive short summary of some MRS pulse sequences pertinent to this thesis.

One pulse sequence The simplest pulse sequence for NMR Spectroscopy is the 'one pulse' sequence. As its name suggests, only one α (often 90°) RF pulse is transmitted, then the signal acquisition occurs. Before another measure is made, the complete regrowth of the longitudinal magnetization must be achieved. In clinical MRS, the value of the one pulse sequence currently lies more in the theoretical domain, as an example of machine implementation, proof of concept, or as a brick for more complex pulse sequences; however it remains routinely used in chemistry, where localization is non essential.

Spin Echo The spin echo sequence has first been introduced by Hahn in 1950 [77] and further improved by Carr and Purcell [31]. The principle of the method is the presence of a 180 ° pulse that partially refocuses the spins in an 'echo'.

Suppose that two magnetizations s_1 and s_2 are under slightly different magnetic fields B_{01} and B_{02}, resulting in precession frequencies f_1 and f_2. If one 90° pulse is applied, after a time t the dephasing between the two spins is $\triangle\varphi(t) = 2\pi(f_2 - f_1)t$. At time T after the 90° pulse the dephasing is $2\pi(f_2 - f_1)T$. If now a 180 ° pulse is applied, the system can be considered as inverted, with the dephasing becoming $-2\pi(f_2 - f_1)T$. The new dephasing evolution is written as $\triangle\varphi(t) = -2\pi(f_2 - f_1)T + 2\pi(f_2 - f_1)(t - T) = 2\pi(f_2 - f_1)(t - 2T)$. It is interesting to observe that if $t = T_E = 2T$ the dephasing becomes exactly zero $\triangle\varphi(T_E = 2T) = 0$, whatever the difference in the B_0 field seen by the spins.

In the case of a large number of spins, the approach is similar, but at a statistical level. The spin dephasing is following the same statistical law as the B_0 field distribution, with a dispersion proportional to time. As the phase (and the dephasing) is defined as periodic over $[0, 2\pi)$, as time tends to infinity the dephasing distribution tends to a uniform distribution, and thus the sum of magnetizations tends to zero. If a 180° pulse is applied at $T = T_E/2$, then at T_E the dephasing distribution will be strictly a degenerate value of zero, creating an echo from all the spins *in phase*.

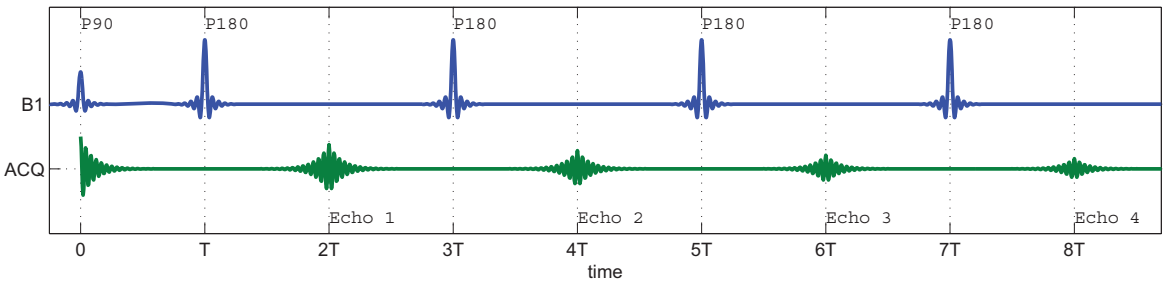

Figure I.4: *Spin Echo Pulse Sequence. First 90° pulse creates a transversal magnetization. Following 180 ° pulses refocus spins so that 4 echoes are visible. Echo magnitude decreases exponentially with T_2 time constant.*

Figure I.4 shows a spin echo pulse sequence that generates 4 echoes. Excitation is achieved by the first 90° pulse, while the following four 180°-pulses refocus [6] the spins. Echoes are present at times nT_E, with magnitudes decaying exponentially with a time constant T_2.

Change of the echo time parameter T_E allows selective acquisition according to the T_2 constants of each metabolite. Long echo time ($T_E > 120$ms for *in vivo* ^{1}H MRS) is used in

6. Spin refocusing cannot be complete, because of spin-spin relaxation. A 180°-pulse refocuses spins that have been defocused by field inhomogeneity, but the coherence of the signal slowly decays, as predicted by the T_2 relaxation constant.

applications where metabolites of interest are NAA, Cr, Cho and Lac. At short echo time (typically $T_E = 30$ ms for *in vivo* ^{1}H MRS) all metabolites, as well as contributions from macromolecules and lipids, become visible.

PRESS Point RESolved Spectroscopy (PRESS) has been introduced by Bottomley [25] to obtain localized NMR Spectra. The sequence is a spin echo sequence, with two 180 ° pulses needed for complete 3D localization.

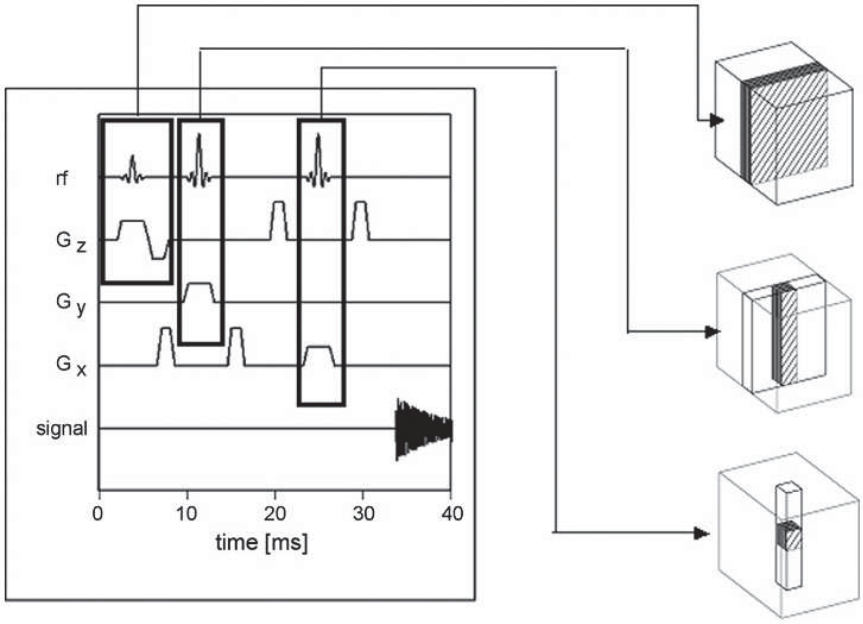

Figure I.5: *Selection of a cube with a PRESS pulse sequence. The three spatially-selective rf pulses within the sequence are marked and the selected regions after each pulse are shown for a cubic object. The selected voxel, resulting from the intersection of the three selected slabs, has the shape of a cube. Signal acquisition time frame is not fully shown. Figure from Klose [89].*

Figure I.5 shows a typical PRESS pulse sequence implementation. Z slice selection is performed using the G_z gradient during the 90° excitation pulse. During the two following 180° pulses G_y and G_x are used to select a 3D cube as the intersection of 3 slices. Noteworthy are the spoiling gradients, that allow dephasing of unwanted resonances.

The use of spin echo techniques has the beneficial effect of decreasing sensitivity to B_0 field inhomogeneity by rephasing, while at the same time being subject to artefacts due to partial volume effect. Furthermore, the spatial selectivity of the gradients is limited by the duration of the pulses, and excitation of spins outside the volume of interest arises frequently. For brain, lipid contamination by the subcutaneous fat in the scalp may arise, for example, when unwanted (fat) molecules are excited outside the intended VOI.

STEAM STimulated Echo Acquisition Mode has been proposed by Frahm[61] and uses a different approach to generate spin echoes. The sequence consists optimally of three 90 ° pulses, allowing, as PRESS, selection of a 3D Volume of Interest. The first pulse turns the magnetization from z to the xy plane, in the same manner as PRESS. A second pulse will rotate the magnetization from the xy plane to the zy. While the transversal component of the

magnetization will be dispersed due to T_{2*}, the longitudinal component remains practically untouched during the T_M (mixing time) period. After the third 90° pulse, the previously longitudinal component is rotated into the xy plane. This pulse functions as a refocusing pulse, generating an echo after $T_E/2$ time, because the total excitation angle seen by the spins that participate in the longitudinal magnetization during T_M is equal to 90° + 90° = 180°. During T_M there is also a T_1 longitudinal regrowth effect, but sequence parameters are chosen such as to make this effect small comparable to T_2.

One of the important advantages of the STEAM sequence is that the total time needed to acquire a spectrum is smaller than in the case of PRESS, since T_M can be chosen to be well inferior to T_E. The sole use of 90° pulses also reduces hardware stress and provides a more energy efficient acquisition process. However, signal amplitudes obtained are only half of those obtained with a PRESS sequence.

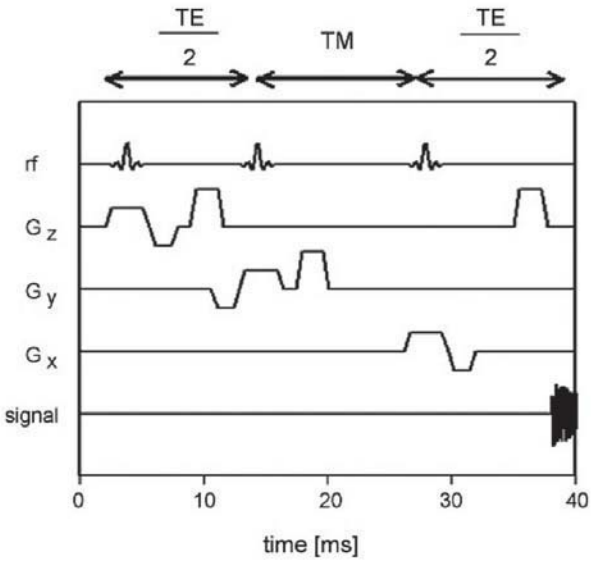

Figure I.6: *Sequence scheme for the STEAM sequence. The refocusing gradients have to be positioned before the second rf pulse and after the third rf pulse. Only the first part of the data acquisition time is shown. Figure from Klose [89].*

A more in-depth comparison of STEAM and PRESS, as well as a more detailed discussion of the artefacts and methods to overcome them has been done by Moonen in [115] and more recently by Klose in [89].

I.3 Magnetic Resonance Spectroscopic Imaging

Magnetic Resonance Spectroscopic Imaging (MRSI), sometimes also referred to as Chemical Shift Imaging (CSI) is a further development of MRS so as to obtain spatial mapping of the metabolite concentrations. Between imaging and spectroscopy, MRSI has considerably longer acquisition times, but provides a more detailed set of data. In the following paragraphs, the basis of MRSI acquisition is described, as well as the current pulse sequences in use. For a more in-depth view of the current advancements and bottlenecks of human brain MRS(I) see Barker and Lin [8], as well as the older contribution of Pohmann et al. [131].

I.3.1 MRI & Principles of space encoding in NMR

Magnetic Resonance Imaging (MRI) is a non-invasive imaging technique that allows spatial mapping of the proton spin density via the use of space- and time-varying magnetic field gradients. MRI has been made possible due to the ground-breaking contributions of Lauterbur [94] as late as 1973. Although bulky installations are needed compared with other medical imaging techniques (X-Ray, Ultrasound, etc.), MRI can have several advantages: it provides very good signal-to-noise ratio, the imaging procedure does not imply radioactive elements or high energy radiation, and different acquisition parameters can adapt to a large range of tissue. As such, MRI is extensively used for studies of the brain or of tissue that is not observable via X-Ray imaging, such as cartilage [99] or mammary tissue [27].

In order to understand the basics of MRI, consider the simpler case of 2D MRI, where a fine slice on the $\vec{z}$ axis has been selected. Then all the z-depending terms associated with the static gradient function G (*cf.* I.1.3) can be ignored, giving only a $G(t, x, y)$ variation.

Consider a very small volume dV situated at the position $\vec{r}$, having all spins rotating in the magnetic field $\mathbf{B_z} = B_z\vec{z}$. Arbitrarily considering the initial magnetization phase null, the instant phase of the magnetization vector at a time t is given by the sum of all the contributions of the time-variable B_z:

$$\varphi(t) = \int_0^t d\varphi = \int_0^t \gamma B_z(t)dt \tag{I.29}$$

Furthermore, the magnitude of the magnetization vector is proportional to the density of spins $\rho(x, y)$. Under the assumption that the T_2 effect is sufficiently small for the duration of the acquisition, and with $B_z(t) = B_0(t) + G_x(t)x + G_y(t)y$ the equation describing the acquired signal becomes:

$$s(t) = \int_{sample} \rho(x, y) \exp\left[\imath\gamma \int_0^t B_0(\tau) + xG_x(\tau) + yG_y(\tau)d\tau\right] dV \tag{I.30}$$

For practical reasons it can be considered that the static field B_0 is not time-varying. After removal of the B_0, modulation, the acquired signal ca be thus written as:

$$s(t) = \int_{sample} \rho(x, y) \exp\left[\imath\gamma \int_0^t xG_x(\tau)d\tau\right] \exp\left[\imath\gamma \int_0^t yG_y(\tau)d\tau\right] dV \tag{I.31}$$

$$= \int_{sample} \rho(x, y)\ \exp(\imath 2\pi x k_x)\ \exp(\imath 2\pi y k_y)\ dV \tag{I.32}$$

with $k_x = \int_0^t \gamma G_x(\tau)d\tau$ and $k_y = \int_0^t \gamma G_y(\tau)d\tau$.

This formalism has been first introduced by Ljunggren [97] and Twieg [185], greatly simplifying the conception and understanding of MRI sequences. Under a more general form the demodulated signal $s(t)$ can be written as:

$$s(t) \equiv \int_0^t \rho(\vec{x}) \cdot e^{2\pi\imath\ \vec{k}\cdot\vec{x}} d\vec{x} \tag{I.33}$$

with $\vec{k}(t) = \int_0^t \vec{G}(\tau)d\tau$ called the *k-space trajectory*. This formalism is of very high importance to NMR, since it allows to write the acquired signal as a Fourier Transform

of the effective spin density ρ. Computation of the spin density image is done via the corresponding inverse Fourier transform:

$$\hat{\rho}(\vec{x}) \approx I(\vec{x}) = \int_0^t s(k(\vec{t})) \cdot e^{-2\pi\imath\ \vec{k}\cdot\vec{x}} d\vec{k} \tag{I.34}$$

I.3.2 Slice Selection

Slice selection (Fig.I.7) is performed by applying a G_z gradient while transmitting a B_1 pulse that has a well defined frequency content. Consider that a linearly varying G_z field is applied so that within the region of interest defined by z_{min} and z_{max} the resulting B_0 field varies from $B_{0,\min} = B_0 + z_{\min}G_{z0}$ to $B_{0,\max} = B_0 + z_{\max}G_{z0}$. This implies that the resonance frequency of the atoms within will be between $f_{0,\min} = \frac{\gamma}{2\pi}B_{0,\min}$ and $f_{0,\max} = \frac{\gamma}{2\pi}B_{0,\max}$. If the $B_1(t)$ excitation is such as to only have frequency components between $f_{0,\min}$ and $f_{0,\max}$, then only the atoms that are between $z_{\min}$ and $z_{\max}$ are excited by the RF B_1 pulse.

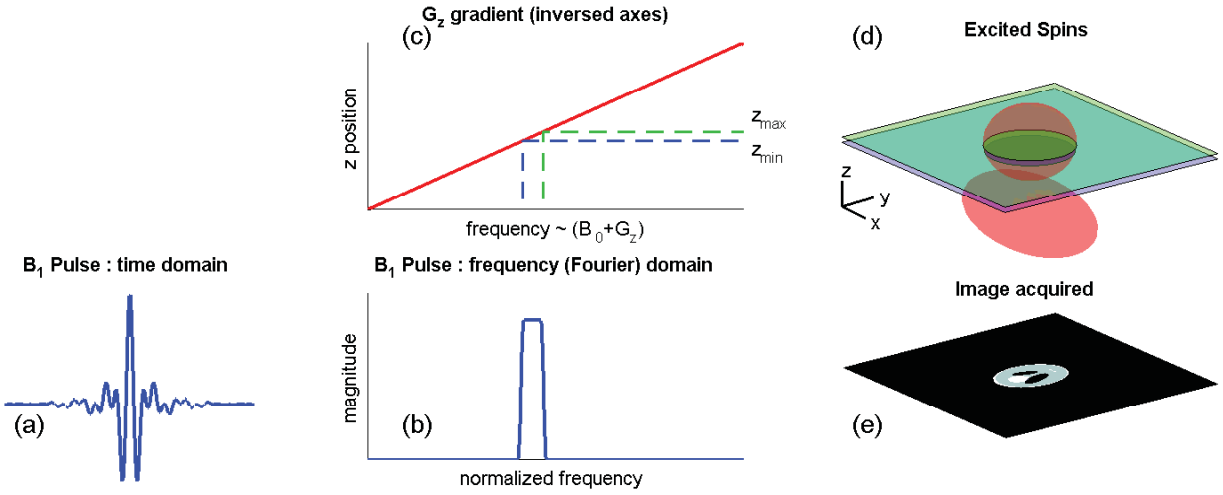

Figure I.7: *Slice selection in MRI. The B_1 pulse (a) is transmitted by the antenna and it excites spins that whose Larmor frequency corresponds to non-null components of the pulse Fourier Transform (b). Spin Larmor frequency is proportional to the local B_0 field, who in turn is proportional to the value of the G_z gradient. To the two limit values of G_z that are excited correspond the two limit values of z (c), since G_z is linear. The excited spins form a slice delimited by the two limit values $z_{\min}$ and $z_{\max}$ (d). The final image obtained (e) depends on the imaging sequence taken, but is representative of the average spatial distribution of the spins in the selected slice.*

The slice thickness $\triangle z = z_{\max} - z_{\min}$ is therefore given by:

$$\triangle z = \frac{2\pi \triangle f_{pulse}}{\gamma G_z} \tag{I.35}$$

In order to achieve better spatial selectivity (decrease $\triangle z$), few options are available: (1) Increase G_z or (2) decrease the frequency passband of the RF pulse. The first option is limited by hardware, as stronger pulses require better RF coils, improved energy heat management and increased power consumption, while the second option is limited by time requirements, since a more passband selective filter also requires a longer time lapse.

It should be noted that due to the limited time available for the transmission of the B_1 magnetic pulse its frequency response is theoretically infinite and thus the excited volume is also theoretically infinite. In practice this is not so problematic, but it can induce artefacts from partial volume effects of contamination from other resonances from outside the acquisition VOI.

I.3.3 MRSI principles

MRSI is based on the hypothesis that the spatial spin density of every metabolite is constant during the time of the acquisition. In this case, the purpose of MRSI is to find the spin density $\rho_m(\vec{r})$ of the metabolite m at the position defined by $\vec{r} = (x, y, z)$, from the results of a series of NMR acquisitions. As such, MRSI is a combination of NMR Spectroscopy (identifying the metabolite m) and NMR imaging (mapping the spin density). In MRSI terminology, we will refer to a "voxel" as the basic unit of volume, from which only one value per metabolite can be extracted.

The simplest way to perform MRSI would be to use single-voxel spectrometry (MRS) over and over, while changing each time the localization of the selected MRS-VOI so as to sweep the entire MRSI region of interest.

To understand the principles of spatial-spectral encoding, the MRI encoding formalism (Eq.I.30) has to be modified to take into account the magnetic field shielding seen by a metabolite with a chemical shift δ:

$$ds(t, \delta, x, y) = \rho(\sigma, x, y) \ \exp\left[\imath\gamma \ \delta \ \int_0^t (B_0(\tau) + xG_x(\tau) + yG_y(\tau))\, d\tau\right] dV \tag{I.36}$$

The total signal given by all metabolites is the integral over all δ of $s(t, \delta)$. Using a similar simplification procedure as in the case of MRI, we obtain the total acquired signal $s(t)$:

$$s(t) \approx \int_\sigma \int_{ROI} \rho(\sigma, x, y) \ \exp(\imath 2\pi \ x \ k_x) \ \exp(\imath 2\pi \ y \ k_y) \ \exp(\imath \ \delta \ k_\sigma) \ dxdyd\sigma \tag{I.37}$$

Equation (I.37) shows that the total signal acquired can be represented as a point $s(t, k_x, k_y)$ of a multi-dimensional Fourier Transform of the MRSI chemical-shift-dependent spin density $\rho(\delta, x, y)$. In order to obtain the spin density, the Inverse Fourier Transform can be applied to the signal S formed by all the individual points $s(t, k_x, k_y)$. By convention, the acquisition of S is said to be in the Fourier Space, further decomposed as *the k space* for the spatial components (k_x, k_y), and *the frequency space* for the temporal components. From now on, the notations $\mathbb{K}_x$,$\mathbb{K}_y$ and $\mathbb{K}^2 = \mathbb{K}_x \times \mathbb{K}_y$ will be used to refer to the k spaces. Similar notation will be used for the other possible spaces : $\mathbb{T}$ for time, $\mathbb{F}$ for frequency and $\mathbb{R}$ for Cartesian coordinates.

Finding the spin density image for each resonance is not always directly sufficient to determine the concentrations of the metabolites, mainly due to spin relaxation and eventually to overlapping. Spectral analysis techniques similar to MRS have to be applied. Classically, the signal is first transformed from $\mathbb{K}^2 \times \mathbb{T}$ to $\mathbb{R}^2 \times \mathbb{T}$ using a 2D inverse Fourier Transform. Then on each time-domain series MRS quantitation methodology is applied, obtaining estimated concentrations that, as a final step, are assembled in concentration maps for each metabolite.

I.3.4 MRSI Pulse Sequences

MRSI pulse sequences, usually derived from single voxel spectroscopy, have been developed to optimize localized spectroscopy on a larger region of interest. Because of hardware limitations and time necessary for a full acquisition, MRSI has not been used on a large clinical scale, but due to recent improvements, both in hardware and in pulse sequences, its use has begun to rise. In the following section some of the pulse sequences used in MRSI are briefly described.

Classical CSI The classical MRSI acquisition sequence is chemical shift imaging (CSI) [29, 107, 147, 78, 111] where one excitation is required to acquire each spatial phase encode. The pulse scheme is roughly a sequence of MRS acquisitions, with the gradient values adjusted at each step so as to provide full coverage of the $\mathbb{K}^2$ space. The major disadvantage of classical MRSI acquisition is the time constraint. When acquiring a MRSI image with a resolution of $N_x \times N_y$ the total time required is $N_x \times N_y \times T_R$ where T_R is the time between two RF excitations (repetition time [7]). This, coupled with the usual technique of averaging over a number of spectra in order to obtain acceptable SNR, makes a classical MRSI acquisition generally too lengthy for routine clinical use.

Fast(er) MRSI In order to render MRSI possible in a clinical environment by severely reducing the total acquisition time, several techniques have been developed to accelerate MRSI. One approach is to change the sampling of the $\mathbb{K}^2$ space, as information is usually concentrated in the centre of it, while also possessing symmetry properties that allow reconstruction from partial datasets. $\mathbb{K}^2$ space trajectories can also be changed from the usual Cartesian sampling to a more adapted one, such as radial or spiral Hugg et al. [83], although this requires a more complicated reconstruction. These two approaches trade speed for spatial resolution, while not touching spectral resolution. The time gain factor is moderate.

Another class of techniques, inspired from fast MRI methods such as EPI manage a much more important gain in terms of time. They use refocusing methods to generate echoes, thus compressing in one RF pulse cycle the acquisition of a number of $\mathbb{K}^2$ space points. Figure I.8 shows a comparison between three fast MRSI techniques : "turbo" MRSI [53], echo planar MRSI (PEPSI) [134] and spiral-MRSI (see the recent review by Delattre et al. [51] on spiral acquisition schemes).

Echo Planar Spectroscopic Imaging Echo planar MRSI sequences combine the space encoding of echo planar imaging (EPI) with spectral encoding to provide spectroscopic imaging. First proposed by Doyle and Mansfield [52] in 1987, EPSI has long suffered from lack of implementation due to insufficiently powerful hardware, as the pulse sequences especially need strong gradients. With the recent developments though, most current scanners allow the necessary gradient power, making EPSI an appealing technique due to its strong reductions of the total acquisition time.

It should be noted that EPSI sequences trade spectral resolution for speed, making them unsuitable for applications where spectral resolution is essential. Following are two examples of currently used EPSI encoding schemes. For a more detailed description of EPSI, as well as an interesting discussion on the method trade-offs, see Mulkern and Panych [119].

7. Repetition time should allow longitudinal magnetization to grow back; it is thus bounded downwards by T_1. Pulse sequences with only partial regrowth exist, but are not discussed in this context.

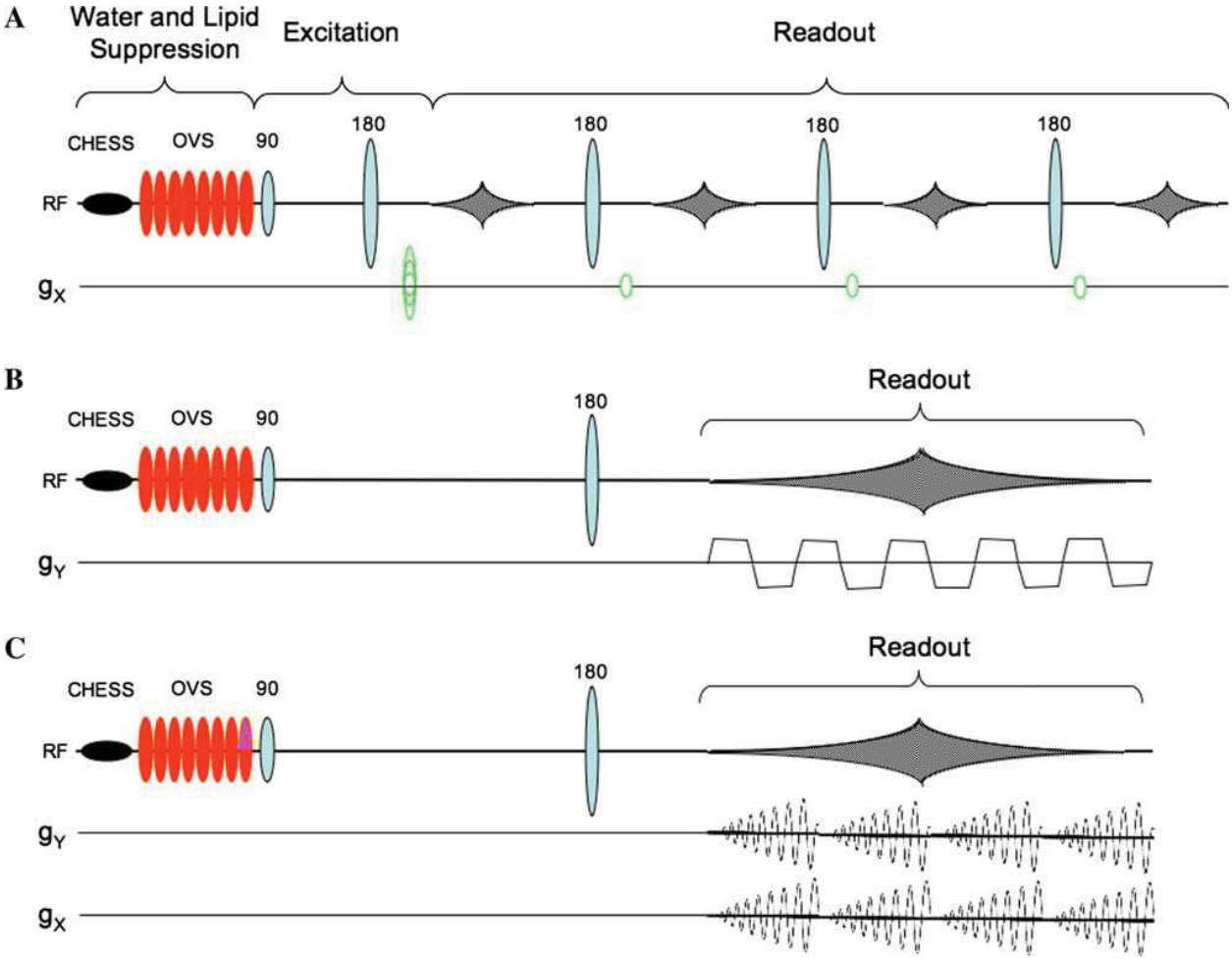

Figure I.8: *Different readout strategies for fast MRSI pulse sequences; in the examples shown here all sequences use spin echo excitation preceded by CHESS water suppression and OVS lipid suppression. (A) In fast-spin-echo , or "turbo" MRSI, multiple spin echoes are acquired, each one with its own phase-encoding gradient, (B) in Proton echo-planar spectroscopic imaging (PEPSI), an oscillating read gradient is applied during data acquisition, and (C) in spiral-MRSI, two oscillating read gradients are applied during data acquisition. Reproduced from Barker and Lin [8].*

Proton Echo-Planar Spectroscopic Imaging (PEPSI), proposed by Posse et al. [134, 135] provides simultaneous acquisition of a $\mathbb{K} \times \mathbb{T}$ space after each RF excitation pulse. This preserves good spectral resolution. Figure I.9 illustrates a (P)EPSI pulse sequence with double outer volume supression.

Echoplanar Chemical Shift Imaging (EP CSI) is a MRSI acquisition method proposed by Guimaraes et al. [74] and designed to acquired a complete $\mathbb{K}^2$ space for each RF excitation pulse. This improves considerably the acquisition time, while trading off spectral resolution. Figure I.10 illustrates a EP-CSI pulse sequence, as well as the corresponding $\mathbb{K}$ space trajectory.

For more information on current state-of-the-art in MR Spectroscopic Imaging, as well as for more information and references concerning basic principles, also see the recent review by Skoch et al. [167].

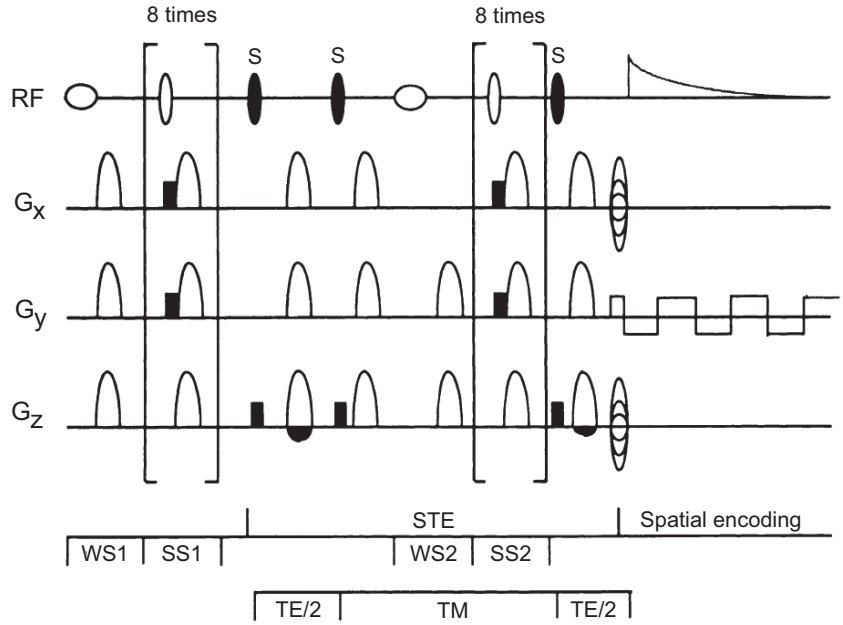

Figure I.9: *EPSI pulse sequence with double-outer volume suppression. The pulse sequence is based on a stimulated echo localization scheme in which all three RF pulses (grey symbols labelled S select the same section. Spatial suppression (SS1 and SS2) is applied orthogonal to the echo-selected section to suppress superficial lipid signals. Multiple (n=8) spatial supression pulses with subsequent gradient dephasing are applied each supression period in different spatial orientations to follow the contours of the brain. Two chemical shift selective water supression pulses (WS1 and WS2) are applied. Spatial localization is achieved by means of echo-planar spectral-spatial encoding in one spatial dimension and by phase encoding in the other dimensions.* $G_{x,y,z}$ *- gradients. Reproduced from Posse et al. [134].*

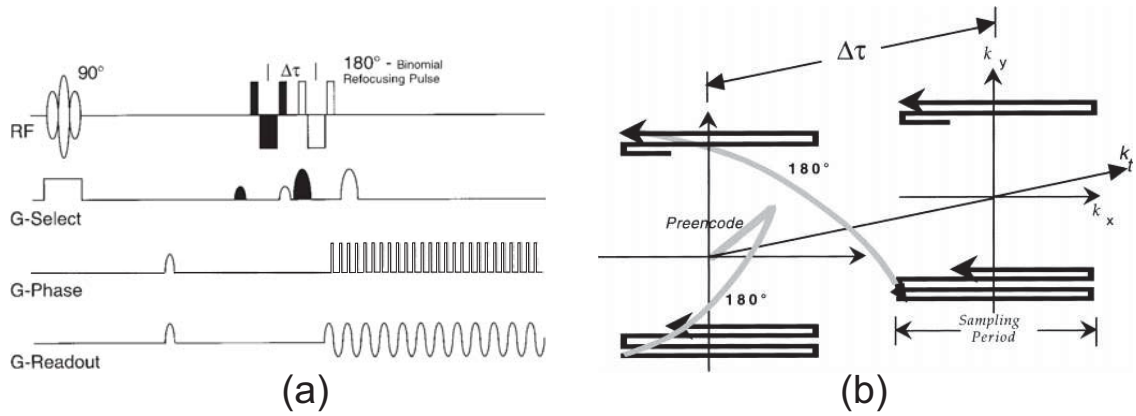

Figure I.10: *(a) Echo Planar CSI sequence, which combines phase encoding of the frequency dimension with the EPI encoding of spatial dimensions. The 180° pulse is shifted* $\triangle\tau$ *on successive excitations while the readout is kept constant. This ensures coding of the spectral information. (b)* $\mathbb{K}$ *space trajectory of EP CSI sequence. Each* $\triangle\tau$ *encodes the chemical shift into the phase of the signal, then a full* $\mathbb{K}$ *space is acquired using EPI. Adapted from Guimaraes et al. [74].*

I.4 Clinical Metabolites of Interest in brain MRS

The number of metabolites whose concentrations are measurable *in vivo* is limited at present times by technical considerations, such as noise, field strength or shim. Figure I.11 shows a rat brain spectrum obtained by Mlynárik et al. [113] at 9.4 T. Seventeen metabolites have been quantified by the authors. Two aspects restrain though such performances for current *in vivo* acquisitions: (1) the field strength used (9.4T) is far superior to any certified clinical scanner (max. 3T) and (2) the acquisition is performed on rats under anaesthesia, currently forbidden for clinical methodology. Human scanners face additional challenges such as field inhomogeneity due to field size, movement artefacts and serious limitations on acquisition time. For example, in 2007 Gottschalk et al. [66] reported being able to identify reliably only seven metabolites at 3T on *in vivo* brain tissue.

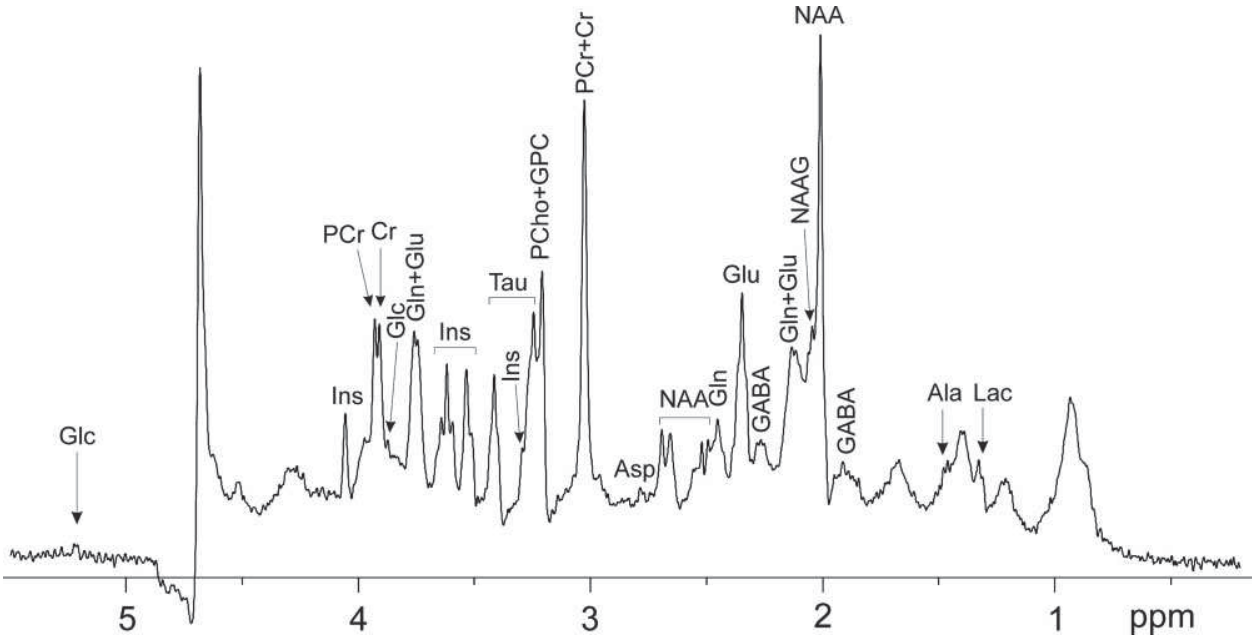

Figure I.11: *A proton spectrum measured with the SPECIAL (SPin ECho, full Intensity Acquired Localized spectroscopy) pulse sequence from a volume of* $4 \times 3 \times 4$ mm^3 *comprising the frontal cortex and putamen of the rat brain (TR = 4000 ms, TE = 2.2 ms, and number of scans = 160). A shifted Gaussian function (gf = 0.12, gfs = 0.08) was used for modest resolution enhancement. No baseline correction or post-processing for water signal removal was applied. Ala = alanine, Asp = aspartate, Cr = creatine, GABA = γ-aminobutyc acid, Glc = glucose, Gln = glutamine, Glu = glutamate, GPC = glycerophosphocholine, Ins = myo-inositol, Lac = lactate, NAA = N-acetylaspartate, NAAG = N-acetylaspartylglutamate, PCr = phosphocreatine, Tau = taurine. Unlabeled peak at 4.7 ppm is residual water. Adapted from Mlynárik et al. [113]. Field strength is 9.4T.*

As the main focus of this thesis is signal processing and parameter estimation for brain MRS and MRS Imaging data, below are listed some of the most relevant metabolites for *in vivo* brain spectra. Some background information, as well as a summary spectral description and a non-exhaustive list of current clinical application is provided for each metabolite.

Creatine (Cr) and Phosphocreatine (PCr), sometimes referred to as their sum tCr - total Creatine, are very important for the energetic cycle of the cells, having the role of

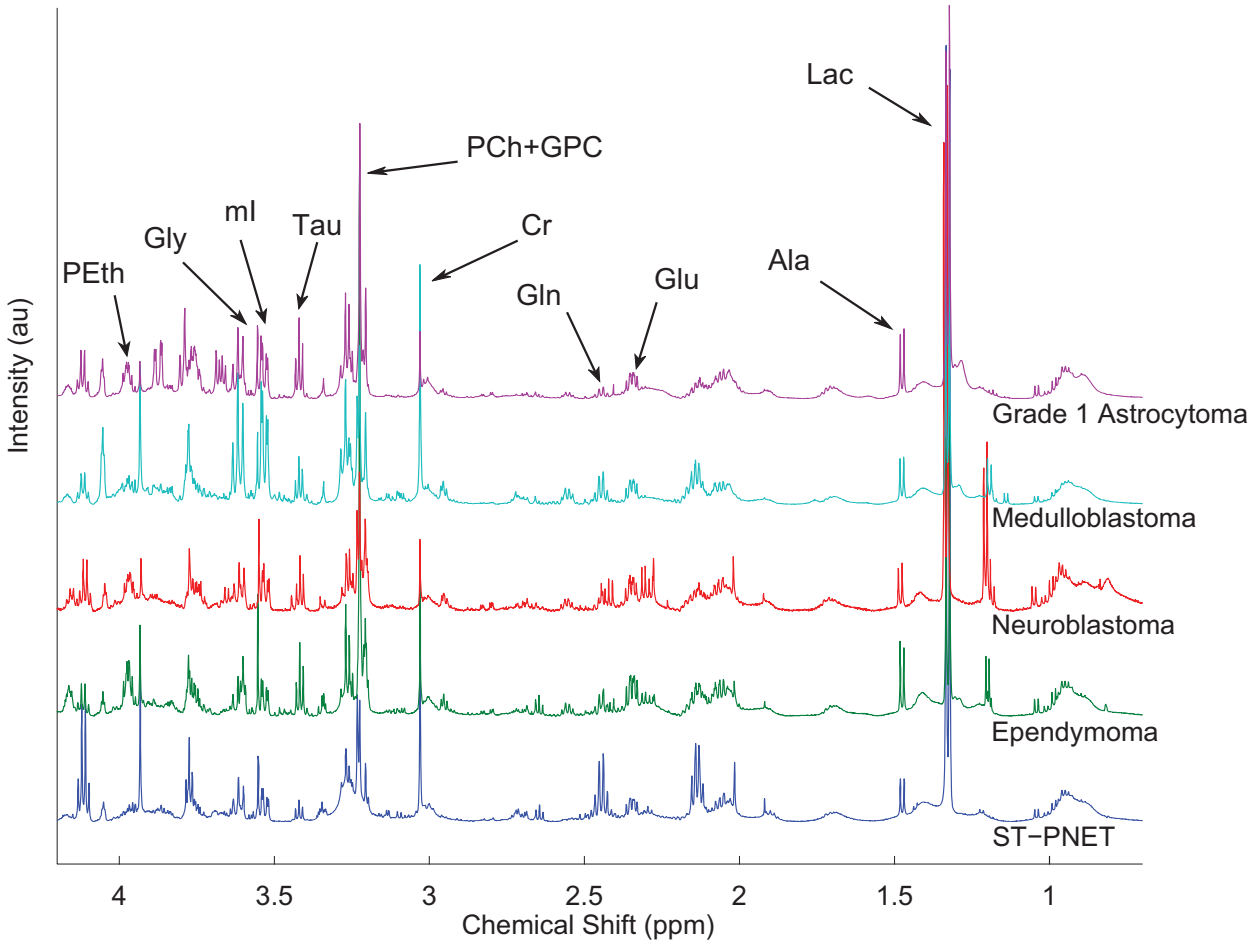

Figure I.12: *High resolution magic angle spinning ^1H NMR spectra for five tumour groups. Spectra were baseline corrected and then scaled to the spectral area between 0.5 ppm and 4.5 ppm. Tau-Taurine, PEth-phosphorylethanolamine, PCho-phosphorylcholine, mI-myo-inositol, Lac-lactate, Gly-glycine, GPC-glycerophosphorylcholine, Gln-glutamine, Glu-glutamate, Cr-creatine. Adapted from Wilson et al. [197].*

energy storage for the quick anaerobic conversion between ATP and ADP. As such, most Cr is found in the skeletal muscle and in the brain, although it can also be found in the liver (where it is synthesized) and in the blood (as it is transported to the muscles). Because of its small variation in the case of brain pathologies, as well as due to the high SNR observed for their singlets, Cr and PCr are generally used as internal references for the estimation of the other metabolite concentrations. Recent studies have, however, questioned this practice, showing tCr variations in pathological cases [158], as well as between different regions of the brain Grachev et al. [68]. Li et al. [95] also provides an analysis of metabolite variance when tCr is used as a reference, concluding that such use may be faulty.

Creatine spectra exhibit singlets at 3.03 ppm, 3.9 ppm and 6.65 ppm. Phosphocreatine NMR resonances are almost indistinguishable from Cr, with frequency shift differences smaller than 0.07 ppm [67]; meanwhile high field MRS or HRMAS provide good separation [35]. Typical concentrations in the human brain have been reported to be 4.0–5.5 $mmol \cdot kg^{-1}$ for PCr and 4.8–5.6 $mmol \cdot kg^{-1}$ for Cr. [136, p.17]. Govindaraju et al. [67] give human brain concentration ranges of 5.1-10.6 $mmol \cdot kg^{-1}$ for Cr and of 3.2-5.5 $mmol \cdot kg^{-1}$ for PCr.

N-acetylaspartate (NAA) and N-acetylaspartateglutamate (NAAG) are highly concentrated acetylated compounds found predominantly in the nervous system of vertebrates and invertebrates, and presumably linked to each other in terms of biosynthesis[114]. Their function in not yet well understood, but current research hints to the role played as an organic osmolyte that removes excess water from neurons. There is also compelling evidence that NAA is essential for the lipid synthesis and myelination [102]. Because of their predominant neuronal localization [62], their high concentrations and the fact that they provide very distinct peaks in water-suppressed proton NMR Spectroscopy, NAA and NAAG have been extensively used as a non-invasive marker for neuronal dysfunction. Most brain pathologies show an important decrease in NAA levels, one exception being the Canavan disease, that shows accumulation of NAA due to the lack of degradative enzyme activity [102] .

NAA spectra spectra are highly recognizable by the 2.01 ppm singlet, with other multiplets at 2.48 ppm, 2.67 ppm, 4.38 ppm and 7.82 ppm. Reported NAA concentrations in the human brain are between 7–16 $mmol \cdot kg^{-1}$. NAAG is primarily detected via the 2.04 ppm resonance peak, therefore appearing as a lineshape deformation of the 2.01 ppm NAA peak.

Lactate (Lac) is a product of anaerobic glycolysis and is usually recycled by the liver as part of the Cori cycle. Recent studies have shown that lactate provides an alternative source of energy for glucose in the brain [188], especially during physical effort, when oxygen and glucose in blood is mainly consumed by muscular cells [148]. During the normal functional cycle, the quantity of lactate in the brain is very small, usually under the detection limit of current MRS studies. Increases in Lac usually show loss of cell oxygenation and are thus considered markers for brain damage due hypoxia, such as stroke, trauma or tumours [159]. Increase of lactate can also be an indicator of increased macrophage activity or of presence of neoplasm, that have been shown to have increased glycolitic activity [204].

Lactate spectra are constituted by a 1.33 ppm doublet and a quartet at 4.09 ppm. Doublet observation can be seriously impaired by lipid resonance at 1.3 ppm, while the quartet is usually not detectable *in vivo* because of the water peak. Lac concentration is normally very small in the brain cells, but concentrations as high as as 5.10 $mmol \cdot kg^{-1}$ have been reported in the brain extracellular fluid [1].

Myo-inositol (mI) is the isomer of inositol most commonly found in human tissue. Its functions have not yet been completely understood, although current research suggests that mI plays various roles in cell membrane potential and intracellular Ca^{2+} concentration maintenance [181], gene expression [162], inositol lipids synthesis and construction of membrane lipids. Myo-Inositol is also known to be an important part of the phosphatidylinositol second messenger system (PI-cycle) and as such it is of special interest to psychiatric research [164].

Myo-Inositol spectra consist of doublet-of-doublet at 3.52 ppm, a triplet at 3.61 ppm, a triplet at 3.27 ppm (typically hidden under Cho) and a triplet at 4.05 ppm (typically under water peak supression area). Typical concentrations are at $4-8\ mmol \cdot kg^{-1}$, although significantly altered values have been reported in pathological cases [67].

Choline is mainly present in the brain under its free form (Cho) or as other choline compounds: glycerophosphocholine (GPCh) and phosphorylcholine (PCh). Due to the very small frequency shift between the choline forms (<0.02 ppm) the total Choline (tCho) signal is usually measured in low-field MR Spectroscopy. Choline participates in the transsulfura-

tion pathway and serves as a precursor for the neurotransmitter acetylcholine. PCh is an intermediate product in the synthesis of the insoluble phospholipids that constitute the cell membrane and also plays a role in the identification of damaged cells by the immune system via C-Reactive Proteins, while GPCh is a product of cell membrane degradation [136, p. 16]. High values of tCho are usually associated with an increased cell membrane construction/deconstruction and have been used as indicators of brain tumours and demyelinating diseases [158].

Choline spectra show a prominent peak at 3.19 ppm and multiplets at 3.50 ppm and 4.05 ppm. PCh has a major peak at 3.21 ppm and multiplets around 4.28 and 3.64 ppm, while GPCh has a more complicated structure, with a singlet at 2.21 ppm and multiplets around 4.3, 3.66 and 4 ppm. Because of the very difficult separation, total choline concentration has more applications in NMR spectroscopy, having typical values of $1-2\ mmol \cdot kg^{-1}$.

D-Glucose (Glc) is the form of aldohexose sugar most present in the human metabolism. Glc is one of the most important cellular energy sources, being used by aerobic respiration, anaerobic respiration or fermentation, while also playing a critical role in protein production and in lipid metabolism. As the primary source of energy for brain cells, D-Glucose has been extensively used as marker for brain activity in functional studies, as well as in traumatic or pathological brain dysfunction cases [87, 141].

D-glucose exists mainly in two anomeric forms, designated α-Glc and β-Glc, found in solution at an approximately stable rate of α:β = 36:64 . This ratio has been shown to vary due to different metabolic properties of the two anomers [125], but in the absence of external mechanisms should return to equilibrium value. Spectra associated to the two anomers have a complex multiplet pattern, that at lower field strengths collapses in multiplets around 3.43 and 3.8 ppm [67], making direct NMR detection under normal circumstances very difficult. Usual Glc brain concentration is around 1 $mmol \cdot kg^{-1}$, although values as high as 9 $mmol \cdot kg^{-1}$ have also been reported [72].

Amino acids in their free form are also detectable in the human brain tissue, having various roles in the brain metabolism, including being the building blocks for protein and being precursors for neurotransmitters, polyamines and nucleotides. In the following paragraphs some of the amino acids most pertinent to brain NMR analysis are shortly described.

γ-Aminobutyric acid (GABA) is the main inhibitory neurotransmitter of the central nervous system. Typical values are of 1 $mmol \cdot kg^{-1}$ and altered values have been used as markers of neurological disorders [149, p. 24].

Glutamine(Gln) and Glutamate (Glu), sometimes grouped under the abbreviation Glx, are the most abundant amino acids in the brain. As standard amino-acids, Glx have roles in protein synthesis. Gln is also a cellular energy source (next to Glc) and a precursor to Glu, while the latter is the most abundant excitatory neurotransmitter in the nervous system. Typical values for Gln and Glu are 12 $mmol \cdot kg^{-1}$ and, respectively, 24 mM [136, p. 17]. Changes in the Gln/Glu ratio have been used as markers for cerebral ischemia, hepatic encephalopathy and Rett's syndrome [67].

Met.	Concentration (mmol/kg$_{ww}$)	Chemical Shifts. (ppm)
Cho	0.9 - 2.5	3.21(3.18), 4.05, 3.50
Cr	5.1 - 10.6	3.03, 3.91, 6.65
GABA	1.3 - 1.9	2.99(3.01), 1.89, 2.28
Glc	1.0	*(see anomers below)*
Glc(α) †	*	5.21, 3.51, 3.70, 3.40, 3.82, 3.82, 3.75
Glc(β) †	*	4.63, 3.23, 3.47, 3.39, 3.45, 3.89, 3.71
Gln	3.0 - 5.8	3.75, 2.13, 2.11, 2.43, 2.45, 6.81, 7.53
Glu	6.0 - 12.5	3.74, 2.04, 2.12, 2.34, 2.35
Lac	0.4	4.10, 1.31
mI	3.8 - 8.1	3.52, 4.05, 3.52, 3.61, 3.27, 3.61
NAA	7.9 - 16.6	2.00, 4.38, 2.67, 2.49, 7.82
NAAG †	0.6 - 2.7	2.04, 4.61, 2.72, 2.52, 4.13, 1.89, 2.05, 2.20, 2.18
PCr	3.2 - 5.5	3.03, 3.93, 6.58, 7.30

Table I.1: *Typical concentrations and spectral NMR resonances for the main human brain metabolites, as reported by Govindaraju et al. [67] and more recently by Rabeson [149, Appendix A]. When reported values do not match, the value in parantheses is the one reported in [67]. The DSS-trimethyl resonance has been used as reference ($\delta_{ref} = 0$ ppm). Spectra have been observed at $f_0 = 500$ or 600 MHz, $T = 37°C$ and pH = 7.0. Metabolites marked with † had their chemical shifts measured in D_2O.*

Glycine(Gly) is the smallest amino acid, with the main role as protein building block and inhibitory neurotransmitter. Gly spectra consist of one singlet around 3.56 ppm. Typical concentrations are around $1 mmol \cdot kg^{-1}$.

Other MRS-relevant amino acids are usually only observable in current *in vivo* brain MRS acquisitions under special circumstances. Examples include Taurine (Tau), with reported concentrations of between 1.3−1.9 $mmol \cdot kg^{-1}$ in the adult brain, Aspartate (Asp), reported between 0.3−1.1 $mmol \cdot kg^{-1}$ and Alanine (Ala), between 0.2−0.8 $mmol \cdot kg^{-1}$ [129].

Lipids (Lip) are present in the brain in their free form mainly due to cell and membrane degeneration, and have been proposed as a marked for necrosis.

Because lipids have T_2 relaxation times much smaller than the main metabolites they produce very large spectral peaks, with the main contributions at 1.3 ppm and 0.9 ppm. Lipid concentrations are typically very small, but have been reported to drastically increase in the case of tumours. Another cause of high Lip peaks in MRS is subcutaneous fat tissue present in the skull, either because the tissue is part of the acquired voxel or because of signal contamination due to chemical shift artefacts.

Macromolecules (MM) are biochemical components whose size is above 3500 Da [8] [101], such as proteins, nucleic acids or polysaccharides [184]. On weight basis, macromolecules

8. Dalton (*Da*, sometimes *d*), also called the unified atomic mass unit (u) is a unit of mass used to express atomic and molecular masses. 1 Da = 1.660538782(83) 10−27 kg, roughly the mass of a ^{1}H atom.

are the most abundant molecule types in living cells, forming about 26% of the wet weight (water represents 70% of the wet weight) . They are also very diverse, counting about than 3000 macromolecular types [3, p.53-73]. Due to their size, macromolecules have a very strong interaction with their environment, that further translates in small T_1 and T_2 relaxation times, with MM signal being typically concentrated only in the first points of the acquired data.

Although some research has suggested possible use of the MM signal [155], it is currently seen in MRS studies as a nuisance signal, being usually assimilated in the baseline. Several techniques have been developed in order to minimize MM influence on the quantification of other metabolites, both at acquisition and post-processing. The difference in T_1 between metabolites and macromolecules allows the so-called inversion-recovery (IR) metabolite nulling, where the pulse sequence parameters are chosen in such a way as to minimize the metabolite contribution, allowing for the modeling of the MM signal [46, 100, 101].

Conclusion

In this chapter, the basic concepts that lead from spins to MR Spectroscopy and Spectroscopic Imaging signals have been discussed. The next chapter focuses on techniques allowing the exploitation of MRS(I) data (quantitation), as well as on signal processing aspects associated with it.

Chapter II

Signal Processing for MRS and MRSI

This chapter introduces the signal processing aspects present in NMR Spectroscopy and briefly describes most common currently used procedures. Section II.1 shows how MRS models are derived from physical phenomena described in the previous chapter. Section II.2 briefly describes important concepts in visualization and analysis of harmonic signals. Section II.3 offers an insight into the theory and implementation of nonlinear least-squares minimization problems. Section II.4 presents the state-of-the-art in MRS quantitation (parameter estimation). Finally, section II.6 provides some insights into the error, incertitude and confidence problems associated with MRS data acquisition and quantitation.

II.1 MRS problem overview

In the previous chapter, we have described the mechanisms that produce a signal in MRS, showing different methods to obtain a signal that depends on the physical and chemical properties of the sample in the NMR scanner. The signal processing paradigm is the inverse problem associated with NMR spectroscopy: from the signal $\mathbf{s}$ obtained via MRS, how can the physical and chemical properties be determined, and with what accuracy. Although different properties have been explored (*e.g.* temperature [36, 84], pH [64], etc.), the main aim of spectroscopy is the identification and concentration estimation of various chemical compounds, a process often referred to as "quantitation".

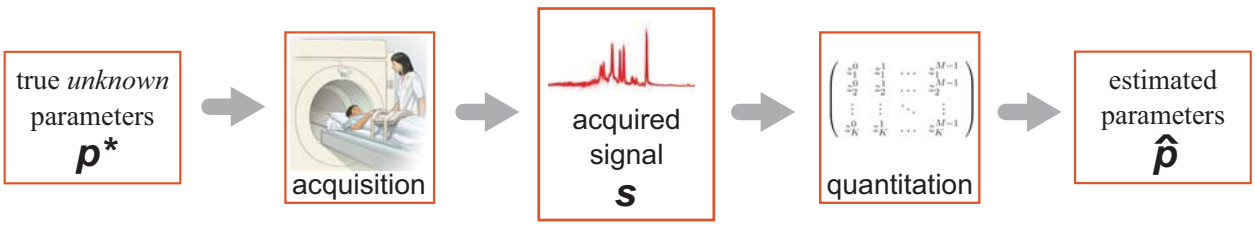

Figure II.1: *NMR acquisition chain. The bio-physical sample is described by the unknown parameters* $\mathbf{p}^*$*. During the acquisition process, a signal* $\mathbf{s}$ *is acquired, representative of* $\mathbf{p}^*$*. During the quantitation step, mathematical methods are applied to estimate* $\hat{\mathbf{p}}$ *from* $\mathbf{s}$*. The parameter estimates* $\hat{\mathbf{p}}$ *are expected to be equal to* $\mathbf{p}^*$*, and the whole process is expected to be transparent to the clinical user. Notice however that acquisition and quantitation are complementary steps, and that the performance of the whole measurement chain cannot be correctly assessed by taking in consideration only quantitation errors.*

In order to understand and properly analyse the various techniques for MRS quantitation, it is necessary to build a satisfactory model for the signal generated according to techniques described in the previous chapter. In order to keep the model as simple as possible, while introducing the effect of static field heterogeneity, several assumptions have been made. Most properties of the acquisition sample (metabolite concentrations, temperature, T_1, T_2, etc.), as well as the static field of the scanner (B_0) are assumed to be constant in time.

Assume that inside a very small volume dV, situated at the position $\mathbf{r} = (x, y, z)$, the static magnetic field is homogeneous and equal to $B_0(\mathbf{r})$. The MRS signal generated by dV can be written as (see Eq.I.27)

$$ds(\mathbf{r}, t) = \sum_{m=1}^{M} \left\{ c_m \sum_{k=1}^{K_m} \left[\exp\left(-\frac{t}{T_{2,m,k}}\right) \exp(\imath\varphi) \exp[\imath\gamma B_0(\mathbf{r})(1-\sigma_{m,k})t] \Upsilon_{m,k}(t) \right] \right\} dV \tag{II.1}$$

where M is the total number of metabolites and K_m is the number of nuclei in each metabolite m.

The total signal obtained from an acquisition where only the spins inside the Volume of Interest (VOI) are assumed to make a contribution is given by the integral sum over the VOI of Eq.II.1:

$$\begin{aligned} s(t) &= \int_{r \in VOI} ds(\mathbf{r}, t) \\ &= \int_{VOI} \sum_{m=1}^{M} \left\{ c_m(\mathbf{r}) \sum_{k=1}^{K_m} \left[\exp\left(-\frac{t}{T_{2,m,k}}\right) \exp(\imath\varphi) \exp[\imath 2\pi \underbrace{\gamma B_0(\mathbf{r})(1-\sigma_{m,k})}_{(a)} t] \Upsilon_{m,k}(t) \right] \right\} d\mathbf{r}^3 \end{aligned} \tag{II.2}$$

In Eq.II.2, the term (a) stands for the frequency of the spin k of the metabolite m, without taking into account J-coupling spectral splitting [1]. Looking closely at (a), several simplifications can be made.

- The local static field $B_0(\mathbf{r})$ can be written as sum of the homogeneous static field B_0 and the local variation $\triangle B_0(\mathbf{r}) = B_0(\mathbf{r}) - B_0$. Using current hardware, the ratio $\frac{\triangle B_0(\mathbf{r})}{B_0}$ is usually under 1 ppm in typical VOIs in the human brain (*cf.* Fig.II.2).
- After demodulation at the frequency $f_0 = \gamma B_0$, the term γB_0 can be subtracted from (a).
- Since σ is also in the order of ppm, the cross-term $\triangle B_0(\mathbf{r})\sigma$ is very small and thus the following approximation is viable [2]:

$$[B_0 + \triangle B_0(\mathbf{r})](1-\sigma) - B_0 \approx \triangle B_0(\mathbf{r}) - \sigma B_0 \tag{II.3}$$

1. As shown in the previous chapter (see Eq.I.25), the J-coupling is conveniently represented in Eq.II.2 by the splitting function Υ.

2. There are certain cases when the shielding - inhomogeneity cross factor must be taken into account, but they do not represent the focus of this thesis. In MRSI, for example, this factor induces a well-known spatial displacement artifact.

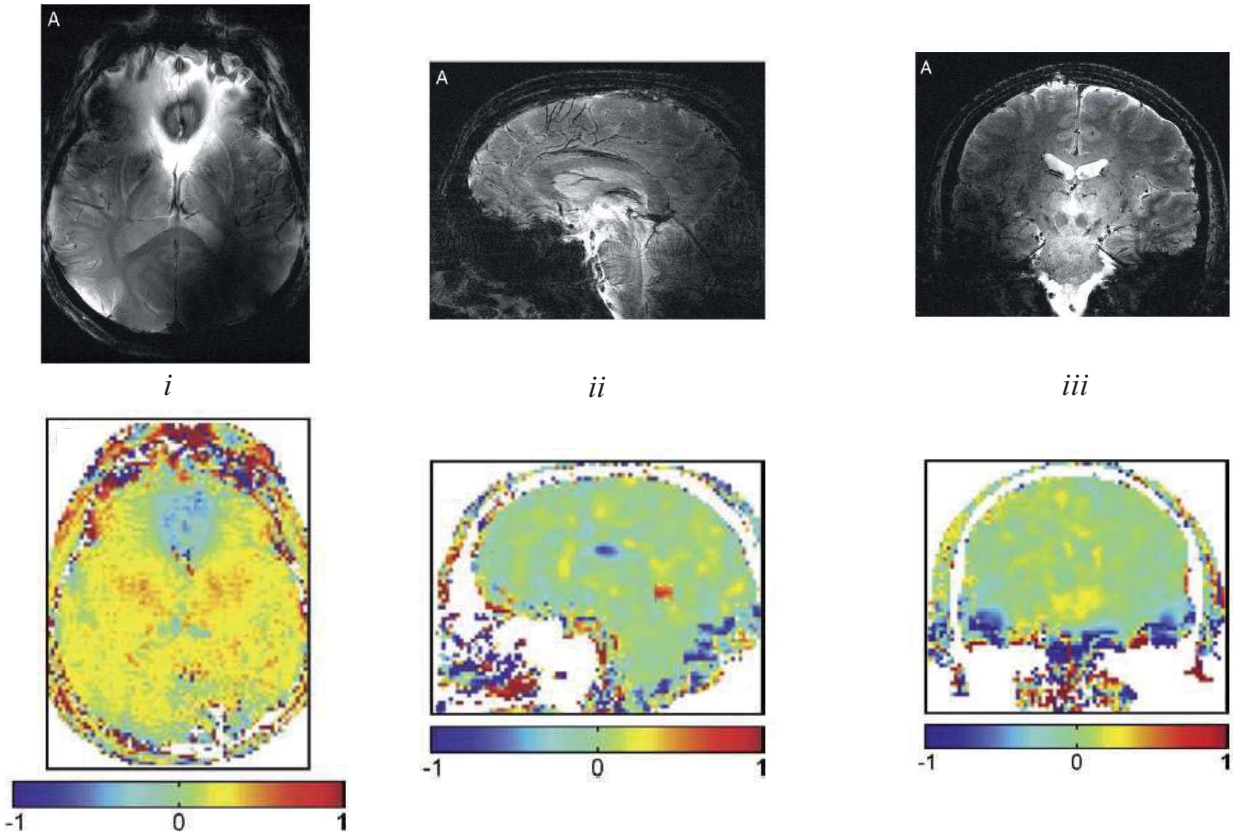

Figure II.2: *MRI images (upper row) and B_0 magnetic field inhomogeneity maps (lower row), corresponding to a healthy human brain, measured in a 8T whole-body MRI system. Inhomogeneity is is ppm/cm. i: axial, ii: mid-sagittal, iii: coronal. Images come from different patients. Adapted from Truong et al. [183].*

Replacing Eq.II.3 in Eq.II.2, allows further factorization to take place:

$$\begin{aligned} s(t) = & \\ &= \int_{r\in VOI} \sum_{m=1}^{M} \left\{ c_m(\mathbf{r}) \sum_{k=1}^{K_m} \left[\exp\left(-\frac{t}{T_{2,m,k}}\right) \exp(\imath\varphi) \cdot \right.\right. \\ &\qquad \left.\left. \cdot \exp[\imath 2\pi \underbrace{\gamma(\triangle B_0(\mathbf{r}) - \sigma_{m,k} B_0)}_{\text{simplified } (a)} t] \; \Upsilon_{m,k}(t) \right] \right\} d\mathbf{r}^3 \\ &= \sum_{m=1}^{M} \left\{ \int_{r\in VOI} c_m(\mathbf{r}) \exp(\imath\gamma \triangle B_0(\mathbf{r}) t) \exp[\imath\varphi(\mathbf{r})] \cdot \right. \\ &\qquad \left. \cdot \sum_{k=1}^{K_m} \left[\exp\left(-\frac{t}{T_{2,m,k}}\right) \exp(\imath\varphi) \; \exp[\imath 2\pi\gamma(-\sigma_{m,k} B_0)t] \; \Upsilon_{m,k}(t) \right] d\mathbf{r}^3 \right\} \end{aligned} \tag{II.4}$$

Although Eq.II.4 does not appear to have a simple form, it is noticeable that the terms inside the sum $\sum_k^{K_m}$ do not depend on $\mathbf{r}$, and are very similar to the single contribution of one spin, as described by Eq.I.27. Therefore these terms are replaced with the metabolite basis-set signals b_m:

$$b_m(t) = \sum_{k=1}^{K_m} \exp\left(-\frac{t}{T_{2,m}}\right) \exp\left(-\imath 2\pi \sigma_{m,k} f_0\right) \Upsilon_{m,k}(t) \tag{II.5}$$

The remaining terms from Eq.II.4 depend on the spatial distribution of the concentrations of each metabolite, coupled with the effect of the inhomogeneity field. We call this the context function $\Psi_m(t)$, computed as:

$$\Psi_m(t) = \int_{\mathbf{r}\in VOI} c_m(\mathbf{r}) \exp\left[\imath\gamma \triangle B_0(\mathbf{r}) t\right] \exp\left[\imath\varphi(\mathbf{r})\right] \, d\mathbf{r}^3 \tag{II.6}$$

The last step in MRS modelling is getting Eq.II.6 to be re-written in the traditional form, similar to the contribution in ideal conditions (see Eq.I.27), introducing the average concentration $\bar{c}_m = \frac{\|\Psi(0)\|}{V_{VOI}}$, the overall phase $\varphi_m = \arg[\Psi(0)]$ and the extra damping function $d_m(t)$, defined as normalized context function $d_m(t) = \frac{\Psi(t)}{\Psi(0)}$. The d_m normalization forces $d_m(0) = 1$. The final model of the signal can now be written as:

$$s(t) = V_{VOI} \sum_{m=1}^{M} \bar{c}_m \exp \imath\varphi_m \quad \underbrace{d_m(t)}_{\text{extra decay function}} \quad \underbrace{b_m(t)}_{\text{m. basis-signal}} \tag{II.7}$$

The function $d(t)$ represents the extra damping due to the inhomogeneity of B_0. It is usual in NMR to replace this extra damping with a Lorentzian damping factor, replacing T_2 with T_2^*. However, in this work we attempt to correct the effect of an *unknown* lineshape, thus placing ourselves in a more general case.

II.2 Spectral analysis : theory and methods

Direct interpretation of the acquired FID MRS signals is very difficult due to the superposed exponentially damped sinusoids. However, mathematical procedures exist that allow

visualization and interpretation of sums of decaying complex exponential signals. This section introduces some of the Spectral Analysis tools commonly used in MRS(I), with a focus on the mathematical models used for signal decomposition. Quantitation methods based on the presented decompositions are reviewed later, in section II.4.

II.2.1 Spectral estimation by Fourier Transform

The metabolite contribution separation problem is often visualized and/or solved using a function space defined by the Fourier Transform (FT). The equation linking a function $s(t)$ and its Fourier Transform $S(f)$ is given by:

$$\mathcal{F}\{s(t)\} = S(f) = \int_t s(t) \exp(\imath 2\pi f t)\ dt$$
$$\mathcal{F}^{-1}\{S(f)\} = s(t) = \int_f S(f) \exp(-\imath 2\pi f t)\ df$$

Several properties of the FT are of special interest for MRS

- The FT is linear, meaning that for any scalars a and b it is true that

$$\mathcal{F}\{a \cdot s_1(t) + b \cdot s_2(t)\} = a \cdot F\{s_1(t)\} + b \cdot \mathcal{F}\{s_2(t)\} \tag{II.8}$$

- The Inverse Fourier Transform (IFT) $\mathcal{F}^{-1}$ is very similar to the direct FT, the only difference being that the direction of the variable t is inverted. It is thus possible to obtain the IFT from the FT just by reversing the signal, equivalent to making the variable transformation $t \to -t$. Because of this property, the IFT is sometimes (inexactly) replaced in literature by the FT.
- The FT of the product of two functions is given by the convolution operator $*(\cdot,\cdot)$, defined as

$$*(s_1, s_2) \equiv s_1(t) * s_2(t) = \int_{-\infty}^{\infty} s_1(\tau) \cdot s_2(t-\tau) d\tau$$

- The area under the FT transform is linked to the first point of the time series:

$$s(t=0) = \int_f S(f) df \equiv \mathcal{A}_{S(f)} \tag{II.9}$$

In the case of discrete signals the Discrete Fourier Transform (DFT) is used to make the conversion between the discrete time series and the discrete FT output. Because of the discrete nature, the DFT is periodic with a period of $F_s = T_s^{-1}$, where T_s is the sampling time and F_s is the sampling frequency. In signal processing, instead of labelling the DFT abscissa in Hz, the normalized frequency [3] is often used, defined as $\nu = f/F_s$, that only takes values between $-\frac{1}{2}$ and $\frac{1}{2}$.

$$S[i] = \sum_{j=0}^{N-1} s[j] \cdot exp(\imath 2\pi \frac{i \cdot j}{N}) \qquad\qquad i = 0\ ,\ \ldots\ ,\ N-1$$

It is interesting to note that the DFT can be written as a matrix multiplication between the signal vector $\mathbf{s}$ and the DFT matrix $\mathbf{F}$. Furthermore, by using normalized frequencies, $\mathbf{F}$

3. The normalization is equivalent to considering the sampling time T_s equal to 1 [s].

depends only on the number of points N in the signal:

$$\mathbf{S} = \mathbf{s} \cdot \mathbf{F} \equiv \mathbf{s} \cdot \begin{pmatrix} \zeta_N^0 & \zeta_N^0 & \cdots & \zeta_N^0 \\ \zeta_N^0 & \zeta_N^1 & \cdots & \zeta_N^{N-1} \\ \vdots & \vdots & \zeta_N^{i\times j} & \vdots \\ \zeta_N^0 & \zeta_K^{N-1} & \cdots & \zeta_K^{(N-1)\times(N-1)} \end{pmatrix}$$

Moreover, as $\mathbf{F}$ is a Vandermonde matrix formed by the N^{th} order complex root of the unit, it is non-singular. This effectively means when a signal is transformed by DFT, *all* the information is conserved, and perfect reconstruction can be made using the Inverse DFT.

Although the DFT can be simply computed as the matrix product previously described, it is usually computed using a much more efficient class of algorithms, commonly referred to as Fast Fourier Transform (FFT). The variant most commonly used was proposed by Cooley and Tukey [43], but multiple approaches exist, with different trade-offs in terms of speed and numerical stability. Section 12.2 of [140] provides a good introduction in FFT computing techniques as well as a list of bibliography concerning the different methods available.

II.2.2 Spectral estimation by HSVD

Hankel Singular Matrix Decomposition (HSVD) [92] is a method to decompose a signal into a sum of complex exponentials. The Hankel matrix associated to a given signal $s[n]$, $n = 1, \cdots, N$ is built by delaying by 1 each consecutive row.

$$H = \begin{pmatrix} s[1] & s[2] & \dots & s[M] \\ s[2] & s[3] & \dots & s[M+1] \\ \vdots & \vdots & \ddots & \vdots \\ s[L] & s[L+1] & \dots & s[L+M-1] \end{pmatrix} \tag{II.10}$$

Consider that s is a sum of K complex exponentials

$$s[n] = \sum_{k=1}^{K} c'_i \cdot z_k^n \tag{II.11}$$

with the complex amplitudes $c'_k = c_k \exp(j\varphi)$ and the poles $z_k = \exp(j2\pi f_k T_s - \alpha T_s)$

Then the Hankel matrix $\mathbf{H}$ associated to the signal can be written as

$$\mathbf{H} = \underbrace{\begin{pmatrix} z_1^0 & z_2^0 & \dots & z_K^0 \\ z_1^1 & z_2^1 & \dots & z_K^1 \\ \vdots & \vdots & \ddots & \vdots \\ z_1^{L-1} & z_2^{L-1} & \dots & z_K^{L-1} \end{pmatrix}}_{\mathbf{F}_{LK}} \underbrace{\begin{pmatrix} c'_1 & 0 & \dots & 0 \\ 0 & c'_2 & \dots & 0 \\ \vdots & \vdots & \ddots & \vdots \\ 0 & 0 & \dots & c'_K \end{pmatrix}}_{\mathbf{C}_{KK}} \underbrace{\begin{pmatrix} z_1^0 & z_1^1 & \dots & z_1^{M-1} \\ z_2^0 & z_2^1 & \dots & z_2^{M-1} \\ \vdots & \vdots & \ddots & \vdots \\ z_K^0 & z_K^1 & \dots & z_K^{M-1} \end{pmatrix}}_{\mathbf{Q}_{MK}^\top} \tag{II.12}$$

$$\mathbf{H} = \mathbf{F}_{LK}\ \mathbf{C}_{KK}\ \mathbf{Q}_{MK}^\top$$

$\mathbf{C}_{KK}$ is a square diagonal matrix composed of the complex amplitudes c'_k and $\mathbf{F}_{LK}$ and $\mathbf{Q}_{MK}$ are Vandermonde matrices associated to the poles z_k. This decomposition is called Vandermonde decomposition, and it would give direct access to the desired parameters $(c\prime_k, z_k)$.

Unfortunately, no algorithm currently exists to compute it. Thus indirect methods have to be used to estimate the $(c\prime_k, z_k)$.

It should be noted that the rank of $\mathbf{H}$ is equal to K if the generating signal $s[n]$ is composed of exactly K components.

Also, it can be easily proven that any Vandermonde matrix $\mathbf{S}$ generated by the vector $\mathbf{Z} = (z_1 \dots z_n)$ has the following property (called shift-invariance):

$$\mathbf{S}^{\uparrow} = \mathbf{S}_{\downarrow}\mathbf{Z} \tag{II.13}$$

where $\mathbf{S}^{\uparrow}$ and $\mathbf{S}_{\downarrow}$ represent cropped versions of $\mathbf{S}$, without the first and respectively the last row.

Any complex matrix can be written using the so-called Singular Value Decomposition (SVD), into a product of three matrices

$$\mathbf{H} = \mathbf{U}\mathbf{\Sigma}\mathbf{V}^{H} \tag{II.14}$$

where $\mathbf{U}$ and $\mathbf{V}$ are unitary matrices and $\mathbf{\Sigma}$ is a rectangular diagonal matrix of the size of H.

Since the rank of $\mathbf{H}$ is K, the SVD will yield only K different values, and thus the size of $\mathbf{U}_K$ corresponding to these values is $L \times K$, is the same as the size of the Vandermonde decomposition matrix $\mathbf{F}_{LK}$. Further more, both $\mathbf{U}_K$ and $\mathbf{F}_{LK}$ have, due to their nature (unitary or Vandermonde), non-zero determinants. This means that there exist a square inversible matrix $\mathbf{Q} \in \mathbb{C}^{K\times K}$ so that

$$\mathbf{U}_K = \mathbf{S}\mathbf{Q} \tag{II.15}$$

Furthermore, the $\mathbf{Q}$ matrix can also be used to express $\mathbf{U}_K^{\uparrow}$ and $\mathbf{U}_K^{\downarrow}$ and thus to re-write the shift-variance property as defined in Eq.II.13:

$$\begin{aligned}
\mathbf{S}^{\uparrow} &= \mathbf{U}_K^{\uparrow}\mathbf{Q}^{-1} \\
\mathbf{S}_{\downarrow} &= \mathbf{U}_{\downarrow K}\mathbf{Q}^{-1} \\
\mathbf{U}_K^{\uparrow}\mathbf{Q}^{-1} &= \mathbf{U}_{K\downarrow}\mathbf{Q}_{-1}\mathbf{Z} \\
\mathbf{U}_K^{\uparrow} &= \mathbf{U}_{K\downarrow}\,\mathbf{Q}_{-1}\mathbf{Z}\mathbf{Q}
\end{aligned} \tag{II.16}$$

From Eq.II.16 one can compute the matrix

$$\mathbf{Z}' = \mathbf{Q}_{-1}\mathbf{Z}\mathbf{Q} = \left(\mathbf{U}_K^{\uparrow}\right)^{+}\mathbf{U}_{K\downarrow} \tag{II.17}$$

where $\left(\mathbf{U}_K^{\uparrow}\right)^{+} = \left(\mathbf{U}_K^{\uparrow\mathbf{H}}\mathbf{U}_K^{\uparrow}\right)\mathbf{U}_K^{\uparrow\mathbf{H}}$ represents the pseudo-inverse of $\mathbf{U}_K^{\uparrow}$.

In order to obtain $\mathbf{Z}$ from $\mathbf{Z}'$ one has only to diagonalize it. If, moreover, $\mathbf{Z}$ is ordered, then the solution is unique, represented by the ordered eigenvalues of the matrix $\mathbf{Z}'$.

Once the poles z_k of the signal have been computed, replacing them in Eq.II.11 gives a linear problem for determining the complex amplitudes c'_k. The simplest method is to determine the LS solution to the over-determined matrix equation

$$\begin{pmatrix} z_1^0 & z_2^0 & \dots & z_K^0 \\ z_1^1 & z_2^1 & \dots & z_K^1 \\ \vdots & \vdots & \ddots & \vdots \\ z_1^{N-1} & z_2^{N-1} & \dots & z_K^{N-1} \end{pmatrix} \begin{pmatrix} c'_1 \\ c'_2 \\ \vdots \\ c'_K \end{pmatrix} = \begin{pmatrix} x_1 \\ x_2 \\ \vdots \\ x_N \end{pmatrix} \tag{II.18}$$

In the case of noisy signals, the shift-invariance property (Eq.II.13) does not hold any more, *stricto sensu*, and the matrix $\mathbf{H}$ becomes full rank. However, if the SNR of implicit HSVD decomposition of the noise-free signal is of sufficient value, the matrix $\mathbf{H}$ can be approximated by a HSVD decomposition $\mathbf{H}_K$ of rank K [136, §2.2.2]:

$$\mathbf{H} = \mathbf{U}\mathbf{\Sigma}\mathbf{V}^\top \approx \mathbf{U}_K\mathbf{\Sigma}_K\mathbf{V}_K^\top = \mathbf{H}_K \tag{II.19}$$

It should be mentioned that in this case the decomposition is not exact any more, and the relative value of the residue (or the modelling error) $\mathbf{s} - \hat{\mathbf{s}}_{HSVD}$ decreases with SNR. Several optimizations exist for the HSVD algorithm. HSLVD [130, 112] uses the Lanczos iterative algorithm to compute SVD in the order of decreasing pole magnitude. When all relevant poles are computed, the algorithm can be stopped, thus considerably speeding up the process. HLSVD Partial Reorthogonalization (HSLVD-PRO) [93] further improves SVD by treating numerical problems of the Lanczos algorithm. HSVD Total Least Squares (HTLS) Vanhuffel et al. [191] uses a Total Least Squares [105] approach instead of a classical LS method.

II.2.3 Spectral estimation by Padé Transform

An alternative to DFT and HSVD approaches for modeling MRS data, the Fast Padé Transform (FPT), has been proposed by Belkić and Belkić [15, 13, 16, 14, 17, 18, 19]. The method is based on the Padé Approximants, and is known under various names in different disciplines [14], particularly Auto-Regressive Moving Average (ARMA) in signal processing. Furthermore, the DFT and its more general form, the z-transform, can be seen as special cases of the Padé Approximants.

As opposed to the DFT, that can be seen as a polynomial model $G_N(z^{-1})$ with the variable $z = \exp \imath\omega t$, the FPT approximates the signal as a ratio of unique polynomials $P_K^-(z^{-1})$ and $Q_K^-(z^{-1})$ of the same variable z:

$$FPT^{(-)}: \; F(z^{-1}) \approx \frac{P_K^-(z^{-1})}{Q_K^-(z^{-1})} = \frac{\sum_{n=0}^{K} p_n^- z^{-n}}{\sum_{n=0}^{K} q_n^- z^{-n}} \tag{II.20}$$

Several properties of the FPT are appealing, according to authors, for MRS analysis:

- **Quadratic Convergence rate** of the FPT, as opposed to the linear convergence of the FFT. This allows a better approximation when the transformation rank is chosen to be smaller than the number of data, as shown in Fig.II.3.
- **Non-linearity** of the FPT, allows, according to [19], a better separation of the noise from the useful signal, and thus better SNR values.
- **Signal approximation without explicit modelling** is available by FPT. This comes in contrast with HSVD, where nonlinear spectral components ζ_k have to be computed first, and the linear parameters are computed in a second step, as a LLS problem (see Eq.II.18).

II.3 Methods for numerical functional minimization

II.3.1 Notations

Unless otherwise specified, the following conventions and symbols hold for the mathematical writing:

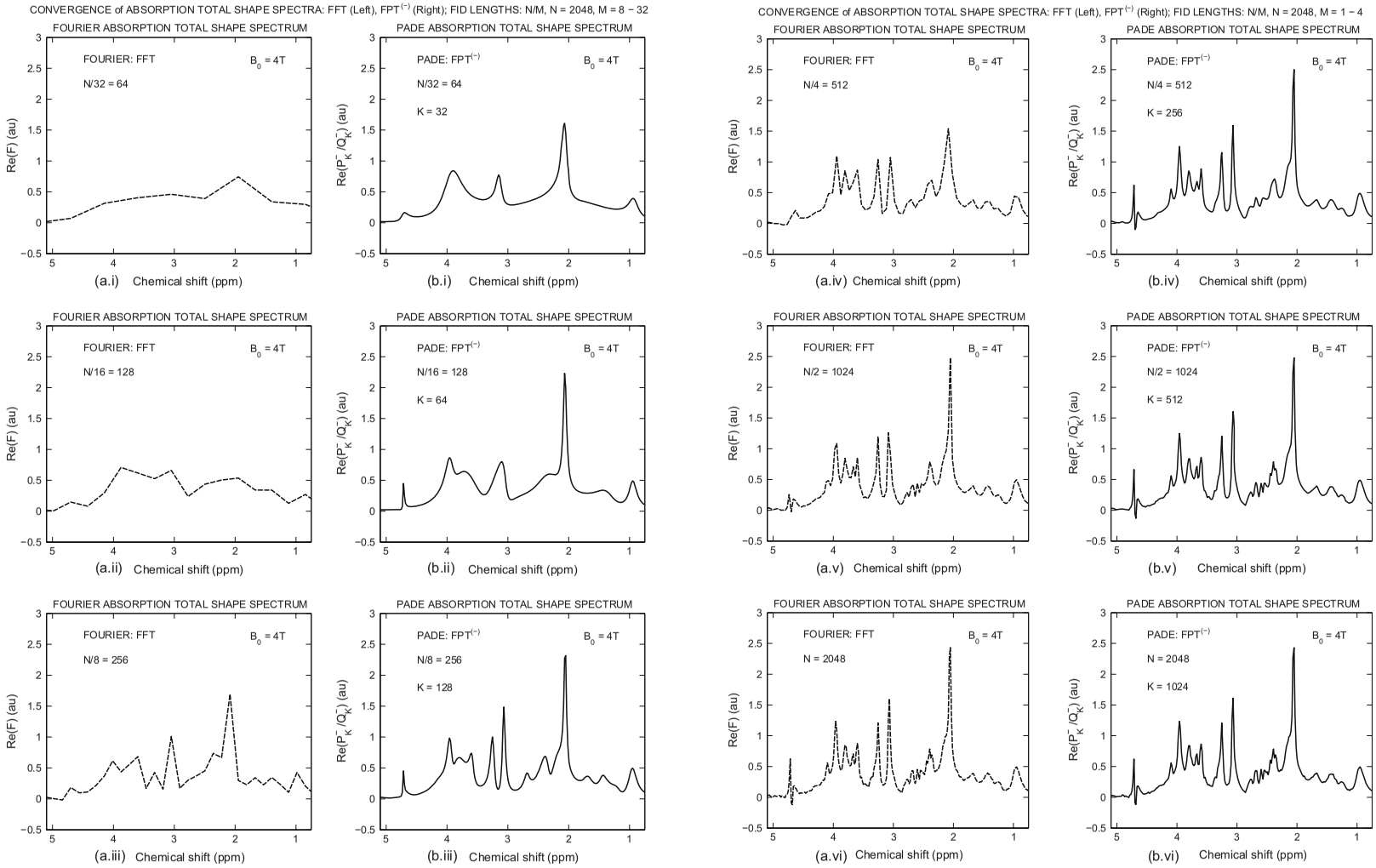

Figure II.3: *Performance comparison of the fast Fourier transform (dashed line) and fast Padé transform (full line) at one 32^{th} (N/32 = 64), one sixteenth (N/16 = 128), one eighth (N/8 = 256), one quarter (N/4 = 512), one half (N/2 = 1024) and full (N = 2048) signal lengths. Spectra correspond to an FID typically encoded clinically from a healthy human brain via MRS using an external static field B0 =4T and a short TE of 20ms, with total length N = 1024 and bandwidth 1000Hz so that t = 1ms. Signal acquired by I. Tkáč et al from occipital grey matter of a healthy volunteer. Reproduced from Belkić and Belkić [16].*

– Symbols in bold (*ie* $\mathbf{v}$) denote matrices, whereas normal font denotes scalars
– $\mathbf{v}^\top$ denotes the transposed version of $\mathbf{v}$
– $\|\mathbf{v}\|$ denotes the L_2 norm of vector a $\mathbf{v}$ of length N, computed as $\|\mathbf{v}\| = \mathbf{v}^\top\ \mathbf{v} = \sum_{i=1}^{N} v_i^2$

symbol	meaning	expression
$\mathbf{s}$	the signal to be fitted	$\mathbf{s}\ (s_i) = [s_1, s_2, \ldots, s_{N_s}]^\top$
N_s	number of data points	
N_p	number of model parameters	
$\mathbf{p}$	the parameter vector	$\mathbf{p} = (p_j) = [p_1, p_2, \ldots, p_{N_p}]$
$\hat{\mathbf{s}}(\mathbf{p})$	the model function †	$\hat{\mathbf{s}}(\mathbf{p}) = (\hat{s}_i(\mathbf{p})) = (\hat{s}_i) = [\hat{s}_1, \hat{s}_2, \ldots, \hat{s}_{N_s}]^\top$
$\mathbf{r}$	the residue †	$\mathbf{r} = \mathbf{s} - \hat{\mathbf{s}}$
$\mathbf{J}$	the model Jacobian †	$\mathbf{J} = \left(\frac{\partial \hat{s}}{\partial p_j}\right) = \left[\frac{\hat{s}}{\partial p_1}, \frac{\hat{s}}{\partial p_2}, \ldots, \frac{\hat{s}}{\partial p_{N_p}}\right]$

† Dependence of $\mathbf{p}$ may be omitted for notation simplification. For example, $\hat{\mathbf{s}}$ is equivalent to $\hat{\mathbf{s}}(\mathbf{p})$.

II.3.2 Non Linear Least Squares fitting

In order to fit a model to a given dataset, a score function is needed to compute the goodness of fit. One of the most commonly used score function is so called 'least squares' criterion. In the following section an overview of the least-squares (LS) formalism is presented.

The least squares problem can be defined as:

$$\texttt{find } \mathbf{p}^*\texttt{, a local minimizer for } F(\mathbf{p}) = \frac{1}{2}\sum_{i=1}^{N_s} r_i^2(\mathbf{p}). \tag{II.21}$$

The F function is referred to as *cost function* or *objective function*, and is generally smooth enough that for a small enough parameter variation $\mathbf{h}$ the following Taylor expansion is valid:

$$F(\mathbf{p}+\mathbf{h}) = F(\mathbf{p}) + \mathbf{h}^\top\mathbf{g} + \frac{1}{2}\mathbf{h}^\top\mathbf{H}\ \mathbf{h} + O(\|\mathbf{h}\|^3) \tag{II.22}$$

where $\mathbf{g} \equiv \mathbf{F}'(\mathbf{p}) = \left[\frac{\partial F}{\partial p_1}(\mathbf{p}), \frac{\partial F}{\partial p_2}(\mathbf{p}), \ldots, \frac{\partial F}{\partial p_{N_p}}(\mathbf{p})\right]^\top$ is the *gradient* and $\mathbf{H} \equiv \mathbf{F}''(\mathbf{p}) = \left[\frac{\partial^2 F}{\partial p_i \partial p_j}(\mathbf{p})\right]$ is the *Hessian*. The gradient can also be written in function of the Jacobian matrix of the model, denoted $\mathbf{J}$, as $\mathbf{g} = \mathbf{r}^\top\mathbf{J}$.

In an analogous manner to a 1D function, the local minima and the local maxima satisfy the cancellation of the first derivative. Solving a LS problem is thus reduced to solving the (matrix) equation

$$\mathbf{F}'(\mathbf{p}^*) \equiv\ \mathbf{r}^\top\ \mathbf{J} = \mathbf{0} \tag{II.23}$$

In the case of linear least squares problems, solving Eq.II.23 is achievable in one step. In the case of the more complex non-linear least squares (NLLS) problems, only an iterative process is possible. This further implies that starting values need to be provided to start the

iterations. Another aspect of the iterative nature of the algorithm is the proof and speed of convergence. To ensure convergence most algorithms enforce that subsequent iterations evaluate the score function lower, a condition that can be written as $\mathbf{h}^\top \mathbf{F}'(\mathbf{p}) < 0$. The vector $\mathbf{h}$ respective of this condition is called a *descent direction*.

Convergence speed is defined as the speed at which the series defined by consecutive iterations $\mathbf{p}_n$ converges to $\mathbf{p}^*$. In function of the error $\mathbf{e}_n = \mathbf{p}_n - \mathbf{p}^*$, method convergence speed can be roughly classified in

- Linear convergence : $\|\mathbf{e}_{n+1}\| \leq \alpha \|\mathbf{e}_n\|$ with $0 < \alpha < 1$
- Quadratic convergence : $\|\mathbf{e}_{n+1}\| \leq \mathcal{O}(\|\mathbf{e}_n\|^2)$
- Superlinear convergence : $\|\mathbf{e}_{n+1}\| / \|\mathbf{e}_n\| \to 0$ for $n \to \infty$

In the following paragraphs some important algorithms used to solve minimization problems in general and NLLS problems in particular are presented.

II.3.3 Constrained minimization and regularization

Often extra information (*a priori* information) is available, and finding a solution that is respective of this information is desirable. The approach most widely used consists of adding constraints to the minimization function. Minimization with constraints a functional $f(\mathbf{x})$ can be summarized as follows

$$\begin{array}{rll} \texttt{minimize} & g(\mathbf{x}) = f(\mathbf{x}) + h(\mathbf{x}) & \\ \texttt{subject to} & \alpha_i(\mathbf{x}) = a_i & \texttt{for } i = 1, \ldots, n \texttt{ Equality constraints} \\ & \beta_j(\mathbf{x}) \leq b_j & \texttt{for } j = 1, \ldots, m \texttt{ Inequality constraints} \end{array}$$

The explicit constraints α_i and β_j are called hard constraints. The introduction of an additional term $h(\mathbf{x})$ in the minimization criterion allows the so called *soft constraints*, that are local cost functions that allow to introduce more flexible *a priori* information. The main difference between the two constraint types is that hard constraints *have* to be respected, while soft constraints point to a *preferred, but not required* solution [10].

In the case of nonlinear minimization problems, it is often the case that the functional $f(\mathbf{x})$ to be minimized is very unstable so that small variations of $\mathbf{x}$ make large variations of $f(\mathbf{x})$ or vice-versa. In this case, the minimization usually converges to significantly different values for very small variations in the dataset, a behaviour that is usually not desirable. In order to limit the output variation, a special case of constraints is imposed: regularization.

Regularized solutions offer a trade-off between the best agreement to the data (f) and the best smoothness [4]. In order to control this trade-off, the cost function is re-written using the smoothness hyper-parameter λ as:

$$g(\mathbf{x}) = f(\mathbf{x}) + \lambda\, h(\mathbf{x}) \tag{II.24}$$

Very small values of λ are equivalent to minimization without regularization, while very large values ignore the underlying model and give only a smooth solution. For more information on inverse problems and the use of *a priori* information see [140, §19.4] or other standard works on inverse problems.

4. In this context smoothness is equivalent to the regularization function, as the latter's purpose is usually to avoid important solution variability.

II.3.4 Steepest descent algorithm

The Steepest Descent method (also called Gradient Descent) is based on the choice of a variation of the parameter $\mathbf{p}$ in the direction opposite to the local gradient, which is also the direction where the function should decrease the fastest.

1. `Compute steepest descent direction` $\mathbf{h}_n = -\mathbf{J}_n$
2. `Find optimal value for` α_n `to minimize` $F(\mathbf{p}_n + \alpha_n \mathbf{h}_n)$
3. `Compute next iteration` $\mathbf{p}_{n+1} = \mathbf{p}_n + \alpha_n \mathbf{h}_n$

The second step of a Newton-Raphson iteration involves finding the length of the variation. This is usually done via *line search* methods. For an introduction in line search see the course by Madsen et al. [103, *cf.* §2.3].

Gradient Descent has a linear convergence rate, making it too slow for most applications. However, combined with a good linear search algorithm to find α it may have good performances in the initial stage of the iterations. Due to this, a number of methods use a hybrid approach, where steepest descent is used at the beginning, and Newton's method when the solution is considered close enough.

II.3.5 Newton-Raphson algorithm

According to Eq.II.23 the point $\mathbf{p}^*$ has to be found as to solve $\mathbf{F}'(\mathbf{p}^*) = \mathbf{0}$. The basis of Newton's method (also called Newton-Raphson method) is given by Taylor's expansion of $\mathbf{F}'$ around $\mathbf{p}^*$:

$$\mathbf{F}'(\mathbf{p} + \mathbf{h}) \simeq \mathbf{F}'(\mathbf{p}) + \mathbf{F}''(\mathbf{p})\mathbf{h} \tag{II.25}$$

Setting the first term of the relation at the target value of $\mathbf{F}'(\mathbf{p} + \mathbf{h}) = \mathbf{0}$ gives $\mathbf{F}''(\mathbf{p})\mathbf{h} = -\mathbf{F}'(\mathbf{p})$ and suggests the following algorithm:

1. `find` $\mathbf{h}_n$ `solution to` $\mathbf{H}_n\mathbf{h}_n = -\mathbf{J}_n^\top \ (\hat{\mathbf{s}}_n - \mathbf{s})$
2. `compute next iteration` $\mathbf{p}_{n+1} = \mathbf{p}_n + \mathbf{h}_n$

Newton's method exhibits quadratic convergence rate, but is very sensitive to initial conditions, making it the method of choice when the desired solution is known to be very close to the initial conditions.

II.3.6 Gauss-Newton algorithm

The Gauss-Newton method is a variation of Newton-Raphson for least squares methods, based on a local approximation of the Hessian matrix. The term h_{ij} of the Hessian $\mathbf{H}$ is written as

$$\begin{aligned}
h_{ij} &= \frac{\partial}{\partial p_i}\frac{\partial}{\partial p_j}\left[[\hat{s}(\mathbf{p}) - s]^2\right] \\
&= \frac{\partial}{\partial p_i}\left[\frac{\partial \hat{s}(\mathbf{p})}{\partial p_j}[\hat{s}(\mathbf{p}) - s]\right] \\
&= \frac{\partial^2 \hat{s}(\mathbf{p})}{\partial p_i \partial p_j}[\hat{s}(\mathbf{p}) - s] + \frac{\partial \hat{s}(\mathbf{p})}{\partial p_i}\frac{\partial \hat{s}(\mathbf{p})}{\partial p_j} \\
&\approx \frac{\partial \hat{s}(\mathbf{p})}{\partial p_i}\frac{\partial \hat{s}(\mathbf{p})}{\partial p_j}
\end{aligned}$$

The last approximation is the basis of the Gauss-Newton algorithm. It enables a faster calculation because the Hessian $\mathbf{H}$ does not have to be computed, only the Jacobian $\mathbf{J}$. Reasons for the validity of the approximation include (1) the fact that curvature should be very small if in proximity to the solution and (2) the fact that $\hat{s}(\mathbf{p}) - s$ represents the modelling error and thus it should take statistical values distributed around zero, thus when summing the contributions of the curvature it should give statistically zero.

In this case $\mathbf{H}$ can be written as $\mathbf{H} = \mathbf{J}^\top \mathbf{J}$ and the iteration equations become

$$\begin{aligned} &1: && \mathbf{J}_n^\top \mathbf{J}_n \ \mathbf{h}_n \ = -\mathbf{J}_n^\top \ (\hat{\mathbf{s}}_n - \mathbf{s}) \\ &2: && \mathbf{p}_{n+1} = \mathbf{p}_n + \mathbf{h}_n \end{aligned}$$

II.3.7 Trust region and damped algorithms

Methods presented so far have been based on the Taylor approximation of the score function in Eq.II.22, but this converges only for very small values of $\mathbf{h}$. We can thus write that for very small $\mathbf{h}$ the function F can be approximated by a quadratic model function $\mathcal{M}$

$$F(\mathbf{p} + \mathbf{h}) \simeq \mathcal{M}(\mathbf{p}) \equiv F(\mathbf{p}) + \mathbf{h}^\top \mathbf{g} + \frac{1}{2} \mathbf{h}^\top \mathbf{H} \ \mathbf{h}$$

The minimization problem can thus locally transformed from minimizing F to minimizing $\mathcal{M}$. In order to integrate the information that the model is sufficiently accurate only in the neighbourhood of the point $\mathbf{p}$, two approaches are mainly used: trust region methods and damped methods.

- In a *trusted region* method the maximum step $\mathbf{h}$ with which the parameters $\mathbf{p}_n$ can evolve are bounded by a positive number $\triangle$, that is assumed to be known. The method can be thus written as

$$\texttt{find } \mathbf{h} \texttt{ to minimize } \mathcal{M}(\mathbf{h}) \texttt{ with } \|\mathbf{h}\| \leq \triangle$$

- In a *damped* method a penalization factor is introduced in the minimization process, so that great variations of $\mathbf{p}_n$ are discouraged. Usually a scaled version of the L_2 norm $\|\mathbf{h}\| = \mathbf{h}^\top \mathbf{h}$ is used. Given a smoothing parameter $\mu \geq 0$, the method can be written as

$$\texttt{find } \mathbf{h} \texttt{ to minimize } \mathcal{M}(\mathbf{h}) + \frac{1}{2} \mu \mathbf{h}^\top \mathbf{h}$$

II.3.8 Levenberg-Marquardt algorithm

Levenberg (1944) and then Marquardt (1963) have suggested a particularly interesting damped Gauss-Newton method, that is used today in most NLLS minimizations. The iteration step $\mathbf{h}_n$ is defined by

$$\left(\mathbf{J}^\top \mathbf{J} + \mu \mathbf{I}\right) \mathbf{h}_n = -\mathbf{J}^\top \ (\hat{\mathbf{s}} - \mathbf{s})$$

An insight on the method behaviour can be obtained when analysing extreme values for μ:

- for large values of μ the Hessian approximation term can be ignored, and the method is equivalent to $\mathbf{h} \simeq -\frac{1}{\mu} \mathbf{J}^\top \ (\hat{\mathbf{s}} - \mathbf{s})$, which is the value computed by steepest descent. This is interesting in the first iterative steps, when the solution is far from the initial guesses.

– for very small values of μ, the smoothing term can be ignored, and the step is equivalent to the Gauss-Newton method: $\mathbf{J}^\top\mathbf{J}\mathbf{h} = \mathbf{J}^\top(\hat{\mathbf{s}} - \mathbf{s})$. This should be the case when the intermediate solution $\mathbf{p}_n$ is close to $\mathbf{p}^*$ and assures quasi-quadratic final convergence.

In order to update the value of μ during the iterative process, the *gain ratio* ϱ is used, defined as $\varrho = [F(\mathbf{p}) - F(\mathbf{p}+\mathbf{h})]/[\mathcal{M}(0) - \mathcal{M}(\mathbf{h})]$. The gain ratio illustrates the ratio between the actual variations of the score functions and the variations predicted by the use of the model $\mathcal{M}$. The general strategy is to change μ in function of ϱ as follows:

– Large values of ϱ indicate that the model is very accurate, and thus μ can be increased.
– Small values of ϱ indicate that the model is inaccurate. Decreasing μ provides two benefits in this case: (1) reducing the step length so as to improve the model accurateness and (2) moving the iteration closer to gradient descent.

II.4 MRS current quantitation methods

Due to the non-triviality of modelling MRS(I) data, as well, perhaps, as to the difficulty of assessing the result accuracy and reliability, numerous methods have been proposed to quantify MRS(I) data. This section attempts to classify them, to briefly describe some methods more relevant to this work, as well as to provide further reference to some reviews and comparative studies.

II.4.1 Classification of MRS quantitation methods

II.4.1.1 Fitting Domain

A first approach to quantitation method classification is possible according to what input is used for the quantitation algorithm: (i) time-domain (TD) methods use the raw signal, as represented the signal representation in the measurement domain), (ii) frequency-domain (FD) methods use a spectral estimate of the raw signal (mostly by DFT), while (iii) TD-FD approaches combine the two.

TD methods benefit from the fact that data are fitted in the same domain as it is measured. This, in turn gives better flexibility and allows usually simpler models to be used. The baseline can also be more easily separated in the TD due to its high T_2^* relaxation time. The main difficulties in TD analysis lie with the (visual) assessment of the fit. VARPRO, AMARES, AQSES and QUEST (*cf.* following subsections) are examples of TD methods. Useful overviews of TD fitting have been compiled by Vanhamme et al. [190] and more recently by Poullet et al. [139]

FD methods have historically been developed first due to the relative ease of interpreting MRS signals in the FD. Visualization of the results, as well as of the goodness-of-fit is usually performed in the FD, even for non-FD methods. Also, FD methods tend to be better suited for frequency-selective analysis, mainly by reducing the number of model parameters [136, §3.5]. However, several drawbacks are also present: artefacts introduced by the DFT, the very high importance of phasing if taking only the spectral absorption mode, or the difficulty of separating metabolites from the baseline. LCModel is an example of FD fitting, as well as Gabr et al. [63]'s method of fitting circles in the Fourier complex plane. For examples of

SVD-based FD techniques see [160], while for a more general overview of FD methods see the review by Mierisová and Ala-Korpela [110] and the FD section in [139].

TD-FD methods combine methodology from TD and FD fitting. Examples include methods proposed by Slotboom et al. [168] and by Young/Soher et al. [171, 200, 199].

II.4.1.2 Parametric, semi-parametric and non-parametric methods

Another classification, very common in MRS quantitation literature, concerns the presence of an underlying Physical model in the quantitation algorithm. Methods that include or approximate a physical model are called *parametric*[5], while models that are based on a pure mathematical decomposition, without direct link to a Physical model are called *non-parametric*. When multiple parametric and non-parametric approaches are used in the same algorithm, it is usually described as *semi-parametric*.

It is very important to mention here that no MRS quantitation is possible without *a priori* information, let it be solely information on the spectral peak locations. While some authors equate *a priori* information to parametric models, the problem is perhaps better described in shades of gray instead of blank and white. Generally, non-parametric methods use the *a priori* information after the data have been mathematically decomposed (separated), while parametric approaches include the information in the decomposition itself.

Another aspect worth mentioning here is linked to the method interactivity. Due to the mathematical description involved, non-parametric approaches tend to have a black-box approach, meaning that the data are decomposed with no user involvement. While this makes the process fully automatic, it may also have the disadvantage of making very small use of possible extra information available (*e.g.* relationship between peaks). Parametric methods tend to be more diverse in user interactivity, as it is fixed not by the algorithm itself but by a compromise between automation and user flexibility. For example, Provencher [146]'s approach for LCModel enables minimal interaction between the user and the software, while QUEST [156] allows the user to modify inner parameters for optimal use. Low interactivity contributes to reproducibility and a certain amount of methodological accuracy even for beginner users, while high interactivity profits the most to expert users.

Non-parametric methods, also called black-box methods, are based on a mathematical description of the signal, such as a decomposition by HSVD or FT. Due to the general possibility of complete or partial signal reconstruction from the mathematical decomposition, black-box methods are also extensively used as preprocessing[6] methods.

Parametric methods, on the other hand, are based on modelling of the underlying physical processes, and tend to give values directly related to Physical measures. Most current physical models used can be derived from Eq.II.7.

5. Please note that the meaning of "parametric" is specific in this context to MRS quantitation methods. In other signal processing fields the definition may considerably differ.

6. Preprocessing means transforming the dataset so that the quantitation algorithm gives better results or for better visualization. Examples include dephasing adjustment, spectral x-axis mirroring, lineshape correction, etc.

Semi-parametric methods usually combine a parametric description of the metabolite spectral components with non-parametric approaches for the unknown or sparsely described components, such as the baseline or lineshape.

II.4.2 Peak Integration

Peak integration methods are based on the model in Eq.II.7. Taking two metabolites m_1 and m_2, and assuming that the two signals can be separated from the signal s given by all metabolites, their ratio can be computed using the formula

$$\frac{c_1}{c_2} = \frac{\|s_{m1}(t=0)\|}{\|s_{m2}(t=0)\|} \frac{\|b_{m2}(t=0)\|}{\|b_{m1}(t=0)\|} \tag{II.26}$$

The ratio $\frac{\|b_{m2}(t=0)\|}{\|b_{m1}(t=0)\|}$, that corrects for the different spin multiplicities in the metabolites is *a priori* known via quantum mechanics.

The separation problem is traditionally solved using the Fourier Transform of the signal $s(t)$, usually referred to as the signal *spectrum*. Visual interpretation is possible in the spectral domain, since contributions centred around sufficiently different frequencies are represented at different abscissa, and thus can be easily separated. Additionally, the average of the spectral component can be usefully linked to the first point of the time series, as shown in Eq.II.9. This enables the computation of the concentration ratios as quotients of the areas defined by the real part of the spectral representation associated to each metabolite contribution [7], thus providing a visual representation of metabolite concentrations:

$$\frac{c_1}{c_2} = \left\| \frac{\mathcal{A}_1}{\mathcal{A}_2} \right\| \frac{\|b_{m2}(t=0)\|}{\|b_{m1}(t=0)\|} \tag{II.27}$$

where $\mathcal{A}_i$ represents the area under the curve of the metabolite m_i.

II.4.3 AMARES / VARPRO

Method summary

Type	NLLS (NL2SOL for AMARES and Levenberg-Marquardt for VARPRO)
	`find` $\mathbf{p}$ `as to minimize` $\|s - \hat{s}(\mathbf{p})\|^2$

Model

$$\hat{Y}_n = \sum_{k=1}^{K} c_k e^{\imath\varphi_k} e^{(-d_k(1-g_k+g_k t_n)t_n)} e^{\imath 2\pi f_k t_n} \tag{II.28}$$

$$t_n = t_0 + n\ t_s$$

$$Y_n = \hat{Y}_n + \epsilon_n$$

c_k	:	component amplitude	φ_k	:	component phase
d_k	:	component damping	f_k	:	component frequency
t_0	:	delay	t_s	:	sampling time
g_k	:	lineshape selector ($\mathbf{g}_k^{\mathrm{LOR}} \equiv 0, \mathbf{g}_k^{\mathrm{GAU}} \equiv 1$)			
ϵ	:	noise (AWGN)	$\mathbf{p}$	=	$(t_0, c_k, \varphi_k, \alpha_k, f_k)\ ,\ k = 1 \ldots K$
K	:	Number of spectral components			

7. One can also say that the metabolite average concentrations are proportional to the area under their spectral peak. It should be noted that the concentrations relate to the *areas* and *not to the amplitudes* of the spectral peaks.

Number of parameters	:	$4 \times K + 2$
Processing Domain	:	Time Domain
Base-line accommodation	:	not estimated, weighting function of the initial data points
Lineshape accommodation	:	Lorentzian and Gaussian
Implementation	:	jMRUI package [175] [1] [Fortran77] upon direct request

AMARES (Advanced Method for Accurate, Robust and Efficient Spectral fitting) [189] is a method based on NLLS modelling, with advanced possibility of *a priori* information integration. Moreover, a more efficient approach to the minimization problem is implemented, a development of variable projection (VARPRO) algorithms previously proposed by van der Veen et al. [187].

Variable projection is a method to simplify the solving of non-linear MRS model minimizations by eliminating, in a first approach, the linear terms. Consider the original nonlinear problem, and its cost function defined by

$$G(\mathbf{a}, \mathbf{d}, \mathbf{f}, \phi, t_0) = \sum_{n=0}^{N-1} \left| y_n - \sum_{k=1}^{K} a_k e^{\imath\phi_k} e^{(-d_k + \imath 2\pi f_k)t_n} \right|^2 = \|\mathbf{y} - \Psi\mathbf{L}\|^2 \tag{II.29}$$

with

$$\Psi = \begin{bmatrix} e^{(-d_1+\imath 2\pi f_1)t_0} & \dots & e^{(-d_K+\imath 2\pi f_K)t_0} \\ \vdots & \ddots & \vdots \\ e^{(-d_1+\imath 2\pi f_1)t_{N-1}} & \dots & e^{(-d_K+\imath 2\pi f_K)t_{N-1}} \end{bmatrix} \tag{II.30}$$

Assume that the non linear parameters that generate $\mathbf{\Psi}$ are known. Then the linear parameters $\mathbf{L}$ can be computed via linear least squares as $\hat{\mathbf{L}} = \mathbf{\Psi}^\dagger\mathbf{y}$, where $\mathbf{\Psi}^\dagger = (\mathbf{\Psi}^\top\mathbf{\Psi})^{-1}\mathbf{\Psi}^\top$ denotes the pseudo-inverse of $\mathbf{\Psi}$. Substituting this estimate in the original cost function G of Eq.II.29 results in a second cost function V, called variable projection functional:

$$V(\mathbf{d}, \mathbf{f}) = \|\mathbf{y} - \mathbf{\Psi}\mathbf{\Psi}^\dagger\mathbf{y}\| \tag{II.31}$$

The variable projection functional V only depends on the signal and on the non-linear parameters of frequency and damping factors. After minimization of V by the method of choice (Levenberg-Marquardt in the original VARPRO), the linear parameters in $\mathbf{L}$ can be estimated by LLS.

Improvements brought in AMARES as compared to VARPRO include : (1) a better numerical implementation of the minimization problem using NL2SOL instead of Levenberg-Marquardt, (2) better *a priori* information management via a singlet approach, unlike the VARPRO multiplet approach, as well as (3) an improved possibility of imposing upper and lower bounds to the parameters. To this day, AMARES is extensively for MRS quantitation, especially when a basis-set approach is less practical, as in the case of ^{31}P MRS.

1. Available at `http://www.mrui.uab.es/mrui/`. (Accessed February 1, 2010)

II.4.4 LCModel

METHOD SUMMARY

Type Regularized NLLS (CONTIN)

`find` $(\mathbf{p}, \mathbf{B}, \mathbf{S})$ `as to minimize`

$$\frac{1}{\sigma^2(Y)} \sum_{k=1}^{N} \left(\Re \left[Y(\nu_k) - \hat{Y}(\nu_k) \right] \right)^2 + \|\alpha_S \mathbf{R_S} \mathbf{S}\|^2 + \|\alpha_B \mathbf{R_B} \mathbf{B}\|^2 + \\ + \sum_{l=1}^{M} \left(\frac{\left[\gamma_l - \gamma_l^0\right]^2}{\sigma^2(\gamma_l)} + \frac{\epsilon_l^2}{\sigma^2(\epsilon_l)} \right)$$

`with constraints:` $\gamma_l \geq 0, \epsilon_l \geq 0, \sum S = 1$

Model

$$\hat{Y}[\nu_k] = e^{-\imath(\phi_0 + \nu_k \phi_1)} \left[\sum_{j=1}^{N_B} \beta_j \mathbf{B}_j(\nu_k) + \sum_{l=1}^{N_M} c_l \sum_{n=-N_S}^{N_S} \mathbf{S}_n M_l(\nu_{k-n}; \gamma_l, \epsilon_l) \right] \tag{II.32}$$

$$Y[\nu_k] = \hat{Y}[\nu_k] + \epsilon[\nu_k]$$

ϕ_0	:	zero-order phase	ϕ_1	:	first-order phase
α_B	:	baseline regularization coefficient	α_S	:	lineshape regularization coeff.
$\mathbf{R_B}$	:	baseline regularization matrix	$\mathbf{R_S}$	:	lineshape regularization matrix
$\mathbf{B}$	:	spline coeffs. for baseline model	$\mathbf{S}$	:	spline coefficients for LS model
β_j	:	spline basis-set for baseline model	ν_k	:	frequency
c_l	:	metabolite concentration	M_l	:	metabolite model including frequency and damping factors
γ_l	:	frequency shift	ϵ_l	:	extra damping
$\mathcal{N}$	:	noise (AWGN)	$\mathbf{p}$	=	$(c_l, \epsilon_l, \gamma_l, \varphi_0, \varphi_1)\ ,\ l = 1 \ldots M$
M	:	Number of metabolite models			

Number of model parameters	:	$3 \times M + 2 + DF(BL_{\alpha_B}) + DF(LS_{\alpha_B})$
Processing domain	:	Frequency Domain (real part only)
Base-line accommodation	:	Parametric-Regularized / Cubic B-Splines
Lineshape accommodation	:	Regularized model (reference peak)
Implementation	:	LCMgui/LCModel package [8] [146]

LCModel (Linear Combination of Model) [145, 146] is the first MRS quantitation method to have proposed a semi-parametric NLLS approach based on the *a priori* information via a metabolite basis-set. The model is built on the real part of the FT spectrum, and is composed of two parts, one representing the spectral lines and a second representing the baseline. Minimization is done using the CONTIN software, developed previously by Provencher [142, 143].

The baseline is modelled by LCModel using a cubic B-spline approach. This method, seen as a generalization of the Bézier [9] curve, allows that given a set of N_k control points $\mathbf{F^c} = (f^c)_{k=1\ldots N_k}$, an interpolation is found that is continuously 2 times differentiable. When this is applied for smoothing a curve, the value of the control points are computed from the

8. Demo available at `http://s-provencher.com/pages/lcmodel.shtml` (Accessed February 1, 2010)

9. Bézier (or Bernstein-Bézier) curves are extensively used in computer graphics for representation of smooth curves. For more information, *cf.* `http://mathworld.wolfram.com/BezierCurve.html` and references therein.

data to be fitted using a least squares approach. In addition, it is possible to introduce a penalty for the smoothness of the curve. LCModel uses for this purpose a smoothness matrix defined as

$$R_{i,j} = \int B_i''(f) B_j''(f) df$$

. Estimation for the smoothness hyper-parameter λ is done internally in CONTIN.

LCModel is a fully automated package, with the intent of very high simplicity of use, at the expense, perhaps, of some tuning possibilities. Metabolite databases are stored internally, mainly from *in vitro* measures and/or GAMMA simulated spectra [144]. Error estimation is provided via CRLB, but up to this date the exact method used has not been published, thus it is not possible to say to what extent and how, for example, the baseline estimation errors are accounted for.

II.4.5 AQSES

Method summary

Type	Regularized NLLS (Levenberg-Marquardt) `find` $(\mathbf{p}, \mathbf{k})$ `as to minimize` $\|s - \hat{s}(\mathbf{p})\|^2 + \lambda^2 \|\mathbf{Dk}\|^2$
Model	$\hat{s}[n] = \sum_{m=1}^{M} (c_m b_m[n] \exp(\imath\varphi_m + \alpha_m t[n] + \imath 2\pi f_m) t[n] + (\mathcal{A}\mathbf{k})[n])$ (II.33) $s[n] = \hat{s}[n] + \mathcal{N}[n]$

c_m	:	metabolite amplitudes	φ_m	:	metabolite extra dephasing
α_m	:	metabolite extra damping	f_m	:	metabolite frequency shift
$\mathbf{k}$	:	spline amplitudes	$\mathcal{A}$	:	spline basis set
b_m	:	metabolite basis signal	M	:	Number of metabolites
$\mathcal{N}$	:	noise (AWGN)	$\mathbf{p}$	=	$(c_m, \varphi_m, \alpha_m, f_m)$, $m = 1 \dots M$

Number of model parameters	:	$4 \times M + DF(\mathcal{A}\mathbf{k}_\lambda)$
Processing domain	:	Time (Measurement) Domain
Base-line accommodation	:	Parametric-Regularized / Splines
Lineshape accommodation	:	Lorentzian (Basis-set can have any lineshape)
Implementation	:	[MATLAB] SPID [137] [java] AQSES GUI [121]

AQSES (Accurate Quantitation of Short Echo time domain Signals) [138], is a time-domain regularized-NLLS method that incorporates *a priori* information via a metabolite basis-set. The model function is built in the complex space $\mathbb{C} = \mathbb{R}^2$ and composed of two parts, one representing the actual signal, and a second one representing the base-line.

The signal is parametrized as a linear combination of a Lorentzian-modified basis-set signals, thus for each metabolite m included in the basis-set four parameters are used: amplitude c_m, dephasing φ_m, extra damping factor α_m and frequency shift f_m. The base line is modelled as the sum of splines in the frequency domain, then transformed in the time domain via the Inverse Fourier Transform (IFT). The base-line model can thus be written as

the matrix multiplication $\mathcal{A}\vec{k}$, where $\mathcal{A}$ is the matrix formed by the IFT-transformed splines and $\vec{k}$ is the vector containing the linear coefficients.

A maximum-phase impulse response filter MP-FIR [180] is also used to confine the minimization procedure to a given spectral zone of interest. The MP-FIR coefficients are computed automatically prior to the actual ACQSES procedure [136, p.36], but the filter is applied at each step of the minimization process, both on the fitted signal s and on the fitting signal $\hat{s}$.

For fitting the model to the data AQSES uses a regularized non linear least squares algorithm (NLLS), based on the Levenberg-Marquardt[116] optimization algorithm. A modified version of variable projection, proposed by Sima and Huffel [166], is used to split the minimization problem in a linear part and a non-linear part, while also imposing constraints on the upper and lower bounds of the nonlinear parameters. Initial values for the non linear parameters, required by the Levenberg-Marquardt algorithm, are initialized at zero.

II.4.6 QUEST

Method summary

Type NLLS (Levenberg-Marquardt)
`find` $\mathbf{p}$ `as to minimize` $\|s - \hat{s}(\mathbf{p}) - \mathcal{B}\|$

Model

$$\hat{s}[n] = \exp(j\varphi_0) \sum_{m=1}^{M} (c_m b_m[n] \exp(\imath\varphi_m + \alpha_m t[n] + \imath 2\pi f_m t[n])) \tag{II.34}$$
$$t[n] = t_0 + n t_s$$
$$s[n] = \hat{s}[n] + \mathcal{B}[n] + \epsilon[n]$$

c_m	:	metabolite amplitude	φ_m	:	metabolite phase
α_m	:	metabolite extra damping	f_m	:	metabolite frequency shift
t_0	:	delay	t_s	:	sampling time
φ_0	:	first order phase	$\mathcal{B}$	:	base-line
ϵ	:	noise (AWGN)	$\mathbf{p}$	=	$(\varphi_0, c_m, \varphi_m, \alpha_m, f_m)\ ,\ m = 1 \dots M$

Number of parameters	:	$4M + 2 + DF(\mathcal{B})$
Processing domain	:	Time (Measurement) Domain
Base-line accommodation	:	Semiparametric / HLSVD
Lineshape accommodation	:	Lorentzian (Basis-set can have any lineshape)
Implementation	:	jMRUI package [175] [10]

QUEST (QUantitation based on QUantum ESTimation), proposed by Ratiney et al. [156, 153] is a time domain NLLS method that incorporates *a priori* information via a metabolite basis-set. The model function is built in the complex space $\mathbb{C} = \mathbb{R}^2$. Base-line accommodation is achieved via a non-parametric procedure based on the presence of the base-line only in the first points of the acquired signal.

10. Available at `http://www.mrui.uab.es/mrui/`. (Accessed February 1, 2010)

The signal is parametrized as a linear combination of a Lorentzian-modified basis-set signals, thus for each metabolite m included in the basis-set four parameters are used: amplitude c_m, phase φ_m, extra damping factors α_m and frequency shift f_m. Two additional parameters allow for overall phasing: zero order phase φ_0 and the receiver dead-time t_0 [11]. In some cases t_0 is estimated before the actual QUEST procedure, and is transmitted as a fixed value to the algorithm, for better convergence.

Base-line accommodation is provided in QUEST via a *semi-parametric* method based on the distinctive time-domain distributions of the metabolite and macromolecule signals. The separation principle is somewhat similar to the approach proposed by Weiland et al. [192], although the two methods diverge considerably in the choice of later modelling and processing, as QUEST makes use of HSVD. The macromolecule signal $\mathbf{s_{MM}}$, due to the high T_2 of its components decays much faster than the metabolite signal $\mathbf{s_{met}}$. Considering that after a known time τ_{MM} the value of the macromolecule signal becomes much smaller than the noise, the overall signal $\mathbf{s} = \mathbf{s_{MM}} + \mathbf{s_{met}}$ can be split in the sections $\mathbf{s}^{0\to\tau_{MM}} = \mathbf{s}_{\text{met}}^{0\to\tau_{MM}} + \mathbf{s}_{MM}^{0\to\tau_{MM}}$ and $\mathbf{s}^{\tau_{MM}\to\infty} = \mathbf{s}_{\text{met}}^{\tau_{MM}\to\infty} + \mathbf{s}_{MM}^{\tau_{MM}\to\infty} \approx \mathbf{s}_{\text{met}}^{\tau_{MM}\to\infty}$.

The algorithm used for baseline accommodation is thus the following:

SUBSTRACT-QUEST

INPUT

$\mathbf{s}$	signal to be quantified.
τ_{MM}	Time after which the macromolecule signal is considered negligible (truncating time).
$\mathbf{b}$	Metabolite basis-set

STEP

01	Compute $\mathbf{s}_{\text{met}}^{\tau_{\text{MM}}\to\infty}$ by time-wise truncation of $\mathbf{s}$.
02	Quantify $\mathbf{s}_{\text{met}}^{\tau_{\text{MM}}\to\infty}$ using QUEST. Store result in $\mathbf{p}^{\text{trunc}}$.
03	Construct the metabolite model for the whole time domain: $\hat{\mathbf{s}}_{\text{met}} = \hat{\mathbf{s}}(\mathbf{p}^{\text{trunc}})$.
04	Estimate the macromolecule signal by subtraction $\hat{\mathbf{s}}_{\text{MM}} = \mathbf{s} - \hat{\mathbf{s}}(\mathbf{p}^{\text{trunc}})$.
05	Model $\hat{\mathbf{s}}_{\text{MM}}$ using HSVD. The result is $\tilde{\mathbf{s}}_{\text{MM}}$.
06	Estimate metabolite only signal $\tilde{\mathbf{s}}_{\text{met}} = \mathbf{s} - \tilde{\mathbf{s}}_{\text{MM}}$
07	Quantify $\tilde{\mathbf{s}}_{\text{met}}$ using QUEST. Store result in $\mathbf{p}_{\text{sub}}$.

OUTPUT

$\mathbf{p}_{\text{sub}}$	Value of final estimated parameters

Due to step 6, the algorithm is referred to as Subtract-QUEST, as the final quantitation is done on a signal from which the baseline components have been subtracted. Another version of the algorithm has been proposed, named InBase-QUEST, where steps 6-7 of Subtract

11. The delay represented by t_0 translates in the frequency domain into dephasing linearly dependent to frequency, according to the relationship $\phi_1(f) = 2\pi f t_0$

QUEST are replaced with one QUEST quantitation, the specificity of which is that the complex exponential components of $\tilde{\mathbf{s}}_{MM}$ have been added to the metabolite basis-set.

II.4.7 Other newly proposed methods

In the following paragraphs some other quantitation methods present in literature are briefly described, with a stress on the novel approaches.

- TARQUIN (Totally Automatic and Robust Quantitation In NMR), proposed in [157] and implemented in the open source TARQUIN package [12] is a fully automated TD method based on a simulated metabolite basis-set. In order to account for effects such as pH, a method is described to iteratively improve the basis-set by adapting it to the signal. Metabolite basis-set signals are subdivided into semi-dependent groups (multiplets) and parameters such as frequency shifts and extra damping factors are computed for each group through line search.
- Elster et al. [57] propose a TDFD semi-parametric method with baseline accommodation via reproducing kernel Hilbert space (RKHS) techniques. An interesting development is the alternative proposed to CRLB, based on a Bayesian approach.
- Belkić and Belkić [18] proposes a quantitation method based on the Fast Padé Transform (FPT). The spectral estimate provided by the FPT is used to compute all the spectral parameters. Froissart doublets (zero-pole cancellations) are used to separate useful peaks from noise. The authors claim [19] that this FPT based method outperforms established ones, such as AMARES or LCModel.
- Artificial Neural Networks (ANN) are used by Bhat et al. [22] to provide an alternative to traditional line-fitting procedures. Wavelet shrinkage Young et al. [200] is used to accommodate the baseline, while QUALITY is used for lineshape processing. Quantitation is performed in the FD, as a combination of Gaussian and Lorentzian peaks, via a radial basis function neural network (RBFNN) approach. The authors emphasize the excellent computational time of the method as compared to line fitting based methods.
- CFIT (Circular FITting) is a method proposed by Gabr et al. [63], based on the fitting of circles in the 2-D $\Re \times \Im$ representation of the signal spectra. Baseline distortions are accounted via an elastic free-form regularized contour called "snake". Baseline accommodation and metabolite-fitting via minimizing the error energy occur in consecutive iterative steps, until convergence criteria are satisfied. Fig.II.4 shows an example of the representation used, in the case of a simulated ^{31}P human brain spectrum.
- Principal Component Analysis (PCA) techniques applied to MRS spectroscopy have been reviewed by Stoyanova and Brown [178], and more recently by Poullet et al. [139]. PCA is a statistical method that performs an orthogonal transformation so that the variance is maximized on consecutive axes (the greatest part of the variance is explained by the first axis/variable, second greatest variance component by the second axis/variable, and so on). In order for PCA to work, a statistical population of spectra with independent concentrations is necessary.
- A Time-Domain Frequency-Domain (TD-FD) approach has been proposed by Slotboom et al. [168], where the model is kept in the TD but the minimization itself is done after FT. While if the whole spectral domain is investigated this is equivalent to a TD approach, when frequency-selective approaches are considered, the use of the

12. Available at `http://tarquin.sourceforge.net/`. Accessed March 1, 2010

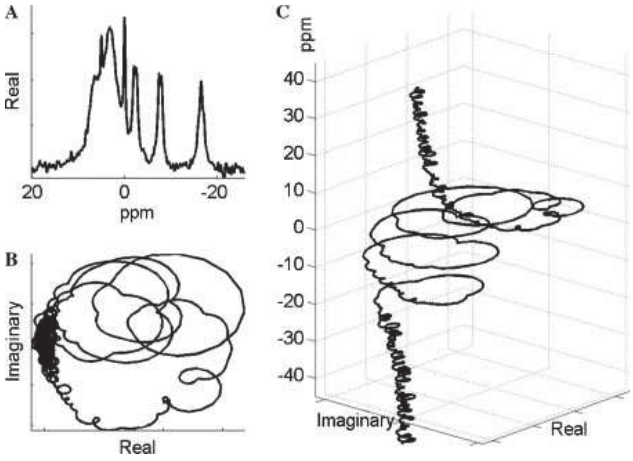

Figure II.4: *CFIT spectral representation. (A) The real part of a simulated ^{31}P human brain spectrum with noise $\sigma = 25$. Part (B) is the 2D projection of the 3D spectrum trajectory onto the real-imaginary plane. Part (C) is a 3D plot of the spectrum showing the helical trajectory of the peaks. Reproduced from Gabr et al. [63].*

signal FT reduces significantly the estimation time.

II.4.8 Some method reviews and comparisons

For a recent review of quantitation methods, as well as further references, see the work of Poullet et al. [139]. While less recent, Vanhamme et al. [190] and Mierisová and Ala-Korpela [110] provide valuable insights in TD and FD methods respectively. To this day no extensive comparison has been made between different methods, although examples of comparative measurement exist for certain method pairs: LCModel-QUEST (Li et al. [96] and Shen et al. [163]) LCModel-AMARES (Weis et al. [193]), AMARES-QUEST (Calvar [30]) , AQSES-QUEST (Poullet et al. [138]), etc.

II.5 Lineshape and decay function

A phenomenon of particular interest to spectroscopy in general, and MRS in particular, is the spectral dispersion resulting in the much faster transverse decay time T_2^*. Consider all the spins belonging to the same species k (experiencing the same nuclear shielding and the same J-coupling). Ideally, all these spins would contribute to the MRS signal at the same center frequency f_k, and, should the T_2 relaxation be left apart, the contributions can be modeled by a value proportional only to the concentration of the spin species and the frequency f_k. This is usually denoted as a Dirac δ, and is mathematically described as a distribution in the Hilbert space. The discrete counterpart is somewhat simpler, as the Dirac is defined as [13].

$$\delta_\tau[t_n] = \begin{cases} 1 & \text{if } t_n = \tau \\ 0 & \text{otherwise} \end{cases}$$

As the transverse relaxation is taken into consideration, the ensuing signal can be written as the composition of the undamped contribution and the T_2 decay. How the two phenomena

13. Referring simply to the Dirac function, or to δ without mention of the parameter τ implies $\tau = 0$

interact depends on the mathematical space: in the measurement domain (time domain) the composition amounts to a time-wise multiplication, while in the frequency domain it amounts to a convolution:

$$\text{time domain} : \quad s_k(t) = c_k \exp \imath\varphi_k \ \exp(\imath 2\pi f_k t) \ \exp(-\frac{t}{T_{2,k}}) \tag{II.35}$$

$$\text{frequency domain} : \quad S_k(f) = c_k \exp \imath\varphi_k \ \delta_{f_k}(f) * D_{L,T_{2,k}}(f) \tag{II.36}$$

where $D_{L,T_{2,k}} = \mathcal{F}\{exp(-\frac{t}{T_{2,k}})\}$ is the FT corresponding to the Lorentzian damping function generated by $T_{2,k}$ relaxation. The function $D(f)$ is termed *lineshape*, and its IFT $d(t)$ is commonly called *decay function*. In the simple case described here, of ideal T_2 decay, an analytical expression is available for both the lineshape and the decay function.

In the real case, the distribution of spectral contributions around f_k depends on many factors, so that an analytical expression is usually unavailable. However, a similar approach is possible, based on Eq.II.7.

$$\text{time domain} : \quad s(t) = V_{VOI} \sum_{m=1}^{M} \bar{c}_m \exp \imath\varphi_m \quad \underbrace{d_m(t)}_{\text{decay function}} \quad \underbrace{b_m(t)}_{\text{m. basis-signal}} \tag{II.37}$$

$$\text{frequency domain} : \quad S(f) = V_{VOI} \sum_{m=1}^{M} \bar{c}_m \exp \imath\varphi_m \ \underbrace{D_m(f)}_{\text{lineshape}} \ * \ \underbrace{B_m(f)}_{\text{m. basis-signal}} \tag{II.38}$$

where$D(f) = \mathcal{F}\{d(t)\}$ is the FT of the decay function d.

Equations II.37 and II.38, as well as figure II.5 show that the two notions very important to MRS spectroscopy: (1) the (known) frequency shifts integrated in the metabolite basis-set and (2) the (unknown) lineshapes associated with different metabolites. In order to measure the parameters of interest (c_m), both terms have to be taken into account. The next paragraphs describe different options for handling the lineshape term, while the whole quantitation process is reviewed in §II.4.

II.5.1 Current approaches to lineshape accommodation in MRS

Quantitation of a MRS signal using *a priori* generally requires that a model of the signal is built up using a basis-set. The most commonly used *a priori* information is the relations that exist between the peaks of metabolite spectra, due mainly to the influence of nearby protons within the molecular structure.

There are two strategies to gather the basis-set: (a) a separate *in vitro* acquisition for each metabolite, using as much as possible the same experimental conditions as the acquisition of interest, or (b) using quantum simulation software (such as NMR-SCOPE [69], GAMMA [170, 172]), or others). The first option has the advantage of providing information that includes partially the imperfections of the acquisition process, that would be otherwise very difficult to model. It is important to notice that while the acquisition sequence is the same, the actual distribution of the B_0 field is not the same, thus the lineshape of the acquired signal is not the same *in vitro* as in *vivo*. Using quantum simulation software, on the other hand, requires no additional acquisition time, which is a very important aspect for clinicians.

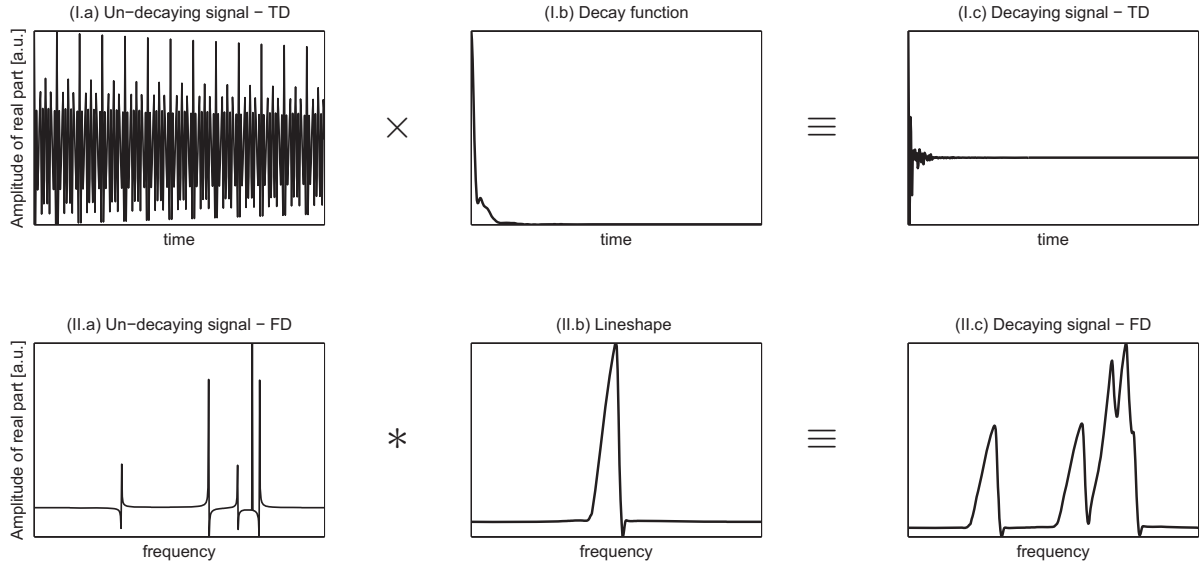

Figure II.5: *Decay function and lineshape. To a signal with a very small TD decay (a), a decay function (b) is applied. In the FD this corresponds to a convolution with a lineshape (II.b). The resulting signal (c) exhibits fast decay (in the TD) and an asymmetric lineshape (in the FD). Top Row (I) : time domain (TD). Bottom Row (II) : frequency domain (FD). Only the real part is plotted (absorption mode). Notice in (II.a) the artefact of DFT representation of very narrow spectra: peaks appear to have different phasing, as well as different amplitudes, although in reality phasing is perfect and all amplitudes are equal. Also notice in (II.c) the difficulty of distinguishing all five peaks.*

Throughout this work, a choice has been made to work with the quantum simulation NMR-SCOPE. Several factors have influenced this decision, among which the complete integration of NMR-SCOPE into the jMRUI software package [175], as well as the need to implement specific lineshapes, which could not have been achieved with *in vitro* acquisition.

Lineshape handling within the MRS quantitation process has two aspects: (1) the choice of a type of accommodation of the unknown acquired lineshape and (2) the decision of the adaptation target (*ie.* should the acquired signal be corrected to accommodate a known lineshape, or should the prior information be adapted so as to fit the acquired signal without modification of the latter). In the following paragraphs these two aspects are analyzed and some pertinent methods in current use are briefly described.

II.5.1.1 Classification by number of accommodation parameters

Any method that accommodates lineshape will introduce a number of degrees of freedom (DF) in the model, thus increasing variance of the estimator. The number of degrees of freedom introduces increases roughly with the number of parameters in the model. In order to classify the methods, it shall be considered that a lineshape model that allows an analytical expression that does not depend on the number of points of the signal is *parametric*. Methods that use approaches similar to filtering are to be considered non-parametric.

Lineshape accommodation methods could thus be classified as follows:

A The *parametric* approach defines analytical expressions of the lineshape, based on a physical underlying model. Most used in MRS are the following lineshapes:

1. **Lorentzian** $d_{\mathrm{L}}(t) = \exp(-\alpha t)$

   The Lorentzian lineshape arises from the intrinsic interactions between spins. Under perfect acquisition conditions, spectra are expected to have a Lorentzian lineshape.

2. **Gaussian** $d_{\mathrm{G}}(t) = \exp(-\beta t^2)$ or $d_{\mathrm{G}}(t) = \exp(-\beta^2 t^2)$

   The Gaussian lineshape is a consequence of the Central Limit Theorem, that states that if a large number statistical distributions are summed, the result will tend to be a Gaussian (Normal) distribution. A Gaussian lineshape can thus be considered as the result of the influence of many unknown/unparameterizable factors. One of the most important factors in this category is the spatial distribution of the actual B_0 magnetic field.

3. **Voigt** $d_{\mathrm{V}}(t) = \exp(-\alpha t - \beta t^2)$ or $d_{\mathrm{V}}(t) = \exp(-\alpha t - \beta^2 t^2)$

   Voigt lineshape is the product of Gaussian and Lorentzian lineshapes. The Lorentz part expresses the ideal T_2 decay mechanism, while the Gaussian part the influence of unknown / unparameterizable factors. One of the difficulties of the Voigt lineshape is that while its TD formula is quite simple, there is not simple analytical expression for the FD formula. However, extensive work has been done in other spectroscopy fields to compute good approximations for the Voigt FD profile. For a description of some of the advantages of using the Voigt lineshape in MRS, see [106] and references therein.

4. Howarth et al. [81] proposes a generalization of the Gauss-Lorentz lineshapes based on the Tsallis distributions, while also providing an interesting review of the current literature for NMR (and Electron Paramagnetic Resonance EPR) spectral lineshape analytical accommodation.

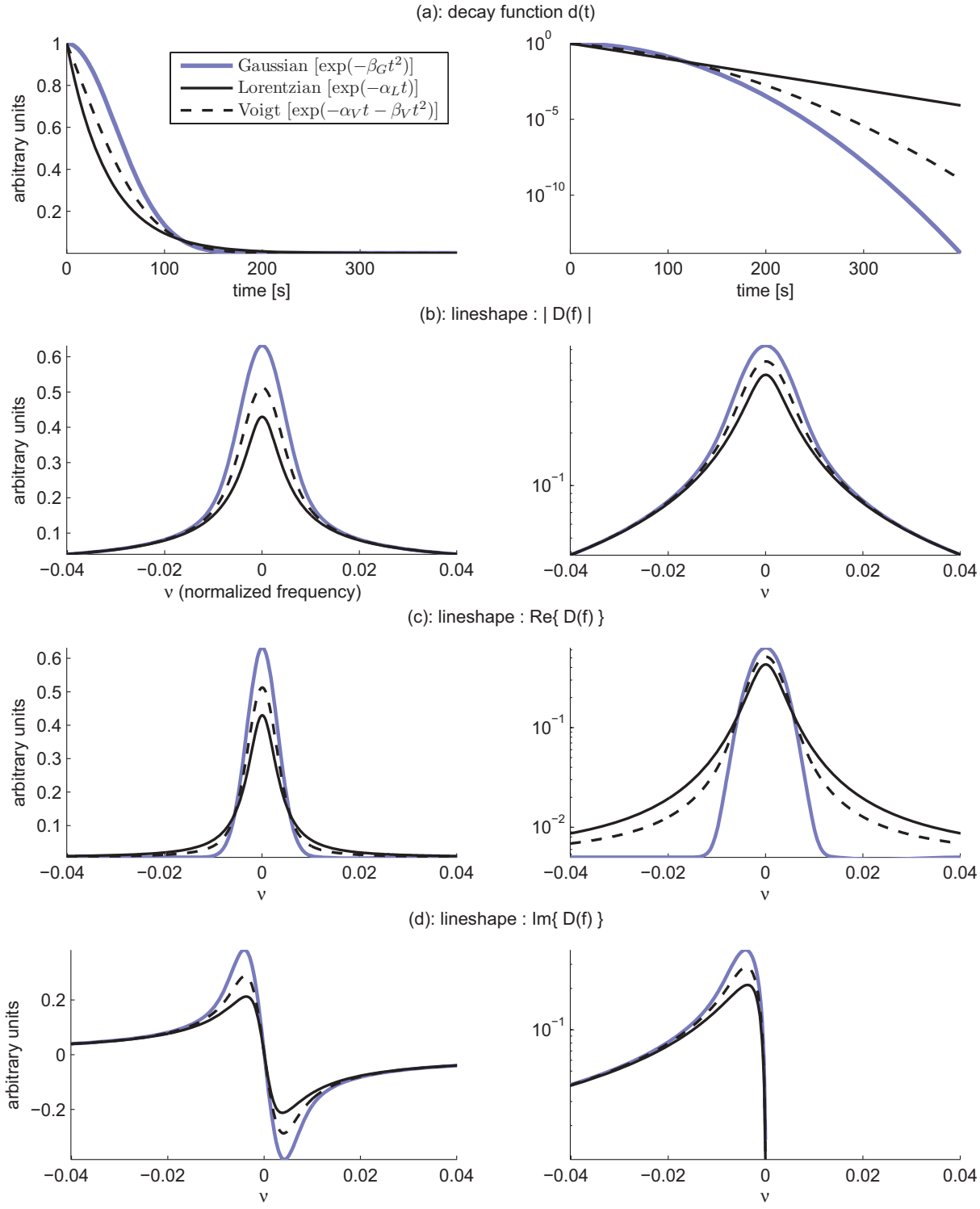

Figure II.6: *Commonly used lineshapes for MRS peak accommodation. Thick blue line: Gaussian profile* $d_G = \exp(-\beta_G t^2)$*, with* $\beta_G = 2 \cdot 10^{-4}\ s^{-2}$ *; continuous thin line : Lorentzian profile* $d_L = \exp(-\alpha_L t)$*, with* $\alpha_L = \sqrt{4 \ln 2\, \beta_G}$ *; dashed thin line: Voigt profile* $d_V = \exp(-\alpha_V t - \beta_V t^2)$*, with* $\alpha_V = \frac{\alpha_L}{2}$ *and* $\beta_V = \frac{\beta_G}{2}$*. All profiles have the area under the real part of the spectra equal to one. Lorentz and Gauss profile parameters have been chosen so that the real part of the spectra have the same width at half-height. Left and right columns have linear and, respectively, logarithmic ordinate scales.*

5. Jimenez-Dominguez et al. [85] propose an asymmetric lineshape based on the plasma dispersion function. The lineshape is derived from the Voigt lineshape, with an asymmetry factor introduced in such a way as to keep the Kramers-Kronig equations [14] valid.

6. Stancik and Brauns [174] propose a simple lineshape variation based on the Lorentz and Gauss models, with an underlying asymmetric distribution.

B The *non-parametric* approach is typically linked to isolation and then mathematical modeling of the lineshape. It is also possible to introduce the mathematical decomposition of the lineshape into the estimator as parameters of 'nuisance' [15]. For example, Barache et al. [7] use Continuous Wavelet Transform (CWT) modeling to correct the lineshape for eddy current effects, while Provencher [145] introduces a spline decomposition of the lineshape in the overall minimization function.

C The *pre-processing* approach is a special case of a non-parametric accommodation of the lineshape. Typically using a reference signal or a reference peak, lineshape parameters are partially extracted, and a processing step is performed on the spectrum, attempting the transformation of the lineshape into a known one, usually Lorentzian. Some of the methods widely used today include:
   – Eddy Current Compensation (ECC), proposed by Klose [88]. Eddy Currents are compensated using a reference peak, usually water non-suppressed signal. Only the phase of the signal points is corrected.
   – QUALITY, proposed by de Graaf et al. [49], is another method of lineshape preprocessing inspired by the earlier work of Morris [117]. The acquired signal is deconvoluted using point-wise division in the time domain, either using a reference peak or separately acquired data. Maudsley et al. [108] proposed further development in automating the process based on self-deconvolution.
   – QUECC, by Bartha et al. [11] is devised to be a combination of QUALITY - for points that have a sufficient SNR, and ECC - for the rest of the points. An algorithm is also devised to internally estimate the limit between the two. By correcting only the phase factor for points with small SNR, the risk of division-by-zero is limited.

II.5.1.2 Classification by accommodation target

There are basically four strategies that are currently proposed to treat lineshape accommodation. Each of them will now be briefly discussed:

I. No lineshape accommodation is a commonly used option. As it will be further discussed, this is a very viable option when the acquisition conditions are very good, and thus the actual lineshape of the acquired signal approaches an analytical model that can be used for quantum simulation.

II. Adaptation of the signal lineshape to the basis-set lineshape is commonly done as a preprocessing step before quantitation. It involves modifying the lineshape of the

14. the Kramers-Kronig equations (Kramers, *Atti Cong Intern Fisica*, **2**, 545–557, 1927 and Kronig, *J Opt Soc Am*, **12**, 547–557, 1926) link the real and imaginary part of complex functions that are analytical in the upper half plane (their imaginary part is always positive).

15. as opposed to parameters of interest, such as concentration.

acquired signal, by deconvolution, and eventually re-convolution with an analytical lineshape specific to the basis-set. Methods such as QUALITY [117] or QUECC [11] use a reference peak to achieve this.

III. Adaptation of the basis-set lineshape to the signal lineshape is the method of choice proposed in this work. Although obvious steps towards this are taken when simulation parameters are chosen as close to the experimental conditions as possible, thus working, for example, with signals that have the same width at half-width, we propose to take this concept even further and apply an estimated lineshape specific to the acquisition on the basis-set.

IV. Introduction of the lineshape as degrees of freedom in the quantitation proper is proposed, for example, by Provencher [145] in LCModel or by Poullet et al. [138] in AQSES.

It should be noted, however, that the classification is a little bit artificial, as most quantitation methodologies today exploit a combination of these methods. Apodisation, for example may be regarded as a preprocessing step, but it amounts to modifying the lineshape of the acquired data.

II.6 Assessing the quality of quantified spectra

Parameter estimation is not only about giving an estimate of the parameter value. Press et al. [140, §15.0] write, perhaps in an overly sarcastic manner, that:

> "The important message is that fitting of parameters is not the end-all of model parameter estimation. To be genuinely useful, a fitting procedure should provide (i) parameters, (ii) error estimates on the parameters or a way to sample from their distribution, and (iii) a statistical measure of goodness-of-fit. When the third item suggests that the model is an unlikely match to the data, then items (i) and (ii) are probably worthless. Unfortunately, many practitioners of parameter estimation, never proceed beyond item (i). They deem acceptable if a graph of data and model "looks good". This approach is known as *chi-by-the-eye*. Luckily, its practitioners get what they deserve."

This quote emphasizes the need of a way of assessing fitting procedure results, mainly by providing objective criteria. However, one should not go into the other extreme: providing only numerical description of data, without a visual representation. As shown by numerous researchers [see 5, 161], visual representation can sometimes prove invaluable for assessment of bad fits. Figure II.7 shows four datasets that seem to be equally well fitted by the same linear model, as shown by dataset statistics (mean, variance, correlation and regression line). On visual inspection, per contra, it is possible to separate noise influence (A), from fitting the wrong model (B) or from the influence of single outliers (C,D). Providing numerical estimates for estimation accuracy and reliability is complementary to visual representation.

This section tries thus to answer two distinct questions:

(Q1) : How appropriate is the model for the data ?

(Q2) : Assuming that the model is appropriate, how much can the estimated parameters be trusted?

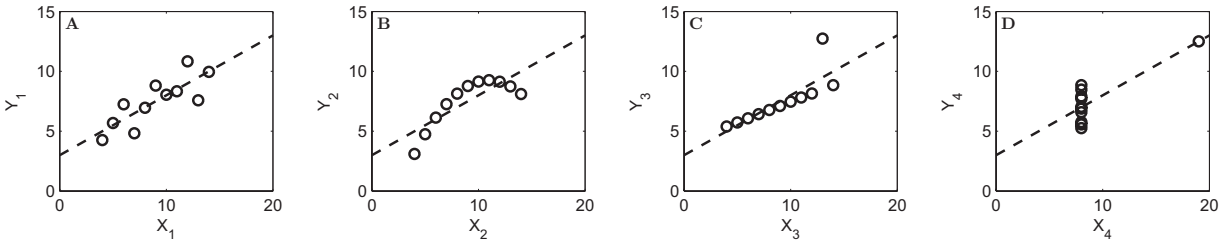

Figure II.7: *Anscombe's Quartet [5] showing some of the pitfalls of using simple numerical statistics for goodness-of-fit assessment. All four data sets have the same mean ($\bar{X}_i = 9.0, \bar{Y}_i = 11.0$), standard deviation ($\sigma_{Xi} = 3.317, \sigma_{Yi} = 2.032$), correlation between x and y ($corr(X_i, Y_i) = 0.816$) and LLS regression line $y_i = 0.5x_i + 3$ (dashed line).*

The first question can be answered numerically by providing objective criteria for rejecting measurements. The second question is usually answered by providing a confidence interval for parameter values.

II.6.1 About estimation accuracy and reliability

In order to provide some answers to the two questions previously asked, the introduction of some statistical concepts is necessary. Although by all means not the only approach, the point of view chosen here is the Bayesian theory, that replaces the terms of error in the result by the probability of the result. In this point of view the estimation question of measuring the true parameters $\mathbf{p}^*$ by analysing the measured signal $\mathbf{s}$ is converted to *What is the conditional probability* $\mathcal{P}(\mathbf{p}^*|\mathbf{s})$ *that the measured parameters* $\mathbf{p}$ *are equal to the true values parameters* $\mathbf{p}^*$ *when the signal* $\mathbf{s}$ *is known ?*

Bayes's theorem provides some clues by linking $\mathcal{P}(\mathbf{p}|\mathbf{s})$ to $\mathcal{P}(\mathbf{s}|\mathbf{p})$, that is the probability that the signal $\mathbf{s}$ is realized if the true parameter values are equal to $\mathbf{p}$.

$$\mathcal{P}(\mathbf{p}|\mathbf{s}) = \mathcal{P}(\mathbf{s}|\mathbf{p})\ \frac{\mathcal{P}(\mathbf{p})}{\mathcal{P}(\mathbf{s})} \tag{II.39}$$

The two new terms appearing in Eq.II.39 are linked to the absolute overall probability of the true values $\mathbf{p}^*$ and of the signal $\mathbf{s}$. Since the signal has been measured, it can be considered that $\mathcal{P}(\mathbf{s}) = 1$. The probability of the model, on the other hand, is linked to *a priori* information. If this information is unavailable, then often a *non-informative prior* is used, that is a constant that does not depend on $\mathbf{p}$.

The final steps towards estimation are the replacement of the signal $\mathbf{s}$ with the error $\epsilon = \mathbf{s} - \hat{\mathbf{s}}$ and the assumption that this error ϵ follows a probability law, usually the normal distribution. In this case the conditional probability of having the signal $\mathbf{s}$ when the model is correct, is given by the product of error probabilities for each point [140, §15.1]:

$$\mathcal{P}(\mathbf{s}|\mathbf{p}) \propto \prod_{i=0}^{N-1} \left\{ \exp\left[-\frac{1}{2} \left(\frac{s_i - \hat{s}_i}{\sigma} \right)^2 \right] \triangle s \right\} \tag{II.40}$$

where σ is the true standard deviation associated with the normal law used $\mathcal{N}(0, \sigma)$ and $\triangle s$ is a very small integration-type variable. The function in formula II.40 , sometimes denoted $\mathcal{L}(\mathbf{s}, \mathbf{p})$ is also called the likelihood function, as it defines how likely is to have $\mathbf{s}$ when $\mathbf{p}$ is known. Maximization of the likelihood function, or more commonly minimization of its

natural logarithm results in the least squares formula. Estimators built in this manner are referred to as Maximum Likelihood Estimators (MLE).

For some examples of explicit Bayesian theory applied to MRS quantitation , see Neil and Bretthorst [120], [28] and references therein. For a brief introduction into Bayesian techniques applied to biomedical research see Eddy [54]'s short discussion.

One key point to mention here is that while the MLE finds the most probable solution, the likelihood function describes the probability of the whole set of possible solutions. Taking a small interval $[\mathbf{p}_{\min}, \mathbf{p}_{\max}]$ it is thus possible to compute the probability that the true, unknown solution lies within the interval. If $\mathcal{P}(\mathbf{p}_{\min} \leq \mathbf{p} \leq \mathbf{p}_{\max}|\mathbf{s}) = \alpha \in [0,1]$, then $\mathrm{CI}_\alpha \equiv [\mathbf{p}_{\min}, \mathbf{p}_{\max}]$ is referred to as the α confidence interval (CI). A more general version of the CI is the α Confidence Region (CR_α), that is defined as a multi-dimensional area with $100 \times \alpha\%$ of probability that the true values are within.

Since the influence of many independent effects can be modelled as a normal distribution (*cf.* Central Limit Theorem in [98] or in any other work on mathematical statistics), in most cases unknown distributions are assumed to be normal. This in turn gives a particularly simple way of estimating CI for parameters, based solely on their standard deviation σ. Values such as $\mathrm{CI}_{0.68} = \pm\sigma$, $\mathrm{CI}_{0.95} = \pm 2\sigma$ or $\mathrm{CI}_{0.997} = \pm 3\sigma$ have been extensively used in literature, to a point that the underlying hypothesis of normal distribution are often disregarded. While using LS estimators is possible even when normality is not verified, it should not be forgotten that the CI computed *do* depend on the desired confidence α, and that CI should be computed taking into account all the specifics probability distribution (and not just the standard distribution).

There are also cases when it is obvious that the estimated parameter cannot have a normal distribution. Some of the cases in MRS are:

- Metabolite amplitudes are computed as the module of a complex function (see the context function at the end of §II.1). If the real and imaginary parts are assumed to be normally distributed, squared amplitudes follow a χ^2 law with two degrees of freedom.
- Dephasing is only defined on an interval of size 2π. If the un-wrapped dephasing distribution may be assumed normal, the result of wrapping should be taken into account.
- Ratios of metabolite amplitudes $\frac{c_1}{c_1}$ appear very often in MRS studies, as to this date few methods exist for absolute quantitation. As seen previously, squared amplitudes can be assumed to follow a non-central χ^2 distribution with 2 degrees of freedom. Follows that the squared relative amplitudes follow a doubly non-central F-distribution [194]. While for high SNR cases this distribution can be conveniently approximated, it can also become messy and give unexpected CI in certain cases, especially for poor choice of the reference metabolite m_2.

II.6.2 Providing a statistical distribution for the estimated parameters

The framework previously discussed for the estimator can be generalized to the whole MRS measurement paradigm. First let the measurement paradigm be defined

> Given an environment perfectly described by a set of (infinite) unknown variables ζ, where a signal $\mathbf{s}$ is produced, estimate the value of a subset $\mathbf{p}^* \in \zeta$, called

variables of interest. The variables $\mathbf{p}^*$ are said to be measured.

It can be seen that the measurement does not only include the estimation itself, but also questions the signal $\mathbf{s}$. Moreover, it puts the focus on the variable of interest, that are the purpose of a measurement.

In order to compute incertitudes and confidence intervals for measurements, as seen previously, the probability distribution $\mathcal{P}(\mathbf{p}|\mathbf{p}^*)$ has to be described. This is done by estimating its cumulative distribution function (CDF), or, if not enough information is available, its empirical distribution function (EDF) [47]. The difference between the two is that in the case of the EDF the same weight is put on each observation, making it a discrete function that depends on the number of observations; while the CDF is an (usually) unknown probability function that generates the data. The two converge as the number of samples increases to infinity [16].

Several possibilities are available to estimate the EDF/CDF:

- **Sufficient experimental realizations** provide an asymptotically true estimation for the measurement CDF. However, most often this solution is unavailable, mainly due to the increased cost, in time and other resources. Another possible obstacle for MRS repeated acquisition is that the variable of interest may vary in time, thus making sufficient experimental realizations impossible to obtain. Un-averaged MRS multiple acquisitions (before the scanner averaging) tend, however, to be included into this category, should the number of signals be sufficient.
- **Analytical methods** focus on the mathematical inner workings of acquisition and estimation to provide estimations for the CDF. As such, these methods make assumptions on the nature of the processes, and are susceptible to giving the wrong results should the assumptions not be verified. Examples in MRS include the Cramér-Rao Lower Variance Bounds (*cf.* §II.6.4) or the alternative Bayesian approach by Elster et al. [57].
- **Monte Carlo methods** (MC) are computer-intensive approaches based on the assumption that if a given model is known for the process, more measurements can be simulated and the EDF sufficiently described to estimate the CDF. This eliminates the need for analytical (mostly very complicated) approaches, at the expense of high computational resources, explaining the recent vast use in experimental science [140, §15.6.1]. The common MC approach to CDF (and thus parameter CI) estimation is shown in Fig.II.8c: the measured signal $\mathbf{s}_0$ is quantified, and the resulting parameter value $\mathbf{p}_0$ is used to simulate a population of signals $\mathbf{s}_i$. The parameter population $\mathbf{p}_i$ estimated from $\mathbf{s}_i$ is used to compute the estimator EDF.
- **Resampling methods** are an alternative to MC approaches, when the model is unknown or incomplete. Resampling methods require that a population of signals already be present, and its focus is on improving the CDF estimation by increasing the population size. Two approaches are generally employed: (1) subsampling, where the new population is chosen as sub-samples of the original population, and (2) bootstrap, where the new population is replicated by random sampling with replacement. More on resampling methods is discussed in §II.6.3.

16. For more information on empirical approaches see [58, §1.6] or other similar statistics works

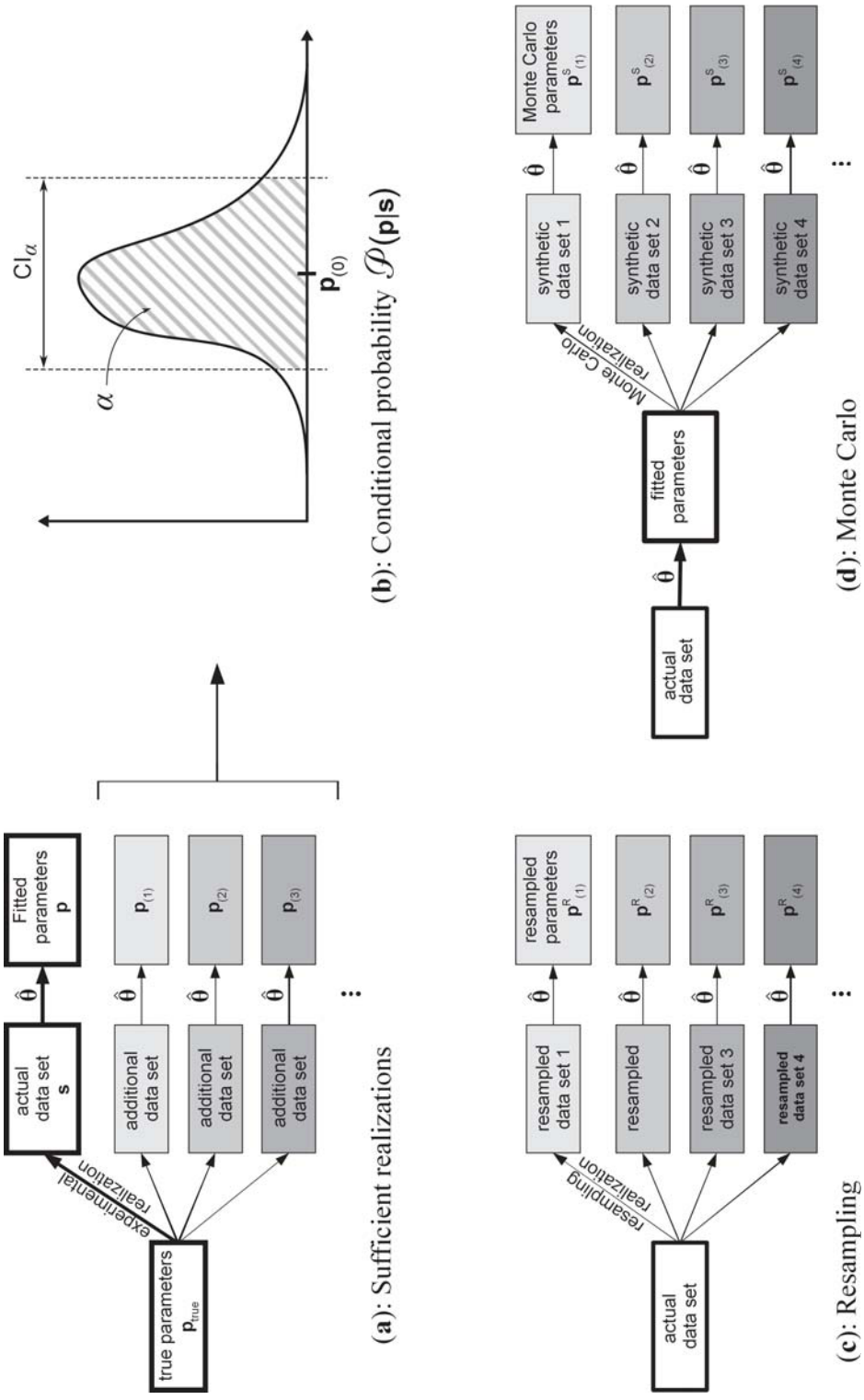

Figure II.8: *Determining Estimator Distribution. When available, sufficient number of realizations (a) lead to good description of the estimator distribution. This, in turn, leads to the incertitude distribution of the estimated value (b), described as the conditional probability* $\mathcal{P}(\mathbf{p}|\mathbf{s})$*. When not enough realizations are available, bootstrapping (c) or Monte Carlo (d) approaches can be used to estimate the incertitude distribution by replacing the extra realizations denoted by grey cases in (a). Bold contours show the actual measurement, whose incertitude is estimated. (a) and (d) adapted from Press et al. [140, §15.6]*

II.6.3 Resampling methods

Resampling techniques are very powerful approaches to replace the MC when not enough information about the underlying processes is known. The idea behind resampling is that the initial data available are resampled so that new sets of data are created, and these new sets are used to estimated the overall CDF in the same way as MC. Instead of using an analytical model, as in MC, resampling uses an estimated probability model from the original population. Although having had a difficult time getting accepted by statisticians, resampling has lately gained a very good reputation, mostly by the publication of theorems and analytical studies showing its validity [140, §15.6.2]. Figure II.9 illustrates the concept of resampling (in the case of bootstrapping).

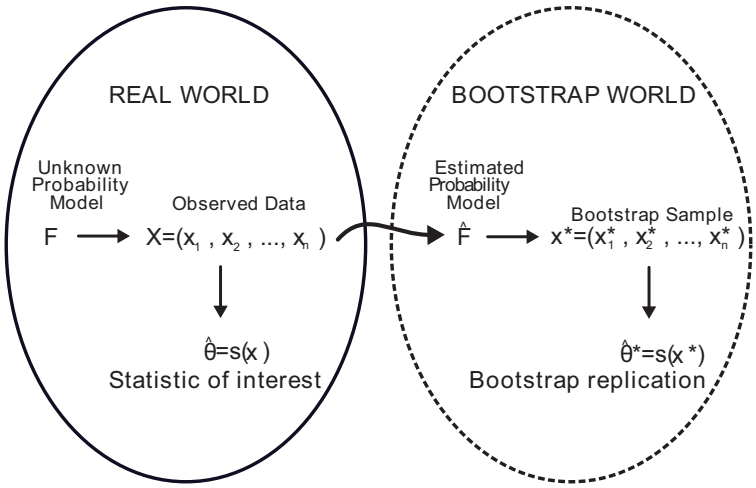

Figure II.9: *Schematic representation of the bootstrap procedure. Unknown probability model* $\mathbf{F}$ *is measured (observed) giving signal* $\mathbf{X}$*. Using the observed samples* $\mathbf{X}$*, the empirical probability model* $\hat{\mathbf{F}}$ *is built and then sampled by* $\mathbf{X}^*$*. Application of the estimator (statistic)* $\hat{\mathbf{s}}$ *on the bootstrap set allows its probability function to be computed, eventually providing confidence intervals for the statistic of interest* $\hat{\theta}$*. Adapted from Efron and Tibshirani [56]*

The two current approaches, consisting of (1) subsampling and (2) bootstrapping are now further discussed. An illustration of the difference between the two is given in Fig.II.10.

Subsampling is a version of resampling where new populations are built by sampling the original population *without* replacement. The direct consequence is that the resampled populations have smaller size, but no duplication of elements. Several flavours exist: (i) jackknifing creates populations of size $M < N$ from the original population of size N and then modifies the estimated statistics to account for size difference; (ii) the "all sub-samples" method creates all possible combinations of sub-samples and uses the particular statistical properties of the ensuing distribution; (iii) half-sampling methods are used for non-parametric delta method for variance approximation. For more information and bibliography on subsampling methods see the review by Davison and Hinkley [47, §2.8-9].

Bootstrapping is a method introduced by Efron [55] and further analysed by Efron and Tibshirani [56], based on the resampling of the original population *with* replacement. Because of the possibility of data replication, bootstrap applications are more limited than jackknifing, as the initial population has to be independent and identically distributed (*iid*).

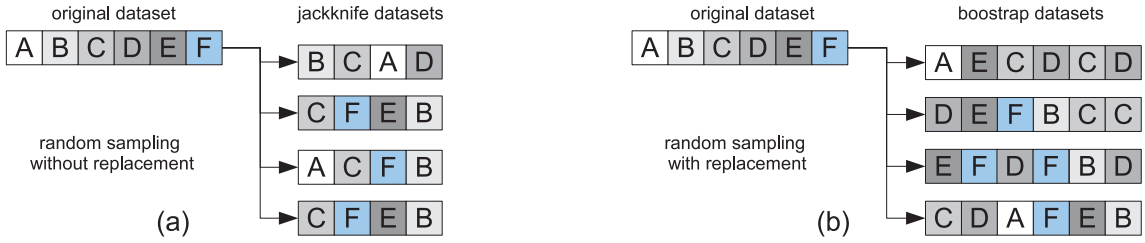

Figure II.10: *Illustration of the difference between jackknife (a) and bootstrap (b) approaches. Jackknifing produces populations of inferior size, without any element repetition, while bootstrapping produces populations of the same size as the original, but replication randomly occurs. Element* F *is highlighted in blue to show possible relative importance of elements: it can be found once or not at all in (a), while it can be found any number of times in (b).*

This eliminates data such as MRS signals (FIDs), where consecutive points are not independent. Furthermore, bootstrap applications for rank statistics have to be closely watched, as data replication might falsify the results.

In signal processing, in most cases the *iid* condition is violated. However, dependent data bootstrap approaches have also been developed that are based either on partial knowledge of the underlying model or the concept of weak-dependence. For more information on bootstrap applications in signal processing, as well as for a good introduction in bootstrapping see the course by Zoubir [206] or the subsequent book [205]. For an introduction in the statistical resampling methods consult the work of Good [65], while for a more in-depth approach see the comprehensive book by Davison and Hinkley [47].

Bootstrap methods have so far seen limited application in NMR, especially due to the lack of independence between samples. In Diffusion Tensor Imaging (DTI), where large data populations are available, bootstrap approaches have been applied to estimate DTI parameter incertitudes (see Zhu et al. [203] and the review by Chung et al. [37]) , as well as by Heim et al. [79] to investigate data quality. In MRI, M'hiri et al. [109] uses bootstrap to speed up unsupervised HMRF-EM brain image segmentation. Ratiney et al. [154] uses bootstrap and jackknife bagging to improve SNR in MRSI experiments designed for brain tissue segmentation. Su et al. [179] provides an example of using bootstrapping in computing performance of the proposed spectral separation MRSI method. Also see the bootstrap application for HR-NMR Spectroscopy feature selection by Brelstaff et al. [26].

In MRS signal processing, Bolan et al. [24] have studied the feasibility of a bootstrap approach for estimating the variance of spectral fitting parameters. In this approach, data should be recorded prior to machine averaging. Simulations are performed to compare bootstrap to CRLB, and it is subsequently shown that bootstrap is less prone to SNR-induced bias than CRLB. However, results concerning *in vivo* signals show CRLB to be more consistent.

II.6.4 Cramér-Rao Lower Bounds (CRLB)

Of special interest to the quality of quantitation are the minimal error levels attainable. The Cramér-Rao inequality (also called the information inequality) expresses a value for the

lower bound of the variance of estimators of deterministic parameters [45, 152]. This bound is usually referred to as the Cramér-Rao bound (CRB), Cramér-Rao lower bound (CRLB) or Cramér-Rao lower variance bound (CRLVB). It should be noted that the true estimator variance depends on the actual estimator used, while, as shown consequently, the CRLB are not method-dependent. An estimator whose variance is equal to the CRLB is called *efficient*.

The Cramér-Rao theorem states that if $\mathbf{p} = \mathbf{p}(\mathbf{s})$ is an unbiased estimator for $\mathbf{p}^*$, then under regularity conditions

$$\mathtt{VAR}(p_n) \geq \mathcal{F}_{nn}^{-1} \tag{II.41}$$

with $\mathcal{F}_{nn}^{-1}$ the n$^{\text{th}}$ diagonal element of the inverse of the Fisher Information matrix $\mathcal{F}$, defined as

$$(\mathcal{F})_{ij} = \mathbb{E}\left[\frac{\partial}{\partial p_j}[\ln(\mathcal{L}(\mathbf{s}, \mathbf{p}^*))]\ \frac{\partial}{\partial p_i}[\ln(\mathcal{L}(\mathbf{s}, \mathbf{p}^*))]\right] \tag{II.42}$$

where $\mathbb{E}[\cdot]$ denotes the Expectancy operator and $\mathcal{L}(\mathbf{s}, \mathbf{p}^*)$ is the likelihood function.

Reported in the NMR community as early as 1986 by Barkhuijsen et al. [9] and applied in frequency shift estimation in 1989 by Stoica and Nehorai [177], the CRLB theory in MRS has been consequently developed in MRS by de Beer and van Ormondt [48] and van den Bos [186]. Moreover, for certain model functions and for limited number of peaks (up to three), methodologies for numerical and analytical approximations for the CRB have been proposed [196, 82, 32].

In order for the computation to take place, it is supposed that the noise b_n is complex additive white Gaussian noise (AWGN). Then the likelihood function for b_n can be computed, leading to the Fisher Information matrix and finally to the corresponding CRLBs. For extensive details for the analytical computation in the case of Lorentzian lineshapes, please refer to [34] and references therein.

The CRLB theory applies only to fully parametric models. In order to account for the errors introduced by the presence of a semi-parametric approach, a method has been proposed by Ratiney et al. [156], inspired by the work of Spall and Garner [173]. It proposes an additive corrective term for the minimal variance, based on the covariance matrix of the nuisance parameters:

$$\mathtt{VAR}(p_n) \geq \mathcal{F}_{nn}^{-1} + \frac{1}{r}\mathcal{D}_\theta F_\theta^{-1}\mathcal{D}_\theta^\top \tag{II.43}$$

where $\mathcal{D}_\theta$ and $\mathcal{F}_\theta$ are representative of the non-parametric[17] part modelling (*ie* splines, HSVD, etc.). The coefficient r is linked by Spall to the quantity of information used to model the non-parametric part. Another CRB extension, more specific to the semi-parametric non-linear least squares problem posed by ACQSES, has been developed by Sima and Van Huffel [165].

While CRLB are widely used today to provide uncertainty evaluation on the estimated parameters, it is important to remember that they offer, in the best of cases, an estimation of the *minimal achievable variance using an unbiased estimator*. As a consequence, following are some aspects that the "unsuspecting" user should consider:

17. In this context 'non-parametric' should be read like 'without physical parameters'. A spline model of the baseline is considered non-parametric, because it's modelling is purely mathematical, without parameters linked to the Physical model (*ie* parameters 'of interest').

- True estimator variance depends on the actual estimator used, while the CRLB depend only on the model. This is particularly true when the estimator's stability is known to be weak under certain conditions, or when the external constraints enforced on the estimator are attained. It is therefore interesting to use CRLB for experimental design and improvement, as well as for an indication of the relative incertitude or the order of magnitude of the true underlying variance.
- It applies only to unbiased-estimators. In the case of biased estimators the CRLB theory has to be modified. Using the CRLB theory when the estimator is biased might give unreliable results, as some biased estimators give better variance (and even better mean squared error) than the values of the CRLB.
- CRLBs need *true* parameter values. In practice, the estimated parameters are used [33], considered to be close to the true values. One important consequence of this is that when the estimation appears to be unreliable then the estimation of the CRLB should also be considered with great caution.
- CRLB computation, as described by Cavassila et al. [32] makes several assumptions on the nature of the noise. Since the noise is assumed to be of AWGN nature, applying the CRLB when the residue is obviously not AWGN might also provide unreliable results. As a special case of this, apodized signals should be treated cautiously, as apodized noise is no longer stationary.

II.6.5 About fit and acquisition quality assessment

As previously represented in Fig.II.1, MRS quantitation results are representative of two distinct phenomena: (i) NMR data acquisition and (ii) quantification procedure. Different practitioners might have a different view and a different level of comprehension about the quality of the results: spectroscopists, usually with in-depth know-how on acquisition procedures might well evaluate acquisition quality, while sometimes misunderstanding the quantitation that follows, while clinical researchers might overlook both source of errors and use MRS as a black-box method.

Not detecting cases when the measurement chain produces bad results might prove very costly, as results might be considered valid and significantly alter the experimental conclusions. In the same way, improper quantitation of the acquisition results, if undetected, can falsify conclusions. It is thus important to define criteria so that measurements can be rejected, or at least flagged so that more care is taken in the ulterior processing. The following paragraphs treat present approaches to these criteria, both in terms of acquisition and quantitation.

II.6.5.1 Acquisition Quality Assessment

Acquisition quality (AQ) assessment is mainly related to experimental conditions, as logistics, protocol or hardware malfunctioning. Due to the important amount of know-how involved, AQ remains to this day based on a subjective approach. Experienced researchers are able to recognize phenomena as patient movement, hardware failures, bad shimming, etc. based on prior experience. Such an approach has several inconvenients: (1) know-how transfer is limited to people working with the experts, (2) increased availability of clinical NMR make experts sparse compared to demand and (3), in the case of local lack of expertise, new researchers in the field have to 'rediscover' techniques and protocols, in the best of cases.

A more numerical approach, on the other hand, would enable computers perform part of the job, while leaving for experts more interesting cases and allowing clinical practitioners better feed-back and reliability measures on their procedures.

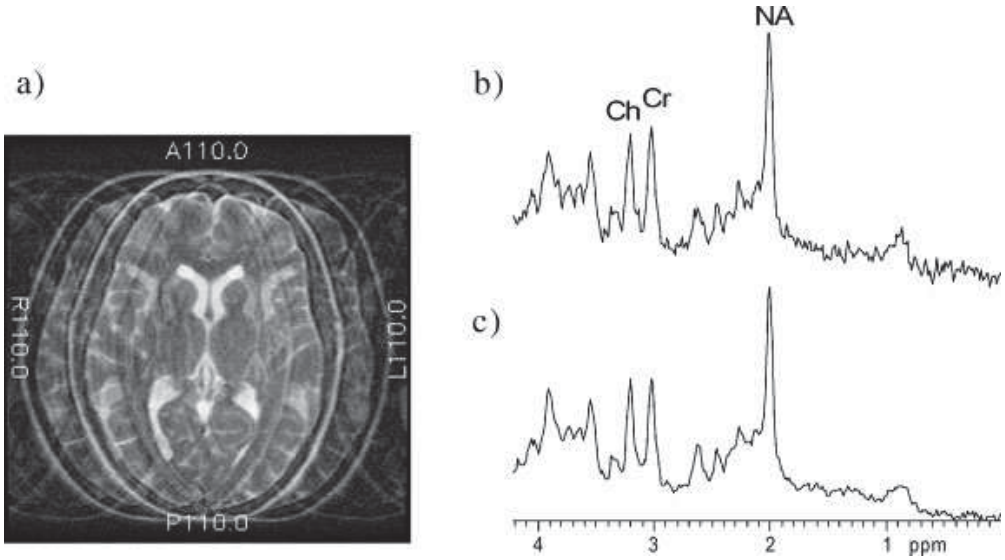

Figure II.11: *Conspicuity of artefacts in MRI and MRS. If a patient leaves the magnet half-way through a scan, even a layman will refrain from interpreting the resulting image (a). If this happens in a MRS scan, even the expert will not be able to recognize this fact from the resulting spectrum (b), since only signal-to-noise and absolute concentrations will be affected. Spectra (b) (half of the acquired FIDs contain noise only) and (c) (normal acquisition) were scaled to the largest peak, resulting in an apparent signal-to-noise difference, while quantitative analysis would yield a 50% deficit for all metabolites. Unless double-checking mechanisms are put in place and plausibility arguments are used, the resulting diagnosis will be completely wrong. (Scan parameters: 38-year-old healthy woman; MRI, fast spin echo with TE 102 ms, TR 3 s, 256 × 256, 4mm slice thickness; MRS, PRESS with TE 20 ms, TR 3 s, 6.7 cm^3 ROI in periventricular grey matter, 128 acquisitions). Adapted from Kreis [91].*

Several attempts have been made in literature to formalize AQ approaches. Kreis [91] makes an ample review of customary MRS and MRSI acquisitions problems, and provides a series of recommendations, mostly centred around checks on phantoms to ensure acquisition reliability. Six data rejection criteria (RC) are also proposed:

[RC1] Full width at half maximum (FWHM) of metabolites between 0.07-0.1 ppm;

[RC2] Cramér-Rao Lower Bounds (CRLB) greater than 50% of the concentration estimation for the given metabolite;

[RC3] If unexplained features appear in residuals, then: (i) reject, if it is an artefact or (2) expand model, if it is an unexpected metabolite;

[RC4] Peaks doubled or patient moved (post-acquisition MRI);

[RC5] Lineshape strongly asymmetric after eddy correction;

[RC6] Outer volume ghosts or other artefacts present (at least exclude metabolites overlaid with artefact).

It is interesting to mention here that only [RC1, 4, 6] truly quantify the AQ proper, while the others depend on the methods used in quantitation, relating as such more to goodness-of-fit than to AQ.

Slotboom et al. [169] propose a different approach to AQ testing, based on normality criteria. Signals are recorded prior to hardware averaging, providing thus not one realization, but M realizations $S_m,\ m = 1 \ldots M$. The null-hypothesis is that for a given n^{th} point in the time series, the series $(S_m[n])_{m=1\ldots M}$ has statistical moments of 3^{rd} degree (skewness) and 4^{th} degree (kurtosis) that are null. Test statistics, called κ-tests, are developed to test the null-hypothesis, and numerical criteria are derived for data rejection criteria.

Conclusions

Section II.1 showed how a model function can be constructed from the physical concepts presented in chapter I. The concepts of basis-set and lineshape are naturally introduced by the model. The link between the average estimated concentration and the actual concentration is not straightforward.

Section II.2 introduced some essential aspects of spectral analysis, in order to achieve better comprehension of the differences between the raw time-domain (measurement-domain) signals and their visualized counterparts. Aspects of the commonly used Fourier Transform are described, as well as the state-space based HSVD decomposition and the Fast Padé Transform. Section II.3 briefly described the methods typically used for NLLS minimization in current MRS quantitation algorithms. The use of possible *a priori* information is briefly discussed.

Current MRS quantitation methods were reviewed in section II.4. Some elements of classification enabling comparative study of various quantitation methods are also provided. LCModel, VARPRO/AMARES, AQSES and QUEST are described more in detail due to their direct interest in the current work. Lineshape issues in MRS, as well as current solutions are discussed in section II.5.

Finally, section II.6 briefly described some useful concepts in assessing how confident should one be in MRS-derived parameters. A statistical point of view is adopted, including elements from Bayes' theory, in order to derive confidence intervals for the measured values. Statistical resampling and the Cramér-Rao Lower Bounds are briefly described as means of estimating the result variance, and the somehow sparse current approaches to assessing the quality of MRS-derived parameters are presented.

Chapter III

Handling of the common metabolite decay

This chapter is composed of two parts. The first part defines more in detail the problems incurred by inappropriate modeling of the transversal decay function. Several solutions currently available are discussed and tested in a Monte Carlo experiment. Conclusions are also interpreted from a more theoretical point of view, using analytical expressions of the Cramér-Rao Lower Bounds.

In the second part of the chapter, a novel method based on the commonly used "common decay" assumption is presented. Reduction of the estimated decay function's degrees of freedom is proposed through the use of local filtering techniques, and the appropriate parameters and their influence on quantification errors is studied. Finally, the new approach is validated on clinically-acquired MRS data.

III.1 Why is the lineshape important in MRS quantitation?

As seen in the previous chapters, quantitation is the process of estimating metabolite concentrations from acquired MRS or MRSI signals. However, even in a reduced model (*cf.* §II.1), where only the heterogeneity of the static field B_0 is taken into account, the link between the actual distribution of a metabolite concentration $c_m(\mathbf{r})$ and the *mean* estimated concentration $\bar{c}_m$ is not immediate. This is due to the fact that contributions of different molecules may be dephased or have different resonance frequencies, leading to a not-trivial accumulation. The complex contribution has been defined as the interaction between mechanisms specific to the molecule species, encoded in the basis-set $\mathbf{b}_m$ and mechanisms specific to the analysed sample, encoded as the context function Ψ (see Eq.III.1). The latter depends on local conditions, such as B_0 heterogeneity and exact distribution of the metabolite concentration.

$$s(t) \propto V_{VOI} \sum_{m=1}^{M} \Psi_m(t)\, b_m(t) \tag{III.1}$$

Furthermore, the metabolite amplitude [1] c_m, the first order phase φ_m, as well as the decay function $d_m(t)$, have all been linked to the context function Ψ_m:

- $c_m = \|\Psi_m(t=0)\|$ The metabolite amplitude is defined as the module of the context function at $t = 0$. This corresponds, when considering the FT properties (*cf.* Eq.II.9), to the area defined under the Fourier Transform of the signal contributed by metabolite m.
- $\varphi = \arg[\Psi_m(t=0)]$. The zero order phase is defined as the phase of the context function at $t = 0$.
- $d(t) = \frac{\Psi(t)}{\Psi(0)}$. The decay function is defined as the normalized context function, so that the first point has unitary module and null phase.

Replacing the context function by the previously defined functions gives the common model in use for MRS modelling.

$$s(t) = \sum_{m=1}^{M} c_m \exp \imath\varphi_m d_m(t) b_m(t) \tag{III.2}$$

The purpose of MRS quantitation is generally the determination of the metabolite amplitudes, so that the proportionally linked concentrations might be consequently calculated. Looking at Eq.III.2, one can see classify the terms in different categories: **s** represents the measured signal, **b** represents the available *prior information*, **c** represents the parameters of interest while φ and **d** represent 'nuisance parameters'. The term used for the latter comes from the fact that while their estimation is not essential, bad estimation might cause important errors in the estimation of **c**.

In order to illustrate the problems incurred by bad modelling of the decay function, consider the situation depicted in Fig.III.1. A Gaussian decay function $d_G(t) = c_G \exp(-\beta t^2)$ has been synthesized, with $c_G = 1$ and $\beta = 2\,10^{-4}$. Sampling is uniform, with $t_s = 1s$ and N = 10000 points. The signal is then NLLS-fitted using a Lorentzian decay $d_L(t) = c_L \exp(-\alpha t)$. The fit model yields an amplitude parameter $\alpha_L = 1.254$, overestimating the original amplitude with over 25%. Inspection of the residue in the time domain (c) shows that while trying to obtain best LS fit in the whole time domain, the NLLS minimization achieves worst fit for the first point (t=0), that in turn represents the estimated amplitude ($d_L(0) = c_L$).

III.2 Comparing Lineshape Accommodation strategies

The problem of possible errors due to sub-optimal modelling of the MRS decay function has already been addressed by the NMR community (see §II.5). Current methods of lineshape handling rely on two major approaches: (1) pre-processing and/or (2) inclusion as free parameters in the quantitation model proper [2].

1. In the previous chapter, the term used has been mean metabolite concentration. Here, we use the term metabolite *amplitude* so that all (unknown) multiplicative terms (gain, V_{VOI}, etc) are included. The metabolite amplitude should thus be proportional to the mean concentration. In the given conditions, the proportionality relationship ($\propto$) from Eq.III.1 can be replaced by equality (=), since the proportionality constant is included in the definition of the amplitude. Please also note that the amplitude pertains to signal processing, while concentration to the underlying bio-chemical reality.

2. We call "quantitation proper" the mathematical procedure of extracting the spectral parameters, usually via NLLS minimization of given criteria. Inclusion of free parameters in the quantitation proper means extending the cost function so as to introduce terms describing the lineshape.

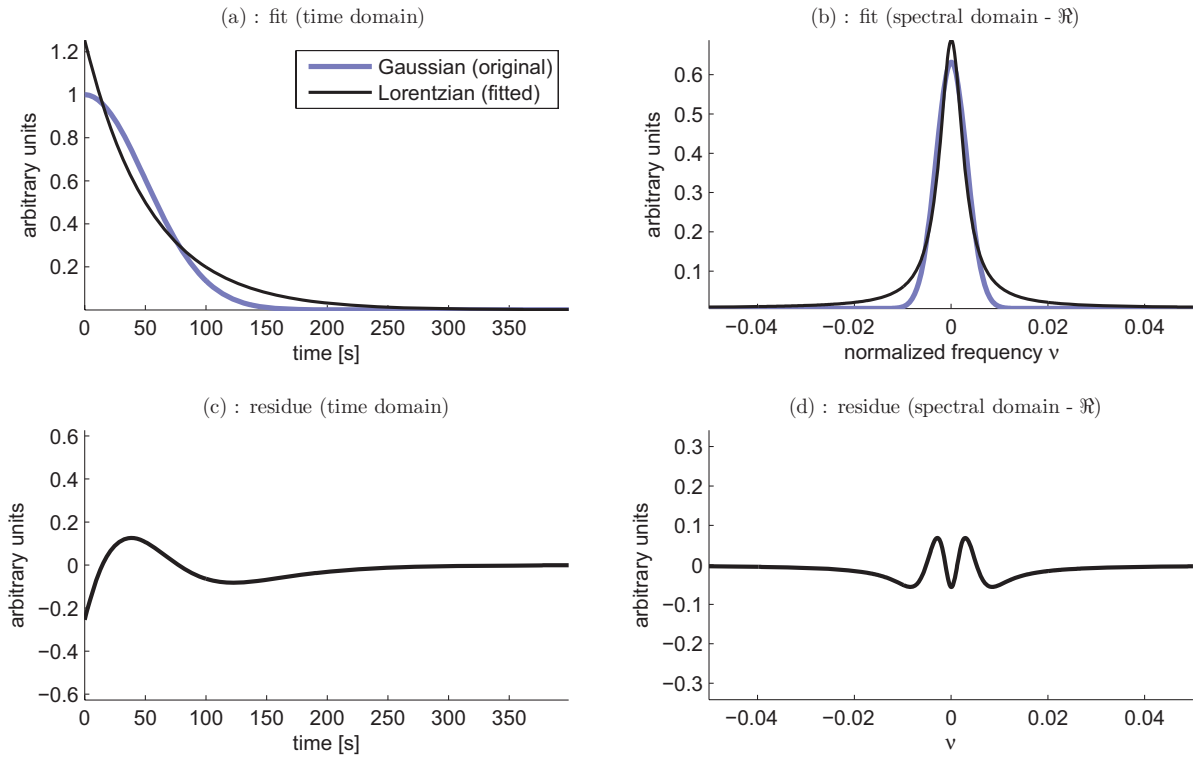

Figure III.1: *Amplitude over-estimation due to application of a Lorentz decay model ($c_L \exp -\alpha t$) on Gaussian decay generated data ($c_G \exp -\beta t^2$). The initial amplitude (c_G = 1) has been overestimated by the Lorentzian model with $c_L = 1.254$, representing a relative error of 25%. The shape of residue in the spectral domain (d) is typical for the use of an inappropriate lineshape model.*

Pre-processing is referred to as the modification of the acquired data so as to eliminate or correct certain features, in order for additional processing to be performed after. In the specific context of lineshape handling, it means modifying the properties of the lineshape associated with the acquired spectra, so that the ensuing quantification method behaves optimally. While preparing the data for quantitation might look appealing, one must not forget the risk of introducing additional artefacts, should the preprocessing not behave as expected.

Quantitation model extension implies adding extra terms describing the lineshape to the model functions to be minimized during the quantitation proper. Two flavours can be distinguished: parametric and non-parametric modelling. (see §II.5). Examples of quantitation model extension include the extra Lorentzian damping factors (parametric) in QUEST [156], or the spline terms (non-parametric) in LCModel [145].

A third approach, currently underexploited in literature [3], is **adapting the prior information** by modifying the lineshape inside the metabolite basis-set so as to accommodate the lineshape of the acquired data. This approach has the advantage of not introducing any artefact in the acquired data, and concentrating all prior information in just one place (the metabolite basis-set). Furthermore, reduction in the number of free parameters in the

3. to the best of the author's knowledge

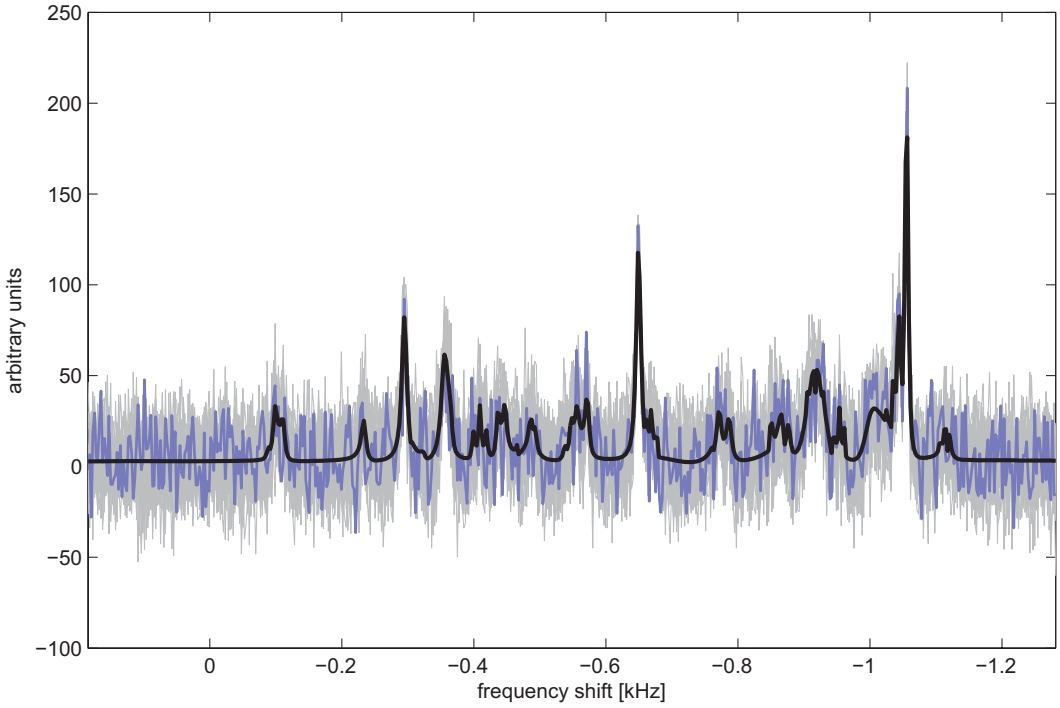

Figure III.2: *Spectra used for the Monte Carlo study comparing different lineshape accommodation schemes. Thick black line : simulated signal without noise. Blue line: example of one signal with a noise realization. Gray lines plot another 15 superposed signals. See text for more details on simulation and noise level.*

quantitation model function might improve convergence performances. In order to test the feasibility of the proposed approach, a comparative Monte Carlo study has been performed. The following subsections describe the methodology and the results.

III.2.1 Methods

In order to remain reasonably close to current state-of-the-art in MRSI acquisition, a Monte Carlo approach has been developed based on *in vivo* 9.4T MRSI acquisitions encoded by V.Mlynarik at EPFL [4], from the brain of a healthy rat., at ultra-short TE = 2.2ms. The *in vivo* signals have been subsequently quantified using Subtract-QUEST inside the jMRUI 3.0 software package, using a metabolite basis-set simulated according to parameters in [67].

Values have then been rounded slightly (see 'true values' in Table III.2, p.82), and metabolites with extremely low SNR have been eliminated from the simulation. Eleven metabolites have been included in the simulation: Aspartate (Asp), Choline (Cho), Creatine (Cr), γ-amino-butyric acid (GABA), Glucose (Glc), Glutamate (Glu), Glutamine (Gl), Myo-Inositol (mI), N-acetylaspartate (NAA and NAAG), Taurine (Tau). Two additional Lipids (Lip) peaks, at 0.9 and 1.3ppm have also been included in the Monte Carlo model (*cf.* Fig.III.2).

The Monte Carlo model has been synthesized using the previously simulated basis-set together with the quantification parameters. The lineshape of the simulated signal had a Voigt damping function $d(t) = \exp(-\alpha t - \beta t^2)$ with coefficients α ranging from 5 Hz to 20

4. Ecole Polytechnique Fédérale de Lausanne, CH

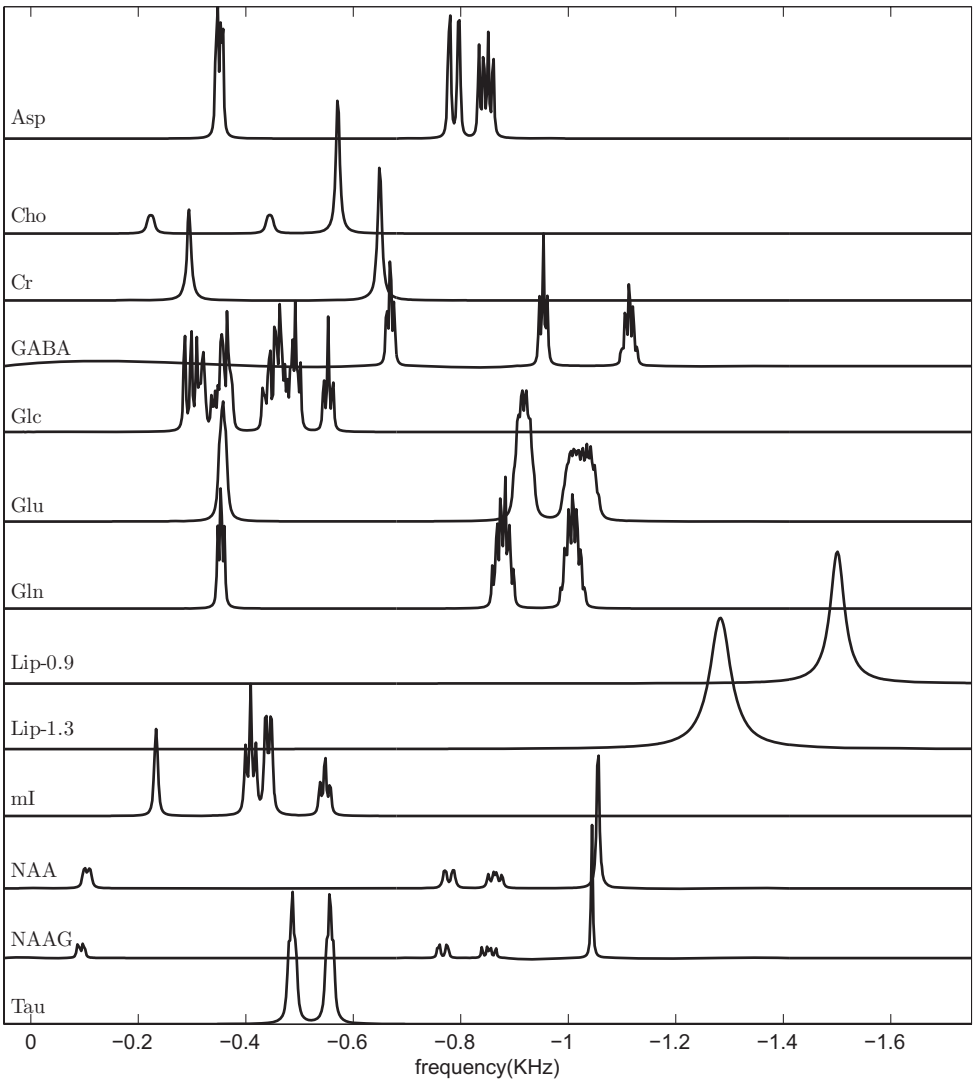

Figure III.3: *Metabolite basis-set used for simulation and quantitation when comparing three lineshape accommodation schemes. Amplitudes have been scaled to allow better visualization.*

Hz and $\beta = 4s^{-2}$.

Finally, in order to provide sufficient reliability for the statistical analysis, 200 signals have been created by adding to the clean MC model 200 different complex additive white Gaussian noise (AWGN) realizations. The complex noise standard deviation σ is such that $c_{\mathrm{Cr}} : \sigma = 8.6 : 16$, where c_{Cr} is the concentration of Creatine.

On the 200-signal Monte Carlo dataset, three approaches based on QUEST have been applied, using three distinctive approaches. First, the data have been quantified using the original basis-set that has a Lorentzian decay function. Secondly, the data-set has been processed with a deconvolution method, so as to adapt its lineshape to a Lorentzian one. Thirdly, the basis-set has been modified so as to have an adapted Voigt lineshape.

The method chosen to assess the performances of the pre-processing by deconvolution is an adaptation by Rabeson [149, p.61–63] of QUECC[11]. The correction algorithm consists of the following steps:

QUECC-TYPE DECONVOLUTION

INPUT	
$\mathbf{s}$	signal to be processed
$\mathbf{s}_{\mathrm{ref}}$	(noisy) reference signal (reference peak).
$\mathbf{s}_{\mathrm{ideal}}$	ideal signal (reference peak).

STEP	
01	The standard deviation of the noise in the reference signal σ_{ref} is estimated from $\mathbf{s}_{\mathrm{ref}}$
02	The reference signal $\mathbf{s}_{\mathrm{ref}}$ is modelled using HSLVD (typical 3 components). Result stored in $\tilde{\mathbf{s}}_{\mathrm{ref}}$
03	The denoised estimated signal $\tilde{\mathbf{s}}_{\mathrm{ref}}$ is centred in the spectral domain. Result stored in $\tilde{\mathbf{s}}_{\mathrm{ref}}$.
04	Initial values for the damping factor of the ideal[5] lineshape are estimated by single-component HLSD decomposition of $\mathbf{s}_{\mathrm{ideal}}$. Damping factor is stored in α_{ideal}, while the corresponding decay is stored in $\mathbf{s}_{\mathrm{Lor}}$
05	N_{QUALITY}, representative of the index of the last points that can be considered above noise level, is computed. $N_{\mathrm{QUALITY}} = \max_n\{\lvert s_{\mathrm{Lor}}(n) - \tilde{s}_{\mathrm{ref}}(n)\rvert < \sigma_{\mathrm{ref}}\}$
06	Depending on the value N_{QUALITY} one of two methods is applied for each point n_i (see sub-steps). Result is stored in $\mathbf{s}_{\mathrm{dec}}$
6.a	For the points $n_i < N_{\mathrm{QUALITY}}$, QUALITY [49] deconvolution is applied (point-wise division) between $\mathbf{s}$ and $\mathbf{s}_{\mathrm{ref}}$.
6.b	For the points $n_i \geq N_{\mathrm{QUALITY}}$, only phase correction (like in ECC [88]) is applied.

5. In this context the ideal lineshape is the lineshape of the basis-set used for quantitation.

07 Lorentzian apodisation of $\mathbf{s}_{\text{dec}}$ by α_{ideal} enables the damping factor of the corrected signal to match the ideal signal.

OUTPUT

$\mathbf{s}_{\text{dec}}$ Deconvoluted signal

III.2.2 Results

The results (Fig.III.4, Table III.2) show that there is an important bias in the estimation of the concentrations when Lorentzian lineshapes are used to quantify data that have a Voigt decay. Generally this is in the form of an over-evaluation, as in the case of Glu (+15%[6]) or Cr(+40%). For low concentration metabolites (Asp, Glc, Gln), the results are unreliable, as the mean value is comparable to one standard deviation.

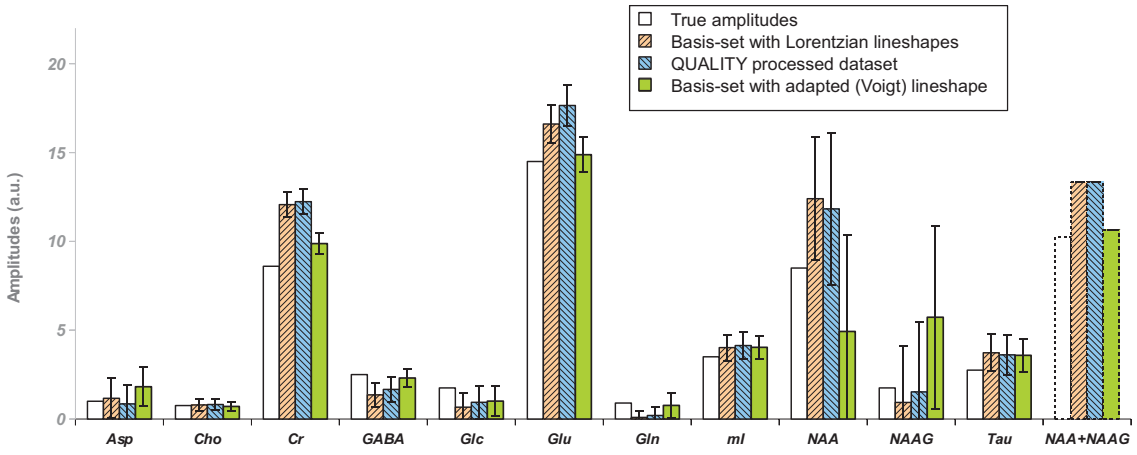

Figure III.4: *Comparison of 3 lineshape accommodation strategies.* ***White*** *: Monte Carlo model (True amplitudes).* ***Red, hatched +45°*** *: use of a Lorentzian lineshaped basis-set.* ***Blue, hatched -45°*** *: Quantitation after deconvolution using a reference peak.* ***Green****: Quantitation using a basis-set with adapted lineshape. Error bars represent one standard deviation.*

Pre-processing by QUECC deconvolution does not reduce significantly the bias in the estimation of the metabolite amplitudes. In some cases it even slightly increases the bias (*e.g.* relative bias: Glu from 15% to 22%, Cr from 40% to 42%). Amplitudes remain generally over-estimated.

However, the adaptation of the basis-set with a Voigt lineshape reduces considerably the bias (*e.g.* Glu from 15% to 3% and Cr from 40% to 15%). The standard deviation of the amplitude estimations is seen in Fig.III.4 (error bars) to be of similar values between the three estimators used.

One possible drawback of the proposed approach can be observed for NAA and NAAG, known for their high correlation due to close spectral proximity. Estimations for NAA and

6. Relative bias has been computed as $(c_{\text{estimated}} - c_{\text{true}})/c_{\text{true}}$

Metabolite	True value	Lorentz. BS		Lor. BS Dec.		Adapted BS	
		mean	*bias*	*mean*	*bias*	*mean*	*bias*
Asp	1.00	1.16	0.16	0.84	-0.16	1.81	0.81
Cho	0.75	0.79	0.04	0.81	0.06	0.70	-0.05
Cr	8.60	12.07	3.47	12.23	3.63	9.88	1.28
GABA	2.50	1.35	-1.15	1.67	-0.83	2.31	-0.19
Glc	1.75	0.67	-1.08	0.93	-0.82	1.00	-0.75
Glu	14.50	16.61	2.11	17.65	3.15	14.88	0.38
Gln	0.90	0.09	-0.81	0.20	-0.70	0.76	-0.14
mI	3.50	4.01	0.51	4.13	0.63	4.03	0.53
NAA	8.50	12.40	3.90	11.83	3.33	4.93	-3.57
NAAG	1.75	0.93	-0.82	1.52	-0.23	5.73	3.98
Tau	2.75	3.72	0.97	3.61	0.86	3.58	0.83
NAA+NAAG	10.25	13.33	3.08	13.35	3.10	10.65	0.40

Table III.2: *Mean metabolite amplitudes for the comparison of different methods for lineshape handling.* ***True values*** *– amplitudes used for the Monte Carlo model.* ***Lorentz. BS*** *– estimates when no lineshape accommodation was used, with Lorentzian lineshaped basis-set.* ***Lor. BS Dec.*** *– signal is processed using a QUECC implementation prior to quantitation.* ***Adapted BS.*** *– Quantitation uses Basis-set with adapted lineshape.*

NAAG levels show significant errors when compared to the established methods. However, when comparing the results for the sum NAA+NAAG, errors are drastically reduced, in agreement with results obtained for the rest of the metabolites. This can be explained by the decreased spectral sensibility of the Voigt lineshape compared to the Lorentzian lineshape. While Lorentzian-based methods can distinguish between proximal peaks NAA and NAAG, the Voigt-based method is unable to, leading to quasi-equal distribution between the two metabolites. Adapting the basis-set lineshape to the acquired lineshape has traded spectral resolution for amplitude precision.

As a conclusion, it can be inferred from the previously shown results that adapting the lineshape of the metabolite basis-set to the signal to be quantified seems the best approach. The implemented deconvolution approach, prior to quantitation, does not seem to produce better results than the application of QUEST without any preprocessing. We have found this fact to be a little surprising, as it was expected that at least some of the bias be eliminated by the QUECC-like technique. However, there is an important point to temper enthusiasm over the performances of the basis-set lineshape adaptation approach: in this study the lineshape was *known*, thus errors in estimating the lineshape have not been taken into account.

In the following sections, adapting the lineshape of the metabolite basis-set to the acquired signal is taken a step further, as a method is proposed to estimate the common metabolite lineshape.

III.2.3 Comparison of amplitude estimation incertitudes using the Cramér-Rao Lower Bounds

In the context of the comparison between different lineshape accommodation strategies, a secondary, more theoretical study has been performed to analyse whether, in equivalent conditions, it would be better to analyse Gaussian or Lorentzian peaks. In order to assess estimation convergence, we have chosen to assume the best possible case, when an ideal non-biased and efficient estimator is available for both lineshape types. In such a case it is possible to predict the quantitation errors with the help of the Cramér-Rao Lower Bounds (CRLB) Theory (see §II.6.4).

Analytical values for the CRLBs have been computed using the approach described in [32]. The majors steps of the computation are as follows:

1. Build the Fisher information matrix $\mathcal{F}$ associated with the model.
2. Simplify the terms in the Fisher matrix by assuming that
   - the model decays to zero values for maximum values of the time
   - the sum can be approximated, as the sampling time is small, by a corresponding primitive.
3. Invert the simplified Fisher matrix $\mathcal{F}$
4. Compute CRLBs as square root of the diagonal values of $\mathcal{F}^{-1}$

In order to automate the computations, the MAPLE software package [104] has been used. A script has been developed that takes as input the model function and then attempts to compute the associated CRLBs. Moreover, simplification of the Fisher information matrix $\mathcal{F}$ is done via a slightly different approach than reported in [32]. Instead of approximating the discrete sum by the corresponding integral, the Whittaker functions (see[195]) are used. Replacement of the simplified terms is done automatically in the Fisher information matrix, that is afterwards inverted. As a final step, a consistency check is performed by computing the measurement units of the CRLBs, and comparing them with the measurement units of the corresponding parameters.

Table III.3 summarizes the results given by the automated script for singlet models of Lorentzian and Gaussian lineshapes. It can be seen that only the amplitude and the damping factor influence the CRLBs. This is due to the fact that the models consist of singlets; the influence of frequency shifts and phases only becomes apparent when multiple peaks are considered.

The parameter of interest is the amplitude of the metabolite, that is representative of the metabolite concentration. Assuming we have unbiased efficient estimators, the errors due to noise will cause the results to have a statistical distribution with the standard deviation given by the CRLBs. The ratio between the predicted incertitude on the amplitudes in the case of Gauss and Lorentz lineshapes is:

$$\frac{\mathrm{CRLB}^{\mathrm{amplitude}}_{\mathrm{Gauss}}}{\mathrm{CRLB}^{\mathrm{amplitude}}_{\mathrm{Lorentz}}} = \frac{\sqrt[4]{\frac{18}{\pi}}\,\sigma\beta^{\frac{1}{4}}\sqrt{t_{\mathrm{s}}}}{2\,\sigma\,\alpha^{\frac{1}{2}}\sqrt{t_{\mathrm{s}}}} = \frac{\sqrt[4]{\frac{18}{\pi}}\beta^{\frac{1}{4}}}{2\alpha^{\frac{1}{2}}} \tag{III.3}$$

In order to further compare the incertitudes on the amplitude, a relationship must be found between the damping factors. In this study we chose to define equivalent lineshapes as lineshapes that have the same amplitude and the same width at half-height (see Fig.III.5).

The latter condition yields:

$$\alpha_{\text{Lorentz}} = \sqrt{4 \log 2 \ \beta_{\text{Gauss}}} \tag{III.4}$$

Replacing Eq.III.4 in Eq.III.3 enables us to compute a numerical approximation:

$$\frac{\text{CRLB}_{\text{Gauss}}^{\text{amplitude}}}{\text{CRLB}_{\text{Lorentz}}^{\text{amplitude}}} = \sqrt[4]{\frac{9}{32\pi \log 2}} \approx 0.5994 \tag{III.5}$$

Eq.III.5 shows that the predicted incertitude on amplitude estimation is about 40% smaller on a Gaussian singlet than on a Lorentzian singlet. Moreover, the result is a constant (under the assumption of equivalence at width at half-height). This effectively means, that under equivalent conditions of noise, amplitudes and peak width, it is always preferable to quantify Gaussian peaks than Lorentzian ones.

An alternative way to look at this finding is to consider, from a more signal processing point of view, why does the Gaussian peak have better amplitude estimation performances than the Lorentzian one. A possible answer lies in the fact that the Gaussian lineshape is wider, yet more prominent (see Fig.III.5), thus containing more information that is separable from noise. In the same time, by having a slower decay, the Lorentzian singlet has values comparable to noise on a much larger extent, thus reducing the components that can be effectively isolated from noise.

III.3 Estimating the Common Decay Function

As seen in the previous section, using an inappropriate model function when modelling the decay function of MRS signals can induce considerable bias in the estimation of metabolite amplitudes. It becomes thus essential to evaluate the properties of damping characteristics of signals to be analysed. Although several analytical models have been proposed in literature (*cf.* §II.5), we concentrate in this work on a *non-parametric* approach, *ie.* one that does not require an overall analytical representation. Using a commonly assumed hypothesis of different metabolites sharing the same lineshape, we discuss a simplified model of Eq.III.2, leading to a way of estimating the common lineshape. The theoretical conditions for the common lineshape assumption are discussed, and its pertinence is analysed in view of current state-of-the-art as well as in view of the other methods available for lineshape handling.

III.3.1 Modelling a decay function common to all metabolites

Consider the common model used in MRS estimation (III.2):

$$\hat{s}(t) = \sum_{m=1}^{M} c_m \exp \imath\varphi_m \underbrace{d_m(t)}_{(a)} \underbrace{b_m(t)}_{(b)} \tag{III.6}$$

The total decay is given by the influence of two factors: (a) the dephasing of spins due to B_0 inhomogeneity and (b) the intrinsic T_2 transversal magnetization decay mechanism. In practice, *in vivo* B_0 induced decay is much stronger than T_2 decay, so that the former can be considered dominant over the second (see [86, 201]). Furthermore, both terms, in the general case, depend on the metabolite m, and can even vary for different spectral peaks of the same

	Lorentzian	Gaussian
model	$c\,\exp\left(-\alpha t + \imath\omega t + \imath\varphi\right)$	$c\,\exp\left(-\beta t^2 + \imath\omega t + \imath\varphi\right)$
amplitude (c)	$2\,\sigma\,\alpha^{\frac{1}{2}}\sqrt{t_\mathrm{s}}$	$\sqrt[4]{\frac{18}{\pi}}\,\sigma\beta^{\frac{1}{4}}\sqrt{t_\mathrm{s}}$
damping factor (α, β)	$2\sqrt{2}\,\frac{\sigma}{c}\,\alpha^{\frac{3}{2}}\sqrt{t_\mathrm{s}}$	$\sqrt[4]{\frac{512}{\pi}}\,\frac{\sigma}{c}\beta^{\frac{5}{4}}\sqrt{t_\mathrm{s}}$
frequency shift (ω)	$2\sqrt{2}\,\frac{\sigma}{c}\,\alpha^{\frac{3}{2}}\sqrt{t_\mathrm{s}}$	$\sqrt[4]{\frac{128\pi}{(\pi-2)^2}}\,\frac{\sigma}{c}\beta^{\frac{3}{4}}\sqrt{t_\mathrm{s}}$
phase (φ)	$2\frac{\sigma}{c}\alpha^{\frac{1}{2}}\sqrt{t_\mathrm{s}}$	$\sqrt[4]{\frac{8\pi}{(\pi-2)^2}}\,\frac{\sigma}{c}\beta^{\frac{1}{4}}\sqrt{t_\mathrm{s}}$

Table III.3: *Cramér-Rao Lower Bounds (CRLBs) for Lorentzian and Gaussian singlets. Noise model is white Gaussian.* t_s *is the sampling time and* σ *is the noise standard deviation. Notice that the CRLB on amplitude does* not *depend on the amplitude of the signal, while the CRLBs corresponding to the other parameters depend on the signal-to-noise ratio* $\frac{c}{\sigma}$.

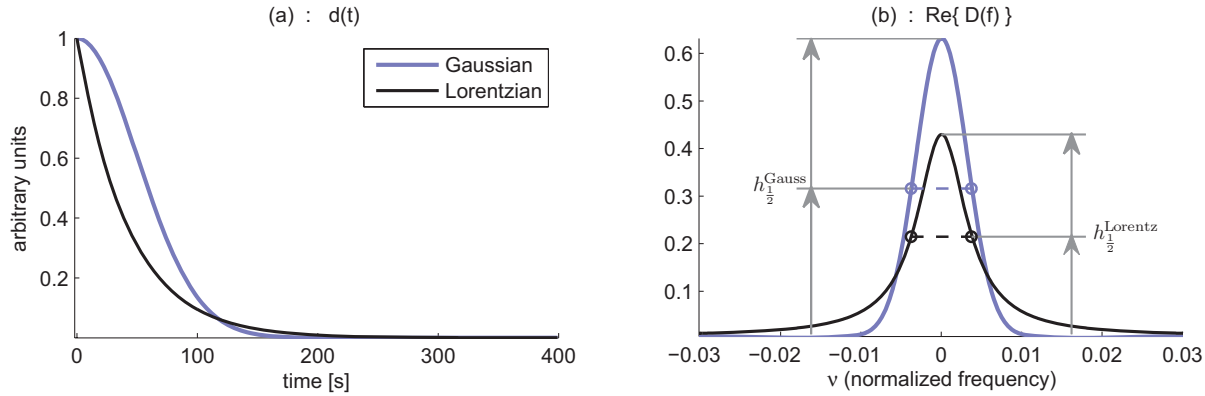

Figure III.5: *Illustration of Lorentzian and Gaussian decay functions, both in the time domain (a) and in the frequency domain (b). Both models have the same amplitude* ($c = 1$). *The damping factors have been chosen so that the corresponding lineshapes have the same width at half height, giving the relationship* $\alpha_{\mathrm{Lorentz}} = \sqrt{4\log 2\;\beta_{\mathrm{Gauss}}}$. *Notice how in the frequency domain the lineshapes have different maximal values, yet the same area under the curve.*

metabolite. While T_2 dependency on m can be measured (*e.g.* for T_2 measurements in rat brain at 9.4T see values reported by Xin et al. [198]), the effect of B_0 spatial distribution is more intricate, involving the context function Ψ_m (*cf.* §II.1 and §III.1).

Let us consider what assumptions and simplifications are necessary in order to be able to factorize all damping factors in Eq.III.6 outside the sum. First of all, the T_2 transverse relaxations time constants need to be considered equal. Secondly, the B_0 heterogeneity-caused damping d_m must also be independent of the metabolite m. However, d_m has been defined as the normalized version of the context function Ψ_m, that directly depends on the magnetic field inhomogeneity distribution $\triangle B_0(\mathbf{r})$ and on the metabolite concentration distribution $c_m(\mathbf{r})$ (see Eq.II.6):

$$\Psi_m(t) = \int_{\mathbf{r}\in VOI} c_m(\mathbf{r}) \exp\left[\imath\gamma\triangle B_0(\mathbf{r})t\right] \exp\left[\imath\varphi(\mathbf{r})\right]\, d\mathbf{r}^3 \tag{III.7}$$

While the $\triangle B_0$ map does not depend on m, a common lineshape means that the concentration of different metabolites must be distributed in the same way across the region of interest, *ie.* $c_m(\mathbf{r}) = c_m \cdot \mathtt{dist}(\mathbf{r})$, where $\mathtt{dist}(\mathbf{r})$ is the spatial distribution. Considering that the metabolites are equally distributed is usually reasonable for small sizes of acquisition voxel, and on the condition that no important boundary [7] lies within the voxel.

Should the aforementioned hypothesis be assumed verified, then it is possible to define an overall decay function $d(t)$, that includes both the decay due to B_0 field heterogeneity and the T_2 decay. In this case Eq.III.6 can be re-written in a much simpler form:

$$\hat{s}(t) = d(t) \sum_{m=1}^{M} c_m \exp \imath\varphi_m \; b_m^{\text{undamped}}(t) \tag{III.8}$$

An important element that is introduced in Eq.III.8 is the *undecaying* (*ie.* non-decaying) metabolite basis-set $\mathbf{b}^{\text{undamped}}(t)$. A basis-signal (or metabolite model) represents known *a priori* information. As such, $\mathbf{b}^{\text{undamped}}(t)$ can be predicted by quantum mechanics and thus simulated via software packages like NMRSCOPE [69]. Measuring the metabolite basis-signal, while also a possibility, has the drawback of naturally including T_2 decay, even in ideal conditions, and thus must be consequently processed so that the decay be eliminated or accounted for. In this work, we have concentrated exclusively on using NMR-SCOPE generated spectra, mainly because of the facilities in direct subsequent exploitation, as well as because of the seamless integration with the QUEST quantitation method inside the jMRUI package[175].

Two more remarks are important at this stage, both concerning Eq.III.8. First, no metabolite-wide frequency shift has been included into the model. Actually, the function $d(t)$ can implicitly include a frequency shift, that arises from the integral context function Ψ. In order to separate the damping from the frequency shift in d, it is necessary to define a criterion; the common choice would be to define the frequency shift as the location of the maximum value of the d Fourier Transform. However, should the lineshape have two peaks, the situation is more delicate. In the following implementations the question of frequency shifts has been omitted for simplicity, and thus the model is further presented without frequency shifts. Should a frequency shift be implemented, it would be common to

7. As an illustration of the case when the lineshape would not be the same, consider the case when the VOI is split into two zones of different $\triangle B_0$ distributions, one containing only metabolite m_1 and the second only m_2.

all metabolites, a consequence of the fact that the Ψ function generating the shift is also common to all metabolites.

The second issue is the possibility of slightly extending the model to accommodate the T_2 dependence on the metabolite m. Adding a Lorentzian decay function specific to each metabolite provides this accommodation, without very much increased complexity in the model. However, due to reasons discussed further on, it is important that the term inside the sum in Eq.III.8 be non- or very slowly-decaying. It is thus preferable that given a set of Lorentzian decay constants $\alpha_m = \frac{1}{T_{2,m}}$, the major part α_0 of the damping factors be included in the common decay function $d(t)$, and only the differences $\triangle\alpha_m = \alpha_0 - \alpha_m$ be left in the sum. Estimating the common decay factor α_0 can be done, for example, by choosing $\alpha_0 = \max_m\{\alpha_m\}$. The extended model can be written as

$$\hat{s}(t) = d(t) \sum_{m=1}^{M} c_m \exp \imath\varphi_m \exp\left(-\triangle\alpha_m t\right) b_m^{\text{undamped}}(t) \tag{III.9}$$

III.3.2 The Estimated Common Decay function

Equation III.8 separated the decay function $\mathbf{d}$ from the *a priori* information included in $\mathbf{b}^{\text{undamp}}(t)$. It is possible to rewrite it so that the decay function d be expressed in function of the signal $\mathbf{s}$, the parameters $\mathbf{p} = (c_m, \varphi_m)$ and the prior information included in $\mathbf{b}^{\text{undamp}}(t)$:

$$d(t) = \frac{\hat{s}(t)}{\sum_{m=1}^{M} c_m \exp \imath\varphi_m \; b_m^{\text{undamped}}(t)} \tag{III.10}$$

Equation III.10 is the key relationship on which our new method is based. However, the true parameters are not known, and neither is the denoised version of the acquired signal. Instead we attempt to compute the Estimated Common Lineshape (ECD) $\hat{d}(t)$, by replacing, in Eq.III.10, $\hat{\mathbf{s}}$ with the acquired signal $\mathbf{s}$ and the true (unknown) parameters with some previously estimated parameters $\hat{\mathbf{p}} = (\hat{c}_m, \hat{\varphi}_m)$, assumed available and close to the true parameters. The ECD function is thus defined as:

$$\hat{d}(t) = \frac{s(t)}{\hat{s}^{\text{undamped}}(t)} \tag{III.11}$$

$$\text{with } \hat{s}^{\text{undamped}}(t) = \sum_{m=1}^{M} \hat{c}_m \exp \imath\hat{\varphi}_m \; b_m^{\text{undamped}}(t) \tag{III.12}$$

The denominator of the right term in Eq.III.11 represents a model of the signal that excludes the decay function, subsequently called the Undamped Estimated Signal (UdES) and denoted $\hat{\mathbf{s}}^{\text{undamped}}$. The signal is a sum of complex harmonic signals, and as such exhibits decreasing probability of cancelling itself in the time domain as the number of components increases. Moreover, as no decay factor is present, the sum is not overall decaying, exhibiting a statistically constant characteristics, such as mean value or mean energy. The properties, restricting the appearance of very small values are particularly useful because the UdES is used as a dividing term in estimating the ECD function.

An important factor to mention here is that, since the acquired signal $\mathbf{s}$ contains noise, the estimated common decay function also contains noise. To illustrate this, as well as to see how the noise inside the ECD behaves, consider that the acquired signal is generating according to the same model used for estimating the ECD function, and with a stochastic

component represented by AWG Noise $\epsilon(t)$. The true, unknown values of the parameters $\mathbf{p}$ are denoted using the caron ˇ symbol.

$$s(t) = \check{d}(t) \sum_{m=1}^{M} \check{c}_m b_m^{\text{undamped}}(t) e^{j\check{\varphi}_m} e^{j\check{\omega}_m t} + \epsilon(t) \tag{III.13}$$

Combining equations III.11 and III.13 enables the estimated common damping $\hat{d}$ to be expressed in function of the true, unknown common decay function $\check{d}$:

$$\hat{d}(t) = \check{d}(t) \frac{\sum_{m=1}^{M} \check{c}_m b_m^{\text{undamped}}(t) e^{j\check{\varphi}} e^{j\check{\omega}t}}{\sum_{m=1}^{M} \hat{c}_m b_m^{\text{undamped}}(t) e^{j\hat{\varphi}} e^{j\hat{\omega}t}} + \varepsilon'(t) \tag{III.14}$$

$$\text{with } \epsilon'(t) = \frac{\epsilon(t)}{\sum_{m=1}^{M} \hat{c}_m b_m^{\text{undamped}}(t) e^{j\hat{\varphi}} e^{j\hat{\omega}t}} \tag{III.15}$$

Equation III.14 shows that if the estimated parameters $\hat{\mathbf{p}}$ are equal to the true ones $\check{\mathbf{p}}$, then the ECD is equal to the true common decay function, plus a noise term ϵ'. However, it should be noted that the statistical distribution of ϵ' is not AWGN, as was assumed for ϵ, but depends strongly on the undamped model $\hat{\mathbf{s}}^{\text{undamped}}$. In the special case when, for example, $\hat{s}^{\text{undamped}}(t)$ becomes very small or null, ϵ' can attain values out of the representation range.

III.3.3 Convergence issues in the case of no ECD filtering

As it can be seen in Eq.III.14, the estimated common decay function depends on the initial parameters $\hat{\mathbf{p}}$, while also including a noise term ϵ'. Since noise is present, direct adaptation of a basis-set using this noisy ECD function may result in unwanted convergence. To illustrate this, consider the aforementioned case. The adapted metabolite basis-set signals $\mathbf{b}_m^{\text{adapted}}$ can be written as

$$\begin{aligned} b_m^{\text{adapted}}(t) &= \hat{d}(t)\ b_m^{\text{undamped}}(t) \\ &= \frac{s(t)}{\hat{s}^{\text{undamped}}(t,\hat{p})}\ s_m^{\text{undamped}}(t) \\ &= s(t)\ \frac{b_m^{\text{undamped}}(t)}{\hat{s}^{\text{undamped}}(t,\hat{p})} \end{aligned} \tag{III.16}$$

Should now a second quantitation take place, using the same QUEST model, and giving the results $\hat{\mathbf{p}}'$, the residue could be written as:

$$\begin{aligned} r'(t,\hat{p}\prime) &= s(t) - \sum_{m=1}^{M} \hat{c}'_m \cdot b_m^{\text{adapted}}(t) \cdot e^{j\hat{\varphi}'_m} \cdot e^{j\hat{\omega}'_m t} \\ &= s(t) - \frac{s(t)}{\hat{s}^{\text{undamped}}(t,\hat{p})} \sum_{m=1}^{M} \hat{c}'_m b_m^{\text{undamped}}(t) e^{j\hat{\varphi}'_m} e^{j\hat{\omega}'_m t} \\ &= s(t) \left[1 - \frac{\sum_{m=1}^{M} \hat{c}'_m \hat{s}_m(t)\ e^{j\hat{\varphi}'_m} e^{j\hat{\omega}'_m t}}{\hat{s}^{\text{undamped}}(t,\hat{p})}\right] \\ &= s(t) \left[1 - \frac{\sum_{m=1}^{M} \hat{c}'_m b_m^{\text{undamped}}(t) e^{j\hat{\varphi}'_m} e^{j\hat{\omega}'_m t}}{\sum_{m=1}^{M} \hat{c}_m \cdot b_m^{\text{undamped}}(t) \cdot e^{j\hat{\varphi}_m} \cdot e^{j\hat{\omega}_m t}}\right] \end{aligned} \tag{III.17}$$

By replacing in Eq.III.17 $\hat{p}' = \hat{p}$, we obtain that the terms in the square brackets cancel themselves out and that the residue is zero in all points, regardless of the values of $s(t)$, $\hat{p}$ or $s_m(t)$. As the norm of the residue is concerned, it can only be greater than zero, and would be zero if and only if the residue is zero in all points. This effectively means that if there is only one global minimum to the equation $\min_{\hat{p}'} \| r\left(t, \hat{p}'\right) \|$ it is equal to zero and it is achieved for $\hat{p}' = \hat{p}$.

It has thus been proved that in the best case scenario, a second QUEST-type minimization using a basis-set on which an estimated lineshape has been applied would theoretically converge to the parameters that have been initially used to estimate the lineshape. The residue of this estimation is zero as all the noise has been inserted in the lineshape. In practical cases, quantitation procedures do not always converge to the exact parameter values corresponding to the global minimum, mainly due to local minima, thus achieving even poorer performances. Reducing the degrees of freedom of the lineshape so as to filter a maximum of the noise components eliminates the global minimum that depends on the previous parameters. Filtering too much, however, eliminates useful information gained by common decay function estimation, eventually making the algorithm equivalent to a pure QUEST application.

III.3.4 Quantitation with Lineshape Accommodation based on Estimated the Common Decay Function

Based on the relationship between the true, unknown, decay function and the estimated common decay function (Eq.III.14), we propose to use the latter as the basis for an estimator for the former. Furthermore, the estimated decay function is then used to shape the metabolite basis-set. The basic algorithm is based on the QUEST[156] quantitation method, although any other measurement (time-) domain method that includes metabolite basis-set prior information could be used. The choice of the method is mainly based on our extensive experience with QUEST, as well as its easy implementation using the jMRUI package.

The proposed approach [8] is described in Fig.III.6, as well as in the following algorithmic view.

QUEST-ECD (Estimated Common Decay)

INPUT	
$\mathbf{s}$	signal to be processed
$\mathbf{b}^{\text{undamped}}$	metabolite basis-set (non decaying version).
$\mathbf{b}^{\text{Lor}}$	metabolite basis-set (decaying version).

STEP	
01	Quantify $\mathbf{s}$ by QUEST using $\mathbf{b}^{\text{Lor}}$. Store result in $\mathbf{p}_{\text{ini}}$.
02	Build the undamped signal model $\hat{\mathbf{s}}^{\text{undamped}}$.
03	Compute raw decay function $d^{\text{raw}}(t) = \frac{s(t)}{\hat{s}^{\text{undamped}}(t)}$.
04	Compute filtered decay function $\mathbf{d}^{\text{filtered}} = \text{FILTER}\{\mathbf{d}^{\text{raw}}\}$.

8. In this section, we chose not to detail a key step of the proposed algorithm that is ECD function filtering. The need for this step will be discussed at the end of this subsection, while actual implementations are described in later sections.

05 Generate new basis-set $\mathbf{b}^{\text{adapted}}$ (having an adapted decay function) from $\mathbf{d}^{\text{filtered}}$ and $\mathbf{b}^{\text{undamped}}$.

06 Quantify $\mathbf{s}$ using QUEST and $\mathbf{b}^{\text{adapted}}$. Store result in $\mathbf{p}_{\text{final}}$

OUTPUT

$\mathbf{p}_{\text{final}}$ Metabolite parameters

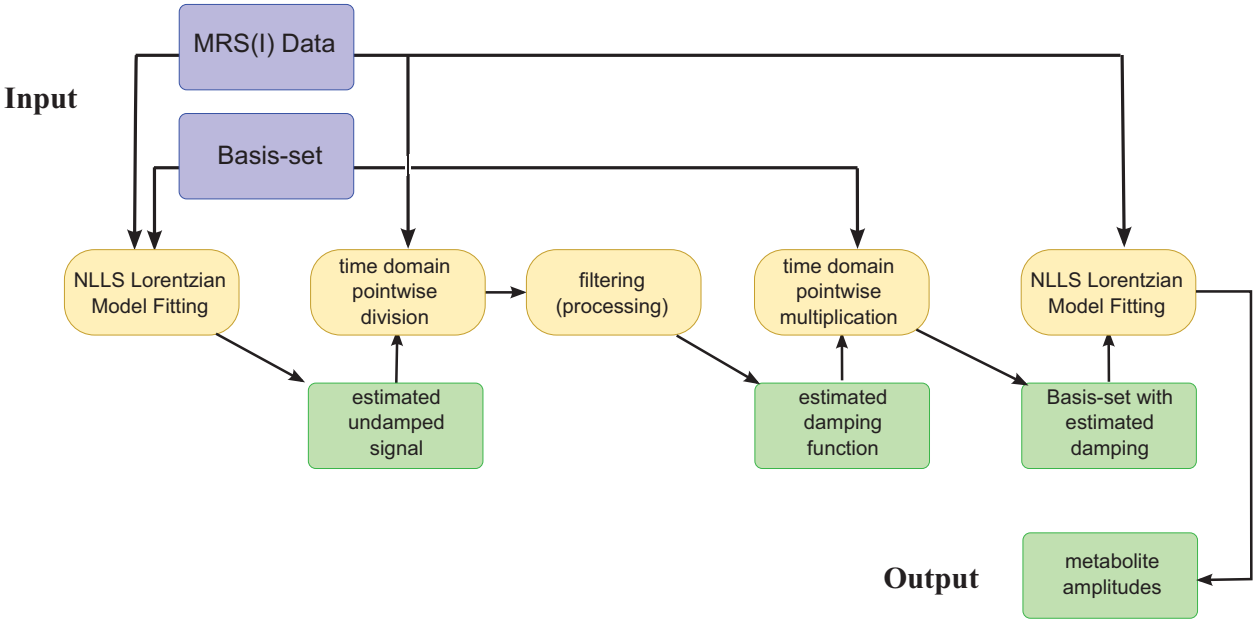

Figure III.6: *Schematic description of the approach proposed for metabolite quantitation with lineshape accommodation. Blue: input data. Yellow: Computation step. Green: intermediary results and final output. See text for detailed description.*

STEP.1 The first step of the algorithm uses QUEST and a Lorentzian metabolite basis-set in order to obtain an initial estimation of the metabolite model parameters. This estimation is subsequently used to estimate the ECD function. Although QUEST can manage a basis-set without decay, it is better at this stage to evaluate the damping factor of $\mathbf{s}$ and to generate $\mathbf{b}^{\text{Lor}}$ accordingly.

STEP.2 The undamped signal model $\hat{\mathbf{s}}^{\text{undamped}}$ is built according to Eq.III.12. Notice that extra damping factors α_m are not used.

STEP.3 The raw estimated common decay (ECD) function is computed by a point-wise division between $\mathbf{s}$ and the previously computed undamped signal model.

STEP.4 A filtered version of the ECD is computed. In the initial implemented version, HLSVD has been proposed for this task, while local filtering is subsequently considered.

STEP.5 Adaptation of the basis-set is performed by point-wise multiplication between the individual undamped metabolite basis-set signals and the filtered estimated decay function.

STEP.6 The final step consists of a second QUEST application on $\mathbf{s}$, using the decay-function-adapted metabolite basis-set.

III.4 LOWESS filtering

In order to use the information in the estimated lineshape, some form of filtering could be used to eliminate the noise ε', thus obtaining a close estimation of the true lineshape. The noise to be reduced is a Gaussian normally distributed noise (AWGN), divided by the undamped estimated signal model (UdES) $\hat{\mathbf{s}}^{\text{undamped}}$. As $\hat{s}^{\text{undamped}}(t)$ can theoretically approach or be equal to zero for some values of t, it means that ε' is theoretically unbounded [9] noise. Simulating different values of UdES shows that as the complexity (number of peaks) increases, the probability that multiple samples of UdES are nearly equal to zero decreases. However, it is still the case for some points, for which the amplitude of the corresponding lineshape estimation becomes significantly larger than the rest of the points.

A filtering method that would improve the estimation of the lineshape should have thus two main characteristics:

1. **Robustness** : Outliers due to division by very small numbers would have to be efficiently removed by the filtering.
2. **Time localization** : A good physical model of the lineshape is hard to create because it depends on the distribution of the magnetic field B_0 , that changes in every experimental setup. However, due to the continuity in time of its evolution, an important characteristic of the lineshape is that it has a local time-wise coherence, meaning that the probability that two time samples having the same value is inversely proportional to the time-span between the samples. The ideal filter should keep (and eventually enhance), the local time coherence, while reducing noise, that is by definition non-coherent.

III.4.1 Local fitting filtering

Local scatter-plot fitting is one of many "modern" modeling methods that build on "classical" methods, such as linear and nonlinear least squares regression [122]. Better perhaps described as locally weighted polynomial regression, the method fits simple models on subsets of data to build up a function that describes the deterministic part of the data. The result is a combination between the simplicity of linear least squares and the advantages of non-liner regression. The major trade-off resides in increased computational complexity.

LOWESS has been originally proposed by Cleveland ([38], 1979) and then improved by Cleveland and Devlin under the name LOESS ([39], 1988). Computational methods and implementation are discussed in [40, 41, 42], and the author's implementation can be found on the NETLIB online library ([10]). At each point in the data a polynomial model is fit using weighted linear regression. The weight function is chosen so as to offer more importance to the points near the estimated point and less weight to points further away. The final value of the output is then computed by applying the local polynomial value to the corresponding abscissa. LOWESS is complete when this process is complete for all the points in the dataset. Figure III.7 summarizes the principles of local polynomial filtering.

Many of the details of the algorithm, such as the degree of the polynomial or the weight function, are flexible, allowing the procedure to be customized to different applications. The

9. By unbounded we mean that it can take arbitrarily high or low values.
10. Available at `http://netlib.sandia.gov/`. Accessed March, 2010

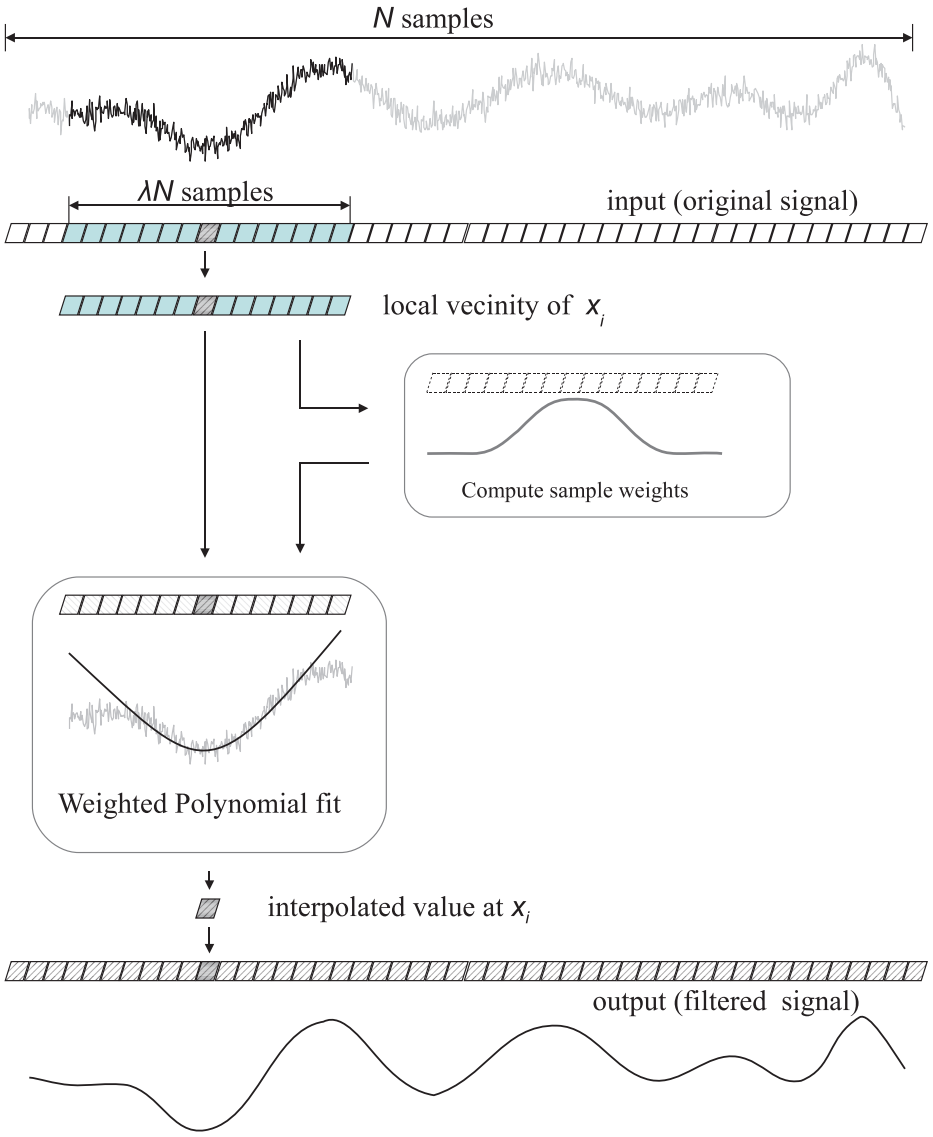

Figure III.7: *The general principle behind local filtering techniques LOESS and LOWESS. This illustration shows the steps taken for finding the value at x_i, denoted by a grey hatched box. First, the local vicinity is computed, as all the λN points nearest to the analysed sample. Weights are then computed for each point in the vicinity, so as to give more importance to samples closer to the analysed sample at x_i. Then a polynomial interpolation is performed using the vicinity and the previously calculated weights. The output point corresponding to x_i is the value of the interpolation polynomial at the point x_i. The process is repeated for all the N samples in the input (original) signal.*

influence of several parameters and the choices that have been made in the study are briefly discussed next.

The local subsets of data are defined by the nearest-neighbours algorithm. A user-supplied "bandwidth" hyper-parameter λ defines the number of points to be taken into consideration $N_{\text{LOCAL}} = \lambda N$. λ can also be referred to as "smoothness parameter" because the higher λ is, the smoother is the output.

Choosing a big value of smoothness produces a very smooth output, that varies little in response to the fluctuations in the data. This can severely reduce the levels of details in the data. On the other hand using a value for λ that is too small will make the output capture random variations (noise) in the data.

Choosing a good value for λ is a non-trivial matter and it can have a great influence on the outcome. It should depend on the inherent structure of the deterministic part of the signal, as well as on the noise characteristics. An algorithm to choose a pertinent smoothness parameter in the case of filtering for MR spectra is discussed later.

The degree of the polynomial used for the local fitting also plays an important role in the method. If the degree is zero, than the method is equivalent to a moving average. This is a somehow trivial solution, and in most cases does not fit well the data structure. High-degree polynomials work, in theory, but the trade-off between increased computation, numerical stability and increased resolution is most of the times not justified. In most cases linear or quadratic polynomials are sufficient to obtain good results.

The weight function is used to give more weight to point that are closer to the point being estimated. The use of a weight function is based on the idea that a local model is explanatory for local points, and thus the local model should be mostly constructed using the local information. The traditional weight function used by LOWESS is the tri-cube weight function

$$w_d(x) = \begin{cases} (1 - |t|^3)^3 & \text{for } |t| < 1 \\ 0 & \text{for } |t| \geq 1 \end{cases} .$$

Other weight functions have also been proposed in [38]. The weight used by the polynomial model is computed after scaling of the weight distance variable x so that the maximum distance corresponding to the subset span determined by λ is 1.

The robustness of the method can be enhanced by an iterative approach, that increases the importance of points that fit the model well and decreases the importance of outliers. At the end of all data-point estimations, the distance difference between the output and the input is computed. Then a weight function is applied and the process is restarted, taking into account the combined weight of the local weight function (different for each point) and of the global weight function. The weight function generally used is the bi-square function

$$w_r(x) = \begin{cases} (1 - |x|^2)^2 & \text{for } |x| < 1 \\ 0 & \text{for } |x| \geq 1 \end{cases} \tag{III.18}$$

Lowess Filtering

→ **Input**: signal **s** having N samples, smoothing hyperparameter λ

1. Initialize $w_r(x_i) = 1$
2. For all points (t_i, s_i)
   1. Create subset from λN nearest points.
   2. Fit linear function $\mathtt{P_i(t)}$ on subset using weights defined by the scaled tri-cubic function multiplied by w_r.
   3. Using P_i compute value $\hat{s}_i$ corresponding to abscissa $\hat{t}_i$.
3. Compute the residue $\mathtt{R} = \mathtt{s} - \hat{\mathtt{s}}$
4. Compute robustness weights w_r based on residues R.
5. If Convergence, stop. Else, go to (2)

← **Output**: Filtered Signal $\hat{\mathtt{Y}}$

III.4.2 Automatic value of the smoothing hyper-parameter

In order to automatically find a suitable value of the λ hyper-parameter, an approach inspired by the CONTIN [142, 143] algorithm has been developed. From Eq.III.14, ignoring the dependence on the parameter set **p**, it can be written that

$$\hat{d}(t) = \check{d(t)} + \varepsilon'(t) \tag{III.19}$$

If we consider $\mathrm{LOWESS}_\lambda\left\{\hat{d}(t)\right\}$ as the filtered version of the estimated common damping $\hat{d}(t)$, and taking into account that LOWESS is a linear filter, then we can write that

$$\mathrm{LOWESS}_\lambda\left\{d(t)\right\} = \mathrm{LOWESS}_\lambda\left\{\check{d}(t)\right\} + \mathrm{LOWESS}_\lambda\left\{\varepsilon'(t)\right\} \tag{III.20}$$

meaning that the filtered ECD is given by the distinct contributions of the filtered true common decay function and the filtered noise. If we subtract now the true value of the lineshape, we obtain the expression of the error of the estimation of the common decay function:

$$\begin{aligned}\mathrm{Error}_{\mathrm{ECD}}(\lambda, \mathrm{t}) &= \check{d}(t) - \mathrm{LOWESS}_\lambda\left\{d(t)\right\} \\ &= \underbrace{\left[\check{d}(t) - \mathrm{LOWESS}_\lambda\left\{\check{d}(t)\right\}\right]}_{(a.)} + \underbrace{\mathrm{LOWESS}_\lambda\left\{\varepsilon'(t)\right\}}_{b.}\end{aligned} \tag{III.21}$$

The first term (a.) of Eq.III.21 represents the error that is incurred by the LOWESS filter. The value of the hyper-parameter should be chosen so as to minimize this error, and since the dependence is direct, it suggests to take the smallest possible value of λ. On the other hand, the second term (b.) of Eq.III.21 shows the error that is given by the noisy first estimation. The dependence of this error on λ is inversely proportional, meaning that we should choose the biggest possible value of λ such as to decrease as most as possible any noise contribution. In order to choose the optimal value of the hyper-parameter, it is needed to find a good compromise between the rejected noise and the error introduced by the filtering. A more in-depth view of the evolution of the two terms is needed.

Evolution of residual variance in function of λ

It can be shown (*cf.* additional material) that the variance of AWG Noise ϵ filtered with LOWESS follows a law of the form

$$\mathrm{VAR}\left[\mathrm{LOWESS}_\lambda\{\epsilon\}\right] \approx A + \frac{B}{\lambda} \tag{III.22}$$

with A and B two constants. Such a dependence only on the hyper-parameter λ is possible because of the time-wise incoherence of AWG Noise.

The ECD function has, unlike AWG noise, a local temporal coherence. As it has been hypothesized that it is smooth, we can suppose that the difference between consecutive values is always small, and that one value cannot be too different that the average of the values around it. It also effectively means that for small values of λ the LOWESS filter has a very small effect.

The evolution of the variance of the filtered signal thus follows only two general rules: (1) the variance is constant at the beginning (λ very small) and (2) the variance decreases as λ increases. The latter property comes from the reduction in effective degrees of freedom. Other than these rules the variation is not predictable and depends on every particular ECD function.

Let us now reconsider Eq.III.21. The two terms (a) and (b) are independent, thus if we apply LOWESS on a noisy ECD signal, we would get the combined effects previously described: (1) AWGN contribution in the form of a function inversely proportional to λ and with most evolution for small values of λ and (2) ECD contribution in the form of a monotone function with small variations for small values of λ.

Figure III.8 illustrates this evolution for a simulated signal consisting of an exponential decay signal to which AWG Noise has been added such that the SNR of the first point is 20:1 ($\approx$ 26 dB). For $\lambda \leq 0.1$ the variance evolution is given mostly by the reduction in noise. Thus the smoothing hyper-parameter should be chosen so as to maximize noise reduction while minimizing the distortion that becomes apparent for $\lambda \geq 0.2$.

Automatic estimation of optimal λ

Based on the previous considerations an automatic procedure to investigate the optimal smoothing parameter λ has been developed. The method consists in computing the evolution of the variance of the residue and identifying which part comes mainly from an AWG noise and which part comes mainly from the underlying "clean" ECD function.

Estimation of LOWESS hyper-parameter λ

$\rightarrow$ **Input**: signal to filter $\mathbf{d}$, smoothing hyper-parameter list (λ_i)

1. For all values λ_i compute residual variance fraction $r_{\lambda_i} = \frac{\mathrm{VAR}[\mathbf{d}-\mathrm{LOWESS}_{\lambda_i}(\mathbf{d})]}{\mathrm{VAR}[\mathbf{d}]}$
2. Compute the weighted linear regression $\hat{r}_\lambda \sim r_\lambda = A - B\frac{1}{\lambda}$
3. Compute $\varsigma = \sqrt{\mathrm{VAR}[r - \hat{r}]}$
4. Search in descending order the first $\lambda_{\mathrm{optimal}}$ value for which $\hat{r}(\lambda_{\mathrm{optimal}}) < r_\lambda - \varsigma$

$\leftarrow$ **Output**: smoothing hyper-parameter $\lambda_{\mathrm{optimal}}$

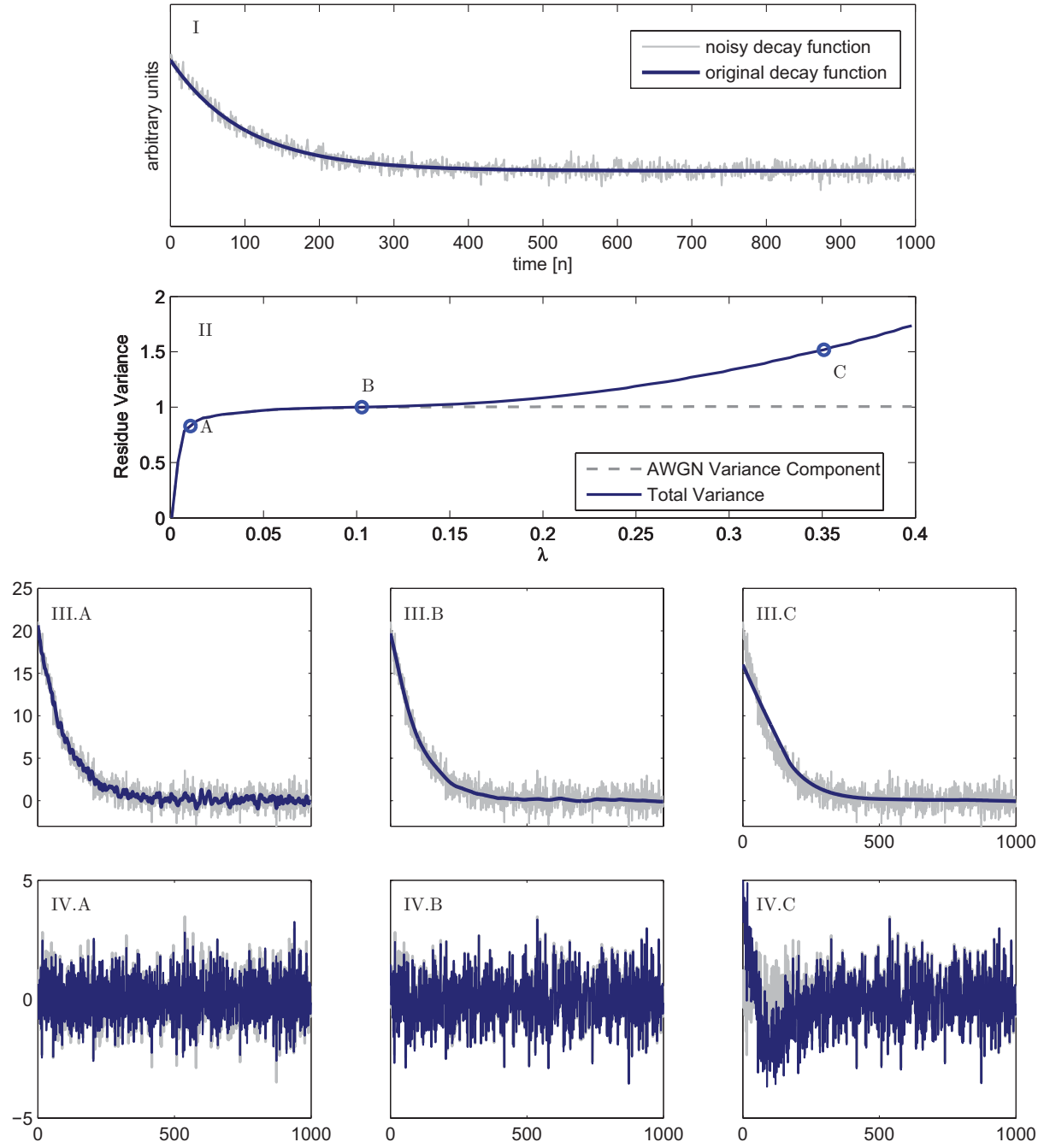

Figure III.8: *Evolution of the residue variance for different values of the smoothness hyper-parameter λ for LOWESS filtering. Top: original signal (Lorentzian model) and the noisy realization that is to be filtered. Top-middle: Evolution of the residual variance for the noisy signal (full line) as well as just for the noise (dashed line). For values at A, B and C, the filtered signal (row III), as well as the residue (row IV) are plotted in the lower half of the figure., together with the unfiltered signal and the noise respectively (in gray). Case A corresponds to an over-fitted line (λ too small); notice the noise in the filtered signal (dark blue) in III.A. Case C corresponds to an under-fitted signal (λ too large); notice the non-random component in the residuals (dark blue) in IV.C. Case B corresponds to a well adapted λ. Axes for plots (III) and (IV) are the same as for (I).*

In order to separate the influence of noise and of useful components in the residue, first a model $\hat{\mathbf{r}}$ of the noise variance needs to be computed. This is performed by doing a weighted least-squares fit on the overall evolution of the residual variance. The weights are chosen so as to give more importance to the first points, where variance evolved predominantly because of noise filtering. The model is derived from Eq.III.22.

The second step is to compute the standard deviation ς of the difference between the LS fitted series $\hat{\mathbf{r}}$ and the computed series $\mathbf{r}$. This is done in order to estimate the goodness of fit , and to provide a useful reference when seeking to separate noise and deterministic influence.

The final step is a search, starting from the maximal value of λ, so as to identify the biggest value λ_{optimal} that verifies the inequality $\hat{r}(\lambda_{\text{optimal}}) < r_\lambda - \varsigma$. In other words, we choose λ_{optimal} so that the quantity of useful information lost to the filtering procedure is of the order of the precision in identifying the noise component's influence.

III.5 QUEST-ECD Validation on synthetic data

In the following section several studies are performed, using synthetic data sets. The reasoning for using simulated data is detailed in §III.5.1, while the rest of the section treats the numerical examples.

III.5.1 Why validation on synthetic signals

Errors in parameter estimation generate estimates that follow a statistical distribution. This distribution gives very important information on statistical properties of the estimator. If the estimator can be accurately described, the distribution of the results can be computed and, therefore, so can be the incertitude of a single estimation.

Among the most used statistics to measure the estimator quality we can find the bias and the variance. If the estimator generates a normal (Gaussian) distribution, then these two parameters alone suffice in fully describing it.

Variance is defined as the "scatter" of the data and often referred as measurement precision. It defines the differences between an estimated value and the average estimated value. In the case of a series of measurements, it can be estimated without knowing the true values.

Bias, sometimes also called measurement **accuracy**, represents the difference between the average of the estimated value and the true value. It can only be accurately computed if the true value is known.

RMSE (Root Mean Square of Error) is defined as the norm of the errors in estimates, and thus provides a measure of the combined effect of bias and variance. $BIAS^2+VAR = RMS^2$.

When quantitation is based on a physical model, the number of parameters in the model can have an important effect on the quantitation results. If too many parameters are included, random effects can be modelled as deterministic, increasing drastically the model variability. However, should the model be inaccurate because the number of model degrees of freedom is not sufficient to describe the physical dynamic, important bias may occur. In "real life" (clinical or black-box use of estimators) the bias effect is very hard to see, and people tend to look only at the data scatter (variance). Yet if for simple simulated cases we can find a bias, then there is no reason why not to consider the existence of a bias in

$d(t) \rightarrow$	known	$\exp(\alpha t)$	Estimation by Eq. (7) & HSVD			
metabolite	(true)	Lorentz	Case 1	Case 2	Case 3	Case 4
$m = 1$	1.0	1.62	2.37	2.09	1.98	2.01
	(0.0)	(-0.27)	(0.09)	(0.14)	(0.12)	(0.09)
$m = 2$	1.0	5.12	2.96	2.78	2.64	2.77
	(0.0)	(3.06)	(0.26)	(0.28)	(0.18)	(0.16)
$m = 3$	1.0	13.30	8.30	7.63	7.12	7.22
	(0.0)	(9.09)	(0.45)	(0.48)	(0.33)	(0.27)

Table III.4: *Relative RMSE's of estimated metabolite amplitudes obtained by Monte Carlo simulation with 1000 noise realizations.*

"real" data. Unfortunately, in order to compute it, the true value of the parameters must be known.

One possibility is to perform measurements on samples with known metabolite concentrations (*in vitro* phantoms). Unfortunately, acquired signals suffer from combined effects of many factors: environment variability (ex. temperature, pH), acquisition process variability (*ie.* type of sequence used, B_0 drift, etc), sample repeatability (*ie.* evolution of concentrations in time). Thus in order to study the quality of a phantom quantitation, one should take into account all the acquisition chain parameters, making for quite a bulky model.

Another possibility is to simulate data that bear the statistical properties of measured signal. Although this approach is intrinsically biased because it uses one model A to check the quality of a model B (A and B can be the same model), it provides valuable insight into the performances of the B estimator, by showing the cases when even in perfect conditions the estimator fails.

In this work, we have chosen to simulate data because, when performing the ECD algorithm with various λ hyper-parameter values, it can be clearly seen that the average of the concentration estimates depend on λ. This means that λ has a direct (but unknown) effect on the bias (as well as on the variance, but this is much easier to assess, even when the true values are not available).

III.5.2 QUEST-ECD using HSVD modelling

A first Monte Carlo study has been performed on a synthetic signal consisting of three metabolites, two of which severely overlap (*cf.* FigIV.3 on p.121). One thousand noisy signal realizations have been quantified, using (1) a Lorentzian basis-set as well as (2) the ECD algorithm with filtering by HSVD. Four different HSVD set-ups have been tested. Results (*cf.* Table III.4) show that QUEST-ECD with HSVD filtering reduces errors for two of the metabolites. Moreover, bias is significantly reduced, by all the HSVD set-ups.

The complete description of the study, including detailed results and discussions is given in [132], included in this thesis in the Additional Material.

III.5.3 QUEST-ECD using LOWESS filtering

A noise-free signal has been simulated using an NMR-SCOPE generated metabolite basis-set at 9.4T composed of Glutamate, Glutamine and Creatine with concentrations found in

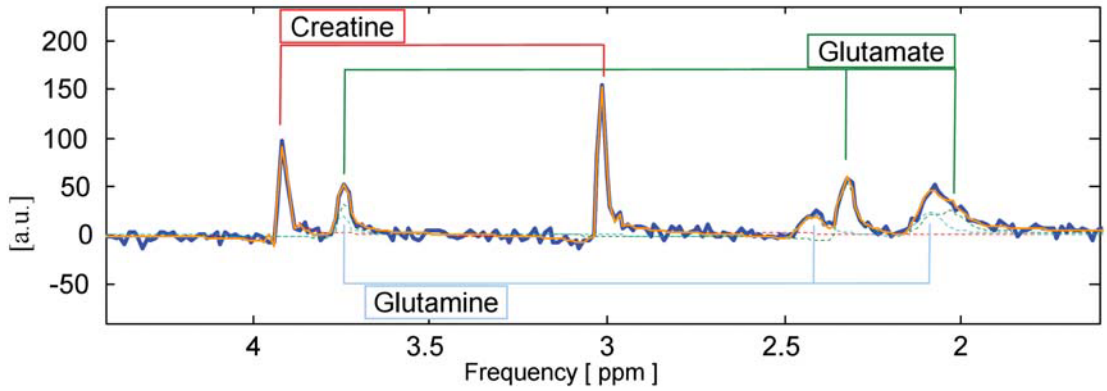

Figure III.9: *9.4 T spectra used for the Monte Carlo study. Blue: Noisy spectrum ($\sigma = 5$). Orange: reconstructed spectrum using estimated lineshape. Dotted fine lines: individual metabolite contributions. Note the distorted lineshape.*

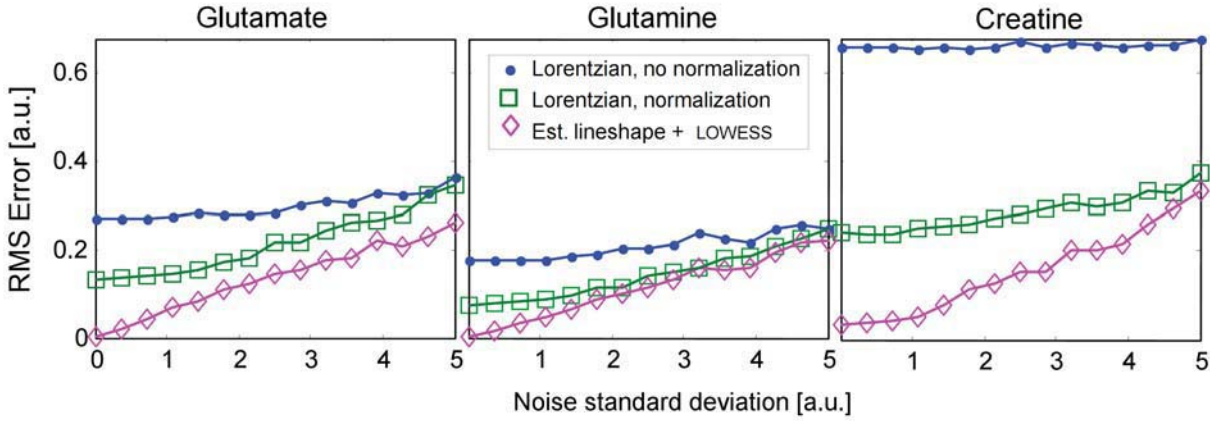

Figure III.10: *Root Mean Square Error for the three metabolites (Glu,Gln and Cr), (250 noise realisations per noise standard deviation) and with a LOWESS smoothing parameter $\lambda = 0.2$. Blue dots represent raw QUEST estimation (Lorentzian lineshape), green boxes represent normalized QUEST estimation and the magenta diamonds represent estimations with the LOWESS processed estimated decay function*

healthy human brain tissue. An asymmetric lineshape including eddy current effects has been applied. Monte Carlo simulations have been performed by adding 250 noise realizations to the noise-free signal for 15 different values of the noise standard deviation σ (Fig.III.9). The data have been fitted using a MATLAB implementation of QUEST [156] enabling a semi-parametric estimation of the lineshape, further processed using LOWESS. The latter is applied to the basis-set and a second fitting with QUEST is performed. The quantitation results have been normalized such that the first estimated data-point fits correctly the corresponding raw data point. This has been done in order to better estimate the advantages of the proposed method compared to using a pure Lorentzian lineshape, in the case of estimation of metabolite amplitudes.

Results (see Fig.III.10) show that the processing of the estimated decay function using LOWESS reduces the bias, which results in an overall better estimation of the metabolite concentrations. As SNR deteriorates, the performances of the three approaches tested converge, showing that the best results with QUEST-ECD can be obtained for very high SNR.

III.6 Applications of QUEST-ECD on acquired MRS data

In this section real data is quantified using the previously proposed QUEST-ECD algorithm, with LOWESS ECD filtering. In order to gain additional knowledge on the possible pitfalls of quantitation (*ie.* the impossibility to truly estimate bias), Monte Carlo techniques are used to assess the estimator performances.

III.6.1 Data Description

Clinical data has been acquired by Bagory et al. [6] at CERMEP [11] during a 3 year time span, in the context of clinical research on multiple sclerosis. In order to validate measurement coherence during such a long period of time, phantom signals, as well as water signals have also been acquired. The phantom used is a sphere containing a stabilized solution of Water (W), Choline (Cho), Creatine (Cr), myo-Inositol (mI) and N-acetylaspartate (NAA), with concentrations as follows

Cho	2 mmol
Cr	8 mmol
mI	8 mmol
NAA	8 mmol

Measurements have been made on a Siemens Magnetom Sonata Maestro Class system at 1.5 T, using a 8-channel head antenna in emission and a birdcage body antenna in reception. The size of the Volume of Interest (VOI) is of 50x50x50mm. Measurements are made using two PRESS sequences, at two different echo times TE = 30ms and TE = 135ms. Water suppression is also active. For some of the signals (69 out of 122) the non-water-suppressed version is also available (see Fig.III.11 for examples of acquired spectra).

11. Centre d'Etude et de Recherche Multimodale et Pluridisciplinaire en Imagerie du vivant CERMEP - Imagerie du vivant, Bron, France

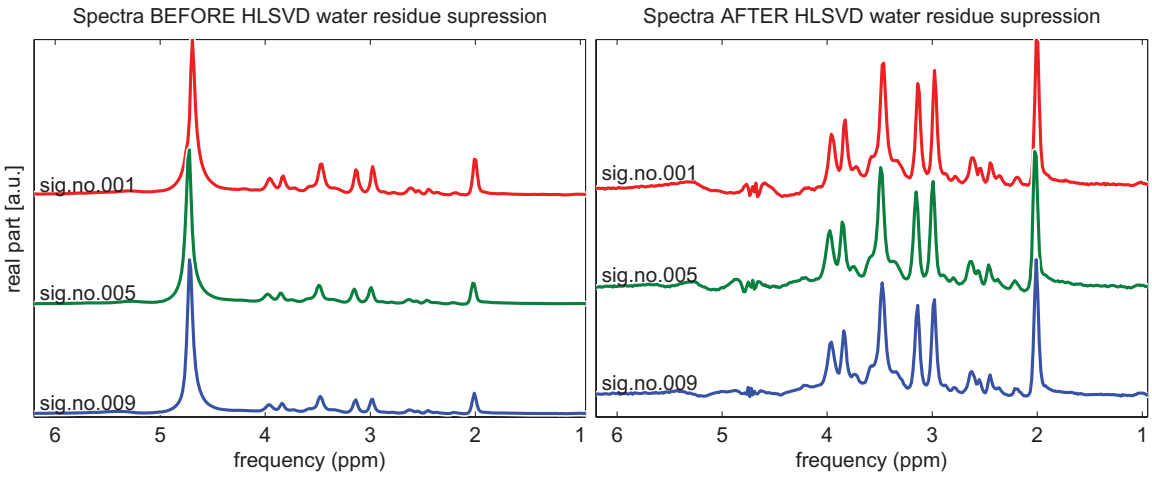

Figure III.11: *Spectra from the 69-signal data. The real part is plotted against the frequency in ppm. The left spectra show the data prior to water suppression and the right spectra after the HSLVD procedure (performed in jMRUI v4.0b)*

III.6.2 Basis-set

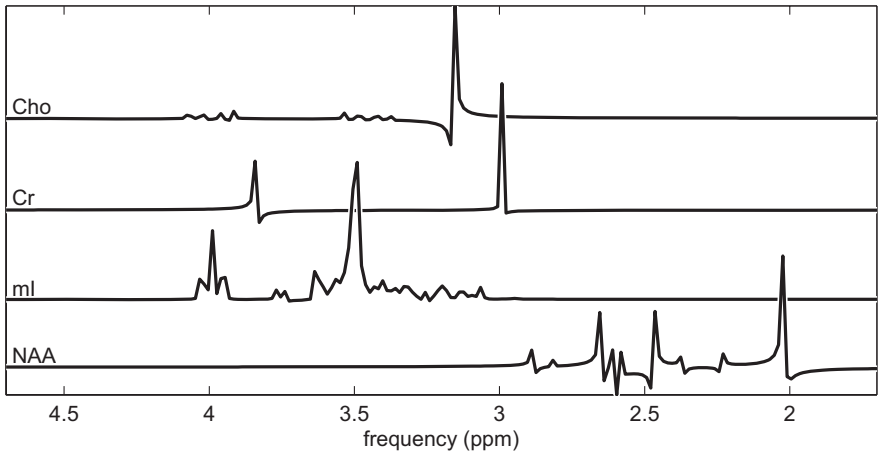

Figure III.12: *Real part of the basis set used for data generation and quantitation. The 4 metabolites are, in descending order, Cho, Cr, mI, NAA. The basis-set has been simulated with NMR-SCOPE. Some components close to the water peak have been omitted because of water suppression distortion. The spectra have been multiplied by scalars to optimize viewing range. Due to very small damping, spectra appear to be dephased, but it is only an artifact linked to the DFT sampling. Spectra are slightly frequency-shifted mimicking phantom acquired signal shifts.*

In order to use QUEST, a metabolite basis-set must be acquired or simulated. In this case the latter variant has been chosen. Spectra (*cf.* Fig.III.12) have been simulated using the NMR-SCOPE module in jMRUI v4.0b. Relevant spin parameters have been initially taken as reported by Govindaraju et al. [67] and subsequently refined (in the research group) by Rabeson [149]. The same HSLVD filter used for water residue removal has been applied on the metabolite basis-set.

The ECD algorithm uses a basis-set with a very small damping factor. This basis-set

has been simulated using a damping of 0.4 Hz. Due to this small damping factor, and to the finite nature of the time domain signal, artefacts appear in the visualization of the basis-set, that make the spectra look dephased. These artefacts are generated by the underlying sinc function associated with the limited acquisition time, and affect only frequency-domain visualizations (and possibly frequency-domain algorithms). Zero-padding the spectra would eliminate the distortion and show the underlying sinc convolution.

III.6.3 Estimation using conventional QUEST

In a first approach, the data acquired at TE=30ms have been quantified using the conventional QUEST method. Two implementations have been used and compared: the jMRUI4 package [175], as well as a customized MATLAB version. The difference between the two results, although non null, was not deemed significant and thus a choice has been made to present only results obtained using the Matlab version of the algorithm. It should be noted that further on, when using QUEST-ECD, only the MATLAB implementation is being used. For an example of quantified spectra, see Fig.III.14.

Out of the 69 signals, one exhibited spurious quantitation convergence, and has been discarded. The algorithm could have been finely tuned to allow improved convergence for that signal (the 47^{th}) as well, but for the purpose of this study it has been chosen to discard it and to do statistics on the rest of the dataset.

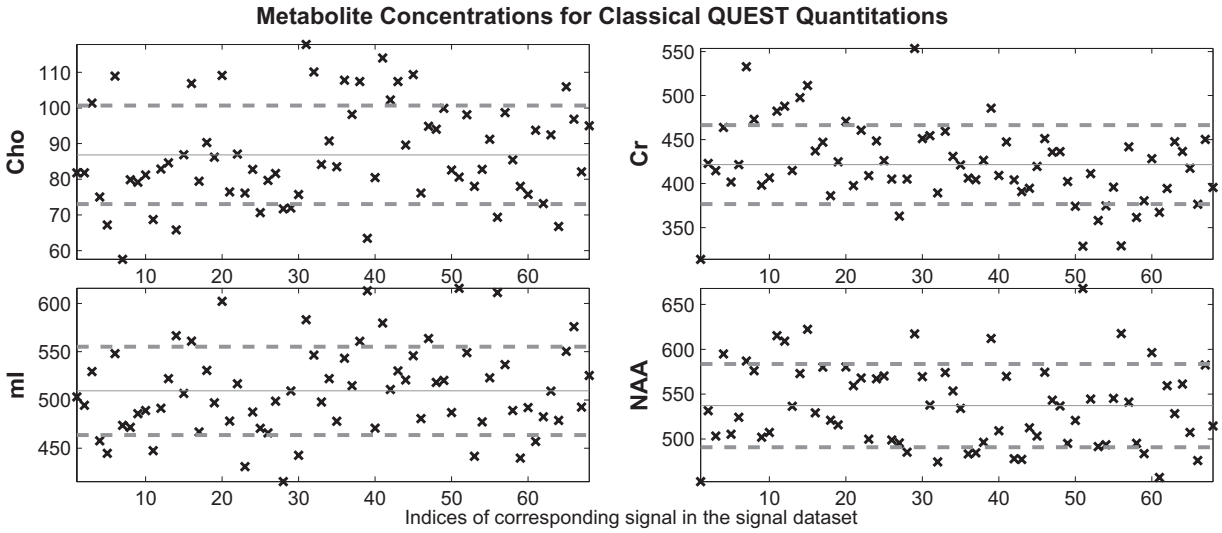

Figure III.13: *Blue crosses represent the distribution for the concentration estimation using a classical QUEST with Lorentzian lineshape correction. The mean (full line) and the errors bars corresponding to one standard deviation (dashed lines) are shown in gray. The x axis represent the signal index, from 1 to 68.*

The amplitude estimates are shown in Fig.III.13, with their means and standard deviations having the following values:

Metabolite	Mean [a.u.]	Standard deviation [a.u.]	True value [mmol]
Cho.	86.9	13.8	2
Ch.	421.6	44.8	8
mI.	509.4	45.7	8
NAA	537.7	45.5	8

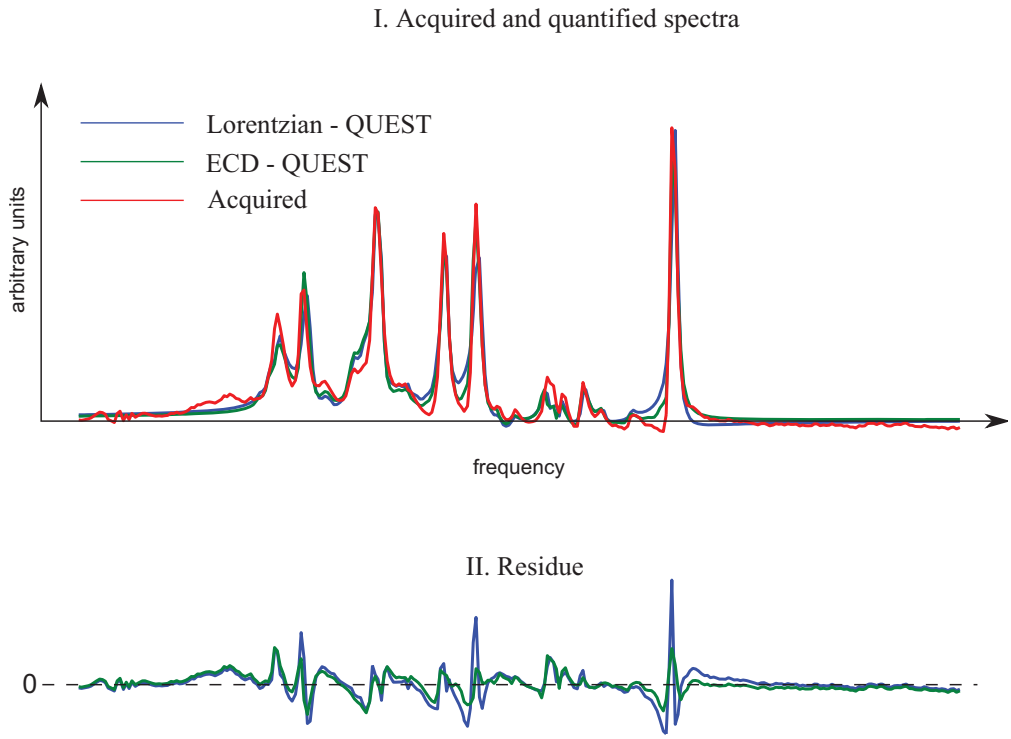

Figure III.14: *Example of quantitation of in vitro acquisitions (red line) using QUEST (blue line) and ECD-QUEST (green line). Plot (II) shows the residues, using the same colors. Notice how residues due to incorrect lineshape model are reduced when using ECD-QUEST.*

Normalization issues

Metabolite amplitude estimates are measured in arbitrary units, whereas the reference concentrations are in mmol. An unknown proportionality constant κ, technically specific to each acquisition, links the metabolite amplitudes and the corresponding mean concentrations:

$$c_m^{[\text{in mmol}]} = \kappa c_m^{[\text{in a.u.}]} \tag{III.23}$$

When performing statistical studies on the metabolite quantitation results, it is desirable to eliminate the influence of the proportionality constant κ_n, specific [12] to each acquisition n. To illustrate the importance of the variance of κ, consider the case when the actual metabolite concentrations have exactly the same values, but due to different factors κ is different for each acquisition. Measuring the variance of the amplitude estimates, supposing that the quantitation itself is ideal, comes to measuring the variance of the proportionality constant κ. The influence of the proportionality constant is typically circumvented in MRS by the use of metabolite concentration ratios, while another possibility is the use of absolute quantitation methodologies.

In order to mitigate the influence of the proportionality factor κ, three approaches have been considered:

1. **No scaling**. In this case no attempt has been made to scale the concentrations.

12. For acquisitions that are performed in the same conditions and in a short lapse of time, it is expected to have the same proportionality constant κ. However, in this case, data have been acquired over a long period of time, on different patients. We can therefore assume the variations in κ significant.

2. **Water scaling**. In this case the concentrations have been normalized with respect to the acquired non-water-suppressed signal. The two signals are independently acquired.

3. **Sum scaling**. In this case the amplitude estimates for each metabolite have been normalized such that the sum of the amplitudes always yields the same amount.

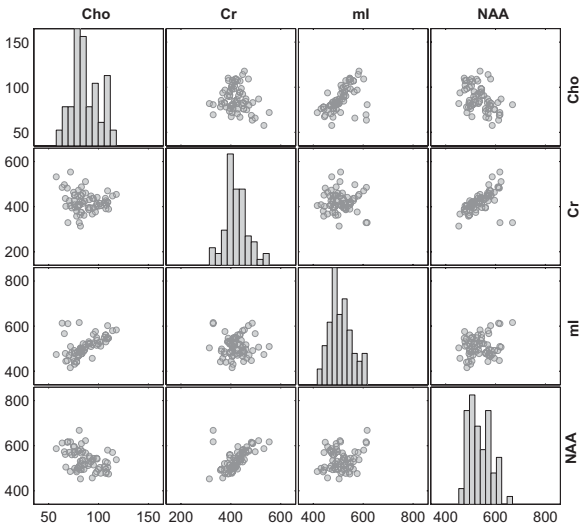

A. Unscaled amplitude estimations

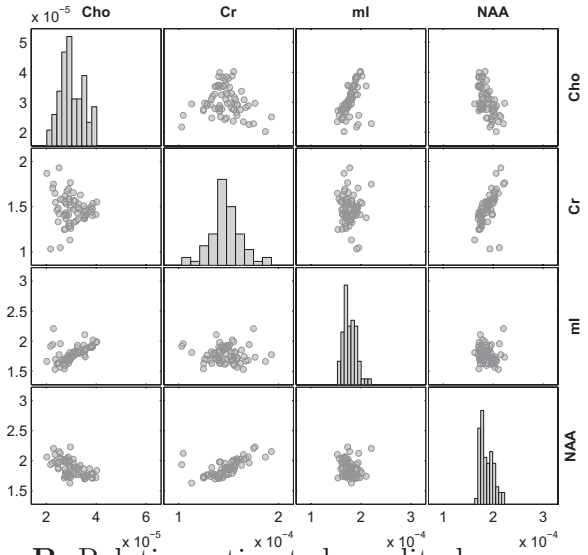

B. Relative estimated amplitudes with respect to water

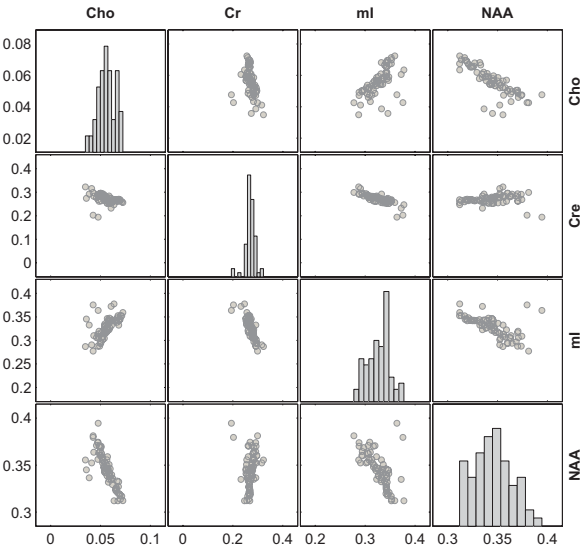

C. Relative estimated amplitudes with respect to the sum of metabolite amplitude estimates

Figure III.15: *Correlation of amplitude estimates using QUEST (lineshape correction using an additional Lorentzian decay term).* ***A:*** *Unscaled amplitude estimates.* ***B:*** *Relative estimated amplitudes, with respect to the water signal.* ***C:*** *Relative estimated amplitudes, with respect to the sum of estimated amplitudes. Diagonal plots represent the histograms for each metabolite concentration estimate. In non diagonal plots each point represents a signal, as a pair of metabolite amplitude estimates. Please be aware that scales are different between metabolites - data have been plotted so as to optimize the viewing range.*

Figure III.15 presents the comparative results of the three methods of scaling in the form of a multiple correlation plot. The diagonal plots represent the histogram of the distribution of the estimated metabolite amplitudes. On all the other graphics, each point represents a quantitation result, represented as a pair of amplitude estimates. Ideally, if quantitation of all signals would render the same results, the plots would consist of precisely overlapping

points. Because of several factors [13], however, points are scattered.

More, if the series defined by two metabolite amplitude estimates are correlated, this tendency would clearly show up in these graphs. If such is the case, it means than, statistically, estimation errors on the amplitudes of the two metabolites are bounded together, hinting at some bias [14]. The graphs should be interpreted in the following way:

- If the scatter plot resembles a line with a slope that is not horizontal or vertical, the errors are correlated and there might be important bias.
- If the scatter plot resembles a horizontal or vertical line, results show a relative difference in variability between the estimated concentrations for two metabolites. From a error correlation point of view, it means that errors are not correlated, the scatter-plot being similar to a 2D independent normal distribution.
- Outliers should be investigated as they show that one (or more) signals has been quantified in a significantly different manner as the others. Possible reasons are different proportionality constant κ or quantitation convergence issues.

Results (*cf.* Fig.III.15a) show that the unscaled amplitudes (as estimated by the QUEST algorithm implemented in MATLAB) tend to have a good error correlation, excepting perhaps the Cr-NAA and Cho-mI pairs, that seems to be slightly linearly correlated with a positive slope [15]. Scaling by the amplitude of the unsuppressed water signal seems to slightly improve this correlation, while making apparent some correlation between NAA and Cho. On the other hand, scaling using the sum of metabolite amplitude estimates deteriorates significantly the independence of amplitude estimations. While this is normal to a certain extent because we have blocked the sum of the metabolite relative amplitudes at 1, the important amount of correlation may suggest that this method may not be optimal in this case.

III.6.4 ECD-LOWESS QUEST estimation

In order to take into account the effect of the lineshape, a series of QUEST-ECD quantitation has been applied. The effect of the lineshape smoothness parameter λ is very important, as it can be seen from the evolution of concentration estimation in function of λ

If the true value of the concentrations would be known, then it would be possible to compute error RMS and thus find the best possible λ. Unfortunately there are several reasons why, although the true concentrations in the test tube are known, true values expected cannot be exactly:

- **The proportionality constant** κ is an unknown [16] factor that links the signals (in arbitrary units) to the concentrations (in mmol) . Because of this factor, in real cases only relative concentrations can be estimated (*ie* ratios between two metabolites). In order to obtain absolute concentrations an internal reference can be used. In our case we have used the non-water-suppressed signal.

13. Most important factors include acquisition noise, time variability of the metabolite concentrations in the phantom, changing conditions between acquisitions.

14. The link between the proportionality constant κ and the estimation bias is given by $\mathrm{BIAS}(c) = c_{\text{true}}^{[\text{in mmol}]} - c_{\text{estimated}}^{[\text{in mmol}]} = c_{\text{true}}^{[\text{in mmol}]} - \kappa c_{\text{estimated}}^{[\text{in a.u.}]}$.

15. The correlation slope is defined as the slope between the regression line representing the data and the x axis. Positive correlation between metabolites A and B suggests that when metabolite A is over-estimated, so is metabolite B.

16. The proportionality constant can be estimated in the case of "absolute" quantitation.

– **Water suppression** during acquisition eliminates water in a given frequency band, allowing to obtain readable metabolite quantities. Unfortunately, the scale difference between water and the other metabolites makes that the water suppression residue is comparable, if not stronger then the other metabolite contributions. It is therefore customary to apply a second water removal procedure, by mathematical preprocessing of the acquired data. However, the frequency suppression range function is not a perfect gate function, having an important transition zone between the passband and the stopband. If metabolite peaks are present in this zone (and they are) their spectra will be non-linearly affected by the water suppression. One of the possible solutions is to ignore peaks that are too close to the water peak. Another solution would be to find a way to predict the effect of water suppression and apply it to the metabolites. In this study we have chosen the latter.

III.6.5 Monte Carlo study

Previous results show that mean amplitude estimates depend on the value of the smoothing hyper-parameter λ. In order to assess the possible bias produced by quantitation, as well as choose an appropriate value for λ, a Monte Carlo study is performed.

III.6.5.1 Methodology

To keep simulations as close to the real acquisition as possible, we have chosen to use "true values" estimated from acquired data. In order to obtain the simulation data, the following steps have been taken

1. **Signal Lineshape** has been extracted from the non-water-suppressed signal. The first points present artifacts due to the digital filter on the scanner, but they have not been corrected. Alternatively, a slightly LOWESS filtered lineshape was used. Please note that the water signal has been used to produce a lineshape mimicking acquisition conditions. It is used *only* for generating the signals, and not for consequent quantitation, where the ECD-QUEST is employed.
2. **The basis-set** is constructed using an undamped simulated basis-set and the previously estimated lineshape.
3. **"True" parameter values** are obtained by performing QUEST on the acquired signal using the previously computed basis-set.

The following parameters are thus considered "true" in the subsequent Monte Carlo study:

no.	metabolite	c $[a.u.]$	$\triangle\alpha$ $[s^{-1}]$	$\triangle f$ $[s^{-1}]$	$\triangle\varphi$ $[deg]$
1	Cho	108.541	-0.0723	-4.810	+13.27
2	Cr	438.134	-2.8700	+1.010	+05.58
3	mI	581.865	+0.0000	-9.710	+13.88
4	NAA	510.808	-0.0312	-0.026	+08.11

Complex AWG Noise has been added with a standard deviation of $\sigma = 150$, larger than the actual noise level in the measured signal.

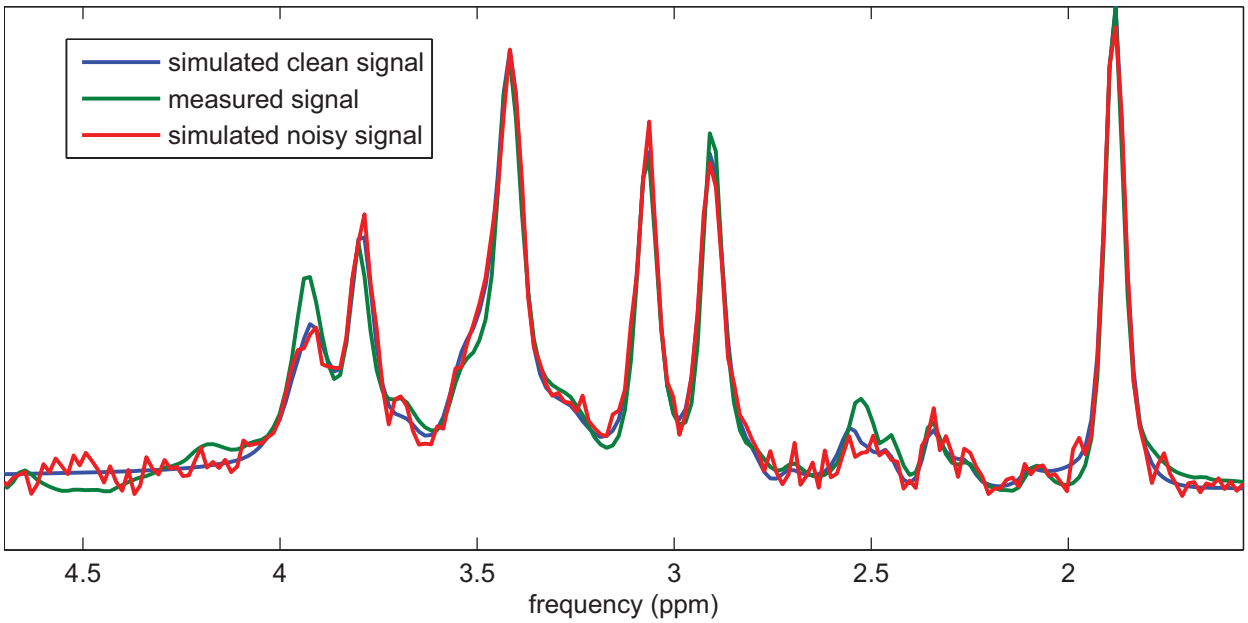

Figure III.16: *Blue: The simulated "clean" spectra used for the Monte Carlo study. Red: Spectra including one noise realization. Green: The acquired corresponding signal. Only the real part of the spectra is plotted. For more details on the acquired signal, see §III.6.1*

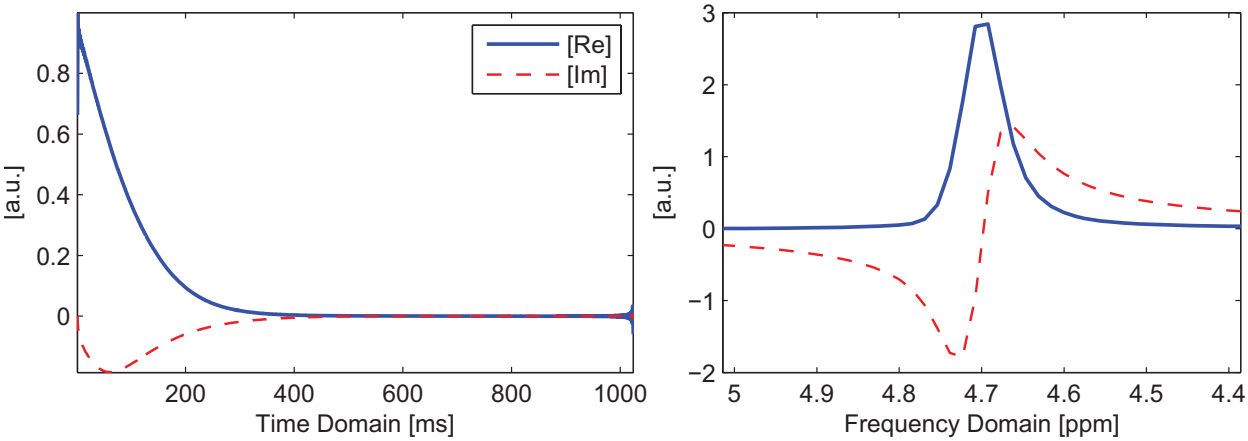

Figure III.17: *Lineshape signal used for simulations (Time and Frequency domains). This lineshape has been extracted from non-water-suppressed acquired signal associated with the metabolite acquired signals.*

In the original signal dispersion measurement of the real part of the signal between the index 400 and 924 yielded an estimated SD of 15.12 using Variance and 14.12 using Inter-Quantile Range (IQR). Thus it can be considered that the complex noise SD is $\sigma_{\text{Noise}}^{\text{measured}} = \sqrt{2}\times 14.5 \approx 20.5$. The same procedure gives a value of the simulated noise of $\sigma_{\text{Noise}}^{\text{simulated}} \approx 147.8$ for the first noise realization.

In order to evaluate the evolution of the quantitation as a function of the smoothing hyper-parameter λ, we have a non-uniform sampling of it. The reason behind this is that the LOWESS procedure is sensitive to small variations for small λ's but not so sensitive for greater values of λ. This is explained by the fact that the number of points taken into

account by the sliding window is roughly λN where N is the length of the signal.Thus the relative weight of a point inside LOWESS is inversely proportional to λ. In order to get a good view of the influence of λ one must plot tight points for small λ and can leave bigger spacing for greater λ.

Sixty (60) values have been chosen for λ, ranging from $\lambda_{\min} = 0.009775$ to $\lambda_{\max} = 0.4995$. The sampling chosen is as follows: linear for $\lambda < 0.255$ and then logarithmic for $\lambda > 0.255$. Please note that for the first value the LOWESS procedure does not actually modify the data, and that the ECD algorithm is thus equivalent to the (Lorentzian-)QUEST quantitation.

III.6.5.2 ECD quantitation results

The results of the ECD/LOWESS - QUEST quantitation are shown in Fig. III.18. Means for each parameter are plotted against λ to understand the general evolution of the quantitation. True value and Lorentzian model value are also plotted, for comparison. One should note the evolution of the extra damping $\triangle\alpha$ that evolves monotonically with λ. This is because as the lineshape is more and more filtered, it behaves more and more like an negatively-apodized signal (but without the effect of enhancing noise). To the extreme, if λ is equal to 1 the filtered signal would be a constant signal, thus having zero-decay (although otherwise-degenerated as well).

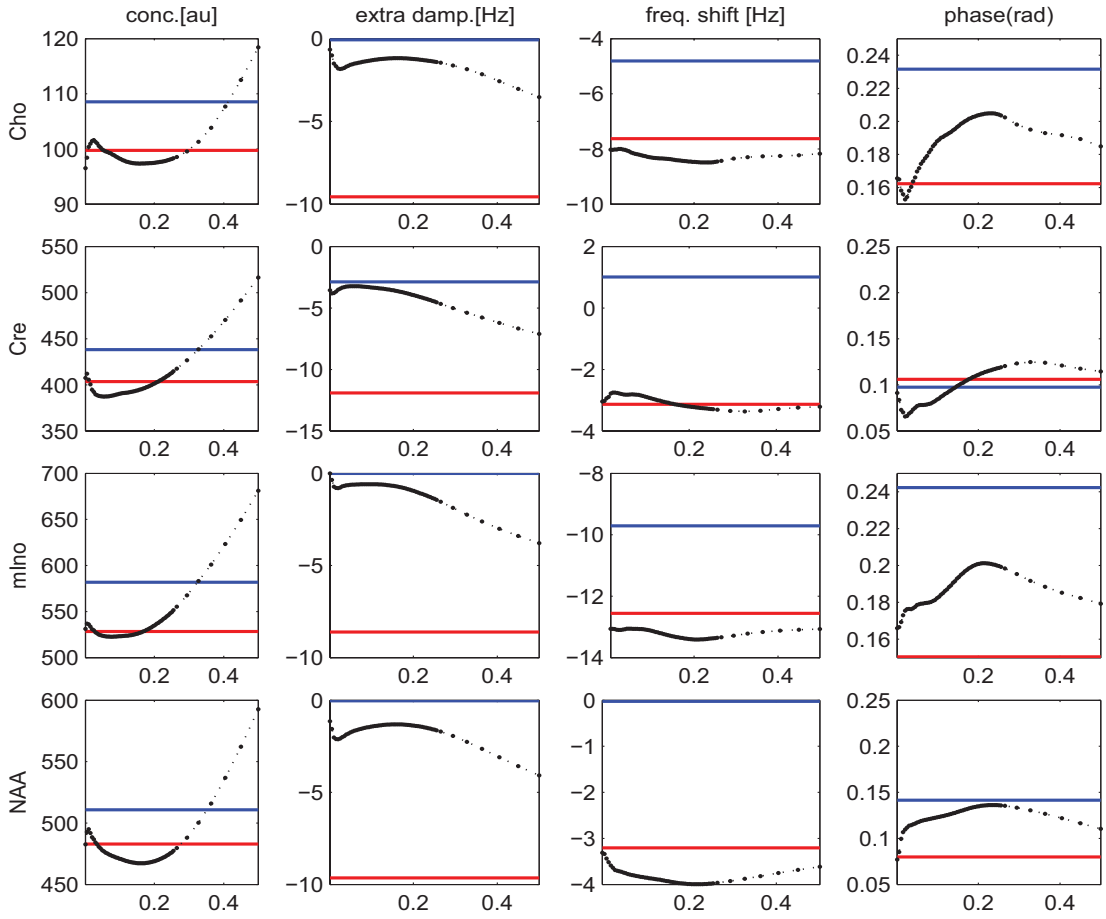

Figure III.18: *Black curve - Mean of ECD parameters $(c, \triangle\alpha, \triangle f, \triangle\varphi)$ against the smoothness hyperparameter λ. Red curve = Lorentzian equivalent. Blue curve = true values. λ sampling density is non-uniform, with more points for smaller λ.*

Also to be noted are the non-negligible differences between the values of the phase, frequency shift and extra damping . This is mainly because the "true" parameters have been considered without the influence of the lineshape, that includes itself and extra dephasing $\triangle\varphi_{\mathrm{LS}}$, extra damping $\triangle\alpha_{\mathrm{LS}}$ and extra frequency shift $\triangle f_{\mathrm{LS}}$.

III.6.5.3 Metabolite amplitudes

Figure III.19 shows the results of the ECD-QUEST algorithm. Concentration estimation error $c_i - c_i^{\mathrm{TRUE}}$ statistics are presented in function of the smoothing hyperparameter λ. The value corresponding to a classical Lorentzian QUEST are also plotted as a dashed red line.

First of all, it can be observed that the bias represents the majority of the total errors, for all metabolites. As it has been seen before this poses a significant problem in real cases, when bias cannot be estimated due to the unknown "true" value.

Secondly, each error curve has a similar form, but present minima at slightly different λ values. This poses a problem because it effectively means that there is a slightly different value of smoothness for which best quantitation is achieved. In order to get a more general view,the fifth row of Fig. III.19 shows the summed errors of all metabolites $RMS^2_{\mathrm{TOTAL}} = \sum_i RMS_i^2$.

The changes in Error RMS value can be summarized, for $\lambda = 0.32$, as follows:

Metabolite	RMS^2 (LOR)	RMS^2(ECD)	Relative change
Cho	1.50 E+2	0.62 E+2	-58 %
Cr	9.93 E+2	0.89 E+2	-91 %
mI	2.60 E+3	0.15 E+3	-94 %
NAA	8.31 E+2	2.04 E+2	-75 %
Sum	4.58 E+3	0.51 E+3	-89 %

III.6.5.4 Relative amplitudes (Concentration ratios)

In most current studies the lack of an efficient reference makes that ratio concentrations are computed. This eliminates any common factor that might bias concentration measurements, and thus might significantly change the error statistics. In order to test the ECD-QUEST performance in this scenario, relative amplitudes have been computed, taking as reference the best defined metabolite (NAA). The measured errors $(\frac{c_i}{c_{\mathrm{NAA}}} - \frac{c_i^{\mathrm{TRUE}}}{c_{\mathrm{NAA}^{\mathrm{TRUE}}}})$ are compiled in Fig. III.20 .

First of all results show that the bias-variance relationship, while still being dominated by bias, is more balanced that in the case of absolute concentrations. This reflects the fact than a part of the bias due to a common proportionality factor has been removed.

Another notable aspect is that the error statistics show minima at different values of λ for different metabolites. This reflects the different effect the lineshape can have on different metabolites and illustrates part of the difficulty in finding the optimal value of smoothness. The fourth row of Fig. III.20 shows the summed errors of all metabolites, thus providing a more general view of the problem. The changes in Error RMS value can be summarized, for $\lambda = 0.2$ as follows:

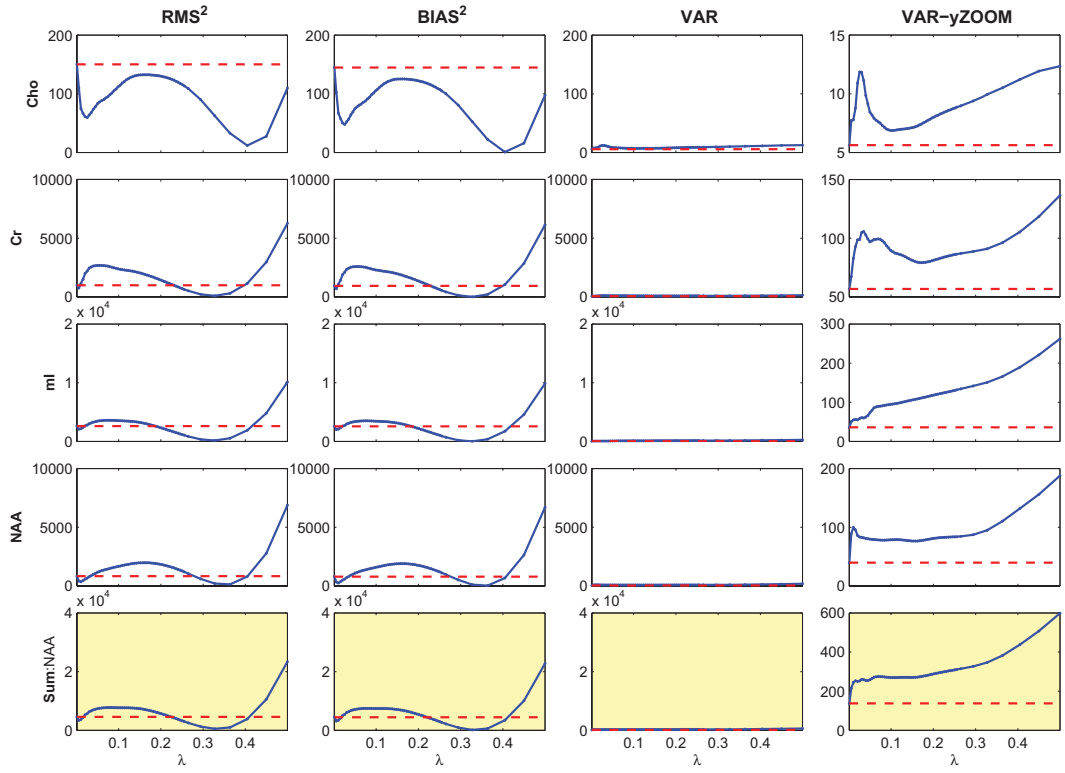

Figure III.19: *Error statistics (RMS^2, $BIAS^2$, VAR) in function of the smoothness hyper-parameter λ. Fourth plot represents the same data as the third plot (VAR), but it is scaled on the Y axis for better visibility. The red dotted curve represents the descriptor equivalent value for the Lorentzian model.*

Metabolite Ratio	RMS^2 (LOR)	RMS^2(ECD)	Relative change
Cho:NAA	1.83 E-4	0.53 E-5	-71 %
Cr :NAA	4.81 E-4	5.19 E-4	+08 %
mI :NAA	1.88 E-3	0.73 E-3	-61 %
Sum:NAA	2.54 E-3	1.30 E-3	-48 %

It is important to notice a significant decrease in Error RMS improvement from the results in Fig. III.19. This illustrates that the Lorentzian lineshape correction introduces a common bias, that is eliminated when using metabolite concentration ratios.

Conclusions

The comparison between different lineshape handling approaches has shown that it is of interest to adapt the basis-set to the acquired signal, and not vice-versa. Based on this approach, we have developed an algorithm that estimates the common decay function, and then uses it to adapt the metabolite basis-set signals.

However, testing the method directly on real data has the disadvantage of not being able to estimate the bias, seen from Monte Carlo studies to be the major source of the error. Because of this, several series of Monte Carlo, mimicking the acquired signals have been performed, and have shown significant bias reduction.

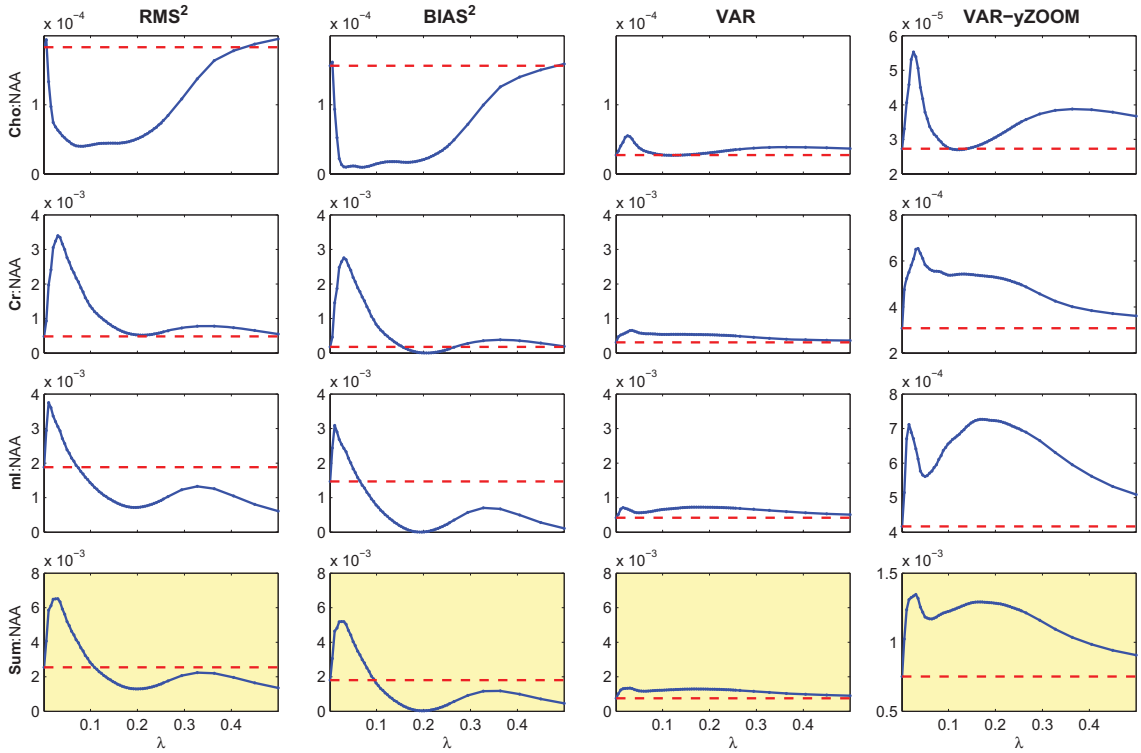

Figure III.20: *Error statistics (RMS^2, $BIAS^2$, VAR) in function of the smoothness hyperparameter λ for concentrations relative to the forth metabolite (NAA). Fourth column represents the same data as the third column (VAR), but it is scaled on the Y axis for better visibility. The red dotted curve represents the equivalent statistics value for the Lorentzian model.*

Finally, the performances of the QUEST-ECD estimator depend very much on the choice of the filtering method inside the ECD part. In the case of LOWESS filtering, a method to automatically optimize the λ hyper-parameter has been developed, and shown to produce significant bias reduction, for both metabolite amplitude ratios and "absolute" metabolite amplitudes.

Chapter IV

ECD Spectral Compactness

In this chapter, we propose another approach to metabolite quantitation, based on the underlying properties of the lineshape. In the previous chapter, the estimated common decay (ECD) function was filtered to eliminate spurious high frequency components. We now propose a method based on the same hypothesis of limited lineshape bandwidth, that allows, by itself or in combination with a more classical approach, the determination of the MRS parameters of interest, and in particular of metabolite concentration.

IV.1 Method concept

It has been shown in the previous chapter that, under the assumption that all metabolites share the same decay function, the "true" MRS signal $\check{s}(t)$, and the ensuing noisy acquired signal $s(t)$ can be written as

$$\begin{aligned} \check{s}(t) &= \check{d}(t) \sum_{m=1}^{M} \check{c}_m \; b_m(t) \; e^{j\check{\varphi}_m} \; e^{j\check{\omega}_m t} \\ s(t) &= \check{s}(t) + \varepsilon(t) \end{aligned} \tag{IV.1}$$

with $\check{d}$ the common decay function and $\check{\mathbf{p}} = (\check{c}_m, \check{\varphi}_m, \check{\omega}_m)_{m=1\ldots M}$ the concentrations, phases and frequency shifts and b_m the metabolite basis-set. In the following sections, the caron symbol $\check{}$ denotes the true, unknown values that need to be estimated, while the hat symbol $\hat{}$ denotes the estimated values. The term inside the sum in Eq.IV.1 has been defined as the undamped signal model:

$$\check{s}_{\text{undamped}}(t) = \sum_{m=1}^{M} \check{c}_m b_m(t) e^{j\check{\varphi}_m} e^{j\check{\omega}_m t} \tag{IV.2}$$

Furthermore, should the parameter values $\check{\mathbf{p}}$ be estimated by the set $\hat{\mathbf{p}}$, then the lineshape can be estimated via equation IV.3:

$$\hat{d}(t) = \check{d}(t) \; \frac{\sum_{m=1}^{M} \check{c}_m b_m(t) \; e^{j\check{\varphi}_m} e^{j\check{\omega}_m t}}{\sum_{m=1}^{M} \hat{c}_m b_m(t) \; e^{j\hat{\varphi}_m} e^{j\hat{\omega}_m t}} + \varepsilon'(t) \tag{IV.3}$$

where $\varepsilon'(t) = \varepsilon(t)[\sum_{m=1}^{M} \hat{c}_m \cdot s_m(t) \cdot e^{j\hat{\varphi}_m} \cdot e^{j\hat{\omega}_m t}]^{-1}$ is the ratio between AWG Noise and the undamped estimated signal. This term is stochastic in nature, and it will be considered for now to be generated by an unknown statistical model.

For later simplicity the noise term is ignored in a first approach, and will be accounted for later. Since the order of metabolites is not essential, a change of notation is performed so that one metabolite may be considered as reference. The generality of the problem is not changed by this, since any metabolite may be chosen. The reference metabolite is denoted by the zero index, with the other metabolite indices ranging from 1 to $M-1$.

$$\hat{d}(t) = \check{d}(t)\ \frac{\sum_{m=0}^{M-1} \check{c}_m b_m(t)\ e^{\imath\check{\varphi}_m} e^{\imath\check{\omega}_m t}}{\sum_{m=0}^{M-1} \hat{c}_m b_m(t)\ e^{\imath\hat{\varphi}_m} e^{\imath\hat{\omega}_m t}}$$

$$\hat{d}(t) = \check{d}(t)\frac{\check{c}_0 b_0(t)\ e^{\imath\check{\varphi}_0} e^{\imath\check{\omega}_0 t} + \sum_{m=1}^{M-1} \check{c}_m b_m(t)\ e^{\imath\check{\varphi}_m} \cdot e^{\imath\check{\omega}_m t}}{\hat{c}_0 b_0(t)\ e^{\imath\hat{\varphi}_0} e^{j\hat{\omega}_0 t} + \sum_{m=1}^{M-1} \hat{c}_m b_m(t)\ e^{\imath\hat{\varphi}} e^{j\hat{\omega}_m t}} \tag{IV.4}$$

$$\hat{d}(t) = \underbrace{\check{d}(t)}_{(a)}\ \underbrace{\frac{\check{c}_0 e^{\imath\check{\varphi}_0} e^{\imath\check{\omega}_0 t}}{\hat{c}_0 e^{\imath\hat{\varphi}_0} e^{\imath\hat{\omega}_0 t}}}_{(b)}\ \underbrace{\frac{b_0(t) + \sum_{m=1}^{M-1} \check{c}_m^{\mathrm{rel}} b_m(t)\ e^{\imath\check{\varphi}_m^{\mathrm{rel}}} e^{\imath\check{\omega}_m^{\mathrm{rel}} t}}{b_0(t) + \sum_{m=1}^{M-1} \hat{c}_m^{\mathrm{rel}} b_m(t)\ e^{\imath\hat{\varphi}_m^{\mathrm{rel}}} e^{\imath\hat{\omega}_m^{\mathrm{rel}} t}}}_{(c)} \tag{IV.5}$$

with the superscript 'rel' denoting relative values with respect to the corresponding values of metabolite m_0: $c_m^{\mathrm{rel}} = \frac{c_m}{c_0}$, $\omega_m^{\mathrm{rel}} = \omega_m - \omega_0$ and $\varphi_m^{\mathrm{rel}} = \varphi_m - \varphi_0$.

Eq.IV.5 shows the dependence for the estimated lineshape on the true and estimated model parameters. The form chosen to represent the equation makes three terms apparent:

(a) The true decay function. The corresponding function in the Fourier Domain is the lineshape.

(b) A shift term that depends only on the choice of the reference metabolite m_0. When performing the FT on this term, the result is a Dirac function, whose frequency position is determined by the frequency error on the reference metabolite.

(c) A more complicated term taking into account the interaction between the metabolites. It is shown later that the FT of this signal has a complicated structure, but its effective bandwidth can be linked to the error $\check{\mathbf{p}} - \hat{\mathbf{p}}$

Figure IV.1 illustrates an example of how the spectral effective compactness of the ECD is influenced by the values $\hat{\mathbf{p}}$ in the undamped model function. Column (I) plots show the case when the correct values are shown, while column (II) shows results for sub-optimal values of $\hat{\mathbf{p}}$. Notice the frequency peaks that appear in (II) around $\nu \approx \pm 0.35$. Also notice the effect in the time domain, where oscillations appear in the ECD (II.a); this effect is used for a later alternative approach to the frequency domain spectral compactness in §IV.3.

IV.1.1 Ratio of two exponentially damped sinusoids

In order to get a better understanding of the link between the term IV.5(c) and the principle of the method proposed, a simple case is now studied more in detail.

Consider the simple model built using two fictitious metabolites, each having a basis-set consisting of only one peak. Moreover, one metabolite (m_0) has its peak at the reference frequency, so that $\omega_0 = 0$, and all its other parameters are known ($\hat{c}_0 = \check{c}_0 = 1, \hat{\omega}_0 = \check{\omega}_0 = 0, \hat{\varphi}_0 = \check{\varphi}_0 = 0$). The common lineshape is of pure Lorentzian nature, with a decay time constant of α^{-1}.

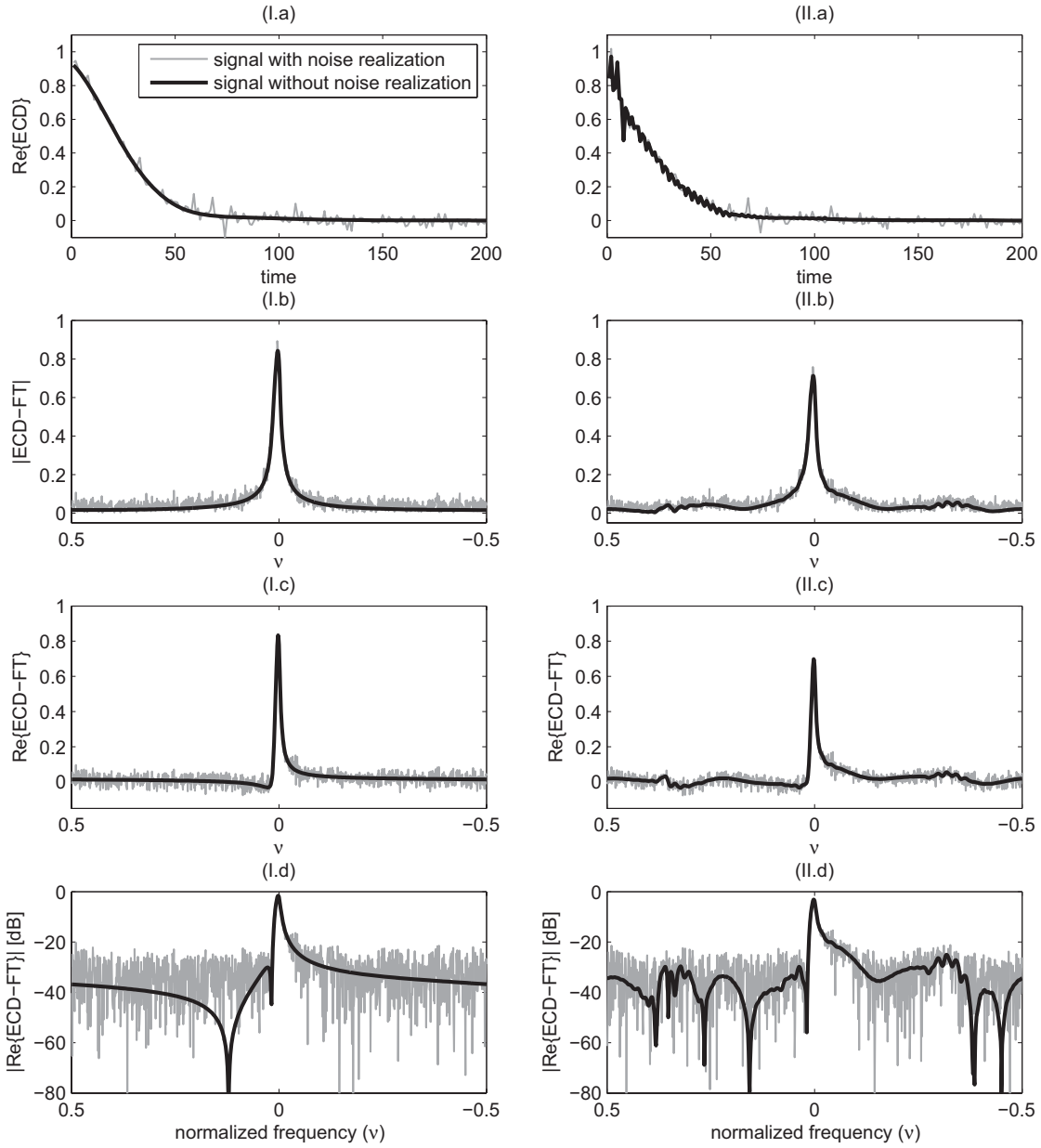

Figure IV.1: *Estimated Common Decay (ECD) functions, represented in the time domain (a), and in the frequency domain (b-d). Time domain representation has been cropped at 200 points for better visualization. Left plots (I), represent the case when the parameters* $\hat{\mathbf{p}}$ *all have the true values, as indicated in Table IV.1 (p.119). Right columns represent the ECD when two parameters have the wrong values :* $\hat{c}_1 = 0.6$ *,* $\hat{c}_3 = 2.5$*. For each plot, the gray fine line represents a signal realization with noise, whereas the thick black line represents the estimation in the case that no noise is present. It should be noted that the latter is not normally available in practice, but has been included here to illustrate how effective spectral compact support is altered when using inappropriate parameter values. When the parameters are not the correct ones, undulations appear in the spectrum, increasing the Out-of-Band components, as well as the effective spectral compact support. This is clearly seen when observing the spectra in dB (d), instead of a linear scale.*

Injection of this model into Eqs.IV.1-IV.5 gives the following signals:

$$\check{s}(t) = \check{d}(t)[1 + \check{c}_1 \exp(\imath\check{\varphi}_1 + \imath\check{\omega}_1 t)] \qquad \text{(noiseless signal)}$$

$$\hat{d}(t) = \check{d}(t) \underbrace{\frac{1 + \check{c}_1 \exp(\imath\check{\varphi}_1 + \imath\check{\omega}_1 t)}{1 + \hat{c}_1 \exp(\imath\hat{\varphi}_1 + \imath\hat{\omega}_1 t)}}_{(c)} \qquad \text{(ECD function)}$$

The aim of the method is to estimate the parameters corresponding to metabolite m_1 *without* direct determination of $\hat{d}(t)$. In order to achieve this, two facts can be observed concerning the ECD function:

- if the estimated parameters $\hat{\mathbf{p}}_1$ are equal to the true parameters $\check{\mathbf{p}}_1$, then the estimated common decay is equal to the true common decay, and therefore has all the properties of the (unknown) function $\check{d}$.
- although the true common decay function is unknown, it can be assumed to have certain properties. One of the most important in this case is that in experimental conditions it is expected that the static field inhomogeneities $\triangle B_0$ be distributed with a reasonably narrow distribution , leading to a lineshape with an important modal component and small tails.

Combining the previously stated remarks yields that when the estimated parameters are equal to the true parameters, then the estimated common decay (ECD) FT should have a narrow peak with small tails. Furthermore, it can be shown that when $\hat{\mathbf{p}} \neq \check{\mathbf{p}}$ the support of the ECD-FT necessarily grows.

In order to show this, consider that the true lineshape has a compact [1] support. According to Titchmarsh [182]'s theorem, the support span of the ECD-FT is equal to the support span of the true CD-FT plus the support span of the term (c) FT. Minimal FT support of (c) is achieved in the case of a Dirac distribution, leading to equality of $\hat{\mathbf{p}}$ and $\check{\mathbf{p}}$. Any other (c) term leads to a FT with larger support, thus increasing the support span of the ECD-FT as well.

The next step towards $\mathbf{p}$ estimation is defining a measure for the ECD bandwidth (the support of the ECD-FT). Without explicitly specifying this measure, consider that it is given by a function $\mathcal{C}$ so that $\|\mathcal{C}(\mathbf{d}(\mathbf{p}))\|$ is representative of the effective bandwidth of the signal $\mathbf{d}(\mathbf{p})$. Since it has been shown that $\|\mathcal{C}\|$ has a global minimum when $\mathbf{p}$ is equal to the true underlying values $\check{\mathbf{p}}$, the algorithm to compute an estimation $\hat{\mathbf{p}}$ is given by:

$$\texttt{Find } \hat{\mathbf{p}} = [\hat{c}_1, \hat{\varphi}_1, \hat{\omega}_1] \texttt{ that is the global minimum of } \|\mathcal{C}(\hat{d}(\mathbf{p}, t))\|\texttt{,}$$
$$\texttt{with } \hat{d}(\mathbf{p}, t) = s(t)[1 + c_1 \exp(\imath\varphi_1 + \imath\omega_1 t)]^{-1}$$

The measure $\|\mathcal{C}(\hat{\mathbf{d}})\|$ is referred to as the *cost function* associated with the optimization procedure. In order to distinguish between the classic least squares (LS) approach to quantitation, based on the minimization of the residue, and the novel approach proposed, we introduce the symbols $\mathfrak{C}_1$ and $\mathfrak{C}_2$ respectively. When speaking of $\mathfrak{C}_1$ the cost function is the $\mathcal{L}_2$ norm of the residue $\mathbf{s} - \hat{\mathbf{s}}$. When $\mathfrak{C}_2$ is mentioned, the cost function is derived from the

1. Two elements need to be specified when approximating the compact support of the true lineshape. First, strictly speaking, the lineshape has an infinite support, but its values decays quickly. It is considered that when the value of the decay function is smaller then an arbitrary constant (close to zero), the function is approximatively equal to zero, thus giving a compact support. Secondly, only a frequency span equal to the sampling frequency is considered, supposing that no aliasing takes place. Time truncation effects are also considered, for now, negligible.

principle of effective spectral compactness of the estimated common decay function. Slightly abusing the notation, we also refer henceforth to minimizing $\mathcal{C}$ instead of $\|\mathcal{C}\|$.

In the following sections, different implementations of $\mathfrak{C}_2$ are explored. Section IV.2 illustrates implementations based on a *spectral domain* approach. Section IV.3 discusses, among other possible improvements to the method, *a time-domain implementation* of $\mathfrak{C}_2$.

IV.2 $\mathfrak{C}_2$ implementation in Frequency Domain

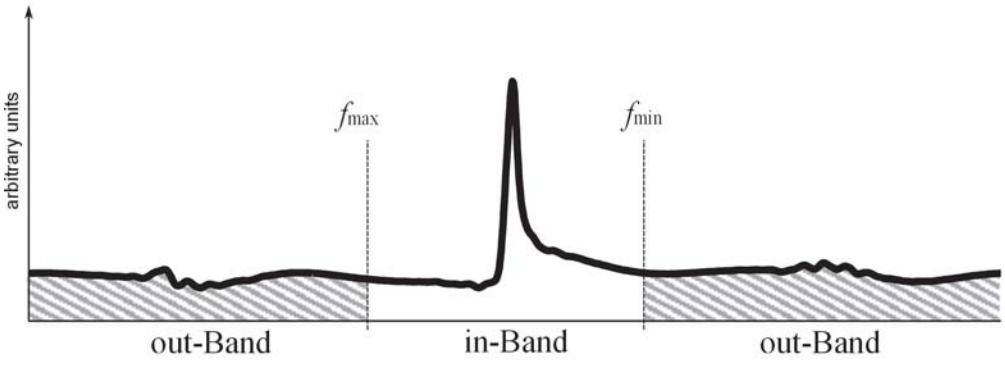

Figure IV.2: *Partitioning of the spectral domain in the in-Band sub-domain and the out-Band sub-domain. For the spectral implementation of $\mathfrak{C}_2$, the spectral components in the out-Band are minimized.*

Since the Fourier Transform of the ECD function is expected to be in a narrow frequency band, one possible criterion is to establish a partition of the frequency domain in two sub-domains, using two constant frequencies $f_{\min}$ and $f_{\max}$. The in-Band sub-domain is defined by all the frequencies that have values in $[f_{\min}, f_{\max}]$, while the rest of the frequencies constitute the out-Band sub-domain (oB),*cf.* Fig.IV.2. If the estimated parameters are correct, and if the in-Band limits have been chosen so that they enclose the support of the true common decay, then it is expected that no spectral components are present in the oB domain. Furthermore, the larger the effective bandwidth, the more components are expected to be present in the out-Band. This leads to the cost function $\mathcal{C}$ being proposed as the quantity of out-Band spectral components of the estimated common lineshape:

$$\mathcal{C}(\mathbf{p}) = \Re\{\hat{D}(f, \mathbf{p})\} \odot \sqcup(f, f_{\min}, f_{\max}) \tag{IV.6}$$

where $\hat{D}$ is the Fourier Transform of the estimated common decay function $\hat{d}$, $\odot$ is the point-wise multiplication and $\sqcup$ is the inverted square function, defined as

$$\sqcup(f, f_{\min}, f_{\max}) = \begin{cases} 0 & \text{if } f_{\max} \leq f \leq f_{\max} \\ 1 & \text{otherwise} \end{cases} \tag{IV.7}$$

Another formulation of the out-Band $\mathfrak{C}_2$cost function can be found in [133], for the special case when $-f_{\min} = f_{\max} \equiv f_{\text{treshold}}$, and implies the minimization of the ECD spectral components for all frequencies $|f| > f_{\text{treshhold}}$.

The same published work also gives an implementation of the method, including a pre-processing step before the actual computation. First of all the ECD function is truncated

at the integer index closest to $n_{\text{lim}} = t_{\text{decay}} t_s^{-1}$. The ECD is further zero-padded up to 1024 points, and the real part of its DFT is computed via FFT. Finally, the result is minimized in function of $\mathbf{p}$ via an additive term to the classical residue LS cost function $\mathfrak{C}_1$. A method to derive the Jacobian matrix associated to the new criterion is also proposed, with direct application in the case of a Newton-Raphson NLLS minimization procedure.

Nevertheless, several aspects of the published $\mathfrak{C}_z$implementation can still be improved. First the published version only takes into account the real part of the components in the out-Band, leading to possible influence of the phase factors. Secondly, the truncation/zero-padding introduces *sinus cardinalis* (sinc) interpolation that might unnecessarily enlarge the support of the actual DFT. Finally, although the implementation seems to require no input from the user, the hyper-parameters $f_{\max}$ and $f_{\max}$ setting the extent of the considered out-Band still have to be set. Prospective improvements on the published method are discussed in section §IV.3.

IV.2.1 Methodology

In order to assess the benefits of spectral compactness as *a priori* information, a Monte Carlo study has been performed, based on simulated signals with properties pertinent to the aim of the method (accommodation of unknown lineshape). This subsection describes in detail the validation methodology. Also see the published material [133] included in the Additional Material section at the end of this thesis.

IV.2.1.1 Metabolite model

The overall model generally used in MRS for quantifying M metabolites is usually written as (*cf.* §II.4 and Eq.III.2):

$$\hat{s}(t) = \exp(\imath\varphi_0) \sum_{m=1}^{M} c_m \hat{d}_m(t) \hat{s}_m(t) \exp[\imath(2\pi \triangle\nu_m t + \varphi_m)] \tag{IV.8}$$

in which the time is discretized at N points $t = t_0 + nt_s$ with $n = 0, 1, \ldots, N–1$ and t_0 the dead time of the receiver, that in this study has been fixed equal to zero. The sampling time has been fixed at $t_s = 1$, reducing the problem to the normalized frequency case $\nu = f/F_s = ft_s$. This does not reduce the generality of the problem, while simplifying notation. The overall phase φ_0 is also chosen for convenience at zero, as it could very well be integrated in the metabolite-specific phase φ_m. Three metabolites ($M = 3$) are simulated, and the different model parameters are set as follows:

- c_m is the quantity or concentration of metabolite m. In this study, their values are, in arbitrary units $c_1 = 0.5$, $c_2 = 2.0$ and $c_3 = 2.0$ a.u..
- φ_m is the phase of metabolite m, and has been put to zero in this study for all metabolites.
- $\hat{d}_m(t)$ is an analytical function that describes the decay function of each metabolite (*cf.* §II.1 and III.1), and usually of little importance to clinicians. The most common choices for analytical modelling are the Lorentzian and Gaussian functions, themselves special cases of the the Voigt function, defined as $d_{\text{Voigt}}(t) = \exp(\alpha_m t + \beta_m t^2)$ with $\alpha_m, \beta_m \in \mathbb{R}_-$ (*cf.* §II.5). Although at high resolution NMR each metabolite may have a different decay function, this study is meant in the previously described estimated

m	c_m	k	$a_{m,k}$	$\nu_{m,k}$	$\varphi_{m,k}$
1	(0.5)	1	0.50	0.150	0
		2	1.50	0.160	60
		3	1.50	0.170	120
		4	0.50	0.180	180
2	(1.0)	1	0.30	0.130	0
		2	0.60	0.150	30
		3	0.90	0.170	60
		4	1.20	0.190	90
3	(2.0)	1	1.00	-0.160	0

Table IV.1: *Model parameters used for signal simulation. $\nu_{m,k}$ is the normalized frequency, corresponding to $\nu_{m,k} = f_{m,k}/F_s$. Dephasing φ is shown in degrees. Values in parantheses (c_m) represent the concentration used in the overall signal, and are shown here for convenience.*

common decay hypothesis (*cf.* §), when the dominant contributor is the field inhomogeneity, and sometimes the eddy currents. Consequently, in the following paragraphs the subscript m of the decay function is dropped. The common decay function used in this study is described in full detail in §IV.2.1.2.

– $\hat{s}_m(t) = \sum_{k=1}^{K_m} a_{m,k} \exp[\imath(2\pi\nu_{m,k}t + \varphi_{m,k})]$ is the *a priori* known, non-decaying version of the model function of metabolite m, in which $a_{m,k}, \nu_{m,k}, \varphi_{m,k}$ are the relative amplitudes , frequencies and phases of individual spectral components of a metabolite model function. Table IV.1 summarizes the values used in the current work. There are nine spectral components, grouped into two quartets (m_1 and m_2) and a singlet (m_3). The two quartets overlap heavily. The frequencies 0.150 and 0.170 are common to the quartets, while the remaining two frequencies of m_1 are enclosed in the remaining frequencies of m_2. Moreover, phases are different for each peak, rendering complex the inter-peak interference.
An important aspect here is the fact that the *a priori* basis-set used has zero-decay. In practice, acquired signals are always decaying, and thus this method cannot be applied to *in vitro* basis-sets without further processing for decay minimization. However, when using basis-sets simulated via quantum mechanics approaches (*e.g.* NMR-SCOPE [69]), the decay can be set to arbitrary low values, thus providing (quasi-) non-decaying basis set signals.

– $\triangle\nu_m$ represent frequency shift corrections, that arise from the average effective B_z longitudinal magnetic field being applied. In this study no extra frequency shifts have been applied ($\triangle\nu_m = 0,\ \forall m$).

IV.2.1.2 Decay Model

In order to simulate the complexity of an acquired decay function, the decay model has been developed to include the intrinsic spin relaxation $\hat{d}_{\text{relaxation}}$, B_0 inhomogeneity effects and eddy current influence. The overall decay function is thus modelled in the time domain

as a product of three independent decay functions:

$$\hat{d}(t) = \mathcal{N} \cdot \hat{d}_{\text{patient}}(t) \cdot \hat{d}_{\text{eddy}}(t) \cdot \hat{d}_{\text{relaxation}}(t) \tag{IV.9}$$

where $\mathcal{N}$ is a normalization constant so that $|\hat{d}(t=0)| = 1$. Furthermore,

– $\hat{d}_{\text{patient}}$ is the decay due to the spatial distribution of the effective longitudinal magnetic field B_z. The main source of B_z inhomogeneity comes from the interface effect of tissues with different magnetic susceptibility, such as fat, bone, air, etc. (*e.g.* see [86]). In this study an asymmetric lineshape determined by the extrema ν_1 and ν_3 and with the centre at ν_2 has been chosen to model the inhomogeneity effect. The complete model is described by Eq.IV.10:

$$\hat{d}_{\text{patient}}(t) = \frac{1}{\pi(\nu_3 - \nu_1)} \left[\frac{\exp(2\pi\imath\nu_2 t) - \exp(2\pi\imath\nu_1 t)}{2\pi(\nu_2 - \nu_1)t} - \frac{\exp(2\pi\imath\nu_3 t) - \exp(2\pi\imath\nu_1 t)}{2\pi(\nu_3 - \nu_1)t} \right] \tag{IV.10}$$

with $\nu_1 = -0.001,\ \nu_2 = 0,\ \nu_3 = 0.015$.

– $\hat{d}_{\text{eddy}}$ is a complex valued decay function caused by eddy currents induced in the walls of the superconductor magnet mainly by the switching of the gradient fields. The effect shows up as a harmonic amplitude modulated component that adds up to B_z. Although present at each gradient field switch, the effect decays quickly in time. In modern scanners the eddy currents are limited through passive and active shielding, reducing its influence considerably. In this study the phase variation induced by the eddy currents has been modelled by Eq.IV.11:

$$\hat{d}_{\text{eddy}}(t) = \exp\left[\sum_{j=1}^{J} c_{j,\text{eddy}} \exp(\alpha_{j,\text{eddy}} t) \right] \tag{IV.11}$$

with $J = 2,\ c_{1,\text{eddy}} = 2.0,\ c_{2,\text{eddy}} = -2.4,\ \alpha_{1,\text{eddy}} = -0.006,\ \alpha_{2,\text{eddy}} = -0.005,$

– $\hat{d}_{\text{relaxation}}$ is representative of the spin relaxation mechanism. In current literature, this is usually modeled together with a simple inhomogeneity effect as the Voigt decay function. In this work, the Voigt function has been degenerated to a Lorentzian decay, completely modelled by Eq.IV.12:

$$\hat{d}_{\text{Voigt}}(t) = \exp\left(\alpha t + \beta t^2\right) \quad \text{with } \alpha = -0.026,\ \beta = 0\ . \tag{IV.12}$$

Furthermore, in this work it is assumed that:

(i) The form of the decay function is *a priori* unknown

(ii) The corresponding lineshape is of reasonably compact support. This assumption can also be translated as reasonable shim quality.

(iii) Although unknown, the decay function is common to each spectral component. This assumption is based on the predominant influence of B_0 heterogeneity and eddy currents. It should be noted here that this common decay hypothesis also stands at the foundation of any method exploiting a reference peak.

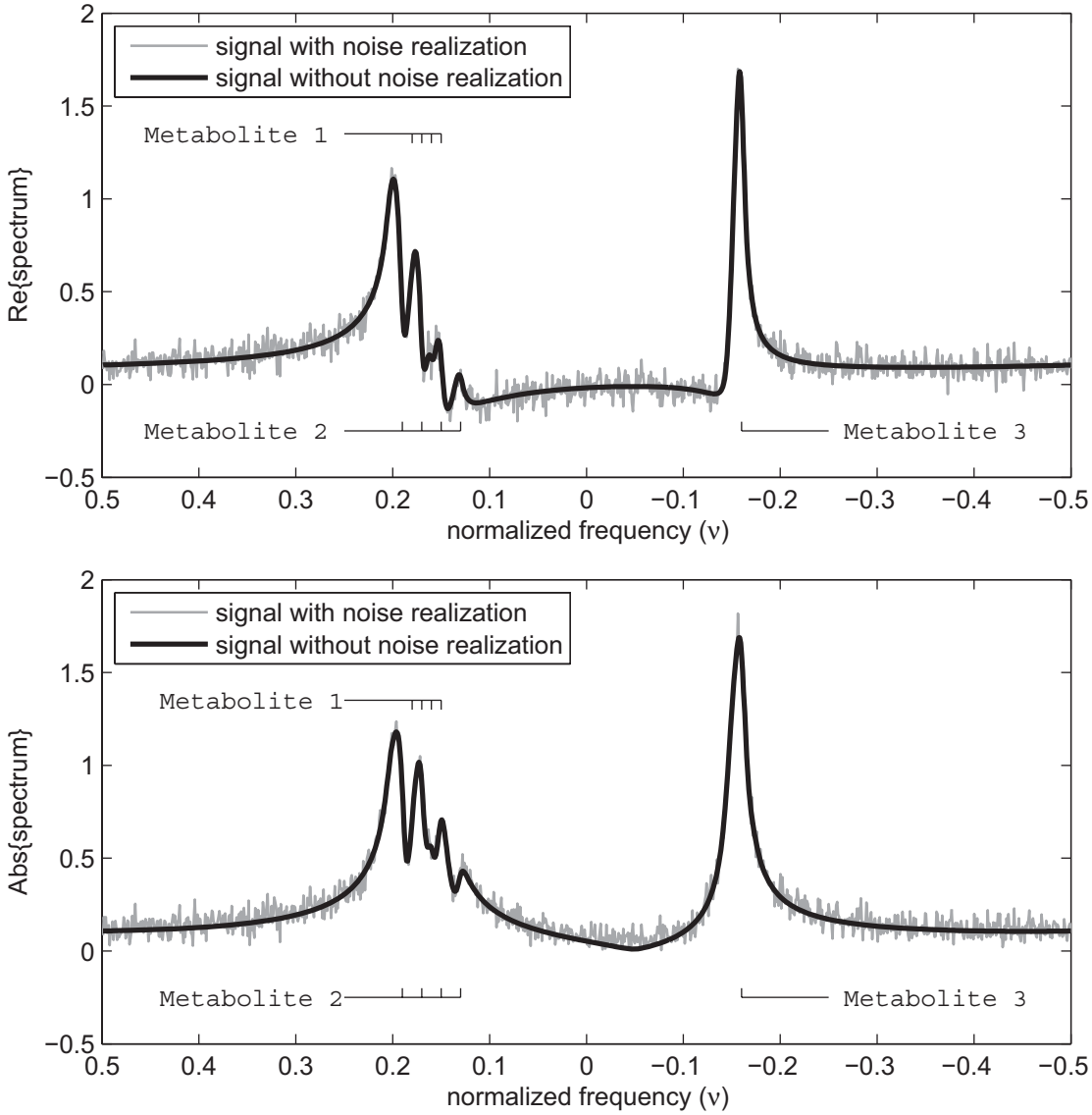

Figure IV.3: *Real part (upper plot) and module (lower plot) of the fictitious, simulated signal used for Monte Carlo validation. For the complete description of the model, please refer to text. Metabolites 1 and 2 have 4 peaks each, while metabolite 3 has a single peak. Please notice that the spectral peak positions do not correspond to exact values in Table IV.1, especially in the plot of the real part. The difference is accounted for by the asymmetric lineshape used, as well as, in the case of metabolites 1 and 2, of the inter-peak interference and different peak dephasing. Notice how plotting the module corrects the peak position and allows better identification of each peak.*

(iv) A reference signal enabling accurate estimation of the decay function is not available. Consequently, the common decay function has to be estimated from the signal itself.

The models described in sections §IV.2.1.1-IV.2.1.2 fully describe the simulation methodology for this work. The resulting fictitious signals serve as substitute of real-world signals from any of the nuclei ^{1}H, ^{13}C, ^{15}N, ^{19}F, ^{31}P.

IV.2.1.3 Quantitation algorithm and implementation

The novel approach implemented in this study consists of enhancing the least-squares classic approach ($\mathfrak{C}_1$) with the newly proposed $\mathfrak{C}_2$approach. The combined method has the following steps. A detailed description of the implementation is given afterwards.

(i) Apply a preliminary NLLS fit of the model function described by Eq.IV.8. This is equivalent to a primary application of QUEST on the data set, using a pure-Lorentzian decay function. The estimated model parameters $\mathbf{p}_{\text{start}}$ serve as a starting point for the rest of the algorithm. The usual set of equations corresponding to minimizing the $\mathcal{L}_2$ norm of the residue $\mathbf{s} - \hat{\mathbf{s}}$ is referred to as criterion one ($\mathfrak{C}_1$).

(ii) Build the undamped model $\hat{s}_{\text{undamped}}$ using Eq.IV.2. The parameters used are the previously computed $\mathbf{p}_{\text{start}}$.

(iii) Compute the estimated common decay function $\mathbf{d}$ [2] by point-wise division of the signal $\mathbf{s}$ to the undamped model $\hat{s}_{\text{undamped}}$. Next, normalize $\mathbf{d}$ with respect to the first point. This yields the following simple estimator of the decay function:

$$d(t) = \mathcal{N}\frac{s(t)}{s^{\text{start}}_{\text{undamped}}(t)} \tag{IV.13}$$

where $\mathcal{N} = \left|\frac{s_{\text{undamped}}(0)}{s(0)}\right|$ is the normalizing factor for the lineshape. This estimator is not exact for two reasons. First, $s(t)$ contains noise, whereas $\hat{s}(t)$ does not. Second, the initial estimates $\mathbf{p}_{\text{start}}$ are only approximate. As a consequence of the second reason, $d(t)$ comprises components with frequencies rather higher than those in the true decay function.

(iv) Impose that components in $d(t)$ with frequencies $|\nu| > \nu_{\text{threshold}}$ have minimal amplitudes. $\nu_{\text{threshold}}$ is derived from physical insight. The ensuing set of equations is referred to as criterion two ($\mathfrak{C}_2$). It has been implemented as follows:

(a) Truncate $d(t)$ to zero once it has decayed into the noise, at $t = t_{\text{decay}} = n_{\text{decay}}t_{\text{s}}$.

(b) Zero-fill d(t) from $n = n_{\text{decay}}$ to 1024.

(c) Calculate the derivatives of the lineshape $\Re[\mathcal{FFT}\{d(t)\})]$, in which $d(t)$ has been derived from Eq. IV.13 with respect to the metabolite parameters c_m and $\triangle\nu_m$, $m = 1, \ldots, M$.

(d) Analogous to minimizing the residue, set up equations for minimizing the real part of $D(\nu) = \text{FFT}\{d(t)\}$ for $|\nu| > \nu_{\text{threshold}}$.

(e) Merge the equations of the two criteria.

2. The hat has been dropped from $\hat{d}(t)$ because the resulting expression is no longer strictly an analytical formula.

(v) Apply a two-criteria NLLS fit of

$$\hat{s}(t) = d(t)\hat{s}_{\text{undamped}}(t) \tag{IV.14}$$

to $s(t)$. In each NLLS iteration, $\mathfrak{C}_2$minimizes the components in $d(t)$ with $|\nu| > \nu_{\text{threshold}}$. Simultaneously, $\mathfrak{C}_1$minimizes the the residue $s(t) - \hat{s}(t)$. Also, $d(t)$ is estimated with Eq.IV.13 in each iteration, using the undamped model function $\hat{\mathbf{s}}_{\text{undamped}}$ built with the latest parameter estimates.

To the best of our knowledge steps (iv) and (v) are new. The use of basis functions such as wavelets or splines and the concomitant setting of hyper-parameters has been circumvented. Hyper parameters to be set here are $\nu_{\text{threshold}}$ and the relative weights of criterion 2 and criterion 1. So far, their values appear not to be too critical.

Following, a detailed description of the algorithm implementation is given. For details on the computation of the Jacobian matrices for $\mathfrak{C}_1$ and $\mathfrak{C}_2$, please refer to Additional Material §B.

ECD Residue and Spectral out-Band Component Minimization

INPUT

$\mathbf{s}$	signal to be quantified. Its length is denoted $\mathtt{N}$
ν_{t}	Threshold frequency delimiting out-Band domain [normalized frequency] (between 0 and 0.5)
$\mathbf{B}$	Basis set (individual components are denoted $\mathbf{b}_m$)
λ	relative weight of $\mathfrak{C}_1$(between 0 and 1)
$\mathtt{N}_{\text{lim}}$	signal index of the last point where SNR is acceptable (between 0 and $\mathtt{N}$)

STEP

01 $\mathtt{N}_{\text{iter}} \leftarrow 0$
Initialize inner variables.

01 $\mathbf{p}^0 \leftarrow \mathtt{argmin}_{\mathbf{p}}\{\mathfrak{C}_1(\mathbf{s}, \mathbf{p})\}$
Preliminary NLLS minimization for $\mathbf{p}$ starting values.

02 FOR ALL $(\mathtt{n})$ DO $\mathtt{d}_{\mathtt{raw}}[\mathtt{n}] \leftarrow \mathbf{s}[\mathtt{n}] \;/\; \hat{\mathbf{s}}_{\mathtt{nd}}(\mathbf{p}^{\mathtt{N}_{\text{iter}}-1})[\mathtt{n}]$
Estimation of the raw unnormalized ECD.

03 FOR ALL $(\mathtt{n})$ DO $\mathtt{d}_{\mathtt{norm}}[\mathtt{n}] \leftarrow \mathtt{d}_{\mathtt{raw}}[\mathtt{n}] \;/\; |\mathtt{d}_{\mathtt{raw}}[\mathtt{n} = 1]|$
ECD normalization.

04 FOR ALL $(\mathtt{n} \leq \mathtt{N}_{\text{lim}})$ DO $\mathtt{d}_{\mathtt{zf}}[\mathtt{n}] \leftarrow \mathtt{d}_{\mathtt{norm}}[\mathtt{n}]$
FOR ALL $(\mathtt{N}_{\mathtt{lim}} < \mathtt{n} \leq \mathtt{N})$ DO $\mathtt{d}_{\mathtt{zf}}[\mathtt{n}] \leftarrow 0$
Truncate at $\mathtt{N}_{\mathtt{lim}}$ and then zero-fill up to N points.

05 $\mathtt{D} \leftarrow \mathtt{fft}(\mathbf{d}_{\mathbf{zf}})$
Compute DFT of processed ECD using FFT algorithm.

06 FOR ALL $(1 \leq \mathtt{j} \leq \mathtt{size}(\mathtt{D}))$ IF $(|\nu[\mathtt{j}]| > \nu_{\mathtt{t}})$ THEN ELIMINATE $\mathtt{D}[\mathtt{j}]$
$\mathtt{N}_{\mathtt{f}} \leftarrow \mathtt{size}(\mathtt{D})$

Crop estimated lineshape so that only out-of-band spectral components (as defined by the interval $[-\nu_t, \nu_t]$) are kept. $\nu[\mathtt{j}]$ represents the reduced frequency corresponding to $\mathtt{D}[\mathtt{j}]$; this depends on the format of the `fft()` output.

07 $\mathbf{J}_{\mathfrak{C}_1} \leftarrow \mathtt{JacobianCriterionOne}(\mathbf{t}, \mathbf{B}, \mathbf{p}^{\mathtt{N}_{\mathrm{iter}}-1})$
Compute Jacobian matrix corresponding to the classic LS criterion $\mathfrak{C}_1$. This step (function `JacobianCriterionOne`) is detailed in text.

08 $\mathbf{J}_{\mathfrak{C}_2} \leftarrow \mathtt{JacobianCriterionTwo}(\mathtt{D})$
Compute Jacobian matrix corresponding to the Out-of-Band Spectral components criterion $\mathfrak{C}_2$. This step (function `JacobianCriterionTwo`) is detailed in text.

09 FOR ALL $(1 \leq \mathtt{n} \leq \mathtt{N})$ DO $\mathbf{J}_{\mathrm{composite}}[\mathtt{n}] \leftarrow \lambda \mathbf{J}_{\mathfrak{C}_1}[\mathtt{n}]$
FOR ALL $(1 \leq \mathtt{k} \leq \mathtt{N_f})$ DO $\mathbf{J}_{\mathrm{composite}}[\mathtt{k}+\mathtt{N}] \leftarrow (1-\lambda)\mathbf{J}_{\mathfrak{C}_1}[\mathtt{k}]$
Build composite Jacobian matrix, from the concatenation of $\mathbf{J}_{\mathfrak{C}_1}$ and $\mathbf{J}_{\mathfrak{C}_2}$. The λ hyper-parameter sets the relative weight of $\mathfrak{C}_1$ and $\mathfrak{C}_2$.

10 FOR ALL $(1 \leq \mathtt{n} \leq \mathtt{N})$ DO $\mathbf{r}_{\mathrm{composite}}[\mathtt{k}] \leftarrow \lambda(\mathtt{s}[\mathtt{n}] - \hat{\mathtt{s}}_{\mathtt{nd}}(\mathbf{p}^{\mathtt{N}_{\mathrm{iter}}-1})[\mathtt{n}]\mathtt{d}_{\mathtt{norm}}[\mathtt{n}])$
FOR ALL $(1 \leq \mathtt{k} \leq \mathtt{N_f}))$ DO $\mathbf{r}_{\mathrm{composite}}[\mathtt{k}+\mathtt{N}] \leftarrow (1-\lambda) \times (-\mathtt{D}[\mathtt{k}])$
Build composite residue vector, from the concatenation of $\mathfrak{C}_1$residue and $\mathfrak{C}_2$out-Band spectral components.

11 $\triangle\mathbf{p} \leftarrow \mathtt{LLSsolve}(\mathbf{J}_{\mathrm{composite}}\triangle\mathbf{p} = \mathbf{r}_{\mathrm{composite}})$
$\mathbf{p}^{\mathtt{N}_{\mathrm{iter}}} \leftarrow \mathbf{p}^{\mathtt{N}_{\mathrm{iter}}-1} + \triangle\mathbf{p}$
Compute the next (better) estimation of the parameters $\mathbf{p}$. This also corresponds to the final step in $\mathbf{p}^{\mathtt{N}_{\mathrm{iter}}} \leftarrow \mathtt{argmin}_{\mathbf{p}}\{\lambda^2\mathfrak{C}_1(\mathbf{s},\mathbf{p}) + (1-\lambda)^2\mathfrak{C}_2(\mathbf{s},\mathbf{p})\}$

12 IF `StopConditions` THEN STOP
ELSE $\mathtt{N}_{\mathrm{iter}} \leftarrow \mathtt{N}_{\mathrm{iter}} + 1$, GOTO (STEP.2)
Algorithm exit conditions. If not satisfied, increment $\mathtt{N}_{\mathrm{iter}}$ and compute next iteration for $\mathbf{p}$.

OUTPUT
$\mathbf{p}^{\mathtt{N}_{\mathrm{iter}}}$ value of final estimated parameters

---

IV.2.2 Results

Validation of the method has been performed in the form of a Monte Carlo study, with a 1000 signal realizations. Each signal is built taken into consideration the noise-free model previously described, to which AWG noise is added, so that the noise standard deviation is equal for each realization to 0.05 for both the real and imaginary parts.

Result assessment is achieved by computing the relative changes of the root-mean-square errors (RMSE), as well as the bias-to-standard-deviation ratio(BSR), of estimated metabolite concentrations ($\hat{c}_m$). In the optimal case, BSR should be as close to zero as possible, while the relative RMSE (rRMSE) should be close to 1. The BSR and (r)RMSE used as a measure

$d(t)$ $\rightarrow$	Known	$\exp(\alpha t)$		ECD NLLS	
metabolite	(true) (a)	Lorentz (b)	Renormalized (c)	HSVD (d)	**2 criteria (e)**
$m = 1$ quartet	1.0 (0.0)	1.62 (-0.27)	2.80 (-1.59)	1.98 (-0.12)	**1.75 (-0.30)**
$m = 2$ quartet	1.0 (0.0)	5.12 (3.06)	1.75 0.41)	2.64 (0.18)	**1.57 (0.27)**
$m = 3$ singlet	1.0 (0.0)	13.30 (9.09)	4.79 (2.34)	7.12 (0.33)	**2.31 (0.26)**

Table IV.3: *Relative RMSEs of estimated metabolite concentrations and bias-to-standard-deviation (in parentheses) obtained by Monte Carlo simulation, with 1000 noise realizations. Results obtained with two-criteria NLLS are indicated in boldface.*

of success are defined by

$$\mathrm{RMSE}(\hat{\mathbf{c}}_\mathbf{m}) = \sqrt{\frac{1}{K}\sum_{k=1}^{K}(\hat{c}_{m,k} - c_m^{\mathrm{true}})^2} \tag{IV.15}$$

$$\mathrm{rRMSE}(\hat{\mathbf{c}}_\mathbf{m}) = \frac{\mathrm{RMSE}\{\text{case when } \hat{d}(t) \text{ is unknown}\}}{\mathrm{RMSE}\{\text{case when } \hat{d}(t) \text{ is known}\}} \tag{IV.16}$$

$$\mathrm{BSR}(\hat{\mathbf{c}}_\mathbf{m}) = \frac{\mathbb{E}[\hat{\mathbf{c}}_\mathbf{m}] - c_m^*}{\sqrt{\frac{1}{K-1}\sum_{k=1}^{K}\left[\hat{c}_{m,k} - \mathbb{E}[\hat{\mathbf{c}}_\mathbf{m}]\right]^2}} \tag{IV.17}$$

$$\mathbb{E}[\hat{\mathbf{c}}_\mathbf{m}] = \frac{1}{K}\sum_{k=1}^{K}\hat{c}_{m,k} \tag{IV.18}$$

where K is the number of noisy signals.

Table IV.3 shows the results of the Monte Carlo study. Column (a) is shown as a reminder that we consider reference results (gold standard) the case when the decay function is known. Column (b) is representative of using a Lorentzian decay function. In order to compensate for a multiplicative constant on all the estimated concentrations, renormalization has been performed. Results after renormalization are tabbed in column (c). Column (d) shows results obtained after application of the ECD algorithm, with non-parametric ECD filtering by HSVD. Finally, column (e) shows the results of NLLS minimization of the combined criteria $\mathfrak{C}_1$ and $\mathfrak{C}_2$.

In all cases the combined $\mathfrak{C}_1 + \mathfrak{C}_2$ approach has better relative RMSE than the HSVD ECD method. When compared to the use of a pure Lorentzian model, the novel method also performs very well, achieving better performances for metabolites 2 and 3, and comparable performances for metabolite 1. A key element to note is the performance in bias reduction; while using just a Lorentz lineshape introduces significant bias, all methods tested have managed to reduce it considerably. Renormalization, by correcting the amplitudes by a multiplicative factor, decreases bias. However, it is common in MRS to use metabolite ratios instead of metabolite amplitudes; such use nullifies the influence of a common multiplicative

factor, thus making renormalization necessary. Best bias reduction is offered by both ECD approaches ($\mathfrak{C}_1$ or $\mathfrak{C}_1$+$\mathfrak{C}_2$).

IV.3 Further developments for $\mathfrak{C}_2$-type criteria

The previous Monte Carlo simulation has proven the potential of significant error reduction when using a cost function that includes both $\mathfrak{C}_1$ and $\mathfrak{C}_2$ principles. However, as is usually the case when the criterion is composed of the sum of two cost functions, a more in-depth analysis is needed to see how each cost function behaves, and how the two criteria compete in the convergence process. In this section a more in-depth analysis of the composite criteria is performed, and several improvements are proposed for the $\mathfrak{C}_2$ cost function.

IV.3.1 Convergence analysis for the composite criterion

First of all, as seen in §III.3.3, applying $\mathfrak{C}_1$ in an iterative way, without any filtering of the lineshape should not improve the results. This is because in the case of unfiltered ECD the next iteration should [3] converge to exactly the previous iteration, giving zero LS residue and achieving the global minimal null score.

On the other hand, writing the ECD as in Eq.IV.5 (arbitrarily choosing a reference metabolite m_0), makes apparent that the parameter values corresponding to *one* metabolite has limited useful influence on the ECD spectral compactness.

$$\hat{d}(t) = \underbrace{\frac{1}{\hat{c}_0 \cdot e^{j\hat{\varphi}_0} \cdot e^{j\hat{\omega}_0 t}}}_{(b)} \underbrace{\frac{s(t)}{b_0(t) + \sum_{m=1}^{M-1} \hat{c}_m^{\text{rel}} \cdot b_m(t) \cdot e^{j\hat{\varphi}_m^{\text{rel}}} \cdot e^{j\hat{\omega}_m^{\text{rel}} t}}}_{(c)} \tag{IV.19}$$

As explained in section IV.1.1, it is actually the term (c) that sets the width of the ECD central peak, while the reference term (b) has the following influences:

The reference concentration acts as a multiplicative factor for the cost function. Since the $\mathfrak{C}_2$ cost function used is linear with respect to $\frac{1}{c_0}$, minimizing only the second criterion might give way to minimization of the inverse of the reference amplitude. This in turn leads to all relative concentrations diverging towards very large values, a numerically very unstable situation. However, should the reference value be fixed, this problem is averted.

The reference phase φ_0 has an influence on $\mathfrak{C}_2$ because the cost function takes into consideration only the real part of the estimated common lineshape. While a minimizing value of this reference phase might exist so as to minimize $\mathfrak{C}_2$, it will only influence the overall dephasing, while introducing extra variability.

The reference frequency shift acts by translating (convolution of a non-centred Dirac distribution) the spectral components of the ECD on the frequency axis. This does not modify the spectral compactness *per se* (*ie.* the frequency span between the furthest non-negligible spectral peaks). However, since the implemented $\mathfrak{C}_2$criterion used fixed limits, the reference spectral shift will converge so as to maximize the number

3. In this context, only the ideal case is considered, when the minimization converges to the *global* minimum. In the implementation case, numerical reasons, as well as method parameter choices (*ie.* effective convergence conditions) can deteriorate performances significantly.

of useful components inside the useful band. This has no physical meaning, while also introducing an extra degree of freedom (thus increasing estimator variance).

Fixing the reference parameters at an arbitrary value eliminates the undesired influence previously explained. However, should the reference values be incorrect, the overall signal model will not fit the measured signal in the least-squares sense, making apparent a residue $\mathbf{s} - \hat{\mathbf{s}}$. It can be said that the $\mathfrak{C}_2$ cost function enables determination only of parameters *relative* to a reference. The reference acts as overall parameters acting on the area, phase and frequency shift of the lineshape, while the criterion minimizes aspects linked to its *shape*. Lack of convergence for $\mathfrak{C}_2$when attempting to use parameters for all metabolites can thus be explained by attempting to estimate both the scale and the shape of a signal by minimizing only criteria that take into account the shape.

Minimizing a composite criterion built from $\mathfrak{C}_1$ and $\mathfrak{C}_2$ eliminates the lack of convergence, as it combines the power of spectral compactness relative estimation with the fitting properties of the classical LS. The overall minimization problem can be separated into (1) finding the best relative parameter values in respect to a reference (Eq.IV.5.(c)) and (2) finding the optimal values of the reference metabolite so that the best LS fit is achieved. At each iterative step, the ECD spectral compactness achieves (1), without modification of the reference values. In the same time, the LS criterion changes all values (including the reference parameters), although it attempts convergence towards the previous iterative values. It becomes thus clear how the parameter values are changed in the minimization process:

- The reference parameters are changed only by the LS $\mathfrak{C}_1$ criterion, attempting to rescale and frequency shift the model so as to best fit the measured signal.
- All the other parameters are only influenced by the $\mathfrak{C}_2$ criterion. Although LS minimization participates at each step, it only adds difficulty in converging to a value different from the previous one.

It is of interest to observe that, in practice, the metabolite amplitudes are rarely directly sought, as the acquired signal is usually expressed in arbitrary units. The usual method is to compute relative amplitudes (and thus relative concentrations), and then to fix a reference metabolite (*ie.* Creatine in ^{1}H MRS) at a known value, so that the other estimated concentrations might be respectively computed. In the case when only one signal is considered, and in the context of the composite criteria used in this study, this amounts to choosing the $\mathfrak{C}_2$ reference to coincide with the measurement reference. It is thus possible to compute *directly* the other concentrations, bypassing use of the LS criterion, as well as the subsequent reference renormalization.

IV.3.2 Minimizing the influence of the choice of the reference metabolite

If the $\mathfrak{C}_2$ type criterion is to work without the use of another criterion, several modifications are of interest so that the influence of the reference metabolite m_0 is nulled. The proposed approaches to eliminate this influence are based on (1) normalization, to eliminate the amplitude factor and (2) use of module instead of the real part to eliminate the possible phase distortion. In the following paragraphs, we discuss on the normalization of the cost function.

One of the most problematic divergence arises because of the fact that if the estimated amplitudes are arbitrarily high, then the corresponding estimated common decay function

will have small values. This in turn has an effect on the cost function used, that is constructed so as to have $\mathfrak{C}_2(\mathbf{0}) = 0$, where $\mathbf{0}$ is a matrix of convenient size composed solely of zero values. Maximizing all the amplitudes of the free concentrations minimizes the score.

One step is taken in the presented algorithm to avoid divergence towards very large values of c: the normalization at STEP.3 (*cf.* Additional Material, §IV.2.1.3). However, the influence of this step is not included when the new parameter values $\hat{\mathbf{p}}^{\mathtt{N}_\mathrm{N}}$ are computed at each step. The alternating process of (1) normalizing the ECD function $\mathbf{d}$ and (2) computing the next iteration can be combined in a single step that includes normalization in the criterion.

The new $\mathfrak{C}_2$ cost function used used can be written as a rescaled version of the $\mathfrak{C}_2$ criterion previously described.

$$\mathfrak{C}_2{}^{\text{rescaled}}(\mathbf{d}) = \frac{\mathfrak{C}_2(d)}{\mathcal{N}}, \tag{IV.20}$$

where $\mathcal{N}$ is the normalizing factor used. The value of $\mathcal{N}$ needs to be proportional of the amplitude-concentration proportionality factor, meaning that if all the amplitudes are multiplied by a factor, the resulting $\mathcal{N}$ should also be modified by the same multiplicative factor. Among the different choices, two have been explored: (1) the value of the first point of the ECD function $\mathbf{d}$ and (2) the L_2 norm of the ECD.

Using the first point of the non-normalized ECD amounts to doing a normalization similar to STEP.3 . The main difference is that it is included *inside* the criterion, meaning that STEP.3 is no longer necessary and that the new $\triangle\mathbf{p}^{N_\text{iter}}$ computed at each step will take into account also the normalization. However, a new, adapted Jacobian matrix has to be derived (see Additional Material B).

Using the $\mathcal{L}_2$ norm of the ECD as normalization constant further improves the isoline profile for the cost function. However, increased complexity for the Jacobian is needed, as instead of computing the partial derivative of $\hat{s}_\text{undamped}(0, \mathbf{p})$, the $\mathcal{L}_2$ norm 0 $\|\hat{\mathbf{s}}_\text{undamped}(t, \mathbf{p})\| = \sum_t |\hat{s}_\text{undamped}|^2$ has to be derived. Using the norm also provides a more intuitive physical interpretation, as it can be seen that the criterion checks the energy fraction represented by the out-Band components.

Figure IV.4 shows the evolution of the score function when two metabolite concentration have been varied around the true values. Applying normalization inside the criterion computation adds a penalty for high concentration values. The convergence domain delimited by the smallest isoline is much smaller (and also much better delimited) when normalization is used (b, c).

IV.4 $\mathfrak{C}_2$ implementation in the Time Domain

Another interpretation of the limited frequency bandwidth of the estimated lineshape can be the smoothness of its time-domain counterpart, the ECD function $\mathbf{d}$. That is because the lineshape is constructed of low-frequency components, it is the sum of locally slowly-varying functions, thus it is slowly-varying. It is thus expected that when the compact spectral support of the ECD increases due to incorrect values of $\hat{\mathbf{p}}$, the lineshape becomes more oscillating. An illustration of this effect can be seen in Fig.IV.1(II.a).

Such an interpretation brings forward another possible criterion: the smoothness of the estimated lineshape. More ways are available to evaluate the smoothness of a curve, but

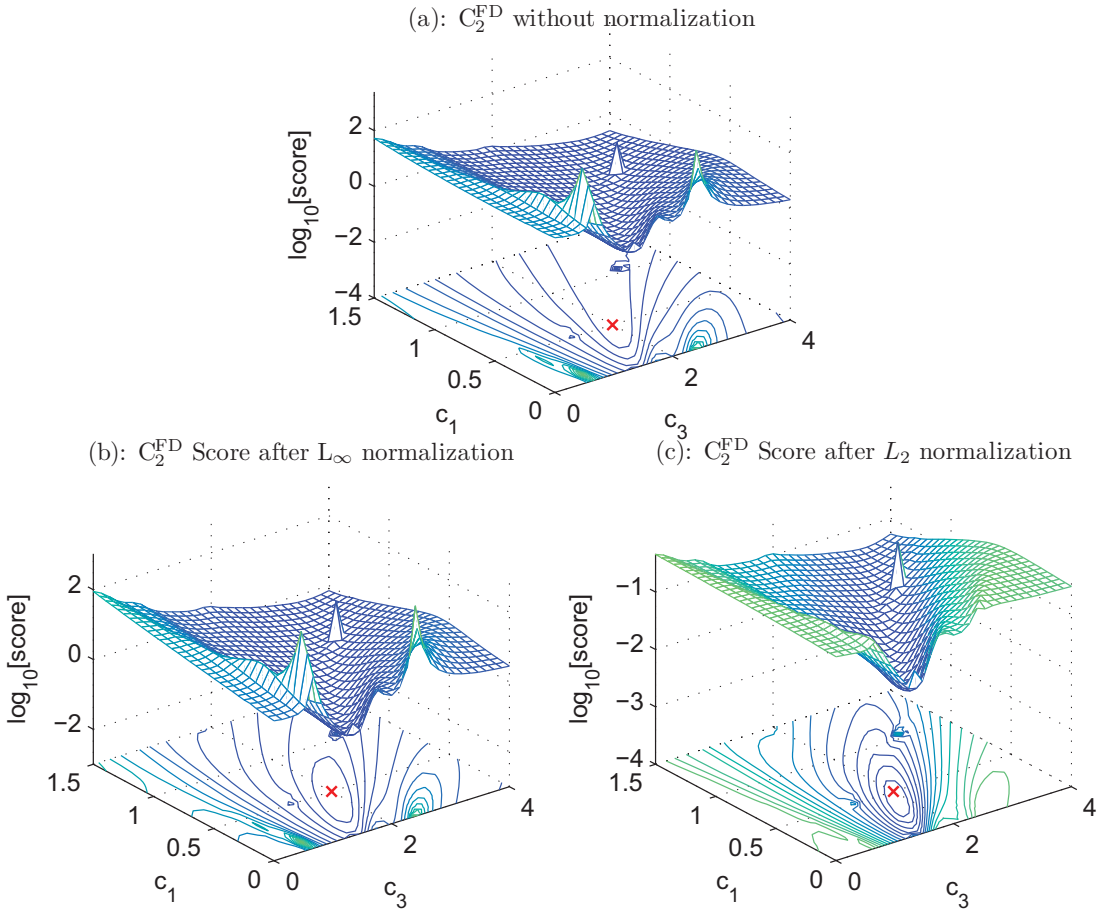

Figure IV.4: *Influence of the normalization procedure on the* $\mathfrak{C}_2^{FD}$ frequency domain *cost function. Upper plot (a) presents the previously validated* $\mathfrak{C}_2^{FD}$ *cost function. Left plot (b) presents the normalized score, using* $\mathcal{N} = \hat{d}(t=0)$*, which corresponds to* $\mathcal{L}_\infty$*. Right plot (c) shows the effect of* $\mathcal{L}_2$ *normalization. In all cases, the signal* $\mathbf{s}$ *has been generated using the methodology in §IV.2.1. Then a gridsearch-like approach has been performed, changing only the values of* $\hat{c}_1$ *and* $\hat{c}_3$*. The red cross represents the true values, where the cost function should have minimal values. Notice how normalization (b, c) eliminates the unwanted 'valley' towards arbitrary big values present in (a).*

here only the local numerical discrete derivatives of first and second orders are considered:

$$\mathfrak{C}_2^{s1}(\mathbf{d}) = \|\frac{\partial d(t)}{\partial t}\| \xrightarrow{discretization} \mathfrak{C}_2^{s1}(\mathbf{d}) = \frac{1}{2}\left[\sum_{n=1}^{N-1} \|d[n+1] - d[n]\|\right] \tag{IV.21}$$

$$\mathfrak{C}_2^{s1}(\mathbf{d}) = \|\frac{\partial^2 d(t)}{\partial t^2}\| \xrightarrow{discretization} \mathfrak{C}_2^{s2}(\mathbf{d}) = \frac{1}{4}\left[\sum_{n=1}^{N-2} \|d[n+2] - 2d[n+1] + d[n+2]\|\right] \tag{IV.22}$$

As with the frequency domain criteria, rescaling is also interesting for this time-domain implementation, henceforth referred to as estimated decay smoothness (EDS). In the following validation plots, a choice has been made to normalize according to the $\mathcal{L}_2$ norm of the ECD, thus effectively comparing the energy of the ECD derivative to the energy of the ECD function.

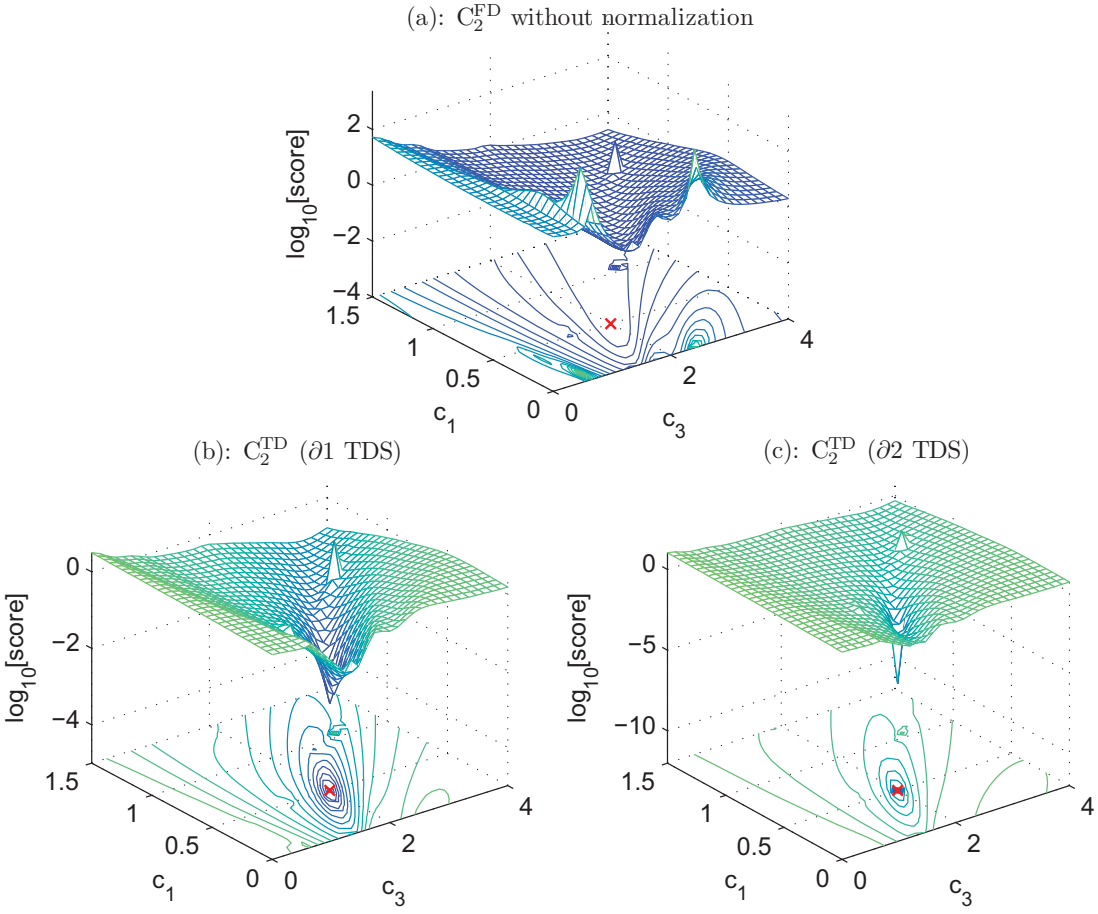

Figure IV.5: Time Domain *Smoothness (TDS) cost function* $\mathfrak{C}_2^{\mathrm{TD}}$ *as alternative to the* $\mathfrak{C}_2^{\mathrm{FD}}$ *cost function. Upper plot (a) presents the previously validated* $\mathfrak{C}_2^{\mathrm{FD}}$ *score. Plots (b) and (c) present the TDS score, with evaluation via the first order (b) and second order(c) numerical derivatives. Normalization using* $\mathcal{L}_2$ *of the ECD has been applied. In all cases, the signal* $\mathbf{s}$ *has been generated using the methodology in §IV.2.1. Then a gridsearch-like approach has been performed, changing only the values of* $\hat{c}_1$ *and* $\hat{c}_3$*. The red cross represents the true values, where the score should be minimal. Notice how well the score functions in (b, c) behave when compared to the frequency domain criteria in Fig.IV.4.*

Figure IV.5 plots the Estimated Decay Smoothness (ECD) cost against amplitude estimates $\hat{c}_1$ and $\hat{c}_3$. The context is the same as in Fig.IV.4. Results exhibit much sharper convergence at the true values, and generally a better behaviour elsewhere. Furthermore, when the score function evolution is observed closely (zoomed) in the immediate vicinity of the true solution (not shown), the actual cost function minimum in the TDS case are much closer to the true solution than in the case of the frequency-domain variant.

IV.4.1 Comparison between time-domain and frequency-domain implementations of $\mathfrak{C}_2$

In order to get a better understanding of the behaviour of the proposed TDS-based criteria for noisy signals, a Monte-Carlo study has been performed, using the same signal described in §IV.2.1. Nine values of noise, ranging logarithmically from [4] 0.001 to 0.1 have been chosen. For each noise value, 35 noise realizations have been computed, and each resulting signal has been quantified using four criteria: $\mathcal{L}_\infty$ and $\mathcal{L}_2$ scaled versions of frequency domain $\mathfrak{C}_2$ and first and second-order estimated decay function smoothness, $\mathcal{L}_2$-scaled. Minimization has been performed by a linesearch-like algorithm, provided by the `fminsearch` function in MATLAB.

Results (*cf.* Fig.IV.6) show a different behaviour, especially at small SNR, when FD and TD approaches are compared. FD criteria tend to converge to a slightly biased solution. In a bid to see if the minimization process is to blame for this, a grid-search study similar to the study in Fig.IV.4 has been performed, with the zone of interest zoomed in to see only the zone immediately adjacent to the cost function minimum. The study (results not plotted here) show that the cost function is not globally minimal at the true values. A possible explanation for this are the DFT artefacts due to a limited time-span signal.

A major advantage of smoothness criteria over spectral out-Band ones is that all computations are performed in the time domain. This eliminates the need to compensate for DFT artefacts, as well as perform processor-intensive computations for DFT estimation. Another advantage is that no hyper-parameters need to be set.

Up to this moment, all validation studies concerning ECD smoothness criteria have been done using either a grid-search approach for validation of the difference between local minima and true values, or using line-search algorithms to study the convergence performance. However, if a trust region method (such as Levenberg-Marquardt) is to be implemented, Jacobian matrices should be computed. The necessary steps are briefly described in the additional material B.

Conclusions

In this chapter a novel approach to MRS quantitation is presented. As opposed to the classical approach, where a common lineshape is derived either from a reference peak, or using some sort of processing, and then this estimated common lineshape is used to improve the performance of a LS-type quantitation, the novel approach used the estimated lineshape itself as a criterion. Signal parameters are thus estimated directly, without need of further processing.

4. In this context the level of the noise has been defined as the standard deviation of its real part. If considering the standard deviation of the whole complex noise, values should be multiplied with $\sqrt{2}$.

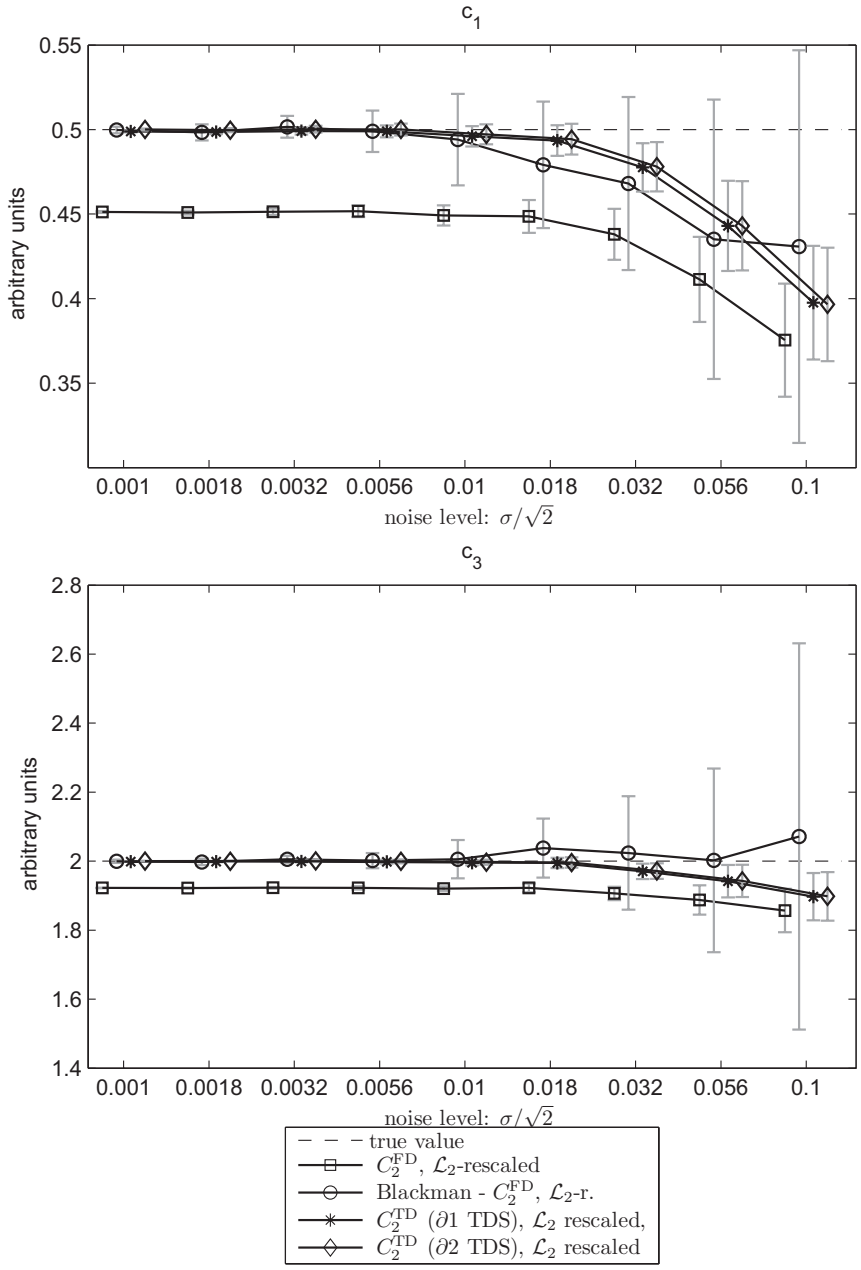

Figure IV.6: *Estimator performance using only spectral compactness criteria. Abscissa represent the 9 noise levels simulated. The values correspond to the standard deviation of the real part of the noise. For each noise value, 4 different criteria have been compared, represented by the four series. Squares (□) represent the $\mathcal{L}_2$ rescaled version of the originally proposed $\mathfrak{C}_2^{\mathrm{FD}}$ Criterion. Circles (○) represent the added Blackman-window apodisation. Stars (∗) and diamonds (◊) represent the TDS approaches with first order and second order derivatives respectively. For each noise level, 35 noisy signal realization have been quantified, using $\mathfrak{C}_2$ minimization with only c_1 and c_3 as free parameters. The central value corresponds to the average estimated value, while the error bars correspond to one standard deviation. True values are $c_1^{\mathrm{true}} = 0.5$ and $c_3^{\mathrm{true}} = 2.0$ (dotted lines). Notice the much improved bias reduction of the* Time Domain Smoothness *criteria (∗ and ◊) when compared to the unapodized* Frequency Domain $\mathfrak{C}_2^{\mathrm{FD}}$ *criteria (□), especially at low σ. The Blackman apodized version of $\mathfrak{C}_2^{\mathrm{FD}}$ (○) exhibits very small bias, but is clearly less stable at low SNR.*

The proposed methods can be combined with LS criteria, or used alone. In the latter case they are particularly adapted to estimation of metabolite concentration ratios. However, once the relative parameters have been computed, an extra final step can also be performed so that metabolite amplitudes (measured in the units specific to the spectra acquisition) can be computed. For this, the first point of the signal is particularly well suited, because it has the highest SNR of all the acquired points. Possible drawbacks of using the first point arise when there is suspicion of signal corruption, such as in the case when digital filtering on the acquisition hardware remains.

Two implementation types for ECD-SC methods have been discussed in this chapter (1) out-Band Spectral Components and (2) ECD Smoothness. Using simulated spectra, the different approaches have been validated, and compared with the performances of previous techniques used in this context. Results show improvement in the bias of the estimators, especially when compared to the use of a pure Lorentzian model.

For all the criteria presented, procedures have been described to compute the Jacobian matrix, and the score itself has been formatted so as to closely resemble NLLS mechanics. This allows immediate implementation using NLLS techniques, such as the widely used Levenberg-Marquardt algorithm. Furthermore, the presented methods for Jacobian computations take advantage, in the case when a simultaneous LS quantitation is performed, of the already-computed $\mathfrak{C}_1$ Jacobian matrices.

Validation results show the feasibility of spectral compactness based criteria, especially in the case when (1) SNR is very good, while (2) the lineshape resulting of B_0 inhomogeneity and eddy-current effects has a non-standard (*ie.* Voigt) profile. In the present study only the case when direct determination of the common lineshape from a reference peak is not possible has been considered.

Results also show some potential drawbacks of the proposed approach. The poor performance of the method with low SNR makes its use prohibitory, if not combined with some other technique. Direct processing of signals that are known not to posses a common lineshape is also not possible. A special case of this is when a baseline or macromolecule signal is present. In this latter case, a more indirect approach is advisable, such as explained in §V.2.3.

Chapter V

Conclusions and Perspectives

This last chapter reviews the main conclusions and original contributions in this thesis. More importantly, it provides possible leads to improving MRS lineshape handling and quantitation.

V.1 Conclusions

Chapters I and II have introduced the main concepts and methods used in this thesis. Beyond the theory presented, several conclusions could be inferred about the state-of-the-art in MRS and MRSI quantitation:

- Users of the quantitation techniques attempt to use them as "one button black-box" methods, *ie.* applying the method without sufficient understanding of the inner workings. This in turn may lead to unexpected or misunderstood results, further leading to possibly flawed conclusions.
- Mechanisms to warn the user of possible problems exist, but are still in an incipient phase. Only two major contributions have been made [91, 169] to judging the quality of MRS/MRSI results.
- Most methods to predict estimation incertitude are based on the Cramér-Rao Lower Bounds (see [33]). Although undeniably a powerful tool, poor understanding of CRLB derived incertitude values can lead to misuse.
- Development of objective criteria for assessing MRS/MRSI quantitation results, as well as review and unification of currently proposed criteria would greatly benefit the research community.

Chapter III focused on shedding new light on the common assumption that all peaks share the same lineshape. First, as a preliminary study, three different approaches for handling the assumed common lineshape have been compared. Results show that, except for metabolites with very close frequency contributions (*ie.* Cr and PCr), adapting the basis-set to the acquired signal gives the best results. The second part of the chapter focuses on introducing an algorithm enabling the estimation of the common decay function. Since it is shown that filtering the estimated common damping (ECD) function is essential, a methodology for this is proposed using LOWESS [38] local filtering. Results convey significant reduction in bias, shown to be responsible for most of the quantitation error.

Chapter IV introduced a novel way of approaching MRS quantitation based on the assumed common lineshape. Effective spectral compact support of the ECD has been shown to be an efficient cost function, that allows by itself convergence of the metabolite parameters to

the true values. Moreover, in order for trust-region methods to be used, a procedure to compute analytically the Jacobian of the score is proposed. Results show that especially for high SNR signals, the proposed method can significantly improve the quantitation performance.

V.2 Future work and open problems

Further research is necessary in the field of MRS and MRSI processing. The ultimate goal is to develop transparent "one button black-box" methods, that can consequently be used by clinical practitioners. In the following paragraphs we provide possible leads towards achieving this goal, for methods described in this thesis as well as for issues encountered during the underlying studies.

V.2.1 Assessing MRS quantitation results

As stated in §II.6, estimating metabolite concentrations should not only return parameter values, but also the parameter incertitudes and a measure of goodness-of-fit, assessing the level of confidence one should have in the results. However, current literature suggests that few methods propose reliable estimates for incertitudes, and only few contributions (*e.g.* [91, 169]) address directly the issue of MRS measurement confidence. We thus consider that an important contribution is to be made into these issues.

A possible lead to better incertitude evaluation is given by Bayes's theory, and the ensuing link between the incertitude distribution on the quantitation results $\mathcal{P}(\mathbf{p}|\mathbf{s})$ and the incertitude on the signal if the true values are known $\mathcal{P}(\mathbf{s}|\mathbf{p})$. (see §II.6)

$$\mathcal{P}(\mathbf{p}|\mathbf{s}) = \mathcal{P}(\mathbf{s}|\mathbf{p})\mathcal{P}(\mathbf{p}) \tag{V.1}$$

where $\mathbf{p}$ are the true parameters, $\mathbf{s}$ is the acquired signal and $\mathcal{P}(\mathbf{p})$ is the probability of $\mathbf{p}$. The prior information $\mathcal{P}(\mathbf{p})$ is usually replaced with a constant, assuming that all parameter values are constant. However, the probability to have a certain concentration of Creatine in healthy human white matter, for example, is *not* uniformly distributed. Using Bayesian theory, it is possible to take into account the prior information (expected values of a metabolite concentration) in the computation of the incertitude [1].

Another possible improvement to estimation of parameter incertitudes could be obtained by applying resampling techniques (bootstrapping, jackknifing, etc.). The current method widely used is to compute Cramér-Rao Lower Variance Bounds, and to assume that measurement incertitudes are of the order of the CRLBs (*cf.* [33]). While presenting many conveniences, the CRLBs remain a semi-analytical tool, and make strong assumptions. Better results could be obtained by estimating the parameter incertitude distribution using a dataset built from resampled signals.

A direct application comes in the case when multiple signals have been acquired in a short time frame, using exactly the same methodology. Typically this is done on current scanners, prior to an averaging step, when data are summed (or averaged), and only the result is given to the user. Slotboom et al. [169] have already proposed a method to use such a data set in order to provide a better result than the averaged default output. We would like to take this a step further and quantify individual spectra, then build the ensuing distribution of $\mathbf{p}$.

1. An even better way to include the probability distribution $\mathcal{P}(\mathbf{p})$ would be to use a Bayesian estimator, thus to use the prior information not only for incertitude computation, but also for metabolite quantitation.

Moreover, re-sampling can be used to increase dramatically the statistical sampling of the output. The estimated $\mathbf{p}$ distribution can then be used to compute confidence intervals for quantitation results.

So far, only parameter incertitudes have been addressed. However, goodness-of-fit issues are just as important, because a bad fit might yield meaningless parameter values *and* incertitudes. Unfortunately, few studies have addressed this issue in MRS so far, generally stopping at rejecting MRS quantitation results if certain criteria are met. Goodness-of-fit generally used are the residue level and 'appearance', as well as the amplitude-CRLB to amplitude ratio [91]. We believe that developing a numerical, objective measure for goodness-of-fit in MRS quantitation is of critical importance; besides providing an automatic way to reject unreliable estimates, it would also enable non-expert users assess when their "fit is good".

V.2.2 Simulation of data

A recurrent criticism in papers evaluating MRS quantitation is that the validation tests are performed on simulated signals, that in turn are too simplistic to realistically mimic *in vivo* MRS and MRSI acquisitions.

Clinical practitioners, as well as researchers focused on acquisition of the MRS(I) data often argue that only acquired data should be used for algorithm validation. However, as seen in this thesis, some aspects of quantitation are very difficult to study without the use of simulated data. Bias, in particular, can only be estimated if the true values are known. Of course, true metabolite concentrations can be measured reliably using non-NMR methods; but comparing estimated concentrations to true concentrations would require the whole acquisition chain to be modelled as well, with possible errors and incertitudes in too many places.

Synthetic data, however, depend only on known factors, that can be included or not in each simulation. This allows customizable datasets, providing insight at what are the factors influencing estimator performance. Moreover, data are 'free', as opposed to the non-negligible cost of data acquisition. MRS(I) data simulators are thus an essential tool for the study and further improvement of quantitation algorithms.

In the following paragraphs we propose two approaches to improving the quality of data simulations.

Enhanced numerical simulation. *In vivo* NMR acquisitions are influenced by two major factors: (1) the intrinsic properties of the molecules in the sample and (2) the local (physical, chemical, geometrical, etc.) properties of the analysed sample. The choice of the acquisition methodology would be a third cause, but we choose to distinguish between its influence on "ideal" spectra and its interaction on the acquisition environment, and include these contributions in either (1) or (2).

The two factors have been addressed by the research community separately. Concerning (1), several methods (for examples see [69] or [170]) have been proposed to predict NMR spectra, based on Quantum Mechanical computations. In the same time, in MRI, methods have been developed to take into account the environment specific to each acquisition (for an example see SIMRI [21]). Combining the two approaches would yield a valuable tool for realistic simulation of *in vivo* spectra, while also taking advantage of all the prior information (for example coupling constants and chemical shifts

for different metabolites, anatomical 3D models for the human body, etc.) already developed.

Extended analytical models. Most signals simulated for testing a quantitation method are based on the underlying model in the associated estimator. Such practice is necessary for model validation, but does not necessary extend validation to *in vivo* signals, mainly due to the limited number of parameters [2] included in estimator models. Development of more complex analytical models for MRS acquisition would allow better mimicking of *in vivo* data, while avoiding the high computational resources needed for a purely numerical approach.

Different analytical approaches have already been proposed for some of the MRS artefacts. For example, macro molecules have been modelled as Gaussian peaks in [138, 156], while a model for eddy current distortions of the decay function has been given by Rabeson et al. [150]. Combining the different analytical partial models for MRS(I), end eventual software implementation of a simulator would provide the community with a common complex model, enabling homogeneous simulation, and even perhaps better insight for the development of quantitation estimators.

An additional advantage of a standard simulation package is its prospective use in comparing MRS quantitation methods. As seen in §II.4, a significant number of quantitation methods has been proposed in literature. While several studies[190, 110, 139] have reviewed and classified them, performance comparison has only been done between a small number of methods. Moreover, published assessments of quantitation performances are based on different data sets, and thus comparison is not trivial. Comparing the methods would thus require universally accepted datasets, obtainable either through acquisition or through simulation.

While being the true golden standard, acquired signals have the disadvantages of (1) including possibly unknown effects and (2) delivering true values for concentrations only at the expense of modeling the whole acquisition process. Simulated signals, on the other hand, can provide true values directly, while giving the user complete control over what artifacts are to be included or not. This allows perfectly reproducible data sets, well suited for quantitation analysis and comparison.

V.2.3 Further development of proposed algorithms

In chapters III we have proposed an algorithm to compute the estimated common decay (EDF) function, and to use a filtered version of it to improve metabolite quantitation. Although we have shown, by applying the method on acquired *in vitro* signals, that it is functional, several improvements need to be made before application on *in vivo acquisitions*.

First of all, the method is to be implemented in the jMRUI package [175], making use of the new plug-in oriented environment provided in the latest version. This allows easy application on data acquired on different platforms, as well as a complete set of tools for preprocessing and comparing with other quantitation algorithms (QUEST, AMARES, etc.).

2. The number of degrees of freedom, or of estimated parameters, is an important characteristic of an estimator. If many parameters are estimated, individual estimation variance will grow, while for few model parameters unaccounted effects will introduce bias. This is usually referred to as *the bias-variance trade-off*. Due to it, an estimator should always have the minimal number of independent parameters, that accounts for most of the signal variability.

Secondly, a baseline accommodation strategy is to be implemented, similar to the approach in QUEST Ratiney [153], Ratiney et al. [156]. The following steps are considered:

STEP.1 Estimate the baseline-free signal by truncation of the first points

STEP.2 Apply ECD-QUEST on the truncated baseline-free signal.

STEP.3 Extrapolate baseline-free model on the first points, and subtract result from raw signal. Result estimates baseline.

STEP.4 Model baseline (HSVD, splines, LOWESS (applied in the spectral domain), etc.).

STEP.5 Use (Subtract- or Inbase-) QUEST to estimate final metabolites, imputing raw signal and the ECD corrected basis-set signals computed inside STEP.2.

In chapter IV, a novel method to estimate metabolites, based on the properties of the assumed common decay function, has been presented. Although validation tests have been performed, they represent a proof-of-concept, and current application to *in vivo* data is not possible *as is*. Some of the most important leads in the further development of $\mathfrak{C}_2$ are:

- Poor convergence of the minimization procedure, although the cost function is shown to have a reachable global minimum, shows, in out opinion, that a tailored minimization procedure should be implemented.
- Combination of $\mathfrak{C}_1$ and $\mathfrak{C}_2$ can be improved by using some sort of filtering for the ECD function inside $\mathfrak{C}_1$, in a similar way as in chapter III.

Bibliography

[1] W. Abi-Saab, D. Maggs, T. Jones, R. Jacob, V. Srihari, J. Thompson, D. Kerr, P. Leone, J. Krystal, D. Spencer, et al. Striking Differences in Glucose and Lactate Levels Between Brain Extracellular Fluid and Plasma in Conscious Human Subjects: Effects of Hyperglycemia and Hypoglycemia. *Journal of Cerebral Blood Flow & Metabolism*, 22(3):271–279, 2002. ↪p.31

[2] M. Ala-Korpela. Critical evaluation of 1H NMR metabonomics of serum as a methodology for disease risk assessment and diagnostics. *Clin Chem Lab Med*, 46(1):27–42, 2008. doi:10.1515/CCLM.2008.006. ↪p.1, 5

[3] B. Alberts, D. Bray, A. Johnson, J. Lewis, M. Raff, K. Roberts, and P. Walter. *Essential Cell Biology: An Introduction to the Molecular Biology of the Cell*. Garland Publishing Inc., 1 edition, 1998. ISBN 0-8153-2971-7. ↪p.34

[4] E. Andrew, A. Bradbury, and R. Eades. Removal of dipolar broadening of nuclear magnetic resonance spectra of solids by specimen rotation. *Nature*, 183:1802–1803, 1959. doi:10.1038/1831802a0. ↪p.19

[5] F. Anscombe. Graphs in statistical analysis. *The American Statistician*, 27(1):17–21, 1973. ↪p.63, 64

[6] M. Bagory, F. Durand-Dubief, D. Ibarrola, C. Confavreux, and D. Sappey-Marinier. "Absolute" quantification in magnetic resonance spectroscopy: validation of a clinical protocol in multiple sclerosis. *Conf Proc IEEE Eng Med Biol Soc*, 2007:3458–3461, 2007. doi:10.1109/IEMBS.2007.4353075. ↪p.100

[7] D. Barache, J.-P. Antoine, and J.-M. Dereppe. The Continuous Wavelet Transform, an Analysis Tool for NMR Spectroscopy. *Journal of Magnetic Resonance*, 128(1):1 – 11, 1997. ISSN 1090-7807. doi:10.1006/jmre.1997.1214. ↪p.62

[8] P. B. Barker and D. D. Lin. In vivo proton MR spectroscopy of the human brain. *Progress in Nuclear Magnetic Resonance Spectroscopy*, 49(2):99 – 128, 2006. ISSN 0079-6565. doi:10.1016/j.pnmrs.2006.06.002. ↪p.22, 27

[9] H. Barkhuijsen, B. DE, et al. Error theory for time-domain signal analysis with linear prediction and singular value decomposition. *Journal of magnetic resonance*, 67(2):371–375, 1986. ↪p.70

[10] R. Barták. Modelling soft constraints: a survey. *Neural Network World*, 12:421–431, 2002. ↪p.45

[11] R. Bartha, D. Drost, R. Menon, and P. Williamson. Spectroscopic lineshape correction by QUECC: combined QUALITY deconvolution and eddy current correction. *Magnetic Resonance in Medicine*, 44(4):641–645, 2000. ↪p.62, 63, 80

[12] N. Beckmann, R. P. Hof, and M. Rudin. The role of magnetic resonance imaging and spectroscopy in transplantation: from animal models to man. *NMR Biomed*, 13(6):329–348, Oct 2000. ↪p.5

[13] D. Belkić. Exact quantification of time signals in Padé-based magnetic resonance spectroscopy. *Phys Med Biol*, 51(10):2633–2670, May 2006. doi:10.1088/0031-9155/51/10/018. ↪p.42

[14] D. Belkić. Exponential convergence rate (the spectral convergence) of the fast Padé transform for exact quantification in magnetic resonance spectroscopy. *Phys Med Biol*, 51(24):6483–6512, Dec 2006. doi:10.1088/0031-9155/51/24/014. ↪p.42

[15] D. Belkić and K. Belkić. The fast Padé transform in magnetic resonance spectroscopy for potential improvements in early cancer diagnostics. *Phys Med Biol*, 50(18):4385–4408, Sep 2005. doi:10.1088/0031-9155/50/18/010. ↪p.42

[16] D. Belkić and K. Belkić. In vivo magnetic resonance spectroscopy by the fast Padé transform. *Phys Med Biol*, 51(5):1049–1075, Mar 2006. doi:10.1088/0031-9155/51/5/001. ↪p.42, 43

[17] D. Belkić and K. Belkić. Decisive role of mathematical methods in early cancer diagnostics: optimized Pade-based magnetic resonance spectroscopy. *Journal of Mathematical Chemistry*, 42(1):1–35, 2007. doi:10.1007/s10910-007-9227-9. ↪p.42

[18] D. Belkić and K. Belkić. Exact quantification of time signals from magnetic resonance spectroscopy by the fast Padé transform with applications to breast cancer diagnostics. *Journal of Mathematical Chemistry*, 45(3):790–818, 2009. doi:10.1007/s10910-008-9462-8. ↪p.42, 56

[19] D. Belkić and K. Belkić. The general concept of signal–noise separation (SNS): mathematical aspects and implementation in magnetic resonance spectroscopy. *Journal of Mathematical Chemistry*, 45(3):563–597, 2009. ↪p.42, 56

[20] D. Bendahan, J. Mattei, S. Guis, G. Kozak-Ribbens, and P. Cozzone. Explorations de la fonction musculaire par spectrométrie et imagerie de résonance magnétique. *Revue Neurologique*, 162(4):467 – 484, 2006. ISSN 0035-3787. doi:10.1016/S0035-3787(06)75038-X. ↪p.1, 5

[21] H. Benoit-Cattin, G. Collewet, B. Belaroussi, H. Saint-Jalmes, and C. Odet. The SIMRI project: a versatile and interactive MRI simulator. *Journal of Magnetic Resonance*, 173(1): 97 – 115, 2005. ISSN 1090-7807. doi:10.1016/j.jmr.2004.09.027. ↪p.137

[22] H. Bhat, B. R. Sajja, and P. A. Narayana. Fast quantification of proton magnetic resonance spectroscopic imaging with artificial neural networks. *Journal of Magnetic Resonance*, 183 (1):110 – 122, 2006. ISSN 1090-7807. doi:10.1016/j.jmr.2006.08.004. ↪p.56

[23] F. Bloch. Nuclear Induction. *Phys. Rev.*, 70:460, 1946. ↪p.12

[24] P. Bolan, W. Aufferman, P. Henry, and M. Garwood. Feasibility of computer-intensive methods for estimating the variance of spectral fitting parameters. In *Proceedings of the 12th annual meeting ISMRM (abstract 304). Kyoto*, 2004. ↪p.69

[25] P. Bottomley. Spatial localization in NMR spectroscopy in vivo. *Annals of the New York Academy of Sciences*, 508:333, 1987. doi:10.1111/j.1749-6632.1987.tb32915.x. ↪p.21

[26] G. Brelstaff, M. Bicego, N. Culeddu, and M. Chessa. Bag of Peaks: interpretation of NMR spectrometry. *Bioinformatics*, 25(2):258, 2009. ↪p.69

[27] M. Brennan, A. Spillane, and N. Houssami. The role of breast MRI in clinical practice. *Aust Fam Physician*, 38(7):513–519, Jul 2009. ↪p.23

[28] G. Bretthorst, W. Hutton, J. Garbow, and J. Ackerman. Exponential parameter estimation (in NMR) using Bayesian probability theory. *Concepts in Magnetic Resonance Part A*, 27 (2):55, 2005. doi:10.1002/cmr.a.20043. ↪p.65

[29] T. Brown, B. Kincaid, and K. Ugurbil. NMR chemical shift imaging in three dimensions. *Proceedings of the National Academy of Sciences*, 79(11):3523, 1982. ↪p.26

[30] J. A. Calvar. Accurate 1H tumor spectra quantification from acquisitions without water suppression. *Magnetic Resonance Imaging*, 24(9):1271 – 1279, 2006. ISSN 0730-725X. doi:10.1016/j.mri.2006.06.001. ↪p.57

[31] H. Y. Carr and E. M. Purcell. Effects of Diffusion on Free Precession in Nuclear Magnetic Resonance Experiments. *Phys. Rev.*, 94(3):630–638, May 1954. doi:10.1103/PhysRev.94.630. ↪p.20

[32] S. Cavassila, S. Deval, C. Huegen, D. van Ormondt, and D. Graveron-Demilly. Cramér-Rao Bound Expressions for Parametric Estimation of Overlapping Peaks: Influence of Prior Knowledge. *Journal of Magnetic Resonance*, 143(2):311 – 320, 2000. ISSN 1090-7807. doi:10.1006/jmre.1999.2002. ↪p.70, 71, 83

[33] S. Cavassila, S. Deval, C. Huegen, D. van Ormondt, and D. Graveron-Demilly. Cramér-Rao bounds: an evaluation tool for quantitation. *NMR Biomed*, 14(4):278–283, Jun 2001. ↪p.71, 135, 136

[34] S. Cavassila, D. van Ormondt, and D. Graveron-Demilly. *Cramer–Rao bound analysis of spectroscopic signal processing methods*, chapter 21, pages 613–637. CRC, 2002. ↪p.70

[35] J. Chen, Y. Wu, P. DeCarolis, R. O'Connor, C. Somberg, and S. Singer. Resolution of creatine and phosphocreatine 1H signals in isolated human skeletal muscle using HR-MAS 1H NMR. *Magnetic resonance in medicine: official journal of the Society of Magnetic Resonance in Medicine/Society of Magnetic Resonance in Medicine*, 59(6):1221, 2008. ↪p.30

[36] C. Childs, Y. Hiltunen, R. Vidyasagar, and R. A. Kauppinen. Determination of regional brain temperature using proton magnetic resonance spectroscopy to assess brain-body temperature differences in healthy human subjects. *Magn Reson Med*, 57(1):59–66, Jan 2007. doi:10.1002/mrm.21100. ↪p.35

[37] S. Chung, Y. Lu, and R. G. Henry. Comparison of bootstrap approaches for estimation of uncertainties of DTI parameters. *NeuroImage*, 33(2):531 – 541, 2006. ISSN 1053-8119. doi:10.1016/j.neuroimage.2006.07.001. ↪p.69

[38] W. Cleveland. Robust locally weighted regression and smoothing scatterplots. *Journal of the American Statistical Association*, pages 829–836, 1979. ↪p.viii, 91, 93, 135

[39] W. Cleveland and S. Devlin. Locally weighted regression: an approach to regression analysis by local fitting. *Journal of the American Statistical Association*, 83(403):596–610, 1988. ↪p.91

[40] W. S. Cleveland. LOWESS: A Program for Smoothing Scatterplots by Robust Locally Weighted Fitting. *The American Statistician*, page 35:54, 1981. ↪p.91

[41] W. S. Cleveland and E. Grosse. Computational Methods for Local Fitting. *Statistics and Computing*, 1:47–62, 1991. ↪p.91

[42] W. S. Cleveland, E. Grosse, and M. Shyu. *Statistical Models in S*. Chapman and Hall, 1992. ↪p.91

[43] J. Cooley and J. Tukey. An algorithm for the machine calculation of complex Fourier series. *Mathematics of computation*, 19(90):297–301, 1965. ↪p.vii, 40, 164

[44] A. D. Costanzo, F. Trojsi, M. Tosetti, T. Schirmer, S. M. Lechner, T. Popolizio, and T. Scarabino. Proton MR spectroscopy of the brain at 3 T: an update. *Eur Radiol*, 17(7):1651–1662, Jul 2007. doi:10.1007/s00330-006-0546-1. ↪p.1, 5

[45] H. Cramér. *Mathematical Methods of Statistics*. Princeton University Press, 1946. ↪p.vii, 70

[46] C. Cudalbu, V. Mlynárik, L. Xin, and R. Gruetter. Comparison of two approaches to model the macromolecule spectrum for the quantification of short TE H MRS spectra. In *IEEE International Workshop on Imaging Systems and Techniques, 2008. IST 2008*, pages 311–314, 2008. ↪p.34

[47] A. Davison and D. Hinkley. *Bootstrap methods and their application*. Cambridge Univ Pr, 1997. ↪p.66, 68, 69

[48] R. de Beer and D. van Ormondt. Analysis of NMR Data Using Time Domain Fitting Procedures. *In-vivo Magnetic Resonance Spectroscopy: Probeheads and radiofrequency pulses spectrum analysis*, page 201, 1992. ↪p.70

[49] A. A. de Graaf, J. E. van Dijk, and W. M. Bovée. Quality: quantification improvement by converting lineshapes to the lorentzian type. *Magn Reson Med*, 13(3):343–357, Mar 1990. ↪p.62, 80

[50] R. de Graaf. *In vivo NMR Spectroscopy: Principles and Techniques*. John Wiley & Sons, second edition edition, 2007. ↪p.17

[51] B. M. Delattre, R. M. Heidemann, L. A. Crowe, J.-P. Vallï¿½e, and J.-N. Hyacinthe. Spiral demystified. *Magnetic Resonance Imaging*, In Press, Corrected Proof:–, 2010. ISSN 0730-725X. doi:10.1016/j.mri.2010.03.036. ↪p.26

[52] M. Doyle and P. Mansfield. Chemical-shift imaging: a hybrid approach. *Mag. Reson. Med*, 5:255–61, 1987. ↪p.26

[53] J. H. Duyn and C. T. Moonen. Fast proton spectroscopic imaging of human brain using multiple spin-echoes. *Magn Reson Med*, 30(4):409–414, Oct 1993. ↪p.26

[54] S. Eddy. What is Bayesian statistics? *NATURE BIOTECHNOLOGY*, 22(9):1177, 2004. URL http://selab.janelia.org/publications/Eddy-ATG3/Eddy-ATG3-reprint.pdf. ↪p.65

[55] B. Efron. Bootstrap methods: another look at the jackknife. *The Annals of Statistics*, 7(1): 1–26, 1979. ↪p.68

[56] B. Efron and R. Tibshirani. An introduction to the bootstrap. *Monographs on Statistics and Applied Probability*, 57, 1993. ↪p.68

[57] C. Elster, F. Schubert, A. Link, M. Walzel, F. Seifert, and H. Rinneberg. Quantitative magnetic resonance spectroscopy: semi-parametric modeling and determination of uncertainties. *Magn Reson Med*, 53(6):1288–1296, Jun 2005. doi:10.1002/mrm.20500. ↪p.56, 66

[58] W. Ewens and G. Grant. *Statistical methods in bioinformatics: an introduction*. Springer Verlag, 2001. ↪p.66

[59] F. Fischbach and H. Bruhn. Assessment of in vivo 1h magnetic resonance spectroscopy in the liver: a review. *Liver Int*, 28(3):297–307, Mar 2008. doi:10.1111/j.1478-3231.2007.01647.x. ↪p.1, 5

[60] E. Fischi Gómez. Inhomogeneity Correction in High Field Magnetic Resonance Images: Human Brain Imaging at 7 Tesla. Master's thesis, Universitat Politècnica de Catalunya, 2009. ↪p.14

[61] J. Frahm, K. Merboldt, and W. Hänicke. Localized proton spectroscopy using stimulated echoes. *Journal of magnetic resonance*, 72(3):502–508, 1987. ↪p.21

[62] S. Furuya, S. Naruse, M. Ide, H. Morishita, O. Kizu, S. Ueda, and T. Maeda. Evaluation of metabolic heterogeneity in brain tumors using 1 H-chemical shift imaging method. *NMR in Biomedicine*, 10(1):25–30, 1997. ↪p.31

[63] R. E. Gabr, R. Ouwerkerk, and P. A. Bottomley. Quantifying in vivo mr spectra with circles. *J Magn Reson*, 179(1):152–163, Mar 2006. doi:10.1016/j.jmr.2005.11.004. ↪p.48, 56, 57

[64] F. Gallagher, M. Kettunen, S. Day, D. Hu, J. Ardenkjær-Larsen, et al. Magnetic resonance imaging of pH in vivo using hyperpolarized 13C-labelled bicarbonate. *Nature*, 453(7197): 940–943, 2008. doi:10.1038/nature07017. ↪p.35

[65] P. Good. *Resampling methods: a practical guide to data analysis*. Birkhauser, second edition edition, 2001. ↪p.69

[66] M. Gottschalk, L. Lamalle, and C. Segebarth. Short-TE localised 1H MRS of the human brain at 3 T: quantification of the metabolite signals using two approaches to account for macromolecular signal contributions. *NMR in Biomedicine*, 21(5):507–517, 2008. ↪p.29

[67] V. Govindaraju, K. Young, and A. Maudsley. Proton NMR chemical shifts and coupling constants for brain metabolites. *NMR in Biomedicine*, 13(3):129–153, 2000. ↪p.30, 31, 32, 33, 78, 101

[68] I. D. Grachev, A. Swarnkar, N. M. Szeverenyi, T. S. Ramachandran, and A. V. Apkarian. Aging alters the multichemical networking profile of the human brain: an in vivo (1)h-mrs study of young versus middle-aged subjects. *J Neurochem*, 77(1):292–303, Apr 2001. ↪p.30

[69] D. Graveron-Demilly, A. Diop, A. Briguet, and B. Fenet. Product-operator algebra for strongly coupled spin systems. *Journal of Magnetic Resonance*, A101:233–239, 1993. ↪p.58, 86, 119, 137

[70] R. Gruetter. Automatic, localized in vivo adjustment of all first- and second-order shim coils. *Magn Reson Med*, 29(6):804–811, Jun 1993. ↪p.14

[71] R. Gruetter and I. Tkac. Field mapping without reference scan using asymmetric echo-planar techniques. *Magn Reson Med*, 43(2):319–323, Feb 2000. ↪p.14

[72] R. Gruetter, K. Ugurbil, and E. Seaquist. Steady-state cerebral glucose concentrations and transport in the human brain. *Journal of neurochemistry*, 70:397–408, 1998. ↪p.32

[73] E. D. Grunewald and R. J. Knight. Conditions leading to non-exponential T2* relaxation and implications for the interpretation of MRS measurements. *AGU Fall Meeting Abstracts*, pages A1+, Dec. 2009. ↪p.15

[74] A. Guimaraes, J. Baker, B. Jenkins, P. Lee, R. Weisskoff, B. Rosen, and R. Gonzalez. Echoplanar chemical shift imaging. *Magnetic Resonance in Medicine*, 41(5):877–882, 1999. ↪p.27, 28

[75] E. Haacke, R. Brown, M. Thompson, and R. Venkatesan. *Magnetic resonance imaging: physical principles and sequence design*. Wiley New York, 1999. ↪p.12

[76] I. S. Haddadin, A. McIntosh, S. Meisamy, C. Corum, A. L. S. Snyder, N. J. Powell, M. T. Nelson, D. Yee, M. Garwood, and P. J. Bolan. Metabolite quantification and high-field mrs in breast cancer. *NMR Biomed*, 22(1):65–76, Jan 2009. doi:10.1002/nbm.1217. ↪p.1, 5

[77] E. Hahn. Spin echoes. *Phys. Rev Phys Rev*, 80:580, 1950. ↪p.20

[78] L. D. Hall, V. Rajanayagam, and S. Sukumar. Chemical-shift-resolved tomography using four-dimensional ft imaging. *Journal of Magnetic Resonance (1969)*, 61(1):188 – 191, 1985. ISSN 0022-2364. doi:10.1016/0022-2364(85)90284-7. ↪p.26

[79] S. Heim, K. Hahn, and D. Auer. Diffusion Tensor Imaging: on the assessment of data quality–a preliminary bootstrap analysis, 2003. ↪p.69

[80] C. Holloway and K. Clarke. Is MR spectroscopy of the heart ready for humans? *Heart Lung Circ*, 19(3):154–160, Mar 2010. doi:10.1016/j.hlc.2010.01.007. ↪p.1, 5

[81] D. F. Howarth, J. A. Weil, and Z. Zimpel. Generalization of the lineshape useful in magnetic resonance spectroscopy. *Journal of Magnetic Resonance*, 161(2):215 – 221, 2003. ISSN 1090-7807. doi:10.1016/S1090-7807(02)00195-7. ↪p.60

[82] C. Huegen. The influence of prior knowledge on Cramér-Rao lower bounds. Master's thesis, TU Delft, 1993. ↪p.70

[83] J. W. Hugg, A. A. Maudsley, M. W. Weiner, and G. B. Matson. Comparison of k-space sampling schemes for multidimensional MR spectroscopic imaging. *Magn Reson Med*, 36(3): 469–473, Sep 1996. ↪p.26

[84] D. Ishigaki, K. Ogasawara, Y. Yoshioka, K. Chida, M. Sasaki, S. Fujiwara, K. Aso, M. Kobayashi, K. Yoshida, K. Terasaki, et al. Brain Temperature Measured Using Proton MR Spectroscopy Detects Cerebral Hemodynamic Impairment in Patients With Unilateral Chronic Major Cerebral Artery Steno-Occlusive Disease: Comparison With Positron Emission Tomography. *Stroke*, 40(9):3012, 2009. doi:10.1161/STROKEAHA.109.555508. ↪p.35

[85] H. Jimenez-Dominguez, S. Cruz-Jiménez, and A. Cabral-Prieto. Spectroscopic applications of the plasma dispersion function. II: An asymmetric lineshape model and the complex susceptibility. *Spectrochimica Acta Part B: Atomic Spectroscopy*, 52(8):1113 – 1124, 1997. ISSN 0584-8547. doi:10.1016/S0584-8547(97)00030-X. ↪p.62

[86] C. Juchem, N. K. Logothetis, and J. Pfeuffer. 1H-MRS of the macaque monkey primary visual cortex at 7 T: strategies and pitfalls of shimming at the brain surface. *Magnetic Resonance Imaging*, 25(6):902 – 912, 2007. ISSN 0730-725X. doi:10.1016/j.mri.2007.03.008. Proceedings of the International School on Magnetic Resonance and Brain Function, Proceedings of the International School on Magnetic Resonance and Brain Function. ↪p.84, 120

[87] G. Kalpouzos, G. Chïż½telat, J.-C. Baron, B. Landeau, K. Mevel, C. Godeau, L. Barrïż½, J.-M. Constans, F. Viader, F. Eustache, and B. Desgranges. Voxel-based mapping of brain gray matter volume and glucose metabolism profiles in normal aging. *Neurobiology of Aging*, 30(1):112 – 124, 2009. ISSN 0197-4580. doi:10.1016/j.neurobiolaging.2007.05.019. ↪p.32

[88] U. Klose. In vivo proton spectroscopy in presence of eddy currents. *Magn Reson Med*, 14(1): 26–30, Apr 1990. ↪p.62, 80

[89] U. Klose. Measurement sequences for single voxel proton MR spectroscopy. *European Journal of Radiology*, 67(2):194–201, 2008. ↪p.21, 22

[90] T. Koch and P. Feist. NMR Theory Course, 2003. URL http://orgchem.colorado.edu/hndbksupport/nmrtheory/NMRtutorial.html. ↪p.17

[91] R. Kreis. Issues of spectral quality in clinical 1h-magnetic resonance spectroscopy and a gallery of artifacts. *NMR Biomed*, 17(6):361–381, Oct 2004. doi:10.1002/nbm.891. ↪p.72, 135, 136, 137

[92] S. Kung, K. Arun, and D. Bhaskar Rao. State-space and singular-value decomposition-based approximation methods for the harmonic retrieval problem. *J. Opt. Soc. Am*, 73:1799–1811, 1983. doi:10.1364/JOSA.73.001799. ↪p.40

[93] T. Laudadio, N. Mastronardi, L. Vanhamme, P. V. Hecke, and S. V. Huffel. Improved Lanczos Algorithms for Blackbox MRS Data Quantitation. *Journal of Magnetic Resonance*, 157(2): 292 – 297, 2002. ISSN 1090-7807. doi:10.1006/jmre.2002.2593. ↪p.42

[94] P. C. Lauterbur. Image Formation by Induced Local Interactions: Examples Employing Nuclear Magnetic Resonance. *Nature*, 242:190–191, 1973. doi:10.1038/242190a0. ↪p.23

[95] B. S. Y. Li, H. Wang, and O. Gonen. Metabolite ratios to assumed stable creatine level may confound the quantification of proton brain mr spectroscopy. *Magn Reson Imaging*, 21(8): 923–928, Oct 2003. ↪p.30

[96] Y. Li, R. Srinivasan, H. Ratiney, Y. Lu, S. Chang, and S. Nelson. Comparison of T (1) and T (2) metabolite relaxation times in glioma and normal brain at 3T. *Journal of magnetic resonance imaging: JMRI*, 28(2):342, 2008. doi:10.1002/jmri.21453. ↪p.57

[97] S. Ljunggren. A simple graphical representation of Fourier-based imaging methods. *J. Magn. Reson*, 54(2):338–343, 1983. ↪p.23

[98] R. Lupton. *Statistics in theory and practice*. Princeton Univ Pr, 1993. ↪p.65

[99] A. Maataoui, J. Gurung, H. Ackermann, N. Abolmaali, K. Kafchitsas, T. J. Vogl, and M. F. Khan. Facilitating cartilage volume measurement using mri. *European Journal of Radiology*, In Press, Corrected Proof:–, 2009. ISSN 0720-048X. doi:10.1016/j.ejrad.2009.05.005. ↪p.23

[100] I. Mader, U. Seeger, R. Weissert, U. Klose, T. Naegele, A. Melms, and W. Grodd. Proton MR spectroscopy with metabolite-nulling reveals elevated macromolecules in acute multiple sclerosis. *Brain*, 124(5):953, 2001. ↪p.34

[101] I. Mader, S. Rauer, P. Gall, and U. Klose. ^{1}H MR spectroscopy of inflammation, infection and ischemia of the brain. *European Journal of Radiology*, 67(2):250 – 257, 2008. ISSN 0720-048X. doi:10.1016/j.ejrad.2008.02.033. Clinical 1H MR Spectroscopy. ↪p.33, 34

[102] C. Madhavarao, P. Arun, J. Moffett, S. Szucs, S. Surendran, R. Matalon, J. Garbern, D. Hristova, A. Johnson, W. Jiang, et al. Defective N-acetylaspartate catabolism reduces brain acetate levels and myelin lipid synthesis in Canavan's disease. *Proceedings of the National Academy of Sciences*, 102(14):5221, 2005. ↪p.31

[103] K. Madsen, H. B. Nielsen, and O. Tingleff. Methods for non-linear least squares problems (2nd ed.), 2004. URL http://www2.imm.dtu.dk/pubdb/views/edoc_download.php/3215/pdf/imm3215.pdf. ↪p.46

[104] Maplesoft. Maple, 2007. ↪p.83

[105] I. Markovsky and S. V. Huffel. Overview of total least-squares methods. *Signal Processing*, 87(10):2283 – 2302, 2007. ISSN 0165-1684. doi:10.1016/j.sigpro.2007.04.004. Special Section: Total Least Squares and Errors-in-Variables Modeling. ↪p.42

[106] I. Marshall, J. Higinbotham, S. Bruce, and A. Freise. Use of voigt lineshape for quantification of in vivo 1h spectra. *Magn Reson Med*, 37(5):651–657, May 1997. doi:10.1002/mrm.1910370504. ↪p.60

[107] A. Maudsley, S. Hilal, W. Perman, and H. Simon. Spatially resolved high resolution spectroscopy by "four-dimensional" NMR . *Journal of Magnetic Resonance*, 51:147–152, 1983. ↪p.26

[108] A. A. Maudsley, Z. Wu, D. J. Meyerhoff, and M. W. Weiner. Automated processing for proton spectroscopic imaging using water reference deconvolution. *Magn Reson Med*, 31(6): 589–595, Jun 1994. ↪p.62

[109] S. M'hiri, L. Cammoun, and F. Ghorbel. Speeding up HMRF-EM algorithms for fast unsupervised image segmentation by Bootstrap resampling: Application to the brain tissue segmentation. *Signal Processing*, 87(11):2544 – 2559, 2007. ISSN 0165-1684. doi:10.1016/j.sigpro.2007.04.010. ↪p.69

[110] S. Mierisová and M. Ala-Korpela. MR spectroscopy quantitation: a review of frequency domain methods. *NMR Biomed*, 14(4):247–259, Jun 2001. ↪p.49, 57, 138

[111] J. B. Miller and A. N. Garroway. Removal of static field inhomogeneity and chemical-shift effects in nmr imaging. *Journal of Magnetic Resonance (1969)*, 67(3):575 – 579, 1986. ISSN 0022-2364. doi:10.1016/0022-2364(86)90397-5. ↪p.26

[112] G. L. Millhauser, A. A. Carter, D. J. Schneider, J. H. Freed, and R. E. Oswald. Rapid singular value decomposition for time-domain analysis of magnetic resonance signals by use of the lanczos algorithm. *Journal of Magnetic Resonance (1969)*, 82(1):150 – 155, 1989. ISSN 0022-2364. doi:10.1016/0022-2364(89)90175-3. ↪p.42

[113] V. Mlynárik, G. Gambarota, H. Frenkel, and R. Gruetter. Localized short-echo-time proton MR spectroscopy with full signal-intensity acquisition. *Magnetic Resonance in Medicine*, 56 (5):965–970, 2006. ↪p.29

[114] J. Moffett and A. Namboodiri. Expression of n-acetylaspartate and n-acetylaspartylglutamate in the nervous system. *Advances in experimental medicine and biology*, 576:7, 2006. ↪p.31

[115] C. Moonen, M. Von Kienlin, P. van Zijl, J. Cohen, J. Gillen, P. Daly, and G. Wolf. Comparison of single-shot localization methods (STEAM and PRESS) for in vivo proton NMR spectroscopy. *NMR Biomed.*, 2:201–208, 1989. ↪p.22

[116] J. More. The Levenberg-Marquardt algorithm: Implementation and theory. *Numerical analysis: proceedings of the Biennial Conference held at Dundee, June 28-July 1, 1977*, page 105, 1978. ↪p.54

[117] G. Morris. Compensation of instrumental imperfections by deconvolution using a internal reference signal. *Journal of magnetic resonance*, 80(3):547–552, 1988. ↪p.62, 63

[118] U. G. Mueller-Lisse and M. K. Scherr. Proton mr spectroscopy of the prostate. *Eur J Radiol*, 63(3):351–360, Sep 2007. doi:10.1016/j.ejrad.2007.06.024. ↪p.1, 5

[119] R. Mulkern and L. Panych. Echo planar spectroscopic imaging. *Concepts in Magnetic Resonance*, 13(4):213–237, 2001. doi:10.1002/cmr.1011. ↪p.26

[120] J. J. Neil and G. L. Bretthorst. On the use of bayesian probability theory for analysis of exponential decay data: an example taken from intravoxel incoherent motion experiments. *Magn Reson Med*, 29(5):642–647, May 1993. ↪p.65

[121] B. D. Neuter, J. Luts, L. Vanhamme, P. Lemmerling, and S. V. Huffel. Java-based framework for processing and displaying short-echo-time magnetic resonance spectroscopy signals. *Comput Methods Programs Biomed*, 85(2):129–137, Feb 2007. doi:10.1016/j.cmpb.2006.09.005. ↪p.53

[122] NIST. N.I.S.T./Sematech e-Handbook of Statistical Methods, 2003. URL http://www.itl.nist.gov/div898/handbook/pmd/section1/pmd144.htm. Section 4.1.4.4. ↪p.91

[123] NIST. The NIST Reference on Constants, Units and Uncertainty, 2006. URL http://physics.nist.gov/cuu/Constants/. ↪p.10

[124] E. Odeblad. Research in obstetrics and gynecology with nuclear magnetic resonance. *Acta Obstetricia et Gynecologica Scandinavica*, 38(4):599–617, 1959. doi:10.3109/00016345909153956. ↪p.1, 5

[125] J. Okuda, I. Miwa, M. Sato, and T. Murata. Uptake of d-glucose anomers by rat retina. *Experientia*, 33(1):19–20, Jan 1977. ↪p.32

[126] M. Osorio, D. Sima, J. Poullet, S. Van Huffel, and D. van Ormondt. Improvement of lineshape estimation for MRS signals. In *IEEE International Workshop on Imaging Systems and Techniques, 2008. IST 2008*, pages 326–329, 2008. ↪p.4, 7

[127] M. Osorio Garcia, D. Sima, J. Poullet, D. Ormondt, and S. Huffel. Iterative improvement of lineshape estimation. In *4th European Conference of the International Federation for Medical and Biological Engineering*, pages 138–141. Springer, 2009. ↪p.4, 7

[128] W. H. Perman, N. C. Balci, and I. Akduman. Review of magnetic resonance spectroscopy in the liver and the pancreas. *Top Magn Reson Imaging*, 20(2):89–97, Apr 2009. doi:10.1097/RMR.0b013e3181c422f1. ↪p.1, 5

[129] T. Perry, K. Berry, S. Hansen, S. Diamond, and C. Mok. Regional distribution of amino acids in human brain obtained at autopsy. *Journal of neurochemistry*, 18(3):513, 1971. ↪p.33

[130] W. W. F. Pijnappel, A. van den Boogaart, R. de Beer, and D. van Ormondt. SVD-based quantification of magnetic resonance signals. *Journal of Magnetic Resonance (1969)*, 97(1): 122 – 134, 1992. ISSN 0022-2364. doi:10.1016/0022-2364(92)90241-X. ↪p.42

[131] R. Pohmann, M. von Kienlin, and A. Haase. Theoretical evaluation and comparison of fast chemical shift imaging methods. *Journal of Magnetic Resonance*, 129(2):145 – 160, 1997. ISSN 1090-7807. doi:10.1006/jmre.1997.1245. ↪p.22

[132] E. Popa, D. Graveron-Demilly, E. Capobianco, R. de Beer, and D. van Ormondt. Lineshape estimation in *in vivo* MR Spectroscopy without using a reference signal. In *Proc. IEEE International Workshop on Imaging Systems and Techniques IST 2008*, pages 315–320, September 2008. doi:10.1109/IST.2008.4659992. ↪p.98

[133] E. Popa, E. Capobianco, R. de Beer, D. van Ormondt, and D. Graveron-Demilly. In vivo quantitation of metabolites with an incomplete model function. *Measurement Science and Technology*, 20(10):104032, 2009. doi:10.1088/0957-0233/20/10/104032. ↪p.117, 118

[134] S. Posse, C. DeCarli, and D. Le Bihan. Three-dimensional Echo-planar MR Spectroscopic Imaging at Short Echo Times in the Human Brain. *Radiology*, 192(3):733–738, 1994. ↪p.26, 27, 28

[135] S. Posse, G. Tedeschi, R. Risinger, R. Ogg, and D. L. Bihan. High speed 1H spectroscopic imaging in human brain by echo planar spatial-spectral encoding. *Magn Reson Med*, 33(1): 34–40, Jan 1995. ↪p.27

[136] J.-B. Poullet. *Quantification and Classification of Magnetic Resonance Spectroscopic Data for Brain Tumor Diagnosis*. PhD thesis, Katholieke Universiteit Leuven, November 2008. ↪p.30, 32, 42, 48, 54

[137] J.-B. Poullet. SPID: Simulation Package based on *In Vitro* Databases, 2008. URL http://homes.esat.kuleuven.be/~biomed/. v0.1. ↪p.53

[138] J.-B. Poullet, D. M. Sima, A. W. Simonetti, B. D. Neuter, L. Vanhamme, P. Lemmerling, and S. V. Huffel. An automated quantitation of short echo time mrs spectra in an open source software environment: Aqses. *NMR Biomed*, 20(5):493–504, Aug 2007. doi:10.1002/nbm.1112. ↪p.vii, 53, 57, 63, 138

[139] J.-B. Poullet, D. M. Sima, and S. V. Huffel. MRS signal quantitation: a review of time- and frequency-domain methods. *J Magn Reson*, 195(2):134–144, Dec 2008. doi:10.1016/j.jmr.2008.09.005. ↪p.48, 49, 56, 57, 138

[140] W. Press, S. Teukolsky, W. Vetterling, and B. Flannery. *Numerical recipes: the art of scientific computing*. Cambridge Univ Pr, 2007. ↪p.40, 45, 63, 64, 66, 67, 68

[141] M. Preul, Z. Caramanos, D. Collins, J. Villemure, R. Leblanc, A. Olivier, R. Pokrupa, and D. Arnold. Accurate, noninvasive diagnosis of human brain tumors by using proton magnetic resonance spectroscopy. *NATURE MEDICINE*, 2(3):323–325, MAR 1996. ISSN 1078-8956. ↪p.32

[142] S. Provencher. A constrained regularization method for inverting data represented by linear algebraic or integral equations. *Computer Physics Communications*, 27(3):213–227, 1982. URL `http://www.s-provencher.com/pub/contin/cpc1.pdf`. ↪p.52, 94

[143] S. Provencher. CONTIN: a general purpose constrained regularization program for inverting noisy linear algebraic and integral equations. *Comput. Phys. Commun*, 27(3):229–242, 1982. URL `http://www.s-provencher.com/pub/contin/cpc2.pdf`. ↪p.52, 94

[144] S. Provencher. LCModel manual, 2010. URL `http://s-provencher.com/pages/lcm-manual.shtml`. ↪p.53

[145] S. W. Provencher. Estimation of metabolite concentrations from localized in vivo proton nmr spectra. *Magn Reson Med*, 30(6):672–679, Dec 1993. ↪p.viii, 52, 62, 63, 77

[146] S. W. Provencher. Automatic quantitation of localized in vivo 1h spectra with lcmodel. *NMR Biomed*, 14(4):260–264, Jun 2001. ↪p.49, 52

[147] I. Pykett and B. Rosen. Nuclear Magnetic Resonance: *invivo* proton chemical shift imaging. *Radiology*, 149:197–201, 1983. ↪p.26

[148] B. Quistorff, N. Secher, and J. Van Lieshout. Lactate fuels the human brain during exercise. *The FASEB Journal*, 22(10):3443, 2008. ↪p.31

[149] H. Rabeson. *Quantification semi-parametrique de signaux de Spectrométrie de Résonance Magnetique, acquis ex vivo et in vivo*. Doctorat, Université Claude-Bernard Lyon I, 2008. D. Graveron-Demilly (dir.), J.P. Antoine, A. Briguet, D. Chechin, F. Fauvelle, J.M. Franconi (rapp.),M. Piotto, D. van Ormondt (rapp.). ↪p.32, 33, 80, 101

[150] H. Rabeson, E. Capobianco, R. de Beer, D. van Ormondt, and D. Graveron-Demilly. Correction for B_0 inhomogeneity and Eddy Current effects without using a reference line. . In *Proc. 12ème congrès du GRAMM, Lyon, France, 2008*, page 101, 2008. ↪p.138

[151] L. Rabiner, R. Schafer, and C. Rader. The Chirp s-Transf orm Algorithm. *IEEE Trans. Audio Electroacoust*, 17:86–92, 1969. ↪p.164

[152] C. R. Rao. Minimum variance and the estimation of several parameters. *Proceedings of the Cambridge Philosophical Society*, 43:280, 1947. `doi:10.1017/S0305004100023471.` ↪p.vii, 70

[153] H. Ratiney. *Quantification automatique de Signaux de Spectrométrie et d'Imagerie Spctroscopique de Résonance Magnétique fondée sur une base de métabolites. Une approche semi-paramétrique*. PhD thesis, Université Claude Bernard - Lyon I, 2004. ↪p.54, 139

[154] H. Ratiney, S. Noworolski, M. Sdika, R. Srinivasan, R. Henry, S. Nelson, and D. Pelletier. Estimation of metabolite T 1 relaxation times using tissue specific analysis, signal averaging and bootstrapping from magnetic resonance spectroscopic imaging data. *Magnetic Resonance Materials in Physics, Biology and Medicine*, 20(3):143–155, 2007. ↪p.69

[155] H. Ratiney, R. Srinivasan, R. Henry, D. Okuda, S. Nelson, and D. Pelletier. Early and progressive disease marker in ms; results from a large cross-sectional spectroscopic imaging study at 3t. In *American Academy of Neurology 59th Annual Meeting*, page P02.041, BostonBoston, USA, May 2007. ↪p.34

[156] H. Ratiney, M. Sdika, Y. Coenradie, S. Cavassila, D. van Ormondt, and D. Graveron-Demilly. Time-domain semi-parametric estimation based on a metabolite basis set. *NMR IN BIOMEDICINE*, 18(1):1–13, FEB 2005. ISSN 0952-3480. doi:10.1002/nbm.895. ↪p.viii, 49, 54, 70, 77, 89, 100, 138, 139

[157] G. Reynolds, M. Wilson, A. Peet, and T. N. Arvanitis. An algorithm for the automated quantitation of metabolites in *in vitro* NMR signals. *Magn Reson Med*, 56(6):1211–1219, Dec 2006. doi:10.1002/mrm.21081. ↪p.56

[158] A. J. Ross and P. S. Sachdev. Magnetic resonance spectroscopy in cognitive research. *Brain Res Brain Res Rev*, 44(2-3):83–102, Mar 2004. doi:10.1016/j.brainresrev.2003.11.001. ↪p.30, 32

[159] T. M. Rudkin and D. L. Arnold. Proton Magnetic Resonance Spectroscopy for the Diagnosis and Management of Cerebral Disorders. *Arch Neurol*, 56(8):919–926, 1999. doi:10.1001/archneur.56.8.919. ↪p.31

[160] N. Sandgren, Y. Selén, P. Stoica, and J. Li. Parametric methods for frequency-selective MR spectroscopy - a review. *Journal of Magnetic Resonance*, 168(2):259–272, 2004. ↪p.49

[161] C. D. Schunn and D. Wallach. *Psychologie der Kognition: Reden and Vorträge anlässlich der Emeritierung von Werner Tack*, chapter Evaluating goodness-of-fit in comparison of models to data., pages 115–154. University of Saarland Press, Saarbrueken, Germany, 2005. URL http://www.lrdc.pitt.edu/schunn/gof/. ↪p.63

[162] X. Shen, H. Xiao, R. Ranallo, W.-H. Wu, and C. Wu. Modulation of atp-dependent chromatin-remodeling complexes by inositol polyphosphates. *Science*, 299(5603):112–114, Jan 2003. doi:10.1126/science.1078068. ↪p.31

[163] Z. W. Shen, Y. W. Chen, H. Y. Wang, Y. Lin, J. K. He, W. W. Liu, F. Y. Chen, and R. H. Wu. Quantification of Metabolites in Swine Brain by ^{1}H MR Spectroscopy Using LCModel and QUEST: A Comparison Study. In *Proc. Congress on Image and Signal Processing CISP '08*, volume 5, pages 299–302, may 27–30 2008. doi:10.1109/CISP.2008.478. ↪p.57

[164] P. H. Silverstone, B. M. McGrath, and H. Kim. Bipolar disorder and myo-inositol: a review of the magnetic resonance spectroscopy findings. *Bipolar Disord*, 7(1):1–10, Feb 2005. doi:10.1111/j.1399-5618.2004.00174.x. ↪p.31

[165] D. Sima and S. Van Huffel. Regularized semiparametric model identification with application to NMR signal quantification with unknown macromolecular baseline. *J. Roy. Stat. Soc. B*, 68(3), 2006. ↪p.70

[166] D. M. Sima and S. V. Huffel. Separable nonlinear least squares fitting with linear bound constraints and its application in magnetic resonance spectroscopy data quantification. *Journal of Computational and Applied Mathematics*, 203(1):264 – 278, 2007. ISSN 0377-0427. doi:10.1016/j.cam.2006.03.025. ↪p.54

[167] A. Skoch, F. Jiru, and J. Bunke. Spectroscopic imaging: Basic principles. *European Journal of Radiology*, 67(2):230 – 239, 2008. ISSN 0720-048X. doi:10.1016/j.ejrad.2008.03.003. Clinical 1H MR Spectroscopy. ↪p.27

[168] J. Slotboom, C. Boesch, and R. Kreis. Versatile frequency domain fitting using time domain models and prior knowledge. *Magn Reson Med*, 39(6):899–911, Jun 1998. ↪p.49, 56

[169] J. Slotboom, A. Nirkko, C. Brekenfeld, and D. van Ormondt. Reliability testing of in vivo magnetic resonance spectroscopy (mrs) signals and signal artifact reduction by order statistic filtering. *Measurement Science and Technology*, 20(10):104030 (14pp), 2009. doi:10.1088/0957-0233/20/10/104030. ↪p.73, 135, 136

[170] S. A. Smith, T. O. Levante, B. H. Meier, and R. R. Ernst. Computer simulations in magnetic resonance. an object-oriented programming approach. *Journal of Magnetic Resonance, Series A*, 106(1):75 – 105, 1994. ISSN 1064-1858. doi:10.1006/jmra.1994.1008. ↪p.58, 137

[171] B. J. Soher, K. Young, V. Govindaraju, and A. A. Maudsley. Automated spectral analysis iii: application to in vivo proton mr spectroscopy and spectroscopic imaging. *Magn Reson Med*, 40(6):822–831, Dec 1998. ↪p.49

[172] B. J. Soher, K. Young, A. Bernstein, Z. Aygula, and A. A. Maudsley. Gava: Spectral simulation for in vivo mrs applications. *Journal of Magnetic Resonance*, 185(2):291 – 299, 2007. ISSN 1090-7807. doi:10.1016/j.jmr.2007.01.005. ↪p.58

[173] J. Spall and J. Garner. Parameter identification for state-space models with nuisance-parameters. *IEEE Transactions on Aerospace and Electronic Systems*, 26(6):992–998, 1990. ↪p.70

[174] A. L. Stancik and E. B. Brauns. A simple asymmetric lineshape for fitting infrared absorption spectra. *Vibrational Spectroscopy*, 47(1):66 – 69, 2008. ISSN 0924-2031. doi:10.1016/j.vibspec.2008.02.009. ↪p.62

[175] D. Stefan, F. D. Cesare, A. Andrasescu, E. Popa, A. Lazariev, E. Vescovo, O. Strbak, S. Williams, Z. Starcuk, M. Cabanas, D. van Ormondt, and D. Graveron-Demilly. Quantitation of magnetic resonance spectroscopy signals: the jMRUI software package. *Measurement Science and Technology*, 20(10):104035 (9pp), 2009. URL http://stacks.iop.org/0957-0233/20/104035. ↪p.51, 54, 60, 86, 102, 138

[176] N. D. Stefano, M. Filippi, D. Miller, P. J. Pouwels, A. Rovira, A. Gass, C. Enzinger, P. M. Matthews, and D. L. Arnold. Guidelines for using proton mr spectroscopy in multicenter clinical ms studies. *Neurology*, 69(20):1942–1952, Nov 2007. doi:10.1212/01.wnl.0000291557.62706.d3. ↪p.1, 5

[177] P. Stoica and A. Nehorai. MUSIC, maximum likelihood, and Cramer-Rao bound. *IEEE Trans. Acoust., Speech, Signal Processing*, 37(5):720–741, 1989. ↪p.70

[178] R. Stoyanova and T. R. Brown. Nmr spectral quantitation by principal component analysis. *NMR Biomed*, 14(4):271–277, Jun 2001. ↪p.56

[179] Y. Su, S. B. Thakur, S. Karimi, S. Du, P. Sajda, W. Huang, and L. C. Parra. Spectrum separation resolves partial-volume effect of mrsi as demonstrated on brain tumor scans. *NMR Biomed*, 21(10):1030–1042, Nov 2008. doi:10.1002/nbm.1271. ↪p.69

[180] T. Sundin, L. Vanhamme, P. V. Hecke, I. Dologlou, and S. V. Huffel. Accurate quantification of 1h spectra: From finite impulse response filter design for solvent suppression to parameter estimation. *Journal of Magnetic Resonance*, 139(2):189 – 204, 1999. ISSN 1090-7807. doi:10.1006/jmre.1999.1782. ↪p.54

[181] J. Thurston, W. Sherman, R. Hauhart, and R. Kloepper. Myo-inositol: a newly identified nonnitrogenous osmoregulatory molecule in mammalian brain. *Pediatric Research*, 26(5):482, 1989. ↪p.31

[182] E. Titchmarsh. The zeros of certain integral functions. *Proceedings of the London Mathematical Society*, 25:283–302, 1926. ↪p.116

[183] T.-K. Truong, D. W. Chakeres, D. Q. Beversdorf, D. W. Scharre, and P. Schmalbrock. Effects of static and radiofrequency magnetic field inhomogeneity in ultra-high field magnetic resonance imaging. *Magnetic Resonance Imaging*, 24(2):103 – 112, 2006. ISSN 0730-725X. doi:10.1016/j.mri.2005.09.013. ↪p.37

[184] P. Turner, A. McLennan, A. Bates, A. McLennan, A. Bates, and M. White. *Instant notes in molecular biology*. Bios Scientific, 2000. ↪p.33

[185] D. B. Twieg. The k-trajectory formulation of the nmr imaging process with applications in analysis and synthesis of imaging methods. *Medical Physics*, 10(5):610–621, 1983. doi:10.1118/1.595331. ↪p.23

[186] A. van den Bos. A CrambRao Lower Bound for Complex Parameters. *IEEE Transactions on Signal Processing*, 42(10):2859, 1994. URL http://repository.tudelft.nl/assets/uuid:3d9b130f-c612-4ec5-8640-4a01654a85ea/ieee_vandenbos_1994.pdf. ↪p.70

[187] J. van der Veen, R. de Beer, P. Luyten, and D. van Ormondt. Accurate quantification of in vivo 31P NMR signals using the variable projection method and prior knowledge. *Magn Reson Med*, 6(1):92–98, 1988. doi:10.1002/mrm.1910060111. ↪p.51

[188] G. van Hall, M. Strømstad, P. Rasmussen, Ø. Jans, M. Zaar, C. Gam, B. Quistorff, N. Secher, and H. Nielsen. Blood lactate is an important energy source for the human brain. *Journal of Cerebral Blood Flow & Metabolism*, 2009. ↪p.31

[189] L. Vanhamme, A. van den Boogaart, and S. V. Huffel. Improved method for accurate and efficient quantification of mrs data with use of prior knowledge. *Journal of Magnetic Resonance*, 129(1):35 – 43, 1997. ISSN 1090-7807. doi:10.1006/jmre.1997.1244. ↪p.51

[190] L. Vanhamme, T. Sundin, P. V. Hecke, and S. V. Huffel. Mr spectroscopy quantitation: a review of time-domain methods. *NMR Biomed*, 14(4):233–246, Jun 2001. ↪p.48, 57, 138

[191] S. Vanhuffel, H. Chen, C. Decanniere, and P. Vanhecke. Algorithm for time-domain nmr data fitting based on total least squares. *Journal of Magnetic Resonance, Series A*, 110(2):228 – 237, 1994. ISSN 1064-1858. doi:10.1006/jmra.1994.1209. ↪p.42

[192] E. Weiland, S. Roell, D. Leibfritz, and G. Krueger. Time-domain fitting of 1H-MR spectra of the human brain: a model-free integration of the macromolecular baseline. In *Int Soc Magn Reson Med 11th Scientific Meeting and Exhibition, Toronto*, volume 1160, 2003. ↪p.55

[193] J. Weis, L. Johansson, F. Ortiz-Nieto, and H. Ahlstrï¿½m. Assessment of lipids in skeletal muscle by lcmodel and amares. *J Magn Reson Imaging*, 30(5):1124–1129, Nov 2009. doi:10.1002/jmri.21900. ↪p.57

[194] E. W. Weisstein. Noncentral F-Distribution. From MathWorld–A Wolfram Web Resource, 2010. URL http://mathworld.wolfram.com/NoncentralF-Distribution.html. ↪p.65

[195] E. W. Weisstein. Whittaker function. From Mathworld–A Wolfram Web Resource, 2010. URL http://mathworld.wolfram.com/WhittakerFunction.html. ↪p.83

[196] T. Wigren and A. Nehorai. Asymptotic Cramer-Rao bounds for estimation of the parameters ofdamped sine waves in noise. *IEEE Transactions on Signal Processing*, 39(4):1017–1020, 1991. ↪p.70

[197] M. Wilson, N. P. Davies, M.-A. Brundler, C. McConville, R. G. Grundy, and A. C. Peet. High resolution magic angle spinning ^{1}H NMR of childhood brain and nervous system tumours. *Mol Cancer*, 8:6, 2009. doi:10.1186/1476-4598-8-6. ↪p.30

[198] L. Xin, G. Gambarota, V. Mlynï¿½rik, and R. Gruetter. Proton t2 relaxation time of j-coupled cerebral metabolites in rat brain at 9.4 t. *NMR Biomed*, 21(4):396–401, May 2008. doi:10.1002/nbm.1205. ↪p.86

[199] K. Young, V. Govindaraju, B. J. Soher, and A. A. Maudsley. Automated spectral analysis i: formation of a priori information by spectral simulation. *Magn Reson Med*, 40(6):812–815, Dec 1998. ↪p.49

[200] K. Young, B. J. Soher, and A. A. Maudsley. Automated spectral analysis ii: application of wavelet shrinkage for characterization of non-parameterized signals. *Magn Reson Med*, 40(6): 816–821, Dec 1998. ↪p.49, 56

[201] Y. Zhang, S. Marenco, and J. Shen. Correction of frequency and phase variations induced by eddy currents in localized spectroscopy with multiple echo times. *Magn Reson Med*, 58(1): 174–178, Jul 2007. doi:10.1002/mrm.21265. ↪p.84

[202] Y. Zhang, S. Li, and J. Shen. Automatic high-order shimming using parallel columns mapping (pacmap). *Magn Reson Med*, 62(4):1073–1079, Oct 2009. doi:10.1002/mrm.22077. ↪p.14

[203] T. Zhu, X. Liu, P. R. Connelly, and J. Zhong. An optimized wild bootstrap method for evaluation of measurement uncertainties of dti-derived parameters in human brain. *NeuroImage*, 40 (3):1144 – 1156, 2008. ISSN 1053-8119. doi:10.1016/j.neuroimage.2008.01.016. ↪p.69

[204] A. Ziegler, M. Kienlin, M. Decorps, and C. Remy. High glycolytic activity in rat glioma demonstrated in vivo by correlation peak 1H magnetic resonance imaging. *Cancer Research*, 61(14):5595, 2001. ↪p.31

[205] A. Zoubir and D. Iskander. *Bootstrap techniques for signal processing*. Cambridge University Press, 2004. ↪p.69

[206] A. M. Zoubir. The bootstrap: A powerful tool for statistical signal processing with small sample sets. In *1999 IEEE International Conference On ACOUSTICS, SPEECH, AND SIGNAL PROCESSING* . IEEE, 1999. URL http://www.nt.tu-darmstadt.de/nt/index.php?id=227. ↪p.69

Publication list

Peer-reviewed papers in international journals

[1] E Popa, E Capobianco, R de Beer, D van Ormondt, and D Graveron-Demilly. *In vivo* quantitation of metabolites with an incomplete model function. *Measurement Science and Technology*, 20(10):104032, 2009. doi:10.1088/0957-0233/20/10/104032.

[2] D Stefan, F Di Cesare, A Andrasescu, E Popa, A Lazariev, E Vescovo, O Strbak, S Williams, Z Starcuk, M Cabanas, D van Ormondt, and D Graveron-Demilly. Quantitation of magnetic resonance spectroscopy signals: the jMRUI software package. *Measurement Science and Technology*, 20(10):104035, 2009. doi:10.1088/0957-0233/20/10/104035.

Peer-reviewed IEEE Proceedings

[1] E. Popa, D. Karras, B.G. Mertzios, D. Sima, R. de Beer, D. van Ormondt, and D. Graveron-Demilly. Handling Arbitrary Unknown Lineshape in In Vivo MRS Without Searching in Function Space. In *Proc. IEEE International Workshop on Imaging Systems and Techniques IST 2008*, Thessaloniki, Greece, July 1-2 July 2010 2010.

[2] E. Popa, E. Capobianco, R. de Beer, D. van Ormondt, and D. Graveron-Demilly. New Lineshape estimation for *in vivo* MR Spectroscopy. In *20th Annual Workshop on Circuits, Systems and Signal Processing (ProRISC 2009), IEEE Benelux*, Veldhoven, the Netherlands, November 2009. 8 pp., full paper on CD.

[3] E. Popa, D. Graveron-Demilly, E. Capobianco, R. de Beer, and D. van Ormondt. Lineshape estimation in *In Vivo* mr spectroscopy without using a reference signal. In *19th Annual Workshop on Circuits, Systems and Signal Processing (ProRISC 2008), IEEE Benelux*, pages 342–347, Veldhoven, the Netherlands, November 2008.

[4] E. Popa, D. Graveron-Demilly, E. Capobianco, R. de Beer, and D.; van Ormondt. Lineshape estimation in *in vivo* MR Spectroscopy without using a reference signal. In *Proc. IEEE International Workshop on Imaging Systems and Techniques IST 2008*, pages 315–320, September 2008. doi:10.1109/IST.2008.4659992.

[5] D. Stefan, A. Andrasecu, E. Popa, H. Rabeson, O. Strbak, Z. Starcuk, M. Cabañas, D. van Ormondt, and D. Graveron-Demilly. jMRUI Version 4 : A plug-in platform. In *Proc. IEEE International Workshop on Imaging Systems and Techniques IST 2008*, pages 346–348, September 2008. doi:10.1109/IST.2008.4659998.

[6] E. Popa, H. Rabeson, D. van Ormondt, and D. Graveron-Demilly. Lineshape Accommodation in Quantitation of Magnetic Resonance Spectroscopy Signals. In *Proceedings of the 18th Annual Workshop on Circuits, Systems and Signal Processing (ProRISC 2007), IEEE Benelux, Veldhoven, the Netherlands*, pages 250 – 253, November 2007.

Peer-reviewed international conferences

Oral Communications

[1] E. Popa, D. Karras, B.G. Mertzios, D. Sima, R. de Beer, D. van Ormondt, and D. Graveron-Demilly. Handling Arbitrary Unknown Lineshape in In Vivo MRS Without Searching in Function Space. In *IST 2010*, Thessaloniki, Greece, 1-2 July 2010.

[2] E. Popa, E. Capobianco, R. de Beer, D. van Ormondt, and D. Graveron-Demilly. Lineshape Estimation in In Vivo MR Spectroscopy without using a Reference Signal. In *ESMRMB 2008*, page 304, Valencia, Spain, October 2-4 2008. Oral.

[3] E. Popa, D. Graveron-Demilly, E. Capobianco, R. de Beer, and D. van Ormondt. LineshapeEstimation in Vivo MR Spectroscopy without using a Reference Signal. In *IEEE International Workshop on Imaging Systems and Techniques – IST*, pages 315–320, Chania, Greece, September 10–12 2008.

[4] D. Stefan, A. Andrasecu, E Popa, H. Rabeson, O. Strbak, Z. Starcuk, M. Cabañas, D. van Ormondt, and D. Graveron-Demilly. jMRUI Version 4: A Plug-in Platform. In *Proceedings of the IST 2008 – IEEE Workshop on Imaging Systems and Techniques*, pages 346–348., Chania, Greece, September 2008.

Posters

[1] E. Popa, E. Capobianco, J. van der Veen, R. de Beer, D. van Ormondt, and D. Graveron-Demilly. New results for metabolite quantitation with arbitrary line-shape. In *2nd Annual Meeting of the Benelux ISMRM Chapter*, Utrecht, NL, January 18 2010.

[2] E. Popa, E. Capobianco, J. van der Veen, R. de Beer, D. van Ormondt, and D. Graveron-Demilly. Handling arbitrary unknown line-shape without introducing extra parameters. In *Joint ISMRM-ESMRMB Meeting*, Stockholm, SE, May 1-7 2010.

[3] E. Popa, D. van Ormondt, and D. Graveron-Demilly. Improved semi-parametric lineshape estimation using locally weighted regression and smoothing scatterplots. In *ESMRMB 2009*, Antalya, Turkey, October 2009.

[4] D. Stefan, A. Andrasecu, E. Popa, A. Lazariev, O. Strbak, M. Cabañas Z. Starcuk, D. van Ormondt, and D. Graveron-Demilly. jMRUI Version 4 : A Plug-in Platform. In *Int. Soc. Magnetic Resonance in Medicine, ISMRM, 17th Scientific Meeting and Exhibition*, page 4340, Honolulu, USA, April 18-24 2009.

[5] E. Popa, E. Capobianco, R. de Beer, D. van Ormondt, and D. Graveron-Demilly. Improved lineshape estimation in absence of a reference peak. In *1st Benelux ISMRM Meeting*, page 75, Antwerp, December 10 2008.

[6] E. Popa, E. Capobianco, R. de Beer, D. van Ormondt, and D. Graveron-Demilly. Lineshape Estimation in In Vivo MR Spectroscopy without using a Reference Signal. In *ESMRMB 2008*, page 304, Valencia, Spain, October 2008.

[7] D. Stefan, A. Andrasecu, E. Popa, H. Rabeson, O. Strbak, Z. Starcuk, M. Cabañas, D. van Ormondt, and D. Graveron-Demilly. jMRUI Version 4 : A Plug-in Platform. In *Proceedings of the ESMRMB 2008 25th Meeting, October 2-4*, page 976, Valencia, Spain, 2008.

[8] E. Popa, H. Rabeson, D. van Ormondt, and D. Graveron-Demilly. Prise en Compte de la Forme de Raie lors de la Quantification de Signaux de Spectroscopie de Résonance Magnetique. In *12eme Congrès du GRAMM*, page 148, Lyon, France, Mars 26-28 2008.

[9] E. Popa, H. Rabeson, D. van Ormondt, and D. Graveron-Demilly. Lineshape Accommodation in Quantitation of Magnetic Resonance Spectroscopy Signals. In *International Society of Magnetic Resonance in Medicine*, page 1626, Toronto, Canada, May 2008.

Talks and contributions in the FAST [3] framework.

[1] 2009 June, Task Meeting Signal Processing, Leuven, Belgium. Lineshape Accommodation in Quantitation of Magnetic Resonance Spectroscopy Signals.

[2] 2009 June, Task Meeting Signal Processing, Leuven, Belgium. Implementation of a jMRUI 4.0 plugin.

[3] 2009 Jan., FAST Midterm Meeting, Lausanne, Switzerland.

[4] 2008 July, Max Planck Institute for Human Cognitive and Brain Sciences, Leipzig, Germany. Lineshape Accommodation in Quantitation of Magnetic Resonance Spectroscopy Signals.

[5] 2008 Sep., IEEE IST 2008, jMRUI workshop, Chania, Greece.

[6] 2007 Dec., FAST Plenary Meeting year I, Leipzig, Germany. Lineshape Accommodation in Quantitation of Magnetic Resonance Spectroscopy Signals.

[7] 2007 Oct., Task Meeting jMRUI, Barcelona, Spain.

[8] 2007 Sep., Katholieke Universiteit Leuven, Leuven, Belgium.

[9] 2007 May, Task Meeting jMRUI & Signal Processing, Lyon, France.

[10] 2007 Feb., Kick-Off Meeting FAST, Lyon, France.

3. FAST, Advanced Signal-Processing for Ultra-Fast Magnetic Resonance Spectroscopic Imaging, and Training, (MRTN-CT-2006-035801) is a Research and Training Network (RTN) granted by Marie Curie Actions in the 6th Framework Program (2007-2010). URL: `http://www.fast-mariecurie-rtn-project.eu/`

Additional Material

Appendix A
Analysis of LOWESS noise reduction in function of smoothing hyper-parameter λ.

Appendix B
Computation of the Jacobian for $\mathfrak{C}_2$.

Appendix C
Lineshape Estimation in *In Vivo* MR Spectroscopy without using a reference signal.

Appendix D
In Vivo quantitation of metabolites with an incomplete model function.

A Analysis of LOWESS noise reduction in function of smoothing hyper-parameter

Consider a AWG Noise distribution, centred on zero and with a mean of σ, noted $\mathcal{N}(0,\sigma)$. On this points the N-average operator is applied, defined by $\bar{X}_N = (1/N) \times \sum_{i=1}^{N} x_i$.

Let $X_1 = (x_i)_{i=1\to N-1}$ and $X_2 = (x_i)_{i=2\to N}$ containing samples from $X = (x_i)_{i=1\to N}$. Since X,X_1 and X_2 are normally distributed with the same variance and zero-centred, their variances are bound by the equation

$$\text{VAR}\left[X_1\right] = \text{VAR}\left[X_2\right] = \text{VAR}\left[X\right] \tag{A.1}$$

The variance of the moving average (MA) with a span of two samples is given by

$$\begin{aligned}
\text{VAR}\left[\text{MA}_2(X)\right] &= \frac{1}{N-1}\left[\sum_{i=1}^{N-1}\left(\frac{x_i + x_{i+1}}{2}\right)^2\right] = \\
&= \frac{1}{4(N-1)}\left[\sum_{i=1}^{N-1}\left(x_i^2 + 2x_i x_{i+1} + x_{i+1}^2\right)\right] = \\
&= \frac{1}{4}\left[\text{VAR}\left[X_1\right] + \text{VAR}\left[X_2\right] + 2\mathbb{E}\left[X_1 \cdot X_2\right]\right] = \\
&= \frac{1}{4}\left[\left[\text{VAR}\left[X\right] + \left[\text{VAR}\left[X\right] + 0\right]\right.\right. \\
&= \frac{\text{VAR}\left[X\right]}{2}
\end{aligned} \tag{A.2}$$

In the more general case of the moving average with a span of N_s, a similar reasoning based on the facts that $\left(\sum_i^N x_i\right)^2 = \sum_i^N x_i^2 + \sum_i^N \sum_{j\neq i}^N x_i x_j$ and that $\mathbb{E}[X_i X_j]_{i\neq j} = 0$ gives that:

$$\text{VAR}\left[\text{MA}_{N_\text{s}}(X)\right] = \frac{\text{VAR}\left[X\right]}{N_s} \tag{A.3}$$

The effect of the LOWESS can be empirically estimated on a AWG Noise realization as the effect of an equivalent moving average filter. Variance of the LOWESS filtered noise is linked to its moving average (MA) correspondent by:

$$\begin{aligned}
\text{VAR}[\text{LOWESS}_\lambda\{X\}] &\approx \frac{1}{\sqrt{2}}\,\text{VAR}\left[\text{MA}_{N_\text{s}}(X)\right] \\
&= \frac{1}{\sqrt{2}}\,\frac{\text{VAR}\left[X\right]}{N_\text{s}}
\end{aligned} \tag{A.4}$$

with

$$N_\text{s} = 2\lambda/N \tag{A.5}$$

If we now look at the residue $\mathcal{R}_\lambda = X - \text{LOWESS}_\lambda\{X\}$ its variance can be computed, as the residue is uncorrelated to the filtered signal:

$$\begin{aligned}
\text{VAR}[X] &= \text{VAR}[\mathcal{R}_\lambda] + \text{VAR}[\text{LOWESS}_\lambda\{X\}] + 2\text{COV}[\text{LOWESS}_\lambda\{X\}, X] \\
\text{VAR}[\mathcal{R}_\lambda] &= \text{VAR}[X] - \text{VAR}[\text{LOWESS}_\lambda\{X\}] = \text{VAR}[X](A - \frac{B}{\lambda}) \\
\frac{\text{VAR}[\mathcal{R}_\lambda]}{\text{VAR}[X]} &= A - \frac{B}{\lambda}
\end{aligned} \tag{A.6}$$

where A and B represent two constants, and COV is the covariance.

B Computation of the Jacobian for $\mathfrak{C}_2$

The Jacobian matrix of a function $f(t_j, \mathbf{p})$ is the matrix with elements $J_{ij} = \frac{\partial f(t=t_j)}{\partial p_i}$. The computation of this matrix is essential for using a method based on the Gauss-Newton algorithm. If no analytical expression can be given, the Jacobian is usually approximated numerically. In the following paragraph the analytical computation of the Jacobian matrix in the case of $\mathfrak{C}_1$ (LS residue minimization) is recalled, and an analogous analytical approach is presented for $\mathfrak{C}_2$ out-of-band spectral component.

B.1 $\mathfrak{C}_1$: Lorentzian model and residue minimization

In the case of the classic Lorentzian model, minimized via NLLS, the computation of the Jacobian is straightforward. Equations (B.1) show the necessary steps for computation of the Jacobian:

- Since the model function $\mathbf{s}(t)$ is written (B.1a) as a sum of independent signals $\hat{s}_m(t)$, its partial derivative in function of a parameter pertaining to metabolite m (B.1b) takes into account only the component generated by m's basis-signal b_m.
- Furthermore, the exponential form allows a particularly simple expression of the m-specific Jacobian $\mathbf{J}_m$ as a product between the m signal component value $\hat{s}_m(t)$ and a simple vector [B.1c].
- Once every m-specific Jacobian $\mathbf{J}_m$ is computed, the overall Jacobian $\mathbf{J}^{\mathfrak{C}_1}$ is built by horizontal concatenation (B.1d).

$$\hat{s}(t, \mathbf{p}) = \sum_{m=1}^{M} \hat{s}_m \qquad \text{with } \hat{s}_m = b_m(t) c_m \exp[\alpha_m t + \imath\omega_m t + \imath\varphi_m] \tag{B.1a}$$

$$\frac{\partial \hat{s}(t, \mathbf{p})}{\partial \mathbf{p}_m} = \frac{\partial}{\partial \mathbf{p}_m}\left[\sum_{\ell=1}^{M} \hat{s}_\ell\right] = \frac{\partial \hat{s}_m}{\partial \mathbf{p}_m} + \underbrace{\sum_{\ell \neq m} \frac{\partial \hat{s}_\ell}{\partial \mathbf{p}_m}}_{0} = \frac{\partial \hat{s}_m}{\partial \mathbf{p}_m} \tag{B.1b}$$

$$\mathbf{J}_m(t, \mathbf{p}_m) = \frac{\partial \hat{s}_m}{\partial \mathbf{p}_m} = \begin{pmatrix} \frac{\partial \hat{s}_m}{\partial c_m} & \frac{\partial \hat{s}_m}{\partial \alpha_m} & \frac{\partial \hat{s}_m}{\partial \omega_m} & \frac{\partial \hat{s}_m}{\partial \varphi_m} \end{pmatrix} = \hat{s}_m \times \begin{pmatrix} c_m^{-1} & t & \imath t & \imath \end{pmatrix} \tag{B.1c}$$

$$\mathbf{J}^{\mathfrak{C}_1}(t, \mathbf{p}) = \begin{pmatrix} \mathbf{J}_1(t, \mathbf{p}_1) & \mathbf{J}_2(t, \mathbf{p}_2) & \cdots & \mathbf{J}_M(t, \mathbf{p}_M) \end{pmatrix} \tag{B.1d}$$

Please note that the Jacobian is a rectangular matrix, and that in the above computations only a line has been explicitly computed. The $\mathbf{J}_m(t, \mathbf{p}_m)$ line is specific of the time. Assembling all the N lines $\mathbf{J}_m(t_n, \mathbf{p}_m)$ for $n = 1, 2, \ldots, N$ gives the rectangular matrix $\mathbf{J}_m(\mathbf{p}_m)$, that has N lines and $M\texttt{size}(\mathbf{p}_m) = 4M$ columns.

B.2 $\mathfrak{C}_1$ minimization of the spectral out-Band components

Analytical computation of the spectral compactness criterion $\mathfrak{C}_2$is similar to the procedure used for the case of the Lorentzian model least squares. The main difference is in the slightly more complicated analytical formula introduced by (1) the Discrete Fourier Transform and by (2) the nonlinear point-to-point division for the estimation of the raw ECD.

The $\mathfrak{C}_2$criterion can be expressed [4] by the point-wise multiplication (also called Hadamard product) of the estimated common lineshape and a inversed-gate function defined by the threshold frequencies ν_{min} and ν_{max}

$$\mathcal{C}(\mathbf{p}) = \mathcal{F}\{\hat{d}(\mathbf{p})\} \odot \sqcup(\nu_{min}, \nu_{max}) \tag{B.2}$$

4. Please note that the explicit dependence on the input signal $\mathbf{s}$ has been omitted for notation simplicity.

where $\mathcal{F}\{\cdot\}$ denotes the Discrete Fourier Transform along the time domain and the symbol $\odot$ denotes the element-wise product (also called Hadamard product) of two equally sized matrices $\{u \odot v\}[n] = u[n]v[n]$. Since the inverse-gate function does not depend on the parameters $\mathbf{p}$, a column of the Jacobian can be developed as:

$$\mathbf{J}^{\mathfrak{C}_2}_{p_i} \equiv \frac{\partial \mathcal{C}(\mathbf{p})}{\partial p_i} = \sqcup(\nu_{\min}, \nu_{\max}) \odot \frac{\partial}{\partial p_i} \mathcal{F}\{\hat{d}(\mathbf{p})\} \tag{B.3}$$

Furthermore, the Discrete Fourier Transform can be expressed as a matrix multiplication of a Vandermonde matrix (*cf.* §II.2) $\mathbb{F}$ and the input vector $\mathbf{d}$. Since $\mathbb{F}$ depends only on the size of the input and output, it is possible to pass the derivative term inside the DFT. The Jacobian can then be written as

$$\mathbf{J}^{\mathfrak{C}_2}_{p_i} = \sqcup(\nu_{\min}, \nu_{\max}) \odot \mathbb{F} \frac{\partial \hat{d}(\mathbf{p})}{\partial p_i} \tag{B.4}$$

The next step consists of computing the remaining unknown partial derivative of the ECD function. This can be done using common derivation rules together with the definition of the ECD function as (*cf.* Eq.IV.13) as ratio between the signal $\mathbf{s}$ and the estimated non-decaying signal $\hat{\mathbf{s}}_{\text{undamped}}$:

$$\frac{\partial \hat{d}(t, \mathbf{p})}{\partial p_i} = \frac{\partial}{\partial p_i} \left[\frac{s(t)}{\hat{s}_{\text{undamped}}(t, \mathbf{p})} \right] = -\frac{s(t)}{[\hat{s}(t)]^2} \frac{\partial \hat{s}_{\text{undamped}}}{\partial p_i}(t, \mathbf{p}) \tag{B.5}$$

The necessary partial derivatives of the non-decaying model $\hat{\mathbf{s}}_{\text{undamped}}$ can be computed in a similar way as shown in section B.1. Moreover, due to the fact that the undamped model is expressed in the same analytical way as $\hat{\mathbf{s}}$, it is possible to obtain the Jacobian of the non decaying model through the trivial process of eliminating from $\mathbf{J}^{\mathfrak{C}_1}$ the terms corresponding to the damping factors α_m:

$$\begin{array}{rcl} \mathbf{J}_{\mathfrak{C}_1} & = & [\ \cdots\ \mathbf{J}_{c_m}\ \ \mathbf{J}_{\alpha_m}\ \ \mathbf{J}_{\omega_m}\ \ \mathbf{J}_{\varphi_m}\ \ \cdots\ ] \\ \Big\downarrow & & \\ \mathbf{J}_{s_{\text{undamped}}} & = & [\ \cdots\ \mathbf{J}_{c_m}\ \ \ \ \ \mathbf{J}_{\omega_m}\ \ \mathbf{J}_{\varphi_m}\ \ \cdots\ ] \end{array}$$

Extracting the non-decaying model Jacobian from the decaying model Jacobian presents a special interest as the latter in in any case computed when $\mathfrak{C}_1$ and $\mathfrak{C}_2$ are used together.

With the values of $\mathbf{J}_{s\text{undamped}}$ available, combining equations (B.4) and (B.5) yields the function used to determine the Jacobian necessary for $\mathfrak{C}_2$ minimization:

$$\mathbf{J}^{\mathfrak{C}_2} = -\underbrace{\sqcup(\nu_{\min}, \nu_{\max}) \odot \mathbb{F}}_{(a)} \times \left[\mathbf{s} \odot \frac{1}{\hat{\mathbf{s}}^2_{ud}} \times \mathbf{J}_{s_{ud}} \right] \tag{B.6}$$

The term (a) in Eq.B.6 deserves some special attention. If the selection function $\sqcup(\nu_{\min}, \nu_{\max})$ is combined with the DFT matrix $\mathbb{F}$, a new matrix $\mathbb{F}_{\text{reduced}}$ can be determined. The reduced matrix extracted from $\mathbb{F}$ only the lines that are actually taken into consideration in $\mathfrak{C}_2$. It is thus possible to reduce the multiplication time by first computing $\mathbb{F}_{\text{reduced}}$ and *then* multiplying with the rest of the terms. This amounts to making only a partial DFT, where only the needed components are computed. In practice, however, the FFT algorithm is usually used for the DFT, that implements a faster relationship than the matrix multiplication. Which is better: (1) computing a partial DFT, eventually by using alternative algorithms that support it (*e.g.* the chirp z-transform algorithm [151]), or (2) computing the whole DFT using FFT [43] and then only extracting the useful information, remains an open question, as it most probably depends on the extension of the support of the selection function $\sqcup(\nu_{\min}, \nu_{\max})$.

B.3 Jacobian for composite criterion ($\mathfrak{C}_{\text{composite}} = \mathfrak{C}_1 + \mathfrak{C}_2$)

In this study the two cont functions representative of $\mathfrak{C}_1$ and $\mathfrak{C}_2$ are combined using an weighted additive approach. with λ between 0 and 1 a weight ratio between the two criteria, the equivalent cost function is computed as:

$$\|\mathfrak{C}_{\text{composite}}\|^2 = \lambda^2\|\mathfrak{C}_1\|^2 + (1-\lambda)^2\|\mathfrak{C}_2\|^2 \tag{B.7}$$

The equivalent Jacobian for the composite cost function can be constructed directly by concatenating $\lambda-$weighted versions of $\mathbf{J}^{\mathfrak{C}_1}$ and $\mathbf{J}^{\mathfrak{C}_1}$.

$$\mathbf{J}_{\text{composite}} = \begin{pmatrix} \lambda\mathbf{J}_{\mathbf{p}}^{\mathfrak{C}_1} \\ \\ (1-\lambda)\mathbf{J}_{\mathbf{p}}^{\mathfrak{C}_2} \\ \\ \end{pmatrix} = \begin{pmatrix} \lambda\mathbf{J}_{1,\mathbf{p}}^{\mathfrak{C}_1} \\ \lambda\mathbf{J}_{2,\mathbf{p}}^{\mathfrak{C}_1} \\ \vdots \\ \lambda\mathbf{J}_{N,\mathbf{p}}^{\mathfrak{C}_1} \\ \\ (1-\lambda)\mathbf{J}_{1,\mathbf{p}}^{\mathfrak{C}_2} \\ (1-\lambda)\mathbf{J}_{2,\mathbf{p}}^{\mathfrak{C}_2} \\ \vdots \\ (1-\lambda)\mathbf{J}_{N_f,\mathbf{p}}^{\mathfrak{C}_2} \end{pmatrix} \tag{B.8}$$

B.4 Jacobian for L_2 normalization of frequency domain $\mathfrak{C}_2$

The analytical approach is similar to what has been shown in §B.2, with the difference that $\hat{d}(t,\mathbf{p})$ is replaced by the normalized version $\hat{d}^{\text{norm.}}(t,\mathbf{p}) = \hat{d}(t,\mathbf{p}) \times [\hat{d}(t=0,\mathbf{p})]^{-1}$. Eq.B.5 is thus replaced by:

$$\begin{aligned} \frac{\partial \hat{d}^{norm}(t,\mathbf{p})}{\partial p_i} &= \frac{\partial}{\partial p_i}\left[\frac{s(t)}{\hat{s}_{ud}(t,\mathbf{p})} \times \frac{\hat{s}_{ud}(0,\mathbf{p})}{s(0)}\right] \\ &= -\frac{s(t)}{[\hat{s}(t)]^2}\frac{\hat{s}_{ud}(0,\mathbf{p})}{s(0)}\frac{\partial \hat{s}_{ud}}{\partial p_i}(t,\mathbf{p}) + \frac{s(t)}{\hat{s}_{ud}(t,\mathbf{p})}\frac{1}{s(0)}\frac{\hat{s}_{ud}(0,\mathbf{p})}{\partial p_i} = \\ &= \frac{s(t)}{\hat{s}_{ud}(t,\mathbf{p})s(0)}\left[-\frac{\hat{s}_{ud}(0,\mathbf{p})}{\hat{s}_{ud}(t,\mathbf{p})}\frac{\partial \hat{s}_{ud}(t,\mathbf{p})}{\partial p_i} + \frac{\partial \hat{s}_{ud}(0,\mathbf{p})}{\partial p_i}\right] \end{aligned} \tag{B.9}$$

B.5 Jacobian for time domain implementation of $\mathfrak{C}_2$

In the case of the time domain $\mathfrak{C}_2$implementation the computation is also based on the procedures described in the previous subsections. However, neither DFT nor selection window are necessary. Instead, for computation of the partial derivative at a point t in time, values of the ECD Jacobian at the points around t are used:

$$\begin{aligned} \frac{\partial}{\partial p_i}(d[n+1] - d[n]) &= \frac{\partial d[n+1]}{\partial p_i} - \frac{\partial d[n]}{\partial p_i} = \\ &= -\frac{s[n+1]}{(\hat{s}_{ud}[n+1])^2}\frac{\partial \hat{s}_{ud}}{\partial p_i}(t_{n+1},\mathbf{p}) + \frac{s[n]}{(\hat{s}_{ud}[n])^2}\frac{\partial \hat{s}_{ud}}{\partial p_i}(t_n,\mathbf{p}) \end{aligned} \tag{B.10}$$

Lineshape Estimation in *In Vivo* MR Spectroscopy without using a Reference Signal

E. Popa, D. Graveron-Demilly
CREATIS-RMN, Univ Lyon 1, CNRS UMR 5220
INSERM U630, INSA Lyon, FR
Email: Danielle.Graveron@univ-lyon1.fr

E. Capobianco
CRS4 Bioinformatics Laboratory
Pula (Cagliari), IT
Email: ecapob@crs4.it

R. de Beer, D. van Ormondt
Applied Physics,
TU Delft, NL
D.vanOrmondt@tudelft.nl,

***Abstract*—Metabolites can serve as *biomarkers*. Estimation of metabolite concentrations from an *in vivo* MRS signal often uses a reference signal from water for correction of the spectral line-shape. When no reference signal is available, other methods must be applied. The present work concerns semi-parametric estimation of the perturbed line-shape from simulated signals of the metabolites themselves. Errors are obtained from a Monte-Carlo calculation. The method can be useful when the water signal has not been acquired or is distorted, or when measuring on, e.g., ^{13}C or ^{31}P.**

***Index Terms*—metabolomics, MR Spectroscopy, *in vivo*, asymmetric lineshape, estimation error, simulations**

I. Introduction

Metabolites [1] serve as markers of specific diseases [2], also called biomarkers [3]. An *in vivo* Magnetic Resonance Spectroscopy (MRS) scanner is the sole instrument enabling *non-invasive* measurement of concentrations of metabolites anywhere in the human body.

An MRS signal is the response to a sequence of radio-frequency pulses and time-dependent gradient-fields and is acquired in the time-domain. Each chemically distinct metabolite contributes a unique set ('fingerprint') of decaying complex-valued sinusoidal components. In frequency-domain terminology, many components overlap severely, making estimation of metabolite concentrations a challenging task. Note that the decay function in the time-domain corresponds to the *lineshape* in the frequency-domain.

In this paper, contributions from macromolecules, water, and lipids, which complicate analysis have been omitted. Rather, we have concentrated on estimating the *a priori* unknown form of a badly perturbed decay function without the help of a so-called [4], [5], [6] reference signal, using a new method [7]. The method is useful in the event that a suitable reference signal is not available, a prevailing situation with the nuclei ^{13}C, ^{19}F, or ^{31}P, but can happen with ^{1}H too. Using a Monte Carlo simulation, we investigated errors and bias-variance trade-off of the estimated metabolite concentrations.

Finally, note that our method works directly in the measurement-domain (time-domain). It will be implemented in the freely available metabolite quantification package MRUI [8]. A commercial package, LC-Model [9], working in the frequency-domain, exists that is capable of accommodating unknown lineshapes too. The structure of this paper is as follows. Sec. II treats the Metabolite model function, its decay function, alternative methods for estimation of the decay function, Monte Carlo simulation. Sec. III lists estimation errors and shows graphical results. Sec. IV discusses starting values, modelling of disentangled decay data, and bias-variance trade-off. Sec. V presents Conclusions.

II. Methods

A. The Metabolite Signal

An *in vivo* MRS signal, $s(t)$, is complex-valued and is acquired in the time-domain. It can be approximately modelled by

$$\hat{s}(t) = e^{\imath\varphi_0} \sum_{m=1}^{M} a_m \, \hat{d}_m(t) \, \hat{s}_m(t) \, e^{\,\imath\,(2\pi\triangle\nu_m t + \varphi_{m,0})} \,, \qquad (1)$$

in which $\hat{}$ denotes model function rather than experimental or simulated data, $\imath = \sqrt{(-1)}$, φ_0 is an overall phase, $t = n\triangle t + t_0$ is time, with $\triangle t$ is the sampling interval and $0, 1, \ldots, N-1$, and t_0 a 'dead' time put to zero in this study; for each metabolite, numbered $m = 1, \ldots, M$, we have:

- a_m is the quantity or concentration of metabolite m, the most important piece of information for clinicians.
- $\hat{d}_m(t) = e^{\alpha_m t + \beta_m t^2}$, $\alpha_m, \beta_m < 0$, is a Voigt [1] decay (or damping) function, usually of no importance for clinicians.
- $\hat{s}_m(t) = \sum_{k=1}^{K_m} a_{m,k} \; e^{\,\imath\,(2\pi\nu_{m,k}t + \varphi_{m,k})}$ is the *a priori* known undamped, *i.e.*, non-decaying, version of model function of metabolite m, in which $a_{m,k}, \nu_{m,k}, \varphi_{m,k}$ are the relative amplitudes, frequencies, and phases of individual spectral components of a metabolite model function. Metabolite model functions can be computed quantum-mechanically with NMRSCOPE [10], [8] or measured with *in vitro* MRS from appropriate liquid metabolite solutions. The set of *a priori* known undamped

[1] or Lorentz if $\beta = 0$, or Gauss if $\alpha = 0$

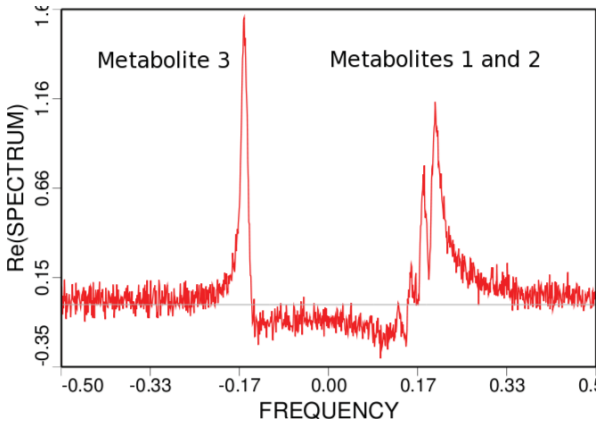

Figure 1. Real part of the FFT of the simulated, fictitious metabolite signal used in this investigation. Contributions from macromolecules, water, lipids were omitted. Three metabolites and added noise contribute to the signal. Metabolites 1,2 each contribute four spectral components; overlap of the spectral lines is extensive so that only five of the eight components can be distinguished. The phases of the individual components were set to different values. Metabolite 3 has only one spectral component. In this Figure all nine components have been given the same damping function that is distorted by simulated inhomogeneity of the static magnetic field B_0 and eddy current effect. The signal could be representative for any of the isotopes ^{1}H, ^{13}C, (^{19}F?), ^{31}P.

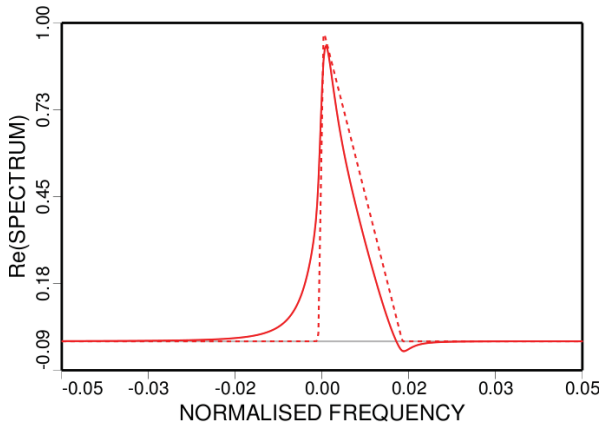

Figure 2. Real part of the simulated lineshape, *zoomed horizontally by a factor of* 10. Each spectral component in Fig. 1 has been given this shape. Solid line: Re[FFT($d(t)$)] in Eq. (2). Dotted line: Re[FFT($d_{\text{patient}}(t)$)] in Eq. (2). Recall that the lineshape in the frequency-domain is the FFT of the decay function in the time-domain.

model functions $\hat{s}_m(t), m = 1, \ldots, M$ is called the metabolite database. (NB. Measured metabolite signals are naturally decaying (damped) and must be rendered undamped by signal processing.)

- $\triangle\nu_m$ and $\varphi_{m,0}$ are corrections of the frequency and phase respectively of the *a priori* known metabolite model function s_m, determined by the experimental conditions of the measurement at hand.

Fourier transformation of an MRS time-domain signal yields the spectrum in the frequency-domain. In the same vein, Fourier transformation of a decay function yields the corresponding lineshape in the frequency-domain. Fig. 1 shows the spectrum of the simulated spectrum. More details are given in [11], [12], except for the decay function. In the present work we perturb the previously used decay function by taking into account 1) asymmetric B_0 inhomogeneity due to tissue heterogeneity of a patient and 2) eddy-currents in the metal walls of the superconducting magnet due gradient-switching. This is treated in the next Section.

B. The Decay of in vivo MRS Signals

1) Introduction: Heterogeneity of living tissue and eddy currents in the magnet walls are the dominant contributors to the decay function of an *in vivo* MRS signal; see, *e.g.* Refs. [13], [14] and references therein. The net decay function $d(t)$ resulting from these effects is *a priori* unknown. In previous work [11], [12], we approximated $d(t)$ with a Voigt function, wielding a different one for each metabolite. Here we aim to estimate a common shape of $d(t)$, valid for all metabolites, from the data.

2) Simulation of a realistic decay function: Given the circumstances described in Sec. II-B1 we model the decay function as a product of three independent contributions

$$\hat{d}(t) = \hat{d}_{\text{patient}}(t) \times \hat{d}_{\text{eddy}}(t) \times \hat{d}_{\text{Voigt}}(t) \;, \qquad (2)$$

in which

- $\hat{d}_{\text{patient}}(t)$ is the decay due to heterogeneity of a patient at the volume of interest. Sources of heterogeneity are boundaries between fat, bone, air, blood vessels, etc., see, *e.g.*, [13]. Heterogeneity in turn causes inhomogeneity of the static magnetic field B_0 at the volume of interest. The ensuing distribution of B_0-values may well be asymmetric. In the latter case, $\hat{d}_{\text{patient}}(t)$ becomes complex-valued. For mathematical ease we chose an asymmetric triangular distribution function, represented by the dotted line in Fig. 2. Ref. [15] describes alternative asymmetric shapes in spectroscopy.
- $\hat{d}_{\text{eddy}}(t)$ is a complex-valued decay function caused by eddy-currents induced in the walls of the superconducting magnet of a scanner by the switching of 'gradient-fields' that focus on a volume of interest. Eddy-currents produce a perturbing modulation of B_0 that decays with time and returns on each new switch.
- $\hat{d}_{\text{Voigt}}(t)$ is a Voigt decay function, introduced in Sec. II-A.

More details are given in Appendix A. In the next Section, we consider the decay function to be *a priori* unknown and treat its estimation from the MRS data.

C. Estimation of an Unknown Decay Function

1) Simplification of the MRS model function: As mentioned in the previous sections, the decay function of an *in vivo* MRS signal is *a priori* unknown. It depends on the location of the voxel of interest and to experimental conditions of the scanner. This poses a problem. Yet, assuming that the dominant contributions to the decay are from patient heterogeneity and

eddy-currents, it follows that all spectral components decay in the same manner. This in turn enables a crucial simplification of the model function. In fact one can re-write Eq. 1 as

$$\hat{s}(t) = \hat{d}(t)\ \hat{s}(t)_{\text{undamped}}\ , \tag{3}$$

where

$$\hat{s}(t)_{\text{undamped}} = e^{\imath\varphi_0} \sum_{m=1}^{M} a_m\ \hat{s}_m(t)\ e^{\imath\,(2\pi\triangle\nu_m t + \varphi_{m,0})}\ , \tag{4}$$

the parameters of which have been explained in Sec. II-A.

2) Alternative Approaches: We distinguish two main approaches, based on whether or not a dominant component that can easily be disentangled from the rest – reference-signal, see *e.g.* [4], [5], [6] – is available.

- Reference-Signal Available Disentanglement of a reference-signal from the rest of the MRS signal is usually easy. Once done, this immediately yields an estimate of $d(t)$. After multiplying the latter with $\hat{s}(t)_{\text{undamped}}$, one can do a conventional NLLS fit of $\hat{s}(t)$ to the data. This approach is to be preferred.
- Reference-Signal NOT Available In this case, the decay function is to be estimated (disentangled) from all data. We distinguish the following two semi-parametric methods to this effect.
  - For $\hat{d}(t)$ in Eq. (3), use a sum of L exponentially damped sinusoids

$$\hat{d}(t) = \sum_{\ell=1}^{L} a_\ell\ e^{(\alpha_\ell + \imath\nu_\ell)t + \imath\varphi_\ell}\ , \tag{5}$$

    with frequencies $\nu_\ell \approx 0$. Then fit Eq. (3) to the data. For $L = 3$, this choice of $\hat{d}(t)$ adds *maximally* $3 \times 4 = 12$ free parameters, namely $a_\ell, \alpha_\ell, \nu_\ell, \varphi_\ell, \ell = 1, 2, 3$, for fitting the experimental damping. This number can be reduced by imposing relations between the otherwise free parameters. Advantages of this method are i) the damping data are not disentangled from the signal in a separate step, in other words ii) all parameters are estimated simultaneously, iii) provided the residue of the NLLS fit contains mainly noise, the Cramér-Rao Bounds may be reliable.
    This method is yet to be implemented.
  - The second method, which is the main subject of this paper, disentangles the decay data from the signal in a separate step. In contrast to the first method, it enables use of *a priori* knowledge about the maximum frequency region covered by the lineshape function. More on this in the Discussion, Sec. IV.
    The method is based on re-writing Eq. (3) as [7]

$$\hat{d}(t) = \frac{\hat{s}(t)}{\hat{s}(t)_{\text{undamped}}}\ . \tag{6}$$

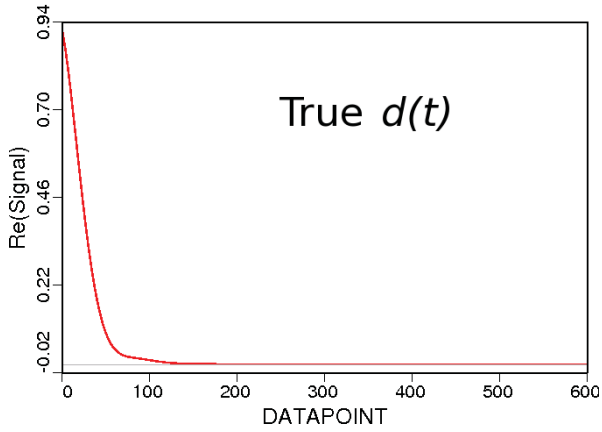

Figure 3. Real part of first 600 (of 1024) datapoints of the true, simulated $d(t)$. Re[FFT($d(t)$)] is shown as solid line in Fig. 2.

Replacing then the model function $\hat{s}(t)$ by the data $s(t)$ immediately yields the wanted result, albeit it an approximate one:

$$d(t) \approx \frac{s(t)}{\hat{s}(t)_{\text{undamped}}}\ . \tag{7}$$

The disentangled decay data $d(t)$ resulting from Eq. (7) are not exact for two reasons. First, $s(t)$ contains noise whereas $\hat{s}(t)$ does not. Second, the amplitudes, phase corrections, and frequency corrections in $\hat{s}(t)_{\text{undamped}}$ are only approximate. In this work, the latter were estimated by fitting the model function Eq. (1), which has Voigt-damping, [2] to the simulated noisy signal. See Sec. IV, Discussion, for a way to exploit sensitivity to starting values, possibly obviating the rest of the method, immediately below.
Next, we model $d(t)$ by a sum a exponentially decaying sinusoids, using the algorithm HSVD [16]. By constraining the frequencies of the sinusoids to a limited region around zero, most contributions to $d(t)$ from metabolites due to sub-optimal starting values in the denominator of Eq. (7) are removed. The result is indicated by $d(t)^{\text{HSVD}}$.
Finally, the wanted metabolite parameters are estimated by NLLS-fitting of Eq. (3) with $\hat{d}(t) = d(t)^{\text{HSVD}}$ as fixed entity, to the data. Related error bounds are yet to be found.
Results are presented in Sec. III.

III. Results

The method described above was applied in a Monte Carlo simulation, using thousand different noise realisations, each with same standard deviation. The signal-to-noise ratio (SNR) can be gleaned from Fig. 1. Fig. 5 shows a typical result of $d(t)^{\text{HSVD}}$, for one of the thousand noise realisations.

[2] In this study, $\beta = 0$, amounting to Lorentz decay.

Table I
RELATIVE RMSE'S † OF ESTIMATED METABOLITE CONCENTRATIONS, OBTAINED BY 'MONTE CARLO' SIMULATION, WITH 1000 NOISE REALISATIONS.

$d(t) \rightarrow$	known	$\exp(\alpha t)$	Estimation by Eq. (7) & HSVD ‡			
metabolite	(true)	Lorentz	Case 1	Case 2	Case 3	Case 4
$m = 1$	1.0	1.62	2.37	2.09	1.98	2.01
	(0.0)	(-0.27)	(0.09)	(0.14)	(0.12)	(0.09)
$m = 2$	1.0	5.12	2.96	2.78	2.64	2.77
	(0.0)	(3.06)	(0.26)	(0.28)	(0.18)	(0.16)
$m = 3$	1.0	13.30	8.30	7.63	7.12	7.22
	(0.0)	(9.09)	(0.45)	(0.48)	(0.33)	(0.27)

NOTES
† Relative Root Mean Square Error =
(RMSE for $d(t)$ is estimated) / (RMSE for $d(t)$ is known = true).
‡ Cases 1-4 pertain to different choices of HSVD hyper-parameters:
Case 1: $-0.10 \leq \nu \leq +0.10$. Case 2: $-0.05 \leq \nu \leq +0.05$.
Case 3: $-0.02 \leq \nu \leq +0.03$. Case 4: $-0.015 \leq \nu \leq +0.025$.
m is the index of a metabolite.
In parentheses: bias-to-standard_deviation ratio (BSR).

For the present study we wish to know the relative changes of the Root Mean Square Errors (RMSE) and the changes of the Bias-to-Standard_deviation Ratio's (BSR) upon changing method. Hence Table I lists the ratio (RMSE for $d(t)$ is estimated) / (RMSE for $d(t)$ is known = true) and related BSR's of the metabolite concentrations a_m for a total of six cases.
The ideal case, yielding the smallest RMSE and BSR = 0, is of course when the true $d(t)$ is used; see column 2. The case of using the approximate model function of Eq. (1) is covered by column 3; as expected, the resulting bias is largest. Columns 4-7 pertain to four different frequency limits (hyper-parameters) used for modelling $d(t)$ with HSVD; see NOTES added to Table I. For $m = 2, 3$ results have improved w.r.t. column 3. Comparing results for different metabolites, it is striking that RMSE and bias are largest for $m = 3$, which is the non-overlapping singlet; no explanation is available yet.

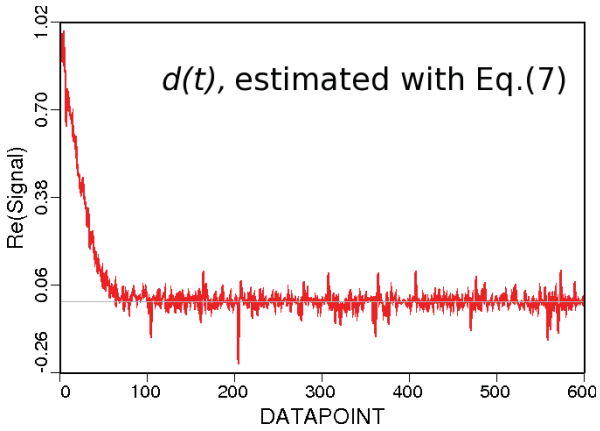

Figure 4. Real part of first 600 (of 1024) datapoints of $d(t)$, estimated with Eq. (7). No more than about the first 120 datapoints will be assigned to $d(t)$; the rest carries no information and can be ignored.

IV. DISCUSSION

Relevant issues in the present study are starting values of the parameters in $\hat{s}(t)_{\text{undamped}}$, modelling of $d(t)$, bias-variance trade-off.

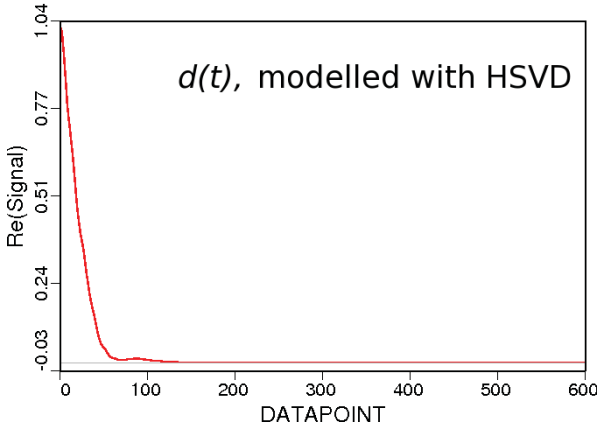

Figure 5. Real part of first 600 (of 1024) datapoints of $d(t)^{\text{HSVD}}$, obtained by first applying Eq. (7), resulting in the signal in Fig. 4, and subsequently modelling the first 120 datapoints with HSVD. The modelling can be seen to deviate from simple exponential decay, implying that at least two sinusoids were used in the modelling. Fig 3 shows the true shape of $d(t)$.

A. Starting Values for $\hat{s}(t)_{\text{undamped}}$

Eq. (6) is correct only if the true values of the parameters of $\hat{s}(t)_{\text{undamped}}$ are used. If this condition is satisfied, $d(t)$ contains no components from metabolites and hence its spectrum is confined to a relatively narrow region around $\nu = 0$, as shown in Fig. 2.
In practice, however, *starting* values have to be obtained in some way. Here, they were estimated by fitting the model function of Eq. (1), based on Voigt (or Gauss, Lorentz) decay, to the data. This appeared adequate. However, with increasing difference between actual decay and Voigt decay, spectral components of $d(t)$ beyond $\nu \approx 0$ will become stronger. Appearance of such additional components indicates that the starting values were not optimal.
At first sight, sensitivity to starting values can be seen as a disadvantage. On the other hand, this property could be used to one's advantage. In fact, one can vary the starting values in a systematic way until the spectrum of $d(t)$ approaches zero for $|\nu|$ greater than some threshold frequency $\nu_{\text{threshold}}$ available from *a priori* knowledge.
The latter approach is yet to be programmed and tested. If successful, obtaining good starting values can pose no problem. Rather, it may even simplify metabolite quantification

significantly. To see this, recall that validity of Eq. (6) requires correct values of the parameters of $\hat{s}(t)_{\mathrm{undamped}}$. Hence, once the spectrum of $d(t)$ has been optimally minimised for $|\nu| > \nu_{\mathrm{threshold}}$, the metabolite concentrations a_m needed to achieve it are by definition optimal too. Often, this is all a clinician wants. Note that it would obviate the subsequent NLLS fit mentioned at the end of Sec. III. Bounds on estimation errors can possibly be derived from an appropriate Jacobian used for the mentioned minimisation.
Finally, note that improvement of starting values is addressed in another contribution, by Osorio *et al.*, to the same Workshop.

B. Modelling of $d(t)$

As mentioned in Sec. IV-A, less than optimal starting values can result in contributions from metabolites in $d(t)$. Modelling $d(t)$ with, *e.g.*, HSVD, enables removal of such unwanted contributions. The same effect can be achieved with wavelets or splines; this is a subject for further research.
Should the method to obtain good starting values described in the second part of Sec. IV-A, namely minimising FFT[$d(t)$] beyond $\pm\nu_{\mathrm{threshold}}$ work out well, then the mentioned rationale for modelling ceases to hold. In that case, modelling could be omitted.

C. Bias-Variance Trade-off

At low SNR, the choice of $d(t)$ is not very important. However, steady improvement of the SNR of *in vivo* MRS data warrants study of non-parametric estimation of the *a priori* unknown decay function previously approximated by simple models. Generally, the following rule applies: The more parameters one estimates, the smaller the bias but the higher the variance (standard deviation), and vice versa. The numbers in Table I confirm this: In column 3, biases are much higher than in columns 4-7. Automatic realisation of an optimal bias-variance trade-off, and this for a one-time measurement with arbitrary SNR and arbitrary metabolite composition, is a challenge for future research. Another challenge is reliable estimation of error bars for the final product, *i.e.*, for metabolite concentrations from one-time measurements in a clinic.

V. Concluding Remarks

- Semi-parametric estimation of a common, asymmetric lineshape (complex-valued decay function) from *in vivo* MRS data without using a reference line is feasible. Obtaining reliable estimation errors from a single measurement in a clinic and related lower bounds remains a challenge.
- The degree of improvement of metabolite quantitation achieved with lineshape estimation depends on the signal-to-noise ratio (SNR).
  - The higher the SNR, the higher the improvement.
  - Automatic adaptation of hyper-parameters to the SNR and the metabolite composition at hand is yet to be achieved.
- Obtaining adequate starting values for our method poses no insurmountable problems. Possible high sensitivity to starting values could open the way to an alternative, more direct estimation of metabolite concentrations.

Appendix

A. This Appendix provides some details about the simulated decay function, according to Eq. 2.

a) Patient Heterogeneity: The dashed line in Fig. 2 depicts an asymmetric triangle, representing a possible inhomogeneity of the magnetic field B_0 due to heterogeneity of a patient. The corresponding decay function in the measurement-(time-)domain is

$$\hat{d}_{\mathrm{patient}}(t) = \frac{1}{\pi(\nu_3-\nu_1)t} \times \left(\frac{e^{2\pi\imath\nu_2 t} - e^{2\pi\imath\nu_1 t}}{2\pi(\nu_2-\nu_1)t} - \frac{e^{2\pi\imath\nu_3 t} - e^{2\pi\imath\nu_2 t}}{2\pi(\nu_3-\nu_2)t} \right) , \quad (8)$$

where ν_1, ν_2, ν_3 are the frequencies of the left-hand, top, and right-hand vertex, respectively, with $\nu_1 = -0.001, \nu_2 = 0, \nu_3 = 0.015$. Furthermore, $1/(\pi(\nu_3-\nu_1))$ is a normalisation factor, such that $\hat{d}_{\mathrm{patient}}(t)$ equals 1 for $t \to 0$. $\hat{d}_{\mathrm{patient}}(0)$, in turn, corresponds to the area of the triangle in the frequency-domain. Note that $\hat{d}_{\mathrm{patient}}(t)$ is complex-valued when the triangle is asymmetric, *i.e.*, when $\nu_2 - \nu_1 \neq \nu_3 - \nu_2$. In contrast, a Voigt decay function is real-valued. As remarked in Sec. II-B2, many alternative asymmetric forms are conceivable [15].

b) Eddy Current Effect: As mentioned in Sec. II-B2, switching of magnetic gradient fields causes time-dependent variations of B_0. In modern scanners the effect is alleviated by active screening. The nature of the remaining effect depends on the instrumentation provided by a scanner manufacturer. We modelled the resulting phase variation of the MRS signal as

$$\hat{d}_{\mathrm{eddy}}(t) = e^{\imath \sum_{j=1}^{J} c_{j,\mathrm{eddy}}\, e^{\alpha_{\mathrm{eddy}} t}} , \quad (9)$$

with $J = 2$, $c_{1,\mathrm{eddy}} = 2.0$, $c_{2,\mathrm{eddy}} = -2.4$, $\alpha_{1,\mathrm{eddy}} = -0.006$, $\alpha_{2,\mathrm{eddy}} = -0.005$.

c) Voigt Decay: We simulated Voigt decay with parameters $\alpha = -0.026$ and $\beta = 0$, amounting to Lorentz decay.

Acknowledgment

This work is supported by Marie-Curie Research Training Network 'FAST' (MRTNCT-2006-035801, 2006-2009), and Philips Medical Systems. Co-author DvO thanks JWC van der Veen for stimulating interactions concerning modelling of eddy current effects, among other things.

References

[1] (2008) Metabolomics. [Online]. Available: http://en.wikipedia.org/wiki/Metabolites

[2] Y. Rosen and R. Lenkinski, "Recent Advances in Magnetic Resonance Neurospectroscopy," *The Journal of the American Society for Experimental NeuroTherapeutics*, vol. 4, pp. 330–345, July 2007.

[3] A. Sorensen, "Magnetic Resonance As a Cancer Imaging Biomarker," *Journal of Clinical Oncology*, vol. 24, pp. 3274–3281, 2006.

[4] G. Morris, H.Barjat, and T. Horne, "Reference Deconvolution Methods," *Journal of Progress in Nuclear Magnetic Resonance Spectroscopy*, vol. 31, pp. 197–257, 1997.

[5] R. Bartha, D. Drost, R. Menon, and P. Williamson, "Spectroscopic Lineshape Correction by QUECC: Combined Quality Deconvolution and Eddy Current Correction," *Magn. Reson. Med.*, vol. 44, no. 4, pp. 641–645, 2000.

[6] K. Metz, M. Lam, and A. Webb, "Reference Deconvolution: A Simple and Effective Method for Resolution Enhancement in Nuclear Magnetic Resonance Spectroscopy," *Concepts in Magnetic Resonance*, vol. 12, pp. 21–42, 2000.

[7] H. Rabeson, E. Capobianco, R. de Beer, D. van Ormondt, and D. Graveron-Demilly, "Correction pour l'inhomogénéité de B_0 et effets de courant de Foucault sans utiliser un signal de référence," in *Book of Abstracts*. $12^{ème}$ Congrès du GRAMM, Lyon, FR, 26-28 March 2008, p. 101.

[8] (2008) MRUI. [Online]. Available: http://www.mrui.uab.es/mrui/

[9] S. Provencher, "Automatic quantitation of localized in vivo H-1 spectra with LCModel," *NMR in Biomedicine*, vol. 14, pp. 260–264, 2001.

[10] D. Graveron-Demilly, A. Diop, A. Briguet, and B. Fenet, "Product-operator algebra for strongly coupled spin systems," *Journal of Magnetic Resonance*, vol. A101, pp. 233–239, 1993.

[11] H. Ratiney, E. Capobianco, H. Rabeson, C. Cudalbu, S. Cavassila, R. de Beer, D. van Ormondt, and D. Graveron-Demilly, "Semi-Parametric Estimation in *In Vivo* MR Spectroscopy," in *ProRISC, IEEE Benelux*. Veldhoven, The Netherlands: STW, November 2005, pp. 658–667, http://www.stw.nl/Programmas/Prorisc/Proceedings.htm.

[12] H. Rabeson, H. Ratiney, C. Cudalbu, S. Cavassila, E. Capobianco, R. de Beer, D. van Ormondt, and D. Graveron-Demilly, "Signal Disentanglement in In Vivo MR Spectroscopy: By Semi-Parametric Processing or by Measurement?" in *ProRISC, IEEE Benelux*. Veldhoven, The Netherlands: STW, November 2006, pp. 176–183.

[13] C. Juchem, N. Logothetis, and J. Pfeuffer, "^{1}H-MRS of the macaque monkey primary visual cortex at 7 T: strategies and pitfalls of shimming at the brain surface ," *Magnetic Resonance Imaging*, vol. 25, no. 6, pp. 902–912, 2007.

[14] Y. Zhang, S. Marenco, and J. Shen, "Correction of Frequency and Phase Variations Induced by Eddy Currents in Localized Spectroscopy With Multiple Echo Times," *Magnetic Resonance in Medicine*, vol. 58, pp. 174–178, 2007.

[15] A. Stancik and E. Brauns, "A simple asymmetric lineshape for fitting infrared absorption spectra," *Vibrational Spectroscopy*, vol. 47, pp. 66–69, 2008.

[16] W. Pijnappel, A. van den Boogaart, R. de Beer, and D. van Ormondt, "SVD-based quantification of magnetic resonance signals," *Journal of Magnetic Resonance*, vol. 97, pp. 122–134, 1992.

Meas. Sci. Technol. **20** (2009) 104032 (9pp) doi:10.1088/0957-0233/20/10/104032

In vivo quantitation of metabolites with an incomplete model function

E Popa[1], E Capobianco[2], R de Beer[3], D van Ormondt[3] and D Graveron-Demilly[1]

[1] CREATIS-LRMN, Univ Lyon 1, CNRS UMR 5220, INSERM U630, INSA Lyon, France
[2] CRS4 Bioinformatics Laboratory, Pula (Cagliari), Italy
[3] Applied Physics, TU Delft, The Netherlands

E-mail: d.vanormondt@tudelft.nl and graveron@univ-lyon1.fr

Received 28 April 2009, in final form 15 July 2009
Published 4 September 2009
Online at stacks.iop.org/MST/20/104032

Abstract
Metabolites can serve as *biomarkers*. Estimation of metabolite concentrations from an *in vivo* magnetic resonance spectroscopy (MRS) signal often uses a reference signal to estimate a model function of the spectral lineshape. When no reference signal is available, the *a priori* unknown *in vivo* lineshape must be inferred from the data at hand. This makes quantitation of metabolites from *in vivo* MRS signals a semi-parametric estimation problem which, in turn, implies setting of hyper-parameters by users of the software involved. Estimation of metabolite concentrations is usually done by nonlinear least-squares (NLLS) fitting of a physical model function based on minimizing the residue. In this work, the semi-parametric task is handled by complementing the usual criterion of minimal residue with a second criterion acting in tandem with it. This second criterion is derived from the general physical knowledge that the width of the line is limited. The limit on the width is a hyper-parameter; its setting appeared not critical so far. The only other hyper-parameter is the relative weight of the two criteria. But its setting too is not critical. Attendant estimation errors, obtained from a Monte Carlo calculation, show that the two-criterion NLLS approach successfully handles the semi-parametric aspect of metabolite quantitation.

Keywords: biomarkers, MR spectroscopy, *in vivo*, lineshape estimation, semi-parametric estimation, hyper-parameters, simulations

(Some figures in this article are in colour only in the electronic version)

1. Introduction

Metabolites [1] serve as markers of specific diseases [2], also called biomarkers [3]. Therefore, measurement of metabolite concentrations is highly relevant. It is important to carry out such measurements *in vivo* and non-invasively. Until today, magnetic resonance spectroscopy (MRS) is the only technique capable of this. The concentrations are estimated by fitting a model function to the data. In MRS jargon, one speaks of quantitation.

The present work concerns *in vivo* quantitation of metabolites for the case that the model function describing the MRS signal is incomplete, i.e., it comprises a parametric and a non-parametric part and requires semi-parametric estimation [4]. This condition is not very uncommon. In fact, real-world measurements are often perturbed by mechanisms for which no physical model function is available. Specifically, the case that the shape of the MRS spectral lines is *a priori* unknown is considered.

An MRS signal is the response of living tissue to a sequence of radio-frequency pulses and time-dependent magnetic-field gradients, and is acquired in the time domain [5]. Each chemically distinct metabolite in the tissue contributes a unique set ('fingerprint') of complex-valued sinusoidal components [6]. Due to various physical processes, the signal decays to zero over time. It is important to recall that signal decay in the time domain corresponds to lineshape in the frequency domain. The faster the decay, the broader the

lines. Under *in vivo* conditions, the dominant cause of decay is often tissue heterogeneity in the patient under investigation, especially at high magnetic fields; see examples in, e.g., [7–17]. Tissue heterogeneity, in turn, causes the magnetic field to be inhomogeneous. Another effect perturbing the lineshape originates from eddy currents in the walls of the magnet of a scanner [18].

Fortunately, a technique called *shimming* can reduce magnetic field inhomogeneity. But in heterogeneous regions such as stroke-affected areas, frontal lobe, heart, breast and prostate, among others, it is less successful; see examples in [17]. In addition, it is difficult to shim well for each voxel of a spectroscopic image. These conditions need not pose a problem so long as a so-called reference signal, from which one can accurately estimate the *a priori* unknown decay function, is available. In that case, simple multiplication of the estimated decay function with non-decaying versions of the metabolite model functions suffices, as will be explained later on in this paper. In the frequency domain, one can resort to procedures like, e.g., QUECC [19].

Unfortunately, availability of a suitable reference signal is not guaranteed. First, in the case of ^{1}H-MRS, the shape of the most commonly used reference signal, namely that of tissue water, can be affected by, e.g., partial suppression. Second, in the cases of ^{13}C-, ^{15}N-, ^{19}F- or ^{31}P-MRS—which are insensitive to water—availability of a sufficiently strong reference signal is not obvious. Therefore, the present work concentrates on the case where a reference signal is not available.

Once a suitable reference signal is lacking, estimation of the decay becomes rather more complicated. The shape of the decay being *a priori* unknown, one must resort to non-parametric techniques assuming no functional form, i.e., one approximates the unknown shape with a series of basis functions such as splines, wavelets, decaying sinusoids. The number of terms in the series is called a *hyper-parameter*; many other types of hyper-parameters exist. For optimal estimation results, hyper-parameters need to be set by an expert. Consequently, their number should be as low as possible, so as to increase user-friendliness and facilitate automation.

This study aims at reducing the number of hyper-parameters by imposing strong, yet simple, *a priori* physical knowledge in a novel way. The method builds on existing ones [20–25]. Errors and bias-variance trade-off of the estimated metabolite concentrations are obtained from a Monte Carlo simulation. The simulated metabolite signal comprises nine sinusoidal components (lines), distributed over two quartets and a singlet. The quartets overlap extensively thus creating a truly difficult case. The lineshape is heavily perturbed by magnetic field inhomogeneity and eddy currents. Contributions from macromolecules, water and lipids, which complicate the analysis of ^{1}H signals [26], were omitted so far, enabling us to concentrate on the method proper. Finally, simulation of the decay function (lineshape) is treated in the appendix.

The algorithm operates directly in the measurement domain (time domain). It will become available in the free metabolite quantification package jMRUI [27, 28]. Another freely available algorithm, also capable of handling unknown lineshapes, combining time- and frequency-domain methods, is TDFDFIT [29]. A commercial package, operating in the frequency domain and capable of accommodating unknown lineshapes is LC-model [30]. Recently, available methods and packages have been reviewed in [26].

Table 1. The concentrations, frequencies and phases of the metabolite database featuring in the non-decaying metabolite model functions of equation (1). The model parameters of the decay function are given in the appendix.

m	k	$a_{m,k}$	$\nu_{m,k}$ [a]	$\varphi_{m,k}$ [b]
1	1	0.50	0.150	0
	2	1.50	0.160	60
	3	1.50	0.170	120
	4	0.50	0.180	180
2	1	0.30	0.130	0
	2	0.60	0.150	30
	3	0.90	0.170	60
	4	1.20	0.190	90
3	1	1.00	−0.160	0

[a] Frequencies are in units of $1/(2\Delta t)$, i.e., $-0.5 \leqslant \nu < 0.5$.
[b] In units of degrees.

2. Methods

2.1. The basic metabolite model function

This section describes the model function of the simulated metabolite signal, excluding the effects of tissue heterogeneity and eddy currents. An *in vivo* MRS signal, $s(t)$, is complex valued and is acquired in the time domain. Apart from noise it can be modelled by

$$\hat{s}(t) = \mathrm{e}^{\imath\varphi_0} \sum_{m=1}^{M} a_m \hat{d}_m(t) \hat{s}_m(t)\, \mathrm{e}^{\imath(2\pi \triangle\nu_m t + \varphi_m)}, \qquad (1)$$

in which a circumflex $\hat{}$ indicates that the symbol in question represents an analytical model function, $\imath = \sqrt{(-1)}$, φ_0 is an overall phase, φ_m is a metabolite-dependent phase, $t = n\triangle t + t_0$ is the time, with $\triangle t$ being the sampling interval, $n = 0, 1, \ldots, N-1$, t_0 a 'dead' time put to zero in this study, and $m = 1, \ldots, M$ are the indices of the metabolites; see also [31]. Furthermore,

- a_m is the quantity or concentration of metabolite m, the most important piece of information for clinicians. In this work, the metabolite concentrations are, in arbitrary units, $a_1 = 0.5, a_2 = 1.0, a_3 = 2.0$, while the phases φ_0 and $\varphi_m, m = 1, \ldots, M$, have been put to zero; see also table 1.
- $\hat{d}_m(t) = \mathrm{e}^{\alpha_m t + \beta_m t^2}$, $\alpha_m, \beta_m < 0$, is a Voigt[4] decay function [32], usually of little importance for clinicians. The given function implies that each spectral component of a metabolite m has the same decay function. When analysing high-resolution data, each spectral component

[4] This class of functions encompasses both Lorentz functions ($\beta = 0$) and Gauss functions ($\alpha = 0$). The actual ratio $\beta/\alpha = 0$ chosen in this study should have no consequence for the conclusions.

of a metabolite m should have a separate decay function [33], but this is too much detail in the case of *in vivo* data. More importantly, in this study the authors assume the effect of field inhomogeneity and eddy currents to be the dominant contributor to the decay. As a consequence, the subscript m of $\hat{d}_m(t)$ will be dropped altogether later on. More details on this are given in sections 2.2 and 4.

- $\hat{s}_m(t) = \sum_{k=1}^{K_m} a_{m,k}\, e^{\imath(2\pi\nu_{m,k}t+\varphi_{m,k})}$ is the *a priori* known, non-decaying version of the model function of metabolite m, in which $a_{m,k}, \nu_{m,k}, \varphi_{m,k}$ are the relative amplitudes, frequencies and phases of individual spectral components of a metabolite model function. Table 1 shows the values of model parameters used in the present and previous simulations; see [31, 34]. There are nine sinusoidal components grouped into two quartets and a singlet. The two quartets overlap heavily. The frequencies 0.150 and 0.170 are shared while the remaining frequencies of $m = 1$ are within the range covered by $m = 2$. Moreover, the phases of all components of the quartets are different. Note that all nine components in table 1 are given the same decay function resulting from inhomogeneity of the static magnetic field B_0, eddy currents and some exponential decay, causing an asymmetric lineshape and phase perturbation, see section 2.2 and the appendix.

  In practice, model functions of real-world metabolites can be computed quantum-mechanically with NMR-SCOPE [27, 28, 35] or measured with *in vitro* MRS from appropriate liquid metabolite solutions. The set of *a priori* known non-decaying model functions $\hat{s}_m(t), m = 1, \ldots, M$ is called the metabolite database. (NB: *measured* database signals are naturally decaying and must be rendered non-decaying by signal processing.)
- $\triangle\nu_m$ and φ_m are corrections of the frequency and phase, respectively, for the *a priori* known metabolite model function, $\hat{s}_m$, determined by the experimental conditions of the measurement at hand.

Figure 1 shows the spectrum of the simulated signal. The phases of the components are those in table 1, combined with the phase of the decay function; see section 2.2 and the appendix for the latter. Since the phases are different for the large majority of the components, phasing of the spectrum makes little sense and was omitted. The resulting fictitious signal is to serve as a substitute of real-world signals from any of the nuclei ^{1}H, ^{13}C, ^{15}N, ^{19}F, ^{31}P.

Finally, as mentioned in section 1, it is assumed that a reference signal from which one can estimate the perturbed lineshape is not available. Semi-parametric approaches for dealing with this condition are treated in sections 2.3.3 and 2.3.4.

2.2. Overall decay of in vivo MRS signals

This section supplements the decay mentioned in section 2.1 with additional terms originating from tissue heterogeneity within and at the borders of a subject under investigation, plus eddy currents in the magnet walls. In *in vivo* MRS, these terms can be dominant; see, e.g., [10, 18] and references therein. The resulting overall decay function $\hat{d}(t)$ is *a priori* unknown

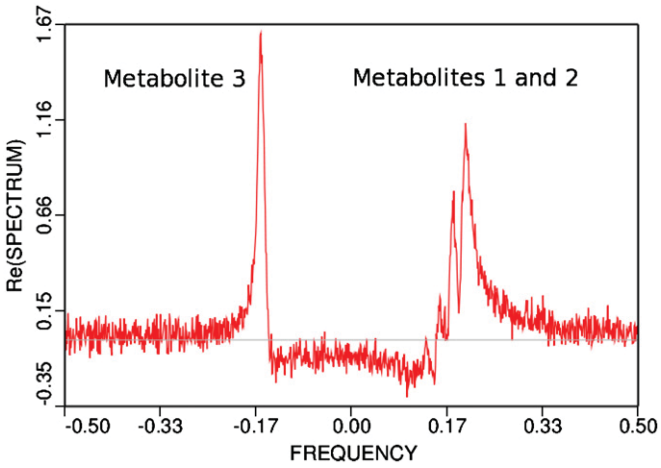

Figure 1. Real part of the FFT of the simulated, fictitious metabolite signal used in this investigation. Contributions from macromolecules, water and lipids were omitted. Three metabolites and added noise contribute to the signal. See the text for details.

and is written as a normalized product of three independent contributions:

$$\hat{d}(t) = \mathcal{N}\hat{d}_{\text{patient}}(t)\hat{d}_{\text{eddy}}(t)\hat{d}_{\text{Voigt}}(t), \tag{2}$$

in which

- $\hat{d}_{\text{patient}}(t)$ is the decay due to heterogeneity of tissue in and around the volume of interest. Sources of heterogeneity are boundaries between fat, bone, air, blood vessels, etc; see, e.g., [10]. Heterogeneity, in turn, causes inhomogeneity of the static magnetic field B_0 at the volume of interest. The ensuing distribution of B_0-values may well be asymmetric. In the latter case, $\hat{d}_{\text{patient}}(t)$ becomes complex valued. For mathematical ease, an asymmetric triangular distribution function was chosen, represented by the dotted line in figure 2. Reference [36] and references therein consider many alternative asymmetric shapes in spectroscopy.
- $\hat{d}_{\text{eddy}}(t)$ is a complex-valued decay function caused by eddy currents induced in the walls of the superconducting magnet of a scanner by the switching of 'gradient-fields' that focus on a volume of interest. Eddy currents produce a perturbing modulation of B_0 that decays with time and returns on each new switch.
- $\hat{d}_{\text{Voigt}}(t)$ is a Voigt decay function [32], introduced in section 2.1. In the present study, the function is restricted to the case $\beta = 0$, i.e., to exponential decay (Lorentz lineshape).
- $\mathcal{N}$ is a normalization factor that constrains $|\hat{d}(0)|$ to 1.

More details are given in the appendix.

In previous work [21, 31, 34], $\hat{d}(t)$ was approximated with only a Voigt function, yet allowing its width to be different for each metabolite. Here, it is assumed:

(i) The form of the decay function is *a priori* unknown.
(ii) Although unknown, the decay function is common to each sinusoidal component. This is because the inhomogeneity of the magnetic field and eddy current effect dominate all other processes causing decay. (This

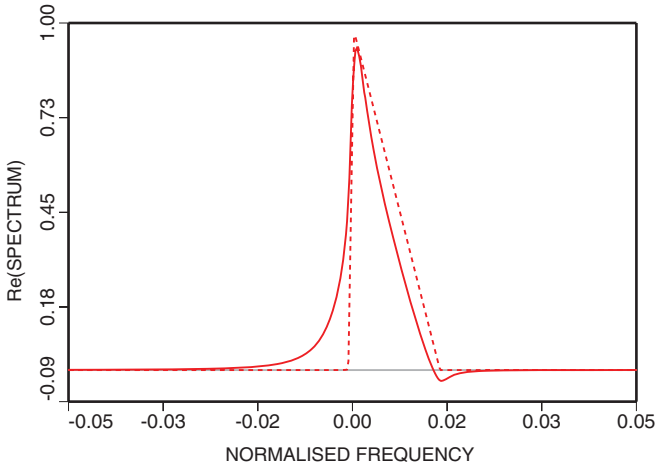

Figure 2. Real part of the simulated lineshape, zoomed horizontally by a factor of 10. Each spectral component in figure 1 has been given this shape. Solid line: Re[FFT($d(t)$)] in equation (2). Dotted line: Re[FFT($d_{\text{patient}}(t)$)] in equation (2).

is the basic assumption whenever exploiting a reference signal; naturally, it applies to the next point too.)

(iii) A reference signal enabling accurate estimation of numerical values of the decay function is not available. Consequently, the common decay function has to be estimated from the metabolite signals themselves.

2.3. Nonlinear least-squares fitting

2.3.1. Preliminaries. In MRS, estimation of model parameters is usually done by nonlinear least-squares (NLLS) fitting of a model function to the data, in either domain; see, e.g., [26] for a very recent review. The prevailing choice of the MRS community is to work in the frequency domain which amounts to NLLS fitting of the Fourier transformation (FT) of the model function of the signal to the fast Fourier transformation (FFT) of the measurement; see, e.g., [30]. This is based on the assumption that FFT is an optimal spectrum estimator. In addition, multiplication in the time domain becomes convolution in the frequency (transform) domain; the latter is more difficult to handle.

The authors' method of choice is to NLLS fit the model function of the signal directly to the data in the time (measurement) domain; see, e.g., [37, 38]. In this way, spectrum estimation and convolution are avoided.

Another important choice to make is whether to adapt the model function to the data or the other way around. In other words, one can (a) multiply the non-decaying metabolite database with the estimated decay function and leave the measurement untouched [22], or (b) divide the measurement by the estimated decay function and subsequently multiply the result with some desired decay function [19, 40, 39]. Here, option (a) is used.

2.3.2. Simplification of the MRS model function. As mentioned above, the decay function of an *in vivo* MRS signal is *a priori* unknown. It depends on the location of the voxel of interest and on experimental conditions of the scanner. This poses a problem. Yet, assuming that the dominant contributions to the decay are from heterogeneity of tissue within a patient and eddy currents, it follows that all spectral components decay in the same manner. This, in turn, enables a crucial simplification of the model function. Thus, one can rewrite equation (1) as

$$\hat{s}(t) = \hat{d}(t)\hat{s}(t)_{\text{nodecay}}, \tag{3}$$

where

$$\hat{s}(t)_{\text{nodecay}} = \mathrm{e}^{\imath\varphi_0} \sum_{m=1}^{M} a_m \hat{s}_m(t)\, \mathrm{e}^{\imath(2\pi \triangle\nu_m t + \varphi_m)}, \tag{4}$$

the parameters of which have been explained in section 2.1.

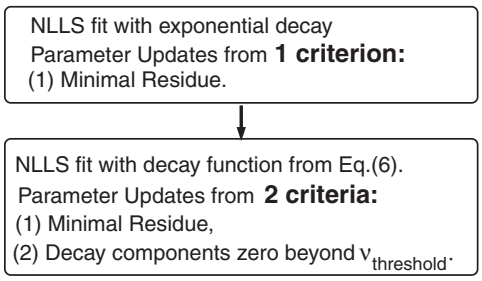

Figure 3. Diagram of metabolite quantitation using first conventional NLLS with exponential decay and subsequently two-criterion NLLS with an estimated decay function.

2.3.3. NLLS with two optimization criteria. First, the decay function is disentangled from the signal in a separate step, using equation (5), below. Importantly, subsequent modelling of the result by a sum of basis functions such as decaying sinusoids, wavelets, splines [22–24] including concomitant setting of hyper-parameters is omitted. Instead, physical *a priori* knowledge about the maximum frequency present in the decay function is used explicitly through introduction of a second criterion, imposed simultaneously with the usual criterion, in a subsequent NLLS fit. It is emphasized that this second criterion does not involve introduction and use of new parameters. Rather, it involves new derivatives with respect to the same parameters used in criterion 1.

This method is new and consists of the following steps. See also the diagram in figure 3.

(i) Apply a preliminary NLLS fit of the model function of equation (1), with exponential decay, to the signal. The model parameters thus estimated serve as starting values for computing $\hat{s}(t)_{\text{nodecay}}$ in the next step. The usual set of equations corresponding to minimizing the residue $s(t) - \hat{s}(t)$ is referred to as criterion 1.

(ii) Replace the model functions $\hat{s}(t)$ and $\hat{s}(t)_{\text{nodecay}}$ in equation (3) by the measurements $s(t)$ and $s(t)^{\text{start}}_{\text{nodecay}}$, respectively. In the latter symbol, $s(t)^{\text{start}}_{\text{nodecay}}$, the starting values of the parameters mentioned in step (i) and the sample times in force have been substituted.

(iii) Divide both sides of the numerical version of equation (3) obtained in step (ii) by $s(t)^{\text{start}}_{\text{nodecay}}$. Next, normalize $d(t)$[5]. This yields the following simple estimator of the decay function:

$$d(t) = \mathcal{N}\frac{s(t)}{s(t)^{\text{start}}_{\text{nodecay}}}, \tag{5}$$

where $\mathcal{N} = \left|s(0)^{\text{start}}_{\text{nodecay}}/s(0)\right|$. This estimator is not exact for two reasons. First, $s(t)$ contains noise whereas $\hat{s}(t)$ does not. Second, the amplitudes, phase corrections and frequency corrections in $s(t)^{\text{start}}_{\text{decay}}$ are only approximate. As a consequence of the second reason, $d(t)$ comprises components with frequencies rather higher than those in the true decay. In the following, the result of this step is referred to as the 'raw estimate of the decay'.

(iv) Impose that components in $d(t)$ with frequencies $|\nu| > \nu_{\text{threshold}}$ have minimal amplitude. $\nu_{\text{threshold}}$ is derived from physical insight. The ensuing set of equations is referred to as criterion 2. It has been implemented as follows:

  (a) Truncate $d(t)$ to zero once it has decayed into the noise, at $t = t_{\text{decay}} = n_{\text{decay}}\triangle t$.
  (b) Zero-fill $d(t)$ from $n = n_{\text{decay}}$ to 1024.
  (c) Calculate the derivatives of the lineshape Re:FFT[$d(t)$], in which $d(t)$ has been derived from equation (5), with respect to the metabolite parameters a_m and $\triangle\nu_m$, $m = 1, \ldots, M$.
  (d) Analogous to minimizing the residue, set up equations for minimizing Re:FFT[$d(t)$] for $|\nu| > \nu_{\text{threshold}}$.
  (e) Merge the equations of the two criteria.

(v) Apply a two-criteria NLLS fit of

$$\hat{s}(t) = d(t)\hat{s}(t)_{\text{nodecay}} \tag{6}$$

to $s(t)$. In each NLLS iteration, criterion 2 minimizes the components in $d(t)$ with $|\nu| > \nu_{\text{threshold}}$. Simultaneously, criterion 1 minimizes the residue $s(t) - \hat{s}(t)$. Also, $d(t)$ is estimated with equation (5) in each iteration, replacing $s(t)^{\text{start}}_{\text{nodecay}}$ by $s(t)^{\text{current}}_{\text{nodecay}}$.

To the best of the authors' knowledge steps (iv) and (v) are new. The use of basis functions such as wavelets, splines, sinusoids and concomitant setting of hyper-parameters has been circumvented. Hyper-parameters to be set here are $\nu_{\text{threshold}}$ and the ratio of the weights of criterion 2 and criterion 1. So far, their values appear not to be critical.

2.3.4. Modelling of the raw estimate of the decay. Modelling of the raw estimate of the decay, i.e., obtained from equation (5), was presented in [22, 23]. Instead of optimizing the disentangled decay with a two-criteria NLLS fit, it was modelled by a sum of exponentially decaying sinusoids with the state space implementation HSVD [41]. By restricting the frequencies of the decaying sinusoids to a limited interval based on *a priori* knowledge, most contributions to $d(t)$ due to sub-optimal starting values in the denominator of equation (5) are removed. The result is indicated by $d(t)^{\text{HSVD}}$. Subsequently, one applies step (v) above, but with criterion 1 only and $d(t)^{\text{HSVD}}$ fixed. Hyper-parameters to be set are the numbers of rows and columns of the Hankel data matrix of HSVD[6], the sizes of the subspaces, and the frequency interval that restricts the number of acceptable components.

[5] The hat has been dropped from $\hat{d}(t)$ because the resulting expression is no longer strictly an analytical formula.

3. Results

The methods described above were applied in a Monte Carlo simulation, using a thousand different noise realizations, each with the same standard deviation, 0.5×10^{-1}, for both its real and imaginary parts. The signal-to-noise ratio (SNR) can be gleaned from figure 1.

The present study uses the relative changes of the root-mean-square errors (RMSE) in the metabolite concentrations a_m and the changes of the related bias-to-standard-deviation ratios (BSR) upon varying the method as a measure of success. Hence, table 2 lists the ratio:

$$\text{Relative RMSE} = \frac{\text{RMSE, in case } d(t) \text{ is adapted or estimated}}{\text{RMSE, in case } d(t) \text{ has true values}} \tag{7}$$

and related BSRs of a_m, $m = 1, 2, 3$, for a total of five methods.

The ideal case, with smallest RMSE and BSR = 0, pertains to using the true $d(t)$; see column 2. Use of the incorrect, yet known parametric model function of equation (1) with adaptable decay constant, is covered by column 3. As expected, the resulting bias can become large; yet no hyper-parameters need be set.

Column 4 shows that errors obtained with an incorrect parametric decay function (column 3) can be reduced by dividing the corresponding concentrations by $\mathcal{N} = \left|s(0)^{\text{start}}_{\text{nodecay}}/s(0)\right|$. This operation—which involves no hyper-parameters—is called 'renormalization', because the function $\exp(\alpha t)$ is already properly normalized. More details on this are given in section 4. Column 5 lists the effect of applying NLLS with a fixed, modelled version of the decay of equation (5). In this case, modelling was done with HSVD (state space), using more than one exponentially decaying sinusoid [22, 23] per decay function.

Finally, column 6 shows that application of NLLS with two criteria is beneficial.

Figure 4 displays the real part of five versions of the decay $d(t)$. The true, simulated version is given in figure 4(*a*). The remaining four graphs pertain to estimated versions for various cases. n_{trunc} was 150 and, therefore, their horizontal display stops at that number. Figures 4(*b*) and (*c*) display $d(t)$ obtained with starting values from a noisy and a noiseless signal, respectively. Especially in the noiseless case, oscillations due to the approximate nature of the starting values are clearly visible. Figure 4(*d*) shows that adding criterion 2 to the NLLS fit successfully removes the oscillations; for better visibility, noise was omitted. The effect of state space modelling of the noisy $d(t)$ in figure 4(*b*) is displayed in figure 4(*e*).

[6] In [22, 23], seven different numbers of rows and columns of the Hankel data matrix were chosen and the median of the resulting seven modelled decay functions was used.

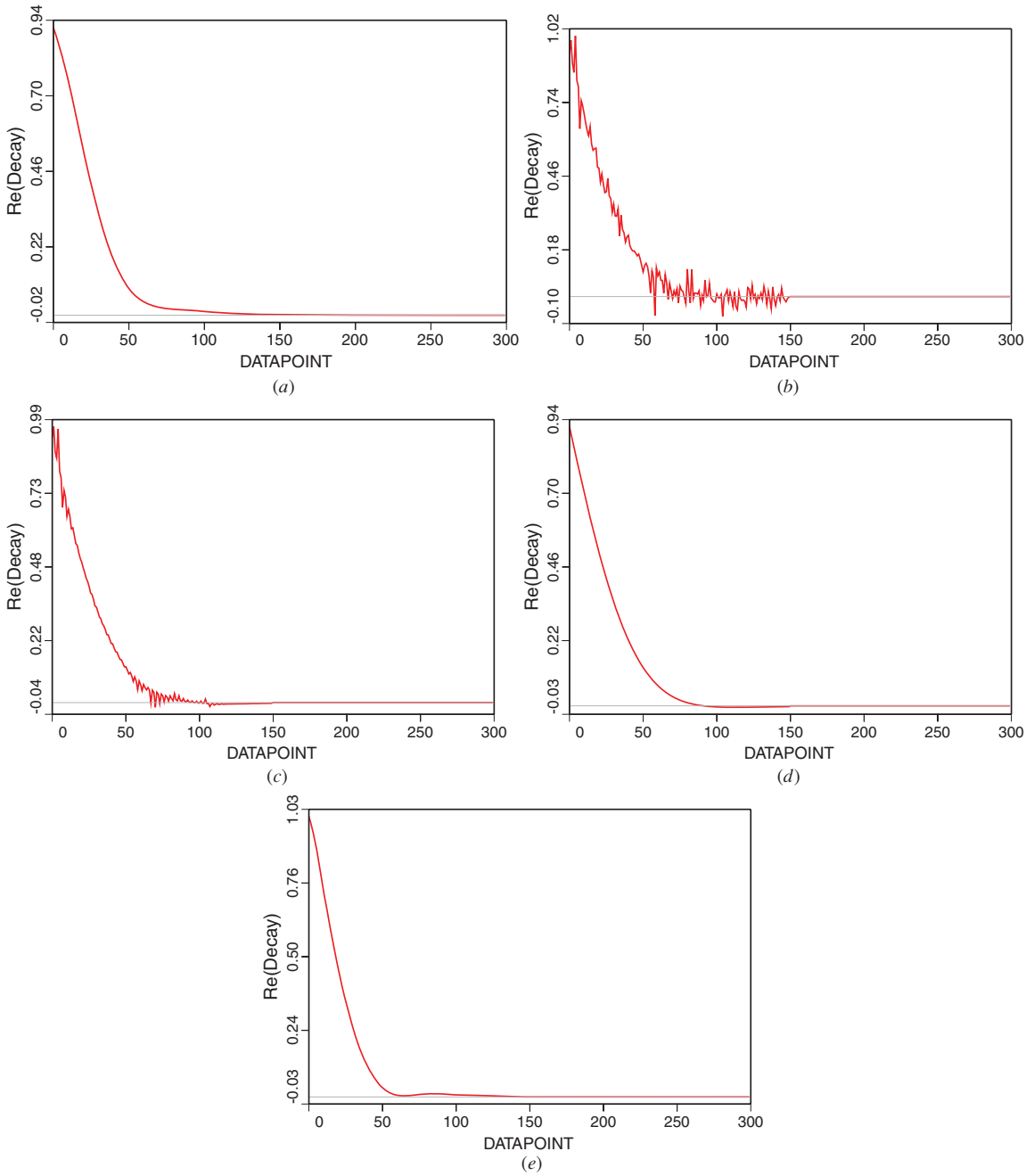

Figure 4. (*a*) First 300 datapoints of the true Re[$d(t)$]. (*b*) First 150 datapoints of Re[$d(t)$] estimated with equation (5) from noisy simulation. (*c*) First 150 datapoints of Re[$d(t)$] estimated with equation (5) from noiseless simulation. (*d*) First 150 datapoints of Re[$d(t)$] estimated with equation (5) from noiseless simulation, followed by a NLLS fit with criterion 2. (*e*) First 150 datapoints of Re[$d(t)$] estimated with equation (5) from noisy simulation, then modelled with HSVD.

4. Discussion

4.1. Overview of issues

First of all, a general remark on decay functions is in order. According to [33], an NMR decay function depends on many factors, such as molecular motion or rigidity, temperature, exchange, etc. All sorts of decay functions can occur. According to [32], a Voigt line is often appropriate for *in vivo* conditions. However, when susceptibility effects are strong, as in, e.g., [10], the effect of field inhomogeneity is the dominant contributor to the decay function. The present study addresses the latter condition. In practice, one has to adapt to the condition at hand, which may be complicated. In the limit of perfect shimming, each spectral feature may have a distinct decay function. When trying to accommodate all in the model function, it should be kept in mind that introducing more parameters decreases bias but increases variance. In fact, minimization of the RMSE should be sought. Research on automation of this process is ongoing.

Table 2. Relative RMSEs of estimated metabolite concentrations and bias-to-standard-deviation ratios (in parentheses) obtained by Monte Carlo simulation, with a thousand noise realizations. Results obtained with two-criteria NLLS are indicated by boldface.

$d(t) \rightarrow$	Known	$\exp(\alpha t)$		Equation (5) and NLLS	
metabolite	(true)	Lorentz	Renormalized[a]	HSVD	**two criteria**
$m = 1$	1.0	1.62	2.80	1.98	**1.75**
quartet	(0.0)	(−0.27)	(−1.59)	(−0.12)	**(−0.30)**
$m = 2$	1.0	5.12	1.75	2.64	**1.57**
quartet	(0.0)	(3.06)	(0.41)	(0.18)	**(0.27)**
$m = 3$	1.0	13.30	4.79	7.12	**2.31**
singlet	(0.0)	(9.09)	(2.34)	(0.33)	**(0.26)**

[a] Using values of a_m obtained with 'renormalized' exponential decay, $\hat{d}(t) = \mathcal{N}^{-1}\exp(\alpha t)$.

Table 2 lists errors incurred with four different methods of estimating metabolite concentrations from a signal whose decay function has an *a priori* unknown, non-exponential form. The errors are relative to those incurred in the ideal case, i.e., when the true form of the decay is given (column 2).

The methods pertain to purely exponential decay and estimated forms of the decay. Use of purely exponential decay (i.e., Lorentz shape) leads to heavily biased estimates because it is strongly incompatible with the true decay; see column 3 of the table. Especially the error of the singlet $m = 3$ is big. Interestingly, the error of the quartet $m = 1$ is relatively low. Probably, this has to do with the strong overlap of quartets $m = 1, 2$, but the authors cannot offer a mechanism for this phenomenon. This being a parametric approach, setting of hyper-parameters is avoided.

Use of an estimated decay function is expected to improve results because it enables adaptation to the true form. The simple estimator of equation (5) was applied, as in, e.g., [20], in new ways. First, it was used in the 'raw' form displayed in figure 4(*b*), without modelling of any kind. Section 4.2 treats where this leads to. A useful result is that metabolite concentrations estimated with incorrect (e.g., purely exponential) decay can be simply improved by a scaling, here called renormalization (column 4); this still avoids setting any hyper-parameter.

Section 4.3 discusses the effect of adding a second criterion to the NLLS fit. This criterion is based on general physical *a priori* knowledge about the form of the decay, and acts in tandem with the usual minimization of the residue $s(t) - \hat{s}(t)$. Modelling of the decay with concomitant hyper-parameters is omitted throughout. It appears that the resulting errors in the metabolite concentrations (column 6) are nearest to those of the ideal case, while only two hyper-parameters need be set.

Finally, column 5 shows the result of modelling of the decay obtained from equation (5) with HSVD, instead of applying criterion 2. It reduces the errors too. Yet, this approach requires more elaborate setting of hyper-parameters [22, 24, 25].

4.2. NLLS with criterion 1 only

Replacing the decay model function $\hat{d}(t)$ in equation (3) by the estimated version $d(t)$ of equation (5), one arrives at the signal model function,

$$\hat{s}(t) = \mathcal{N}\frac{\hat{s}(t)_{\text{nodecay}}}{s(t)^{\text{start}}_{\text{nodecay}}}s(t). \tag{8}$$

NLLS fitting of $\hat{s}(t)$ to $s(t)$ subject to criterion 1 amounts to minimizing $s(t) - \hat{s}(t)$. It is important to note that $s(t)$ can be divided out from $s(t) - \hat{s}(t)$, and that the remaining term, $1 - \mathcal{N}\hat{s}(t)_{\text{nodecay}}/s(t)^{\text{start}}_{\text{nodecay}}$, can be made exactly zero for

$$s(t)_{\text{nodecay}} = \mathcal{N}^{-1}s(t)^{\text{start}}_{\text{nodecay}}. \tag{9}$$

Equation (9) can be satisfied by substituting in $s(t)_{\text{nodecay}}$ the same parameter values as those in $s(t)^{\text{start}}_{\text{nodecay}}$ but with $a_m, m = 1, \ldots, M$ replaced by $\mathcal{N}^{-1}a_m, m = 1, \ldots, M$. With this substitution, the residue of the fit becomes zero, which is the minimum. It follows that NLLS fitting of equation (8) to the signal subject to criterion 1 yields new estimates to the extent that the original concentrations, obtained from traditional exponential decay, have been scaled by $\mathcal{N}$. Table 2 shows that such scaling, indicated by renormalization, is beneficial. It can be viewed as a compensation of using the incorrect exponential decay for NLLS fitting to the signal at hand.

It should be emphasized that the very result of section 4.2 has to do with the fact that the estimated version $d(t)$ of equation (5) *was left unchanged*. After modelling equation (5), $s(t)$ can no longer be divided out. In that case NLLS fitting with criterion 1 yields a new solution [22, 24, 25].

Yet more is possible without resorting to modelling. This is described below in section 4.3.

4.3. NLLS with two criteria

Section 4.2 shows that applying criterion 1 without modelling equation (5) amounts to renormalizing the exponential decay function of the first step in section 2.3.3 and figure 3. Applying a second criterion in the same NLLS fit can pull the parameters away from those satisfying only criterion 1. For instance, criterion 2 forces the reduction of high-frequency components contained in the decay (see figure 4(*c*)), in compliance with physical *a priori* knowledge. It achieves this by adapting the parameters in the denominator in equation (5), leading to a different solution; see figure 4(*d*)). Possibly, even criterion 2 alone could deliver an optimal solution. However, the corresponding minimum may not be global. Therefore,

criterion 1 was maintained. It is emphasized that criterion 2 does not involve a new parameter space with attendant increase of degrees of freedom and variance.

Only two hyper-parameters need to be set, the ratio of the weights of criterion 2 and criterion 1, and $\nu_{\text{threshold}}$. So far, they appeared not critical. More research on this aspect is necessary. Also, optimization of the convergence rate under the influence of two criteria needs investigation.

5. Concluding remarks

In this work, new methods were devised to reduce estimation errors of metabolite concentrations for the case that the decay function is *a priori* unknown. They are:

- A physically incorrect decay function can be improved by a simple renormalization procedure that uses no hyper-parameters.
- An estimated decay function can be improved by adding a second minimization criterion—based on general physical knowledge about decay functions—to the nonlinear least-squares (NLLS) fit procedure. Only two non-critical hyper-parameters need be set.

These methods reduce involvement of clinical personnel.

Acknowledgments

This work is supported by Marie-Curie Research Training Network 'FAST' (MRTNCT-2006-035801, 2006-2009, www.fast-mrs.eu) and Philips Healthcare.

Appendix

This appendix provides details about the decay function, simulated according to equation (2).

A.1. Heterogeneity of tissue within a patient

The dashed line in figure 2 depicts an asymmetric triangle, representing a possible inhomogeneity of the magnetic field B_0 due to heterogeneity of tissue within a patient. The corresponding decay function in the measurement (time) domain is

$$\hat{d}_{\text{patient}}(t) = \mathcal{N}\left(\frac{e^{2\pi\imath\nu_2 t} - e^{2\pi\imath\nu_1 t}}{2\pi(\nu_2-\nu_1)t} - \frac{e^{2\pi\imath\nu_3 t} - e^{2\pi\imath\nu_2 t}}{2\pi(\nu_3-\nu_2)t}\right), \quad \text{(A.1)}$$

where ν_1, ν_2, ν_3 are the frequencies of the left-hand, top and right-hand vertices, respectively, with $\nu_1 = -0.001, \nu_2 = 0, \nu_3 = 0.015$. Furthermore, $\mathcal{N} = 1/(\pi(\nu_3 - \nu_1))$ is a normalization factor, such that $|\hat{d}_{\text{patient}}(0)| = 1$. Note that $\hat{d}_{\text{patient}}(t)$ is complex valued when the triangle is asymmetric, i.e., when $\nu_2 - \nu_1 \neq \nu_3 - \nu_2$. In contrast, a Voigt decay function is real valued. As remarked in section 2.2, many alternative asymmetric forms are conceivable [36].

A.2. Eddy current effect

As mentioned in section 2.2, switching of magnetic gradient fields causes time-dependent variations of B_0. In modern scanners, the effect is alleviated by active screening. The nature of the remaining effect depends on the instrumentation provided by a scanner manufacturer. The resulting phase variation of the MRS signal was modelled as

$$\hat{d}_{\text{eddy}}(t) = e^{t\sum_{j=1}^{J} c_{j,\text{eddy}} e^{\alpha_{\text{eddy}} t}}, \quad \text{(A.2)}$$

with $J = 2$, $c_{1,\text{eddy}} = 2.0$, $c_{2,\text{eddy}} = -2.4$, $\alpha_{1,\text{eddy}} = -0.006$, $\alpha_{2,\text{eddy}} = -0.005$, respectively.

A.3. Voigt decay

Additional decay was simulated with parameters $\alpha = -0.026$ and $\beta = 0$, amounting to Lorentz decay.

References

[1] http://en.wikipedia.org/wiki/Metabolites
[2] Rosen Y and Lenkinski R E 2007 Recent advances in magnetic resonance neurospectroscopy *J. Am. Soc. Exp. NeuroTher.* **4** 330–45
[3] Sorensen A G 2006 Magnetic resonance as a cancer imaging biomarker *J. Clin. Oncol.* **24** 3274–81
[4] Bickel P J, Klaassen C A J, Ritov Y and Wellner J A 1998 *Efficient and Adaptive Estimation for Semiparametric Models* (Berlin: Springer)
[5] Barker P B and Lin D D M 2006 *In vivo* proton MR spectroscopy of the human brain *Prog. Nucl. Magn. Reson. Spectrosc.* **49** 99–128
[6] Soares D P and Law M 2009 Magnetic resonance spectroscopy of the brain: review of metabolites and clinical applications *Clin. Radiol.* **64** 12–21
[7] Gruber S, Mlynarik V and Moser E 2003 High-resolution 3D proton spectroscopic imaging of the human brain at 3 T: SNR issues and application for anatomy-matched voxel sizes *Magn. Reson. Med.* **49** 299–306
[8] Bao Y F and Maudsley A A 2007 Improved reconstruction for MR spectroscopic imaging *IEEE Trans. Med. Imaging* **26** 686–95
[9] de Graaf R A, Rothman D L and Behar K L 2007 High resolution NMR spectroscopy of rat brain *in vivo* through indirect zero-quantum-coherence detection *J. Magn. Reson.* **187** 320–6
[10] Juchem C, Logothetis N K and Pfeuffer J 2007 ^{1}H-MRS of the macaque monkey primary visual cortex at 7 T: strategies and pitfalls of shimming at the brain surface *Magn. Reson. Imaging* **25** 902–12
[11] Rosen Y, Bloch B N, Lenkinski R E, Greenman R L, Marquis R P and Rofsky Neil M 2007 3T MR of the prostate: reducing susceptibility gradients by inflating the endorectal coil with a barium sulfate suspension *Magn. Reson. Med.* **57** 898–904
[12] Dietrich O, Reiser M F and Schoenberg S O 2008 Artifacts in 3-t MRI: physical background and reduction strategies *Eur. J. Radiol.* **65** 29–35
[13] Balchandani P, Pauly J and Spielman D 2008 Interleaved narrow-band PRESS sequence with adiabatic spatial-spectral refocusing pulses for H-1 MRSI at 7T *Magn. Reson. Med.* **59** 973–9
[14] Dagia C and Ditchfield M 2008 3 T MRI in paediatrics: challenges and clinical applications *Eur. J. Radiol.* **68** 309–19
[15] Fleysher R, Fleysher L, Liu S T and Gonen O 2009 On the voxel size and magnetic field strength dependence of spectral resolution in magnetic resonance spectroscopy *Magn. Reson. Imaging* **27** 222–32
[16] Haddadin I S, McIntosh A, Meisamy S, Corum C, Powell N J, Styczynski Snyder A L, Nelson M T, Yee D, Garwood M

and Bolan P J 2009 Metabolite quantification and high-field MRS in breast cancer *NMR Biomed.* **22** 65–76

[17] Koch K M, Rothman D L and de Graaf R A 2009 Optimization of static magnetic field homogeneity in the human and animal brain *in vivo Prog. Nucl. Magn. Reson. Spectrosc.* **54** 69–96

[18] Zhang Y, Marenco S and Shen J 2007 Correction of frequency and phase variations induced by eddy currents in localized spectroscopy with multiple echo times *Magn. Reson. Med.* **58** 174–8

[19] Bartha R, Drost D J, Menon R S and Williamson P C 2000 Spectroscopic lineshape correction by QUECC: combined quality deconvolution and eddy current correction *Magn. Reson. Med.* **44** 641–5

[20] Maudsley A A 1995 Spectral lineshape determination by self-deconvolution *J. Magn. Reson.* B **106** 47–57

[21] Popa E, Rabeson H, van Ormondt D and Graveron-Demilly D 2007 Lineshape accommodation in quantitation of magnetic resonance spectroscopy signals *ProRISC, IEEE Benelux (Veldhoven, The Netherlands)* pp 250–3 (http://www.stw.nl/Programmas/Prorisc/Proceedings.htm)

[22] Rabeson H, Capobianco E, de Beer R, van Ormondt D and Graveron-Demilly D 2008 Correction pour l'inhomogénéité de B_0 et effets de courant de Foucault sans utiliser un signal de référence *12ème Congrès du GRAMM (Lyon, France, 26–28 March)* Book of Abstracts p 101

[23] Popa E, Capobianco E, Beer R de, Ormondt D van and Graveron-Demilly D 2008 Lineshape estimation in *in vivo* MR spectroscopy without using a reference signal *IEEE Int. Workshop on Imaging Systems and Techniques, IST (Chania, Greece, 10–12 Sept.)* pp 315–20

[24] Osorio M I, Sima D, Poullet J-B, Van Huffel S and van Ormondt D 2008 Improvement of lineshape estimation for MRS signals *IEEE Int. Workshop on Imaging Systems and Techniques, IST (Chania, Greece, 10–12 Sept.)* pp 326–9

Sima D M, Osorio Garcia M I, Poullet J, Suvichakorn A, Antoine J-P, Van Huffel S and van Ormondt D 2009 Lineshape estimation for magnetic resonance spectroscopy (MRS) signals: self-deconvolution revisited *Meas. Sci. Technol.* **20** 104031

[25] Popa E, Rabeson H, van Ormondt D and Graveron-Demilly D 2008 Lineshape accommodation in quantitation of magnetic resonance spectroscopy signals *Proc. ISMRM (Toronto, CA, 3–9 May)* abstract # 1626

[26] Poullet J B, Sima D M and Van Huffel S 2008 MRS signal quantitation: a review of time- and frequency-domain methods *J. Magn. Reson.* **195** 134–44

[27] http://www.mrui.uab.es/mrui/

[28] Stefan D, Andrasecu A, Popa E, Rabeson H, Strbak O, Starcuk Z, Cabanas M, van Ormondt D and Graveron-Demilly D 2008 JMRUI Version 4 : a plug-in platform *IEEE Int. Workshop on Imaging Systems and Techniques, IST (Chania, Greece, 10–12 Sept.)* pp 346–8

[29] Slotboom J, Boesch C and Kreis R 1998 Versatile frequency domain fitting using time domain models and prior knowledge *Magn. Reson. Med.* **39** 899–911

[30] Provencher S W 2001 Automatic quantitation of localized *in vivo* H-1 spectra with LCModel *NMR Biomed.* **14** 260–4

[31] Ratiney H, Capobianco E, Rabeson H, Cudalbu C, Cavassila S, de Beer R, van Ormondt D and Graveron-Demilly D 2005 Semi-parametric estimation in *in vivo* MR spectroscopy *ProRISC, IEEE Benelux (Veldhoven, The Netherlands, November STW)* pp 658–67 (http://www.stw.nl/Programmas/Prorisc/Proceedings.htm)

[32] Marshall I, Higinbotham J, Bruce S and Freise A 2005 Use of Voigt lineshape for quantification of *in vivo* ^{1}H spectra *Magn. Reson. Med.* **37** 651–857

[33] Abragam A 1961 *The Principles of Nuclear Magnetism* (Oxford: Clarendon)

[34] Rabeson H, Ratiney H, Cudalbu C, Cavassila S, Capobianco E, de Beer R, van Ormondt D and Graveron-Demilly D 2006 Signal disentanglement in *in vivo* MR spectroscopy: by semi-parametric processing or by measurement? *ProRISC, IEEE Benelux (Veldhoven, The Netherlands, November STW)* pp 176–83 (http://www.stw.nl/Programmas/Prorisc/Proceedings.htm)

[35] Graveron-Demilly D, Diop A, Briguet A and Fenet B 1993 Product-operator algebra for strongly coupled spin systems *J. Magn. Reson.* A **101** 233–9

[36] Stancik A L and Brauns E B 2008 A simple asymmetric lineshape for fitting infrared absorption spectra *Vib. Spectrosc.* **47** 66–9

[37] de Beer R and van Ormondt D 1992 Analyis of NMR data using time-domain fitting procedures *NMR Basic Principles and Progress* vol 26 (Berlin: Springer) pp 201–48

[38] Ratiney H, Sdika M, Coenradie Y, Cavassila S, van Ormondt D and Graveron-Demilly D 2005 Time-domain semi-parametric estimation based on a metabolite basis set *NMR Biomed.* **18** 1–13

[39] Morris G A, Barjat H and Horne T J 1997 Reference deconvolution methods *J. Prog. Nucl. Magn. Reson. Spectrosc.* **31** 197–257

[40] Metz K R, Lam M M and Webb A G 2000 Reference deconvolution: a simple and effective method for resolution enhancement in nuclear magnetic resonance spectroscopy *Concepts Magn. Reson.* **12** 21–42

[41] Pijnappel W W F, van den Boogaart A, de Beer R and van Ormondt D 1992 SVD-based quantification of magnetic resonance signals *J. Magn. Reson.* **97** 122–34

TITRE en français

Algorithmes pour le traitement des distorsions de forme de raie en Spectroscopie et Imagerie Spectroscopique par Résonance Magnétique

RESUME en français

La Spectroscopie et l'Imagerie Spectroscopique de Résonance Magnétique (ISRM) jouent un rôle émergent parmi les outils cliniques, en donnant accès, d'une manière complètement non-invasive, aux concentrations des métabolites *in vivo*. Néanmoins, les inhomogénéités du champ magnétique, ainsi que les courants de Foucault, produisent des distorsions significatives de la forme de raie des spectres, induisant des conséquences importantes en terme de biais lors de l'estimation des concentrations. Lors des traitements post-acquisition, cela est habituellement traité à l'aide des méthodes de pré-traitement, ou bien par l'introduction de fonctions analytiques plus complexes.

Cette thèse se concentre sur la prise en compte de distorsions arbitraires de la forme de raie, dans le cas des méthodes qui utilisent une base de métabolites comme connaissance *a priori*. L'état de l'art est évalué, et une nouvelle approche est proposée, fondée sur l'adaptation de l'amortissement de la base des métabolite au signal acquis. La forme de raie présumée commune à tous les métabolites est estimée et filtrée à l'aide de la méthode LOWESS. L'approche est validée sur des signaux simulés, ainsi que sur des données acquises *in vitro*. Finalement, une deuxième approche novatrice est proposée, fondée sur l'utilisation des propriétés spectrales de la forme de raie commune. Le nouvel estimateur est testé seul, mais aussi associé avec l'estimateur classique de maximum de vraisemblance, démontrant une réduction significative du biais dans le cas des signaux à haut rapport signal-sur-bruit.

TITRE en anglais

Algorithms for Handling Arbitrary Lineshape Distortions in Magnetic Resonance Spectroscopy and Spectroscopic Imaging.

RESUME en anglais

Magnetic Resonance Spectroscopy (MRS) and Spectroscopic Imaging (MRSI) play an emerging role in clinical assessment, providing *in vivo* estimation of disease markers while being non-invasive and applicable to a large range of tissues. However, static magnetic field inhomogeneity, as well as eddy currents in the acquisition hardware, cause important distortions in the lineshape of acquired NMR spectra, possibly inducing significant bias in the estimation of metabolite concentrations. In the post-acquisition stage, this is classically handled through the use of pre-processing methods to correct the dataset lineshape, or through the introduction of more complex analytical model functions.

This thesis concentrates on handling arbitrary lineshape distortions in the case of quantitation methods that use a metabolite basis-set as prior knowledge. Current approaches are assessed, and a novel approach is proposed, based on adapting the basis-set lineshape to the measured signal. Assuming a common lineshape to all spectral components, a new method is derived and implemented, featuring time domain local regression (LOWESS) filtering. Validation is performed on synthetic signals as well as on *in vitro* phantom data. Finally, a completely new approach to MRS quantitation is proposed, centred on the use of the compact spectral support of the estimated common lineshape. The new metabolite estimators are tested alone, as well as coupled with the more common residual-sum-of-squares MLE estimator, significantly reducing quantitation bias for high signal-to-noise ratio data.

DISCIPLINE: EEA Traitement du signal, Application au Génie Biologique et Médical

MOTS CLES

Magnetic Resonance Spectroscopy, Magnetic Resonance Spectroscopic Imaging, Signal Processing, Parameter Estimation, Line-shape correction

INTITULE ET ADRESSE DE L'U.F.R. OU DU LABORATOIRE :

Laboratoire Creatis-LRMN CNRS UMR 5220, Inserm U630 Universite Claude Bernard LYON I, CPE Domaine Scientifique de la DOUA 3 rue Victor Grignard, Aile C 69616 Villeurbanne, FRANCE.